Numerical studies of nucleation pathways of ordered and disordered phases

Academisch Proefschrift

ter verkrijging van de graad van doctor aan de Universiteit van Amsterdam op gezag van de Rector Magnificus Prof.Dr.D.C.van den Boom ten overstaan van een door het college voor promoties ingestelde commissie, in het openbaar te verdedigen in de Aula der Universiteit op vrijdag 16 november 2007, te 14:00 uur.

door

Chantal Valeriani

geboren te Rome, Italië

Promotor: Prof. Dr. D. Frenkel

Overige leden: Prof. Dr. P. G. Bolhuis
Prof. Dr. Ir. M. Dijkstra
Dr. E. J. Meijer
Prof. Dr. F. Sciortino
Prof. Dr. Ir. B. Smit

Faculteit: Natuurwetenschappen, Wiskunde en Informatica

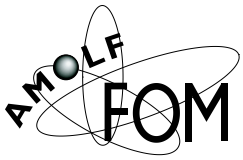

The work described in this thesis was performed at the FOM Institute for Atomic and Molecular Physics, Kruislaan 407, 1098 SJ, Amsterdam, The Netherlands. The work is part of the research program of the Stichting voor Fundamenteel Onderzoek der Materie (FOM) and was made possible by financial support from the Nederlandse Organisatie voor Wetenschappelijk Onderzoek (NWO).

Cover: Julien Husson.

Subject headings: / computer simulation / homogeneous nucleation / phase transitions / rare events / crystallization / bubble formation / nucleation under shear

A Edu.
Alla mia "grande" famiglia.

The work in this thesis is based on the following publications

Chapter 3:
Computing stationary distributions in equilibrium and non-equilibrium systems with Forward Flux Sampling.
C. Valeriani, R. J. Allen, M. J. Morelli, D. Frenkel and P. R. ten Wolde.
J. Chem. Phys. **127**, 114109 (2007).

Chapter 4:
Rate of homogeneous crystal nucleation in molten NaCl.
C. Valeriani, E. Sanz and D. Frenkel.
J. Chem. Phys. **122**, 194501 (2005).

Chapter 5:
Evidence of out-of-equilibrium crystal nucleation in suspensions of oppositely charge colloids.
E. Sanz, C. Valeriani, D. Frenkel and M. Dijkstra.
Phys. Rev. Lett. **99**, 055501 (2007).

Chapter 6:
Local structure of liquid carbon controls diamond nucleation.
L. M. Ghiringhelli, C. Valeriani, E. J. Mejer and D. Frenkel.
Phys. Rev. Lett. **99**, 055702 (2007).

Chapter 7:
Perturbation-theory estimates for the liquid-solid and the liquid-vapor γ of Lennard-Jones systems.
C. Valeriani, Z. Wang and D. Frenkel.
Accepted, *Mol. Sim.*

Chapter 8:
Homogeneous bubble nucleation in a Lennard-Jones fluid: pathway analysis and rate calculation.
Z. Wang, C. Valeriani and D. Frenkel.
In preparation.

Chapter 9:
Irreducible finite-size effects in surface free energies from crystal-nucleation data.
T. Zykova-Timan, C. Valeriani, E. Sanz, E. Tosatti and D.Frenkel.
Submitted for publication.

Chapter 10:
Study of homogeneous nucleation under shear in a 2D Ising model.
R. J. Allen, C. Valeriani, S. Tanase, D. Frenkel and P. R. ten Wolde.
In preparation.

Other publication not in this Thesis:
Fluctuation-Dissipation Relations and Energy Landscape in an Out-of-Equilibrium Strong-Glass-Forming Liquid.
A. Scala, C. Valeriani, P. Tartaglia and F. Sciortino.
Phys. Rev. Lett. **90**, 115503 (2003).

Contents

I. Nucleation 1

1. Introduction 3

2. Nucleation 9
2.1. The physical phenomenon . . . 9
2.2. Classical Nucleation Theory . . . 11
2.2.1. The free-energy barrier . . . 12
2.2.2. Equilibrium distribution of cluster sizes . . . 16
2.2.3. The nucleation rate according to CNT . . . 17
2.3. Numerical techniques to study rare events . . . 19
2.3.1. Bennett-Chandler method . . . 23
2.3.1.1. The Umbrella Sampling technique . . . 24
2.3.1.2. Estimation of the attachment rate in the kinetic pre-factor . 27
2.3.2. Forward Flux Sampling . . . 28
2.3.2.1. Numerical computation of the steady-state flux . . . 29
2.3.2.2. Numerical computation of $P_{0\to B}$ . . . 30
Appendix A: Order parameter used to study homogeneous crystal nucleation . . . 32
Appendix B: Landau free energy . . . 36
Appendix C: Details on the FFS calculations . . . 37
Appendix D: Tips for beginners . . . 38

II. Forward Flux Sampling technique applied to nucleation phenomena 41

3. Computing stationary distributions with FFS 43
3.1. Introduction . . . 43
3.2. Stationary distributions: the theory . . . 44
3.3. Stationary distributions: the method . . . 46
3.4. Results . . . 48
3.4.1. Testing on a one-dimensional system . . . 48
3.4.2. Testing on the two-dimensional Maier-Stein system . . . 50

3.4.3. Homogeneous nucleation in a two-dimensional Ising model 53
3.5. Conclusions 57

III. Ionic systems 59

4. Rate of homogeneous crystal nucleation in molten NaCl 61
4.1. Introduction 61
4.2. Simulations details 62
4.3. Results 64
4.4. Conclusions 71
Appendix A: Tail corrections of the total energy 72
Appendix B: Crystalline clusters in NaCl 73
Appendix C: Computing $\beta\Delta\mu$ 74

5. Out-of-equilibrium crystal nucleation in suspensions of oppositely charged colloids 77
5.1. Introduction 77
5.2. Simulation details 78
5.3. Results 80
5.4. Conclusions 84
Appendix A: Charge swap move 85
Appendix B: Order parameter 85

IV. Covalent systems: the Carbon case 87

6. Local structure of liquid carbon controls diamond nucleation 89
6.1. Introduction 89
6.2. Simulation details 90
6.3. Results 91
6.4. Conclusions 94
Appendix A: $LCBOPI^+$ 96
Appendix B: Order parameter to study diamond nucleation from molten carbon . . 97
Appendix C: Self-diffusion coefficient 99
Appendix D: Computation of the crystal nucleation rate at state point A and B . . . 100
Appendix E: Computing the super-saturation 101
Appendix F: Inter-facial free-energy estimate via the free-energy barrier 102
Appendix G: Estimating the nucleation rates throughout the region of the phase diagram between T_A and T_B 104

V. Bubble nucleation 107

7. Perturbation-theory estimates of liquid-solid and liquid-vapour γ for Lennard-Jones **109**
7.1. Introduction . . . 109
7.2. Method . . . 110
7.3. Results . . . 114
7.3.1. Calculation of the liquid-solid inter-facial free energy . . . 114
7.3.2. Calculation of the liquid-vapour surface tension . . . 115
7.4. Conclusions . . . 117
Appendix A: Comparison with Fowler's expression . . . 120

8. Homogeneous Bubble Nucleation in the Lennard-Jones fluid. **123**
8.1. Introduction . . . 123
8.2. Simulation details . . . 125
8.3. Results . . . 128
8.4. Conclusions and future work . . . 129
Appendix A: Details on the thermostat and the barostat . . . 132
Appendix B: TSF-LJ liquid-vapour phase diagram . . . 132
Appendix C: Lowe-Andersen thermostat and the FFS scheme . . . 134

VI. The γ mystery 137

9. Irreducible finite-size effects in surface free energies from crystal-nucleation data **139**
9.1. Introduction . . . 139
9.2. Simulation details . . . 140
9.3. Results . . . 141
9.4. Conclusions . . . 146
Appendix A: Averaged cluster shapes and numerical Wulff's construction . . . 147
Appendix B: Thermodynamic versus geometric N . . . 149
Appendix C: Different choices of the dividing surface bring to different values of γ 149
Appendix D: Gibbsian droplet model and the compressibility effect . . . 153
Appendix E: Comparison with edge and corner free energies at 0 Kelvin . . . 162
Appendix F: Comparison with experiments . . . 164

VII.Homogeneous nucleation under shear 165

10. Study of homogeneous nucleation under shear in a 2D Ising model **167**
10.1. Introduction . . . 167
10.2. Simulation details . . . 169
10.3. Results . . . 171
10.4. Conclusions . . . 176
Appendix A: Shear algorithm . . . 179

Bibliography **181**

Summary **192**

Samenvatting **196**

La nucleazione **200**

Acknowledgments-Ringraziamenti **203**

Part I.

Nucleation

1. Introduction

It is common experience that liquid water if cooled at ambient pressure below its melting temperature of 0 $^{\circ}C$, freezes into ice. However, ice formation happens only when liquid water is thermalised at a much lower temperature than the melting one. It is indeed possible to test in the laboratory that a sample of distilled water can be thermalised at -10 $^{\circ}C$ without freezing and, if divided into small droplets, it can be even super-cooled down to -30 $^{\circ}C$ without converting into ice. More in general, many purified liquids can be maintained in a metastable state for long time until a spatially and temporally localised density fluctuation of the new stable phase is larger than a *critical* size, and the all system transforms into ice. The same holds if the starting system is a super-heated liquid changing into a vapour. This mechanism demonstrates the existence of a kinetic barrier to first order phase transitions, and is called *homogeneous nucleation*. Due to the presence of a free-energy barrier, the nucleation process can be considered as an example of a *rare event* happening in Nature. Rare events are activated processes, for which the average waiting time between events can be orders of magnitude longer than the event itself. As such, rare events are intrinsically difficult to investigate.

Fahrenheit was the first who did a systematic study of crystallisation of water in 1714 [1], experimenting for the first time the concept of super-cooling. Later on, Gay Lussac extended Fahrenheit's observations showing that the phenomenon of super-cooling was not only valid for water [2]. However, the first one who gave a detailed description of the criteria for phase equilibria was Josiah Willard Gibbs in 1878 [3]. He suggested the distinction between stable metastable and unstable phases, and that in order to understand phase transformations in the metastable region, it is necessary to measure the work needed to form a droplet of the new stable phase. This concept was revisited in 1926 by Volmer and Weber [4], who formulated a phenomenological theory that describes the nucleation phenomenon, the so-called Classical Nucleation Theory (CNT). Volmer and Weber stated that the metastability of a supersaturated phase was mainly a kinetic effects. Studying nucleation of a liquid droplet (new phase B) from a metastable vapour (parent phase A), they adopted the Gibbs formulation of the reversible work for the formation of a nucleus of phase B from the metastable phase A to calculate the equilibrium cluster density distribution; they also obtained an expression for the nucleation rate. Later on, Becker and Döring derived the steady-state nucleation rate [5]

$$R = N_1 k_{+,\mathrm{n}^*} \left(\frac{|\Delta G''(n)|_{n^*}}{2\pi k_B T} \right)^{1/2} e^{-\beta \Delta G(n^*)} \tag{1.1}$$

where N_1 is the equilibrium distribution of particles, k_{+,n^*} the attachment rate of single particles to the critical cluster, $|\Delta G''(n)|_{n^*}$ the second derivative of the Gibbs free energy $\Delta G(n)$ as a function of the phase B-cluster of size n, n^* is the critical cluster size, corresponding to the top of the free-energy barrier $\Delta G(n^*)$.

CNT is based on the capillary approximation, in which small portions of the new phase are treated as if they represent macroscopic regions of space. According to CNT, the Gibbs free-energy barrier ΔG of the growing phase-B cluster with respect to phase A, is computed by means of few *a priori* assumptions on the growing cluster, such as that it should have a geometrically well defined shape, should be characterised by bulk properties of the B phase (like density and inter-facial free energy), and be incompressible. Thus, ΔG for a spherical cluster of radious R is written as

$$\Delta G(R) = \gamma_\infty 4\pi R^2 + \frac{4}{3}\pi R^3 \rho_B \Delta\mu, \tag{1.2}$$

where γ_∞ is the inter-facial free energy between phase A and B, ρ_B the phase B density, and $\Delta\mu$=$\mu_B(P_B) - \mu_A(P_A)$ the chemical potential difference between the two phases, also driving force for the nucleation of phase B. ΔG is characterised by a surface term, that corresponds to the free-energy cost (positive) to make the surface of the new phase B (first addendum), and a free-energy gain (negative) the system gets while the cluster of phase-B is growing. The two terms balance and ΔG reaches its maximum ($\Delta G(n^*)$) at a size of the cluster n^* defined as *critical cluster*; $\Delta G(n^*)$ is the height of the free-energy nucleation barrier.

Thus, once the nucleation rate is measured in experiments, it is possible to use CNT to estimate the height of the nucleation barrier $\Delta G(n^*)$ [6], and from this the inter-facial free energy by means of eq. 1.2.

Even though widely spread, there are many cases where CNT fails in describing the nucleation process. Experiments on non-polar fluids have shown that CNT predicts very accurate nucleation rates, whereas for strongly polar fluids CNT fails in predicting the rates by several orders of magnitude. Oxtoby and Evans [7] demonstrated that by increasing the range of the attractive tail on a realistic potential, the initial agreement between CNT and a non-classical theory, based on Density Functional Theory, completely vanished. Although nucleation theory is one of the few areas of science in which agreement of predicted and measured rates to within several orders of magnitude is considered a major success, few years ago Oxtoby pointed out that a reason why CNT works in many cases is due to a " cancellation of errors" [8]:

1. on one side, the assumptions that the surface free energy of a small cluster is the same as of an infinite planar interface and does not depend on the cluster's curvature, should lower the value of the nucleation rate;

2. on the other side, the fact that the nucleation barrier does not vanish at the spinodal point, whereas it should, should increase the rate.

Both factors lead to a cancellation of errors at certain temperatures, but not avoiding the incorrect temperature dependence of the nucleation rate estimated by Classical Nucleation Theory. Nevertheless, CNT is nowadays the most used theory to understand the nucleation processes from experimental or numerical measurements.

Computer simulations are a natural tool to understand the nucleation mechanism at a microscopic level. Simulations might help where experiments have limitations: in fact, experiments cannot detect nucleation pathways of clusters containing only few particles. Moreover,

simulations might also be useful to support the develop of a "new" theory of nucleation, that could improve the already existing CNT.

Being nucleation a rare event, it is characterised by a time-scale separation: on one side, the long average waiting time between two events; on the other side, the very short event itself. In studying activated processes, such as nucleation, *brute force* numerical simulations might not be enough, as they tend to be computationally very demanding. Thus, we need to employ *ad hoc* simulation techniques. Over the past few years, there has been a flourishing of computational methods for finding transition pathways for rare events in both equilibrium and non-equilibrium systems.

The above-mentioned time-scales separation allows to describe the kinetic of the process as a two-step procedure, as presented in the Transition State Theory (TST) theory [9, 10]. Central in TST, is the use of a reaction coordinate Q, that quantifies the transition from phase A to phase B. For a crystal nucleation, Q can be considered as the biggest solid cluster size. By means of Q is then possible to identify in the phase space the dynamical bottleneck for the rare transition to happen: Q^*, the saddle point in the phase space that separates the two phases A and B, which only rarely visited by the system. Once Q^* is known, the nucleation rate can be written as the product of two factos

$$R = \kappa(Q^*)P(Q^*), \tag{1.3}$$

where the probability for the system to be at Q^*, $P(Q^*)$, is multiplied by the frequency at which the saddle point Q^* is crossed. $P(Q^*)$ is a function of the reversible work needed to allow the system to reach Q^*: $\beta\Delta G$. This is the procedure followed in the Bennett-Chandler (BC) scheme, one of the techniques we have used in our nucleation studies. The Gibbs free-energy barrier to nucleation can be computed via the Landau free-energy function of the order parameter Q, by means of the Umbrella Sampling technique [11]; while $\kappa(Q)$ can be computed by means of Molecular Dynamics or kinetic Monte Carlo, as explained in subsection 2.3.1.2.

The other technique we have utilised to study nucleation phenomena is the so-called Forward Flux Sampling technique. The Forward Flux Sampling (FFS) technique is a novel simulation technique developed to both analyse the nucleation pathways and calculate the rate to nucleation. FFS needs an order parameter to follow the transition from A to B, but this choice does not determine the results obtained. Being at $Q = \lambda_0$ the boundary of phase A, the FFS nucleation rate is expressed as

$$R_{AB} = \Phi_{A\to 0} \cdot P_{0\to B}, \tag{1.4}$$

where $\Phi_{A\to 0}$ is the steady-state flux of trajectories leaving state A, which is the number of crossings per unit of time and volume of the first interface λ_0, and $P_{0\to B}$ is the overall probability that trajectories, coming from A and initially at λ_0, manage to reach the final state B.

As dated as widespread in our daily life experience, nucleation is still a not completely understood phenomenon. Thus, our contribution is devoted to add another piece to this intriguing puzzle.

Overview

This thesis focus on the study of the homogeneous nucleation process in different systems.

In chapter 2 we discuss Classical Nucleation Theory, and present the techniques used in this thesis: Umbrella Sampling(US) [11, 12] to compute the free-energy barrier that must be known to compute nucleation rates if the process can be described as a diffusive barrier crossing, and Forward Flux Sampling(FFS) [13, 14, 15] to analyse the nucleation pathways and compute the nucleation rate. We employ for the first time Forward Flux Sampling to compute the free-energy barrier for nucleation, as we will explain in chapter 3. Having introduced the necessary numerical tools, we apply them to study crystal nucleation in ionic, covalent bonded, and dispersive forces systems.

In chapter 4 we investigate crystal nucleation from the melt in an super-cooled sodium chloride liquid, and compute the nucleation rate using both US and FFS.

In chapter 5 we test the Stransky-Totomanow [16] conjecture, by over-compressing a system made of oppositely charged colloids [17]. In this system, there are several possible crystal-nucleation pathways. We use simulations to investigate which of the many possible crystal phases [17] will form under what circumstances.

In chapter 6 we study the effect of the local structure of the parent liquid on crystal nucleation. We focus on the example of diamond nucleation from liquid carbon. Liquid carbon is peculiar because its local structure changes dramatically with temperature and pressure. At temperatures around 5000K and pressures around 80GPa, it mainly manifests a *four-fold coordinated* structure, whereas at temperatures around 3800K and pressure around 30GPa it exhibits a *three-fold coordinated* structure. By simulation, we can study how such a change in the structure of the liquid affects the pathway for crystal nucleation.

In chapter 7 we apply the standard thermodynamic perturbation theory to estimate the effect of small changes in the attractive part of the inter-molecular potential on the liquid-vapour surface tension and, for the first time, on the liquid-solid inter-facial free energy in a system with different truncations of the Lennard-Jones potential. These calculations provide useful input for analytical (CNT) estimates of nucleation rates in a number of systems.

We then focus on the bubble nucleation phenomenon from a super-heated Lennard-Jones fluid. We compute the nucleation rate and analyse the pathways (chapter 8). To our knowledge, this is the first time Forward Flux Sampling is used in combination with a Molecular Dynamics simulation.

In chapter 9 we investigate the origins of the discrepancy between the liquid-solid inter-facial free energy of sodium chloride as obtained from Classical Nucleation Theory with estimates based on a study of partial wetting at the solid-liquid-vapour interface [18].

Finally, we show how the Forward Flux Sampling technique can be used to calculate the steady-state distributions of non-equilibrium systems. In chapter 10 we apply an external shear to a two-dimensional Ising system, initially thermodynamically metastable, and study the effect the shear has on the nucleation process.

Before starting the reading of this thesis, we want to add few useful remarks:

- the word "solid" is always used with the reference to "crystal", a periodically long-range ordered solid. We have not taken under consideration other classes of solids, like the amorphous ones.
- the word "state" is quite often used with the same meaning as "phase". This is correct as long as each state exists only in one phase: as an example, if we look at diamond and graphite, both are in a solid state but correspond to different phases of solid carbon. More in general, this is the case whenever a material presents different crystal structure;
- quotations at the beginning of the chapters might refer to the work done with collaborators.

2. Nucleation

Tu se' lo mio maestro e 'l mio autore,
tu se' solo colui da cu' io tolsi
lo bello stilo che m'ha fatto onore.
Dante Alighieri, Primo canto, Inferno, Divina Commendia.

This chapter, is devoted to a description of the physics behind the nucleation phenomenon and the numerical tools needed to study it.

In section 2.1 we introduce the nucleation phenomenon, describe the distinction between homogeneous and heterogeneous nucleation, and explain the importance of studying homogeneous nucleation. In section 2.2 we illustrate the Classical Nucleation Theory (CNT), an empirical theory to interpret homogeneous nucleation phenomena. We show the way to define the reversible work for the formation of a nucleus of the stable phase, that leads to the free energy nucleation barrier, and the steady-state nucleation rate, a quantity that can be measured both in experiments and in computer simulations. To conclude, we devote section 2.3 to give a short overview on few numerical techniques developed to study rare events, and we mainly focus our attention on two of them we have used along our studies to compute the nucleation rate: the Bennett-Chandler scheme [10] and the Forward Flux Sampling technique [13, 14, 15]. Within the Bennett-Chandler scheme, the free-energy barrier can be computed by means of the Umbrella Sampling technique [11] (see subsection 2.3.1.1): this gives the probability to find a critical-size solid cluster in the system; whereas the kinetic prefactor κ can be computed as the flux of trajectories at the top of the free-energy barrier, as explained in subsection 2.3.1.2. Concerning the Forward Flux Sampling (see section 2.3.2), the computation of the flux through the first interface $\Phi_{A\to 0}$ is described in subsection 2.3.2.1, whereas the computation of the probability that configurations at the first interface can reach the final state ($P_{0\to B}$) is analytically described in subsection 2.3.2.2. Appendix D contains few tips hopefully useful to start simulating nucleation problems.

2.1. The physical phenomenon

Nucleation is the onset of a *first order phase transition* [19]. According to Ehrenfest, a first order phase transition happens whenever the first derivative of the free energy with respect to a thermodynamic variable is discontinuous. The various liquid-to-solid, liquid-to-vapour and vapour-to-solid phase transitions are classified as first-order phase transitions, because they involve a discontinuous change in the density ρ, which corresponds to the first derivative of

the Gibbs free energy per particle (the chemical potential μ) with respect to the pressure (P) at constant temperature (T): $\left(\frac{\partial \mu}{\partial P}\right)_T = \frac{1}{\rho}$.

In 1906, Gibbs was the first to propose in a liquid-to-vapour phase transition a distinction between two different types of instability, which characterise the early stages of phase transitions [20]. Figure 2.1 shows an isotherm curve of a mono-atomic simple fluid in the pressure(P)-volume(V) plane: P_{coex} indicates the pressure at which the two phases coexist, V_L and V_V the respective volumes. The region between V_L and V_V is the *coexistence* region.

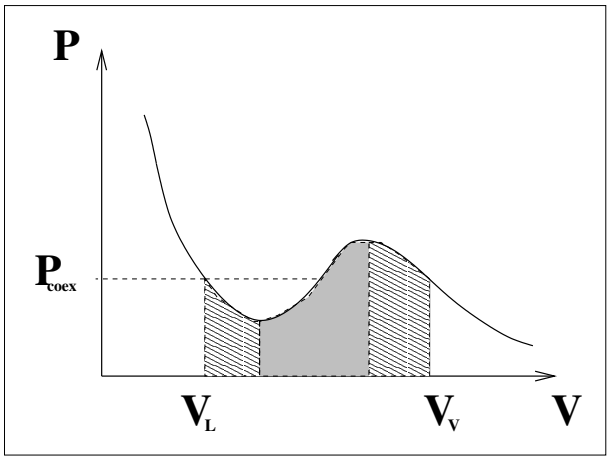

Figure 2.1.: Isotherm curve of a mono-atomic simple fluid in the pressure(P)-volume(V) plane. P_{coex} indicates the pressure at which the two phases coexist, at volumes V_L and V_V. The uniform-grey zone is the spinodal region, whereas the dashed is the binodal region.

A phase is considered to correspond to a minimum in the Gibbs free energy, if its isothermal compressibility κ_T is positive [1], where κ_T is defined as

$$\kappa_T = -\left(\frac{1}{V}\right)\left(\frac{\partial V}{\partial P}\right)_T . \tag{2.1}$$

Let's consider the system initially in the vapour phase (V_V in fig. 2.1) and compress it (increasing the pressure) at constant temperature in the coexistence region: the system is now in a *non equilibrium* state. Classical mean-field theories predict a Van der Waals loop in the non-equilibrium region: there are two kinds of transformations to put a thermodynamically stable system in a non-equilibrium state. The dashed in the coexistence region is characterised by $\partial P/\partial V < 0$, meaning that the isothermal compressibility stays positive: this is the so-called *binodal* region, where a compression leads the system to a a *metastable* state. Thus, both stable and metastable phases are distinguished by a positive value of κ_T. However, there

[1] Since κ_T is proportional to the second derivative of the Gibbs free energy.

are two inflection points where $\partial P/\partial V$ changes sign. This happens in the uniform-grey region where κ_T becomes negative: the so-called *spinodal* region, where a compression leads the system to an *unstable* state.

Phase transformations in the metastable region are initiated by *nucleation*, a process generated by finite-amplitude and localised fluctuations. Whereas phase transformations in the unstable region occur by *spinodal decomposition* mechanism [21], identified by infinitesimal amplitude and non localised fluctuations, that can be governed by the Cahn-Hilliard equation [22].

Once the metastable phase is formed in the binodal region, there is a finite free-energy barrier the system has to overcome in order to phase transform into the stable phase. Whereas at the spinodal point, the free-energy barrier vanishes, and a small perturbation in density leads to a decrease in free energy, and thus a spontaneous growth of the perturbation.

When talking about nucleation, it is important to distinguish between *heterogeneous* and *homogeneous* nucleation. Heterogeneous nucleation happens whenever the phase transition can be assisted by walls or impurities within the system: clusters of the new phase are then formed at the surface of these "foreign bodies". In contrast, homogeneous nucleation occurs due to spontaneous density fluctuations in the bulk of a pure phase, as shown in fig. 2.2.

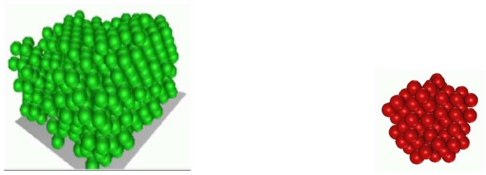

Figure 2.2.: On the left-side: an example of heterogeneous crystal nucleation at the wall. On the right-side: critical density fluctuation representing a solid in a mono-atomic system. In both cases, the surrounding metastable liquid is not represented. (Courtesy of Angelo Cacciuto)

Even though in real life heterogeneous nucleation is more likely to happen, homogeneous nucleation is more than just the theoretician's desire to idealise (and simplify) the physics of phase transitions. There are a number of real world situations in which homogeneous nucleation is the dominant mechanism for phase transitions, like condensation in supersonic nozzles [23], explosions occurring when a cold liquid comes in contact with a much hotter one [24], and formation of heavily microcrystallised ceramics [25]. A deep and clear understanding of the process of homogeneous nucleation is still lacking, making homogeneous nucleation a challenging topic to study.

2.2. Classical Nucleation Theory

The most used theory to describe homogeneous nucleation is Classical Nucleation Theory (CNT). CNT is commonly employed to predict the rate of nucleation and estimate the height

of the nucleation barrier. The theory was first formulated by Volmer and Weber [4], then modified by Farkas [26], Becker and Döring [5], and Turnbull and Fisher [27]. Looking at the phase transition of a new stable phase happening in a metastable parent phase, Volmer and Weber applied the Gibbs formulation of the reversible work of the formation of a static cluster of the new phase, thus building the first theory of nucleation that would calculate the nucleation rate. The latter was considered to be proportional to the rate of formation of critical-sized clusters in equilibrium. Later on, Farkas formulated a kinetic model for cluster evolution that became the basis for subsequent modifications. Afterwards, Becker and Döring argued that a steady-state distribution was more suitable than the equilibrium distribution proposed by Volmer and Weber, and obtained an expression for a *steady-state* nucleation rate in a vapour condensation experiment. Turnbull and Fisher first applied the Becker and Döring formalism to the case of nucleation in condensed systems.

In the following subsection, we show the derivation of the reversible work for the formation of a cluster in a metastable parent phase according to CNT, define the equilibrium distribution of cluster sizes, and finally derive the expression for the nucleation rate,

2.2.1. The free-energy barrier

We now consider a metastable phase A, for instance a vapour (left-side of fig. 2.3), at thermodynamic conditions where phase B (for instance a liquid) is the stable phase. As figure 2.3 shows, clusters of phase B will then start growing in phase A (right-side of fig. 2.3).

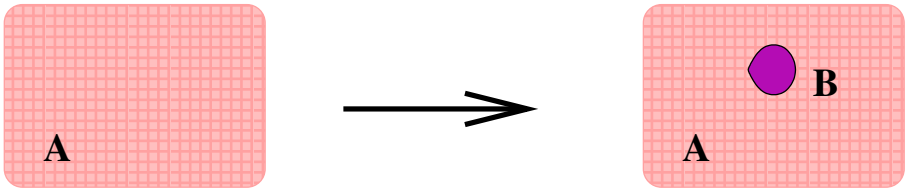

Figure 2.3.: Metastable phase A (on the left-hand side). Nucleation of the new stable phase B (on the right-hand side).

In what follows, we indicate with system I, the initial metastable phase A (on the left-hand side of fig. 2.3) and system II the metastable phase A where a phase B cluster is growing (on the right-hand side of fig. 2.3). Our aim is to compute the reversible work for the formation of a cluster of the new phase B in the parent phase A at constant temperature and pressure. We start with computing the internal energy of both systems I and II. The internal energy of system I containing only the A phase, can be written as

$$U_A^I = T^I S^I - P^I V + \mu^I N, \tag{2.2}$$

where T is the temperature of the system, S the total entropy, P the pressure, V the total volume, μ the chemical potential and N the total number of particles ($N = N_A$ in this case).

The internal energy of system II, where the metastable phase A contains the phase B cluster, is

$$U^{II}_{A+B} = T^{II}S^{II} - P^{II}_A V^{II}_A - P^{II}_B V^{II}_B + \mathbf{A}\gamma + \mu^{II}_A N_A + \mu^{II}_B N_B \quad (2.3)$$

where P_A and P_B are the pressures of phase A and B, respectively, V_A and V_B their volumes, γ the inter-facial free energy existing between A and B, $\mathbf{A}$ the surface area of the growing stable phase, μ_A and μ_B their chemical potentials, and N_A (N_B) the number of A (B) particles in the system.

We assume uniformity in the temperature throughout the system ($T^I = T^{II}$), but not uniformity of the pressure or the chemical potential. We anticipate that the uniformity of the chemical potential only holds for a system containing the critical cluster. Considering the Gibbs's *capillarity approximation*, according to which the surface dividing the two phases is sharp, contains no particles and has no volume, the total number of particles in the system is given by $N = N_A + N_B$ and the total volume $V = V_A + V_B$. Thus, eq. 2.3 can be written as

$$U^{II}_{A+B} = T^{II}S^{II} - P^{II}_A V + (P^{II}_A - P^{II}_B)V^{II}_B + \mathbf{A}\gamma + \mu^{II}_A N + (\mu^{II}_B - \mu^{II}_A)N_B. \quad (2.4)$$

In a constant temperature - constant pressure ($P^I = P^{II}_A = P$) transformation, we can assume that $\mu^{II}_A = \mu^I$, being $N_A \gg N_B$. Thus, the reversible work to grow a cluster of phase B from the metastable phase A is expressed by the change in the Gibbs free energy between G^I_A and G^{II}_{A+B}. As in an NPT ensemble, $\Delta G = \Delta U + P\Delta V - T\Delta S$, using eqns. 2.2 and 2.4

$$\Delta G = G^{II}_{A+B} - G^I_A = (P - P^{II}_B)V^{II}_B + \mathbf{A}\gamma + (\mu^{II}_B - \mu^{II}_A)N^{II}_B, \quad (2.5)$$

where $\mu^{II}_B = \mu^{II}_B(P_B)$ and $\mu^{II}_A = \mu^{II}_A(P_A)$. In order to obtain the final Classical Nucleation Theory expression of the nucleation barrier, there are few assumptions to make:

1. the growing cluster is characterised by the bulk properties of the stable phase B;

2. the inter-facial free energy γ is independent on the radius R of the cluster, or $\gamma = \gamma_\infty$, being γ_∞ the inter-facial free energy of a sphere with an infinite radius, i.e. a flat interface. This condition is satisfied at the surface of tension. In case the Gibbs absorption at the surface of tension is zero, the surface of tension coincides with the equimolar dividing surface. This allow to set the mathematical surface dividing the two phases at the equimolar dividing surface (or equivalently, at the surface of tension), i.e. $R = R_e = R_s$;

3. the cluster is incompressible, meaning that its density ρ does not change with pressure. As we know that, at constant temperature $\frac{d\mu}{dP} = \frac{V}{N} = \frac{1}{\rho}$, the chemical potential of the new phase B can then be written as

$$\mu^{II}_B(P^{II}_B) = \mu^{II}_B(P^{II}_A) + \frac{P^{II}_B - P^{II}_A}{\rho_B}, \quad (2.6)$$

where ρ_B is the B phase density.

Using eq. 2.6 and all the CNT assumptions, eq. 2.5 becomes the CNT expression of the excess free energy to form a cluster of area $\mathbf{A}$ containing N_B particles

$$\begin{aligned} \Delta G(N_B) &= \mathbf{A}(N_B)\gamma_\infty + [\mu_B^{II}(P_A) - \mu_A^{II}(P_A)]N_B \\ &= \mathbf{A}(N_B)\gamma_\infty - |\Delta\mu|N_B \end{aligned} \tag{2.7}$$

where the expression of $\mathbf{A}$ depends on the cluster shape, and $|\Delta\mu| = [\mu_B^{II}(P_A) - \mu_A^{II}(P_A)]$ is the chemical potential difference between the two phases, and it is a negative quantity.

CNT also assumes that the cluster of the new phase B should have a spherical shape with radius R. Hence, being $\mathbf{A} = 4\pi R^2$ and using the relation $\rho_B = N_B/V_B$ being $V_B = \frac{4}{3}\pi R^3$, the Gibbs free energy of formation of a spherical cluster of phase B with radius R in the metastable phase A is

$$\Delta G(R) = 4\pi R^2\gamma_\infty - |\Delta\mu|\rho_B\frac{4}{3}\pi R^3 \tag{2.8}$$

A representation of ΔG is given in fig. 2.4. Eq. 2.8 contains two terms:

1. the first is a "surface" term, that takes into account the free-energy cost of creating an interface between phases A and B. This term is positive and proportional to the surface area of the cluster (*surface free energy*);
2. the second is a "bulk" term, that expresses the fact that phase B is more stable than the supersaturated phase A. This term is negative and proportional to the volume of the cluster (*volume free energy*). $\Delta\mu$ is the driving force for nucleation to happen.

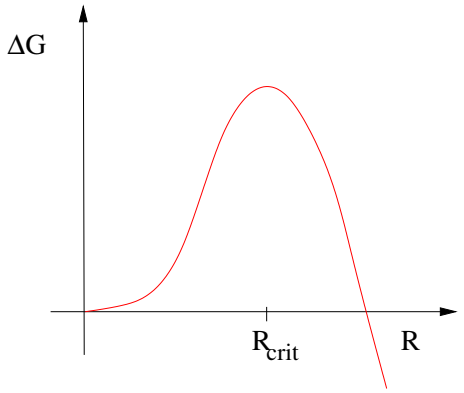

Figure 2.4.: Gibbs free energy of a cluster as a function of its radius R according to the CNT.

The function ΔG goes through a maximum at

$$R^* = \frac{2\gamma_\infty}{\rho_B|\Delta\mu|}, \tag{2.9}$$

that denotes the critical cluster size. The value of ΔG at this maximum, i.e. the height of the nucleation barrier, is

$$\Delta G^* = \frac{16\pi}{3}\frac{\gamma_\infty^3}{(\rho_B|\Delta\mu|)^2}. \tag{2.10}$$

We stress the fact that the height of the nucleation barrier is directly proportional to the third power of the inter-facial free energy (γ_∞), and inversely proportional to the square of both the density of the stable phase (ρ_B) and the super-saturation ($|\Delta\mu|$). When the two phases A and B coexist, $\Delta\mu = 0$ and the barrier goes to infinity; if the system is in a stable phase, it will never transform by homogeneous nucleation into the other coexisting phase.

Within the CNT framework, we define the Laplace pressure, that is the difference between the pressure of the metastable phase A surrounding the cluster and the pressure inside the growing cluster B:

$$\Delta P = \frac{2\gamma_\infty}{R^*}. \tag{2.11}$$

the Laplace pressure depends on the critical cluster size and γ_∞.

Eq. 2.8 can also be expressed as a function of the number of particles in the growing cluster of the new phase N_B:

$$\Delta G(N_B) = (36\pi)^{1/3}\gamma_\infty(N_B/\rho_B)^{2/3} - N_B|\Delta\mu|. \tag{2.12}$$

It follows that N_B^*, the number of particles in the critical cluster, is given by

$$N_B^* = \frac{32\pi\gamma_\infty^3}{3\rho_B^2|\Delta\mu|^3}. \tag{2.13}$$

In what follows, we will indicate the number of phase-B particles N_B as n.

When Classical Nucleation Theory is compared with experiments or theory (like density functional theory), it shows an incorrect temperature dependence [8]. Two possible reasons might be:

1. the inter-facial free energy of small clusters should depend on curvature, and within the CNT framework it does not;

2. the nucleation barrier ΔG should vanish at the spinodal.

While the first feature should lower the nucleation rate, the second feature should increase it. This effects can lead to a cancellation of errors at some temperature.

γ_∞ computed from the top of the nucleation barrier

Using the CNT assumption of incompressibility of the cluster we known that $N_B = \rho_B V_B$, where V_B is the cluster volume. In case of a cubic cluster $N_B = \rho_B L^3$, where L is the edge of the cluster. Eq. 2.7 then becomes

$$\Delta G(L) = 6L^2\gamma_\infty - L^3\rho_B|\Delta\mu|, \tag{2.14}$$

while for a spherical one we refer to eq. 2.8. From eq. 2.14, the top of the free-energy barrier corresponding to a cubic critical cluster is

$$\Delta G^* = \frac{32\gamma_\infty^3}{(\rho_B|\Delta\mu|)^2}. \tag{2.15}$$

By means of equation 2.15, we can estimate the value of γ_∞. The same procedure has to be followed in case of a spherical cluster, leading to

$$\gamma_\infty = \left(\frac{3}{16\pi}\Delta G \times (|\Delta\mu|\rho)^2\right)^{1/3} \qquad \text{and} \qquad \gamma_\infty = \left(\frac{1}{32}\Delta G \times (|\Delta\mu|\rho)^2\right)^{1/3}, \tag{2.16}$$

for a spherical and cubic cluster shape respectively.

2.2.2. Equilibrium distribution of cluster sizes

The Gibbs free-energy difference between system II and system I at constant temperature is given by eq. 2.7, where we call $N_B = n$ and introduce the chemical potential of a cluster of size n as $\mu_n(P) = \gamma\mathbf{A} + n\mu_B(P)$, being P the pressure of phase A.

In order to compute the equilibrium distribution of phase-B clusters, we assume a low concentration of clusters forming in the metastable phase A. This assumption allows us to ignore the interactions between the clusters, and consider the system as an "ideal" mixture, made of N_1 monomers, N_2 dimers, up N_n clusters of size n, all embedded in phase A. Thus, a size n cluster exerts a partial pressure P_n on the system (such as $\sum_{i=1}^{\infty} P_i = P$). The chemical potential of a size n cluster at P_n is

$$\mu_n(P_n) = \mu_n(P) + k_B T \ln\left(\frac{P_n}{P}\right), \tag{2.17}$$

obtained by means of $d\mu/dP = 1/\rho$ and the equation of state of an ideal gas ($P = \rho k_B T$). It is then possible to rewrite eq. 2.7 as

$$\Delta G = \mu_n(P_n) - k_B T \ln\left(\frac{P_n}{P}\right) - n\mu_A(P). \tag{2.18}$$

Using the fact that, at equilibrium, $\mu_n(P_n) = n\mu_A(P)$, the expression of the free-energy barrier within CNT becomes

$$\Delta G = -k_B T \ln\left(\frac{P_n}{P}\right). \tag{2.19}$$

By means of Raoult's law, P_n/P is equal to $N_n/N_A \sim N_n/N$, and the final CNT expression of the equilibrium distribution of clusters of size n is

$$\Delta G = -k_B T \ln\left(\frac{N_n}{N}\right) = -k_B T \ln\left(P(n)\right), \tag{2.20}$$

where $P(n)$ is the probability to have clusters of size n.

2.2.3. The nucleation rate according to CNT

Experimental nucleation data are generally interpreted via a phenomenological reaction rate theory, the Classical Nucleation Theory, first formulated by Volmer and Weber [4]. Classical Nucleation Theory (CNT) consents to understand the kinetics of the nucleation process of clusters of the new phase B from the metastable initial phase A, by computing the nucleation rate.

CNT assumes that phase B clusters slowly grow or shrink via the attachment of single particles:

$$\begin{aligned} \mathrm{B}_{n-1} + \mathrm{B}_1 &\underset{k_{-,\mathrm{n}}}{\overset{k_{+,\mathrm{n}-1}}{\rightleftharpoons}} \mathrm{B}_n \\ \mathrm{B}_n + \mathrm{B}_1 &\underset{k_{-,\mathrm{n}+1}}{\overset{k_{+,\mathrm{n}}}{\rightleftharpoons}} \mathrm{B}_{n+1} \end{aligned} \tag{2.21}$$

where B_{n-1} is a cluster with $n-1$ particles, B_1 with one particle (monomer) $k_{+,\mathrm{n}-1}$ the attachment rate of one single monomer to a $n-1$ cluster, and $k_{-,\mathrm{n}}$ the detachment rate. This assumption was initially made for vapour-liquid nucleation, where the concentration of monomers is much larger than the one of dimers, trimers, etc., and where collisions between growing clusters are extremely rare [30]. It is possible to compute the time-dependent cluster distribution $N_n(t)$, by solving the following Master equation [31]:

$$\frac{dN_n(t)}{dt} = N_{n-1}(t)k_{+,\mathrm{n}-1} - [N_n(t)k_{-,\mathrm{n}} + N_n(t)k_{+,\mathrm{n}}] + N_{n+1}(t)k_{-,\mathrm{n}+1}. \tag{2.22}$$

The net nucleation rate at a given cluster size n is the time-dependent flux of clusters that reached n, and is given by

$$R_{n,t} = N_n(t)k_{+,\mathrm{n}} - N_{n+1}(t)k_{-,\mathrm{n}+1}. \tag{2.23}$$

To compute the rate in eq. 2.23, Volmer and Weber made few assumptions:

1. the back flux was zero when the clusters were larger than the critical cluster size: $N_n(t) = 0$ for $n > n^*$;
2. for $n \leq n^*$, they assumed that $N_n(t)$ was the *equilibrium* clusters distribution N_n (see eq. 2.20), with $N \sim N_1$ the total number of monomers, and $e^{-\beta\Delta G(n^*)}$ determines the probability to find the critical cluster in equilibrium with its environment.

Therefore, eq. 2.23 is expressed as

$$R = N_n k_{+,\mathrm{n}^*} = N_1 k_{+,\mathrm{n}^*} e^{-\beta\Delta G(n^*)} \tag{2.24}$$

where k_{+,n^*} is the attachment rate of a single particle to the critical cluster, and $\Delta G(n^*)$ is the free-energy barrier to nucleation.

Subsequently, Becker and Döring replaced the equilibrium clusters distribution N_n with a *steady-state* clusters distribution N_n^s, and changed eq. 2.23 into

$$R = N_n^s k_{+,\mathrm{n}} - N_{n+1}^s k_{-,\mathrm{n}+1}, \tag{2.25}$$

equation that can be solved by recurrence (see e.g. ref. [32])

$$R = N_1 \left[\sum_{i=1}^{\infty} \frac{1}{k_{+,\mathrm{n}} \xi_n} \right]^{-1}, \tag{2.26}$$

being

$$\xi_n = \prod_{j=1}^{n-1} \frac{k_{+,\mathrm{n}}}{k_{-,\mathrm{n}+1}} \qquad \text{for} \qquad n > 1. \tag{2.27}$$

To explicitly determine R, it is assumed that the rate constant does not depend on the system being in equilibrium. Imposing the system initially in equilibrium,

$$n N_1 \overset{K}{\rightleftharpoons} N_n, \tag{2.28}$$

where N_1 is the equilibrium distribution of monomers, N_n the equilibrium distribution of clusters of size n, and K the equilibrium constant, and relate the ratio of rate constants $\frac{k_{+,\mathrm{n}}}{k_{-,\mathrm{n}+1}}$ in eq. 2.27 to the equilibrium constant. The equilibrium constant K for this reaction is then given by eq. 2.20, thus eq. 2.26 becomes

$$R = N_1 \left[\sum_{i=1}^{\infty} \frac{1}{k_{+,\mathrm{n}} e^{-\beta \Delta G(n)}} \right]^{-1}. \tag{2.29}$$

Finally, in order to compute the steady-state nucleation rate R, Becker and Döring made several approximations:

1. the terms of the sum corresponding to clusters near the top of the free-energy barrier $\Delta G(n^*)$ dominate the sum in eq. 2.29;
2. $\Delta G(n)$ is replaced by the first two non-zero terms of the Taylor expansion around n^*;
3. $k_{+,\mathrm{n}}$ is replaced by k_{+,n^*};
4. the sum replaced by an integral from $n - n^* = -\infty$ to $n - n^* = \infty$, considering N_n to be a continuous function of n.

Therefore, the final expression of the steady-state nucleation rate is

$$R = N_1 k_{+,\mathrm{n}^*} \left(\frac{|\Delta G''(n)|_{n^*}}{2\pi k_B T} \right)^{1/2} e^{-\beta \Delta G(n^*)}, \tag{2.30}$$

where $|\Delta G''(n)|_{n^*}$ is the second derivative of the Gibbs free energy $\Delta G(n)$ with respect to n computed at the critical cluster size n^*, and

$$Z = \left(\frac{|\Delta G''(n)|_{n^*}}{2\pi k_B T} \right)^{1/2} \tag{2.31}$$

is the Zeldovitch factor. Z was called after J. Zeldovitch [33] showed the need to introduce a factor of this form whenever instead of solving the original Becker-Döring Master Equation one solves the limiting Fokker-Planck equation. In practise, the Zeldovitch factor considers that during the steady-state nucleation process, the concentration of critical clusters is not "really" an equilibrium concentration.

Using the CNT expression of ΔG as a function of n (see eq. 2.10 for a spherical cluster), the CNT steady-state nucleation rate per unit volume can then be written as

$$R = N_1 k_{+,\mathrm{n}^*} \left(\frac{|\Delta\mu|}{6\pi k_B T n^*} \right)^{1/2} e^{-\beta \Delta G(n^*)}. \tag{2.32}$$

where

$$Z = \left(\frac{|\Delta\mu|}{6\pi k_B T n^*} \right)^{1/2}. \tag{2.33}$$

Eq. 2.32 can also be written as

$$R = \kappa e^{-\beta \Delta G(n^*)}, \tag{2.34}$$

where

$$\kappa = N_1 k_{+,\mathrm{n}^*} Z \tag{2.35}$$

is the *kinetic pre-factor*.

Turnbull and Fisher for the first time applied eq. 2.32 to the nucleation process in condensed systems, and rewrote the steady-state nucleation rate as

$$R = N_1 \frac{24 D_S (n^*)^{2/3}}{\lambda^2} Z e^{-\beta \Delta G(n^*)}, \tag{2.36}$$

and the kinetic pre-factor becomes

$$\kappa = N_1 \frac{24 D_S (n^*)^{2/3}}{\lambda^2} Z, \tag{2.37}$$

where N_1 is the number density of the initial parent phase (ρ_L is the initial phase is a liquid), and D_S the self-diffusion coefficient. The atomic jump distance λ comes from the jump frequency $6D_S/\lambda$, related to the attempt frequency of attach/detach one single particle. Finally, the term $4(n^*)^{2/3}$ counts the number of available attachment sites on a cluster assumed to be spherical. From eq. 2.37, it is clear that increasing the super-saturation ($\Delta\mu$), both the barrier $\Delta G(n)*$ and the critical cluster size n^* decrease, leading to a consequent increase of the rate R.

2.3. Numerical techniques to study rare events

Computer simulations can be a useful tool to get a microscopic understanding of the nucleation phenomenon. However, in order to observe nucleation happening by means of *brute*

force simulations on reasonable time-scales and on the small length scales dictated by system size limits, we have to impose an extreme super-saturation to the system. This is, for instance, what happens in a Lennard-Jones fluid, where nucleation events *spontaneously* appear once the system is super-cooled to around 50% of its melting temperature [34]. If we reduce the super-saturation applied to the system, the barrier to nucleation gets higher, and the probability to detect a nucleation event on such time and length-scales gets extremely low. Thus, *brute force* numerical simulations become prohibitively time consuming. The system will spend a long time in a stable state and *rarely* jump to another state in a short time. Nucleation is indeed an example of a *rare event* observable in Nature. This separation of time scales makes it possible to describe the kinetics of rare events as a product of two factors. The basic idea behind this approach was already contained in Eyring's Transition State Theory(TST) [9, 10]. The first stage in the description is the definition of a *reaction coordinate* Q that measures the progress of the system from the initial *reactant* state A to the final *product* state B [2]. Q is defined such that for $Q < Q^*$, the system is in the basin of attraction of state A, while for $Q > Q^*$ the system will most likely end up in state B. The transition surface is the collection of all the points in the in the configurational space where the probability to evolve to state A or B is 0.5. If Q is a relevant reaction coordinate, TS can be viewed as the dynamical bottleneck for the rare event, and the more rarely visited hyper-surface separating A and B. Ideally, TS corresponds to the hyper-surface defined at $Q = Q^*$. However, in practise, the surface $Q = Q^*$ provides only an approximation to the true TS.

If the location of the TS surface is known, it is then possible to formulate a "two-stage" scheme to compute the rate of the rare event under study. Such a computation involves the following steps:

1. computing the *reversible work* ($\Delta W(Q)$) required to move the system from A to TS (located at Q^*), allows to estimate the probability that a spontaneous equilibrium fluctuation can bring the system all the way up to TS:

$$P(Q^*) = e^{-\beta W(Q^*)}, \tag{2.38}$$

   where β is $1/k_BT$. As we have previously showed, the reversible work to grow a new phase with size Q^* in the metastable parent phase, is proportional to the Gibbs free energy ΔG. Therefore, $P(Q^*) = e^{-\beta \Delta G(Q^*)}$. It is natural to locate the dividing surface Q^* at the top of the free-energy barrier $\Delta G(Q)$ separating the two states, considered to be the rate-limiting step for the phase transition;

2. once the system is at TS, it is possible to compute the frequency of successful crossings of trajectories fired from the Transition Surface: this calculation yields the crossing rate $\kappa(Q^*)$.

The combination of step 1 and step 2 give a measurement for the rate of the rare event:

$$R = \kappa(Q^*)P(Q^*). \tag{2.39}$$

[2] The reaction coordinate, as defined in chemical kinetics, is the trajectory of the path in the free-energy landscape along which the system progresses, and characterises the dynamical mechanism of the reaction.

This shows that the rate constant is given by the product of two terms: the probability of being at the top of the free-energy barrier times the rate at which it is crossed.

The Bennett-Chandler [10] method is based on this two-step procedure. As explained in ref. [10], the rate computed when $t \to 0$ corresponds to the Transition State Theory approximation for the rate constant. Transition State Theory also assumes that trajectories at Q^* going towards B will always end up in state B (the same holding for state A), assumption that is correct if there is never "recrossing" of trajectories starting from the top of the barrier. Nevertheless, this is not the case in diffusive barrier-crossing processes, like crystal nucleation. In the Bennett-Chandler [10] scheme $P(Q^*)$ can be computed known by means of the Umbrella Sampling technique [11, 12]. Drawbacks of this method are that it is computationally demanding, and that its success depends strongly on the choice of Q. If poorly chosen, the system will sample the wrong part of the phase space, which will not only conceal the mechanism of the transition, but also impede the computation of the rate constant. Therefore, a reasonably good initial guess is needed to select a reaction coordinate relevant for the nucleation process under study: this requires an *a priori* insight into the reaction mechanism, something that is particularly difficult to obtain for highly dimensional complex systems.

Is is important to introduce the concept of "order parameter", that will be widely used in the rest of the thesis. The order parameter is the variable that identifies the "basin of attractions" A and B and, in principle, not the dynamical mechanism of the reaction. An example is given in the following sketch: at the top we represent the phase space projected onto two order parameters Q and Q', where Q is used to define the basins of attractions A and B; at the bottom, the free energy as a function of Q. The left-hand side of the sketch shows a case when the order parameter Q is "also" a good reaction coordinate, as the Transition State coincides with Q^*. However, this does not happen on the right-hand side, where Q clearly distinguish state A from state B, but the TS does not correspond to Q^*. Moreover, it emerges from the right-hand side of fig. 2.5 that other order parameter Q' is even more important to describe the A to B transition. Computing the distribution of the commitment probabilities for the configurations belonging to the ensemble at the Transition State Surface, allows to understand the relevance of the chosen order parameters. In a transition from A to B the commitment probability is the probability that short trajectories initiated from a configuration in the phase space with randomly chosen momenta, will reach state B. Thus the Transition State Surface consists of the ensemble of configurations such that $P_A = P_B \sim 1/2$. A good test to ensure that the order parameters describe well the transition, is to measure the distribution of P_B, and verify if it is a delta-function distribution peaked at $1/2$. Initially introduced by Du et al. [36], it has been further elucidated by Bolhuis et al. [37].

As already mentioned, the Bennett-Chandler method is strongly based on a good choice of Q. Transition Path Sampling (TPS) [38, 39, 35] has been developed to alleviate this problem. This scheme generates an ensemble of trajectories between initial and final state using Monte Carlo sampling in the trajectory space. TPS only requires an order parameter to distinguish both the initial and the final state; this order parameter does not need to be the *true* reaction coordinate. TPS thus makes it possible to compute the rate constant without prior knowledge of the reaction mechanism. However, this method does require knowledge of the steady-state phase space distribution, which is needed for the acceptance/rejection step in the Monte-Carlo scheme, and it does not allow direct computation of the free-energy barrier separating

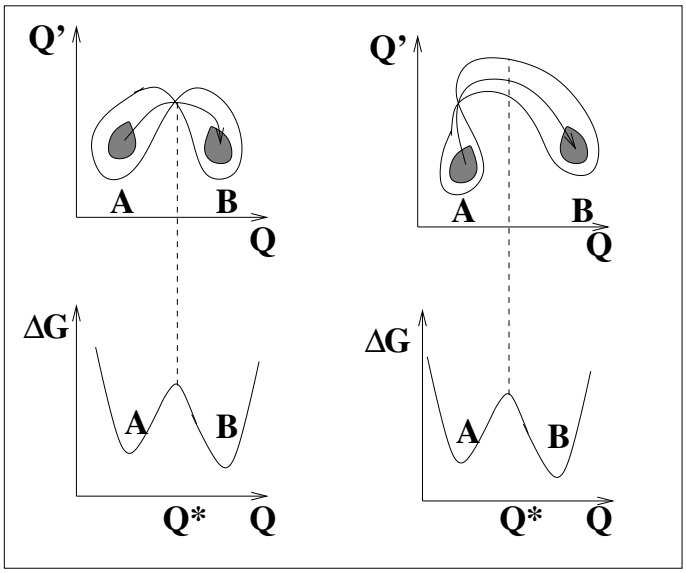

Figure 2.5.: At the top, the phase space is projected onto two order parameters Q and Q', A and B being the basins of attractions; at the bottom, the free energy as a function of Q. On the left-hand side, Q is a good reaction coordinate, differently from the right side (figure copied from ref. [35]).

the two states. The main drawback of TPS is that the calculation of the rate constant is rather time consuming. Moroni, van Erp and Bolhuis developed an efficient approximation to TPS, called Transition Interface Sampling (TIS) [40, 41, 42].This method relies on the computation of the crossing probabilities of a series of interfaces (or hyper-surfaces) located between the initial and final state. The same authors also derived a variant of this method, called Partial Path TIS (PPTIS) [43], which assumes the loss of time correlations in the transition paths over a distance of two interfaces. After proving that PPTIS calculations yielded not only the nucleation rate, but also the free-energy barrier [44], Moroni and coworkers used this method to study crystal nucleation from a moderately super-cooled Lennard Jones fluid [45]. A similar method to PPTIS is the mile-stoning method of Faradjian and Elber [46], which also employs a series of interfaces to compute rate constants, and also assumes that the interface-crossing probability does not depend upon the full history of the path. A string method has also been developed by Vanden-Eijnden and coworkers [47, 48], which can be used to compute minimum free-energy paths and the probability current of reactive trajectories.

In the last few years, a novel simulation technique was developed by Allen and coworkers, named Forward Flux Sampling (FFS) [13, 14, 15]. This technique allows to calculate rate constants and transition paths for rare events in both equilibrium and non-equilibrium systems with stochastic dynamics. Among the algorithms mentioned above, TPS, (PP)TIS, mile-stoning and the string method are only applicable to systems that obey *detailed balance*

and *microscopic reversibility*. They are thus limited to systems that are in thermodynamic equilibrium. Whereas Forward Flux Sampling can be applied to both equilibrium and non-equilibrium systems with stochastic dynamics. Like TIS, PPTIS, and mile-stoning, it uses a series of interfaces to compute the rate constant. However, unlike PPTIS and mile-stoning, FFS does not make the Markovian assumption that the distribution of paths at the interfaces is independent of the paths histories. Importantly, the order parameter used to define the location of the interfaces need not be the reaction coordinate.

We briefly list other rare-event techniques, that are useful when studying nucleation processes. The Blue Moon approach by Ciccotti and coworkers [49, 50] is a constrained Molecular-Dynamics method to estimate rates of rare events. The Meta-Dynamics by Parrinnello and coworkers [51] is a technique that allows an accurate determination of the free-energy landscape, by means of constructing a non-Markovian coarse-grained dynamics in an M-dimensional space, characterised by M collective coordinates relevant for the transition under study. Among many applications, the technique has been used to study bulk melting of hexagonal ice [52], and homogeneous crystal nucleation in a super-cooled Lennard-Jones fluid [53]. Radhakrishnan and Trout [54] applied the committor analysis to examine nucleation of hexagonal ice in liquid water, together with a two-dimensional Umbrella sampling scheme to compute the free-energy nucleation barrier. Reguera and coworkers [55] have proposed a method based on the calculation of mean first-passage time to evaluate reaction rates and locate the Transition State Surface. Lately, an approach for calculating reaction coordinates based on TPS and likelihood maximisation has been proposed by Peters and Trout [56]. Finally, an order-parameter-based Monte Carlo simulation to compute the free-energy profile between liquid and solid in crystal nucleation processes has been explored by de Pablo and coworkers [57]. For more details on some of these techniques, we refer the reader to an exhaustive review by van Erp and Bolhuis [58] on different interface sampling methods.

In what follows, we describe the techniques we have used to study homogeneous nucleation in this thesis, namely the Umbrella Sampling, employed to compute the free-energy nucleation barrier within the Bennet-Chandler approach, and the Forward Flux Sampling technique, to compute the nucleation rate, analyse the pathways to nucleation, and, for the first time, also calculate the free-energy barrier. Whenever studying crystal nucleation, we have employed the local bond-order parameter explained in details in appendix A.

2.3.1. Bennett-Chandler method

As already mentioned, the Bennett-Chandler method consists of a two-step procedure to compute the nucleation rate constant [10]: the calculation of the free-energy barrier can be obtained by means of the Umbrella Sampling scheme [12, 11], while a Molecular Dynamics simulation "constraint" at the top of the free-energy barrier gives information about the kinetic pre-factor. Even though the rate constant R is independent of the choice for Q, the efficiency by which it is computed can strongly depend upon it.

2.3.1.1. The Umbrella Sampling technique

The Umbrella Sampling technique was firstly proposed by Torrie and Valleau [12], and afterwards van Duijneveld and Frenkel [11] suggested to apply it in a nucleation process as a scheme to estimate the free-energy barrier.

Considering a phase transition of a complex system from state A to state B, it is possible to use a Monte Carlo algorithm (MC) in an NPT ensemble to equilibrate the system in the initial A state. According to MC, regions of the phase space are sampled depending on the Boltzmann factor $\exp^{-\beta[U(\vec{r}^N)+PV]}$ (being $U(\vec{r}^N)$ the total internal energy of an N particles system with coordinates $\vec{r}^N$, V its volume and P the pressure). When studying a phase transition, a Monte Carlo sampling leads to a poor statistics of the transition region where the Boltzmann factor is very small. This is due to the fact that the system spends most of its time either in state A or in state B, and only *rarely* and *quickly* crosses the Transition State Surface. Introducing an order parameter $Q(\vec{r}^N)$ relevant for the transition, the probability that a spontaneous fluctuations of Q happens to be around Q_0 is:

$$P(Q_0) = \frac{\int \exp^{-\beta[U(\vec{r}_N)+PV]}\, \delta(Q(\vec{r}_N) - Q_0) d\Gamma}{\int \exp^{-\beta[U(\vec{r}_N)+PV]}\, d\Gamma} = \langle \delta(Q - Q_0) \rangle_{NPT}, \tag{2.40}$$

where the integral is extended to the $3N$ configurational space (Γ).

Following Van Duijneveldt's approach, the knowledge of the Landau free energy allows to compute the Gibbs free-energy nucleation barrier as a function of a chosen order parameter Q from its probability distribution $P(Q)$ (see appendix B). $P(Q)$ is an equilibrium property of the system, and can be measured by means of either Molecular Dynamics and Monte Carlo simulations [3]: small values of $P(Q)$ corresponds to values of Q rarely visited by the system. The procedure to get better statistics for small values of $P(Q)$, is based on the use of a *non Boltzmann* Monte Carlo sampling of the phase space:

$$\exp^{-\beta[U(\vec{r}^N)+PV]}\, W(Q), \tag{2.41}$$

where $W(Q)$ is a weighting function meant to enhance the sampling at certain values of Q, and is expressed in terms of a bias potential $w(Q)$:

$$W(Q) = \exp^{-\beta w(Q)}. \tag{2.42}$$

Thus the probability for Q to be Q_0 becomes

$$P_w(Q_0) = \frac{\int \exp^{-\beta[U(\vec{r}_N)+PV]+w(Q)}\, \delta(Q(\vec{r}_N) - Q_0) d\Gamma}{\int \exp^{-\beta\{[U(\vec{r}_N)+PV]+w(Q)\}}\, d\Gamma}. \tag{2.43}$$

In general, to compute the NPT ensemble average of a thermodynamic variable A measured in the Monte Carlo simulations (such as the energy):

$$\langle A \rangle_{NPT} = \frac{\langle A/W(Q) \rangle_w}{\langle 1/W(Q) \rangle_w}, \tag{2.44}$$

[3] It was shown that constrained Molecular Dynamics turn out to be less straightforward than Monte Carlo simulations [59].

where the index w in eq. 2.44 refers to averages taken in the biased ensemble. Since the Gibbs free energy is computed in the NPT ensemble as $\beta\Delta G(Q) = -\ln(P(Q))$, the probability distribution obtained in the biased Monte Carlo simulations has to be re-weighted:

$$\langle\delta(Q-Q_0)\rangle_{NPT} = \frac{\langle\delta(Q-Q_0)/W(Q)\rangle_w}{\langle 1/W(Q)\rangle_w}. \tag{2.45}$$

Thus, the unbiased Gibbs free energy around Q_0 is computed as

$$\begin{aligned}\beta\Delta G(Q) &= -\ln\left[\langle\delta(Q-Q_0)\rangle_{NPT}\right] \\ &= -\ln[\langle\delta(Q-Q_0)/W(Q)\rangle_w] + constant.\end{aligned} \tag{2.46}$$

We mention only few drawbacks of the Umbrella Sampling technique are: the need of an *a priori* knowledge of Q, the dependence of the free-energy barrier on the order parameter chosen, and the fact that an unlucky choice of $W(Q)$ would not affect the correctness of the calculation, even though it might adversely affect its the statistical accuracy.

Q as the biggest cluster size n

We now show how to compute $P(n)$ in eq. 2.20 in order to obtain the nucleation free energy barrier. For a moderate supersaturation, $P(n)$ is sketched in fig.2.6. For small clusters that appear spontaneously in the system, we use the definition of the probability, $P(n) = \langle N_n\rangle/N$. In practise, we just average the number of clusters of size n along an unbiased simulation.

However, the probability of appearance of big clusters is very small and a bias potential must be introduced in order to compute $P(n)$. The system is then biased to have a biggest cluster whose size fluctuates around n_0, as we will see in the next paragraph. As Ten Wolde et al. showed [103, 29], for big clusters (that at moderate supersaturation do not appear spontaneously) $P(n)$ is equivalent to the probability that the biggest cluster present in the system has size n.

The probability distribution $P(n)$ of all the solid clusters in a moderately super-saturated liquid is equal to:

$$P(n) = 1\times P_1(n) + 2\times P_2(n) + 3\times P_3(n) + ... = \sum_i iP_i(n), \tag{2.47}$$

where $P_i(n)$ is the probability to have i clusters of size n. If we assume that the formation of different clusters is uncorrelated, then $P_i(n) = P_1^i(n)$. Thus, eq. 2.47 becomes

$$P(n) = \sum_i iP_1^i(n). \tag{2.48}$$

At these thermodynamic conditions it is possible to neglect terms of order higher than one in the sum of eq. 2.48, as the probability to sample even one single cluster with size n is relatively small. Hence,

$$P(n) \approx P_1(n), \tag{2.49}$$

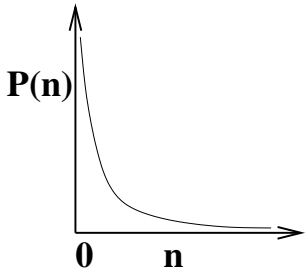

Figure 2.6.: Probability distribution $P(n)$ of all the solid clusters in a metastable liquid.

that is the probability to have "only" one big cluster of size n in the metastable liquid. $P(n)$ is calculated in an umbrella sampling scheme by biasing the simulation to explore configurations with a biggest cluster of size n.

Thus, at moderate super-saturations, the biggest cluster size n can be considered a good order parameter: Q=n. In crystal nucleation n is identified by means of local bond order parameters explained in details in appendix A.

Choosing the biasing function $w(Q)$

The optimum choice of the biasing function $w(Q)$ would be the Gibbs free-energy barrier itself ($G(Q)$), as this would guarantee an equally probable sample of all values of Q. However $G(Q)$ is not *a priori* know. A way to overcome this problem was presented by Lynden-Bell et al. [60]. The authors used the $G(Q)$ obtained from unbiased Monte Carlo simulations, extrapolated this function to higher values of Q, and then "iteratively" computed the free energy for all values of the order parameter. However, this approach might not give a good estimate of the Gibbs free energy in complex systems characterised by a steep free-energy barrier.

Thereafter, Ten Wolde et al. [103, 29] introduced a biasing function $w(n)$, function of the biggest cluster size n and modelled as an harmonic potential in the order parameter n:

$$w(n) = \frac{1}{2}\kappa \left(n - n_0\right)^2 , \tag{2.50}$$

where κ and n_0 determine the width and the location of the equilibrium position; the phase space around n_0 defined by this width is called "window". By using consecutive and overlapping windows, all having the same width (κ) it is possible to compute the equilibrium distribution of all n values needed to compute the free-energy barrier [4]. Thus, $P(n)$ after having applied the biasing potential is represented in figure 2.7.

[4] In order to choose the best window width, we should remember that the system should freely diffuse within each window. Therefore, the larger the window, the longer the system will take to explore the window phase space, making the sampling less efficient. Hence, we rather consider many small overlapping windows.

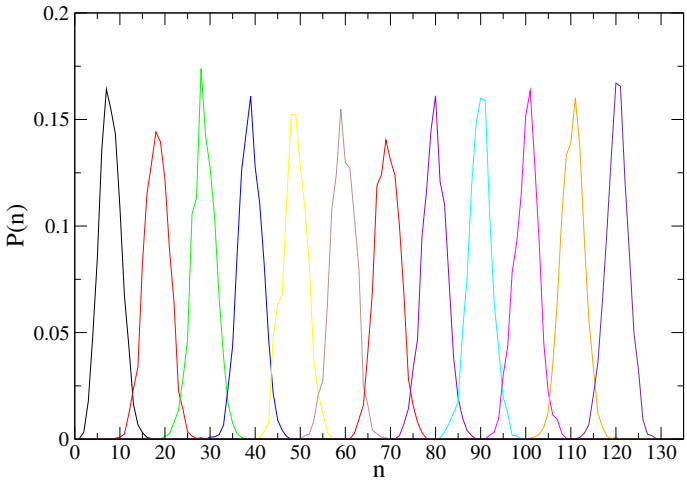

Figure 2.7.: $P(n)$ from numerical simulations as a function of the biggest cluster size n.

Fitting the computed free-energy barrier

As we already showed in chapter 2, the Umbrella Sampling technique allows to calculate the equilibrium probability distribution of the biggest cluster size $P(n)$, and thus the free-energy barrier to nucleation. The free energy in each window ΔG_i is then computed by means of eq. 2.20. ΔG_i is computed but a constant different in each window. Once ΔG_i is known with its statistical error $(\sigma(\Delta G)_i)$ [5], we assume that the best curve passing through two adjacent windows is an order $k_{max} = 8$ polynomial function [61], whose coefficients come from minimising the χ^2 function:

$$\chi^2 = \sum_{n=1}^{n_{max}} \left[\sum_{i=1}^{n_w} \frac{1}{\sigma^2} \left(\Delta G_i(n) - \sum_{k=1}^{k_{max}} a_k n^k - b_i \right) \right]^2 . \tag{2.51}$$

The use of a polynomial fit is preferred to the self-consistent procedure of Flyvbjerg [62], as it can be used even when the adjacent windows do not or slightly overlap.

However, $\Delta G(n)$ is the free energy needed to grow a size-n cluster in the metastable liquid. Thus, the metastable liquid is the reference state of the nucleation process. Therefore, it is necessary to compute the free energy of the metastable liquid in an *unbiased* Monte Carlo simulation to obtain the first part of the barrier by means of eq. 2.20.

2.3.1.2. Estimation of the attachment rate in the kinetic pre-factor

According to Classical Nucleation Theory, the kinetic pre-factor is given by eq. 2.35. However, it is also possible to estimate it without making use of CNT. The only assumption we

[5] The standard deviation for each value of $G(n)$ is obtained by means of a block average within each window.

make is that the barrier crossing is a diffusive process and the Zeldovitch pre-factor is well approximated by the form presented in eq. 2.33. The attachment rate of particles to the critical cluster k_{+,n^*} takes into account the number of available attachment sites on the surface of a spherical cluster. Assuming a diffusive attachment or detachment of single particles from the critical cluster, Auer and Frenkel [63] related the forward rate k_{+,n^*} at the top of the barrier to the spontaneous diffusion of n at the top of the nucleation barrier:

$$k_{+,\mathrm{n}^*} = \lim_{t\to\infty} \frac{1}{2} \frac{\langle (\Delta n^*(t))^2 \rangle}{t} \tag{2.52}$$

where $\langle (\Delta n^*(t))^2 \rangle = \langle [n^*(t) - n^*(0)]^2 \rangle$ is the mean square change in the number of particles belonging to the critical cluster during a time interval t. In order to compute the attachment rate k_{+,n^*}

1. we generate a set of uncorrelated configurations at the top of the free barrier;
2. we carry out NVT MD simulations, whilst the system is diffusing near the top of the free energy barrier without falling in either of the free-energy basins;
3. from eq. 2.52, we compute the slope of $\langle (\Delta n^*)^2(t) \rangle$ as a function of t for long times and obtain k_{+,n^*}.

It is important to distinguish between k_{+,n^*}, which is the rate at which particles are added to a cluster with the critical size, and the net flux across the nucleation barrier. In steady-state, this net flux is equal the number of clusters that go from n^* to $n^* + 1$ minus the number of clusters that go from n^*+1 to n^* [4, 26, 5]. Hence, the actual nucleation rate is a combination of the forward rate k_{+,n^*} and the backward rate k_{-,n^*}. However, because of detailed balance, knowledge of k_{+,n^*} (combined with knowledge of the barrier height and shape) is enough to compute the nucleation rate.

2.3.2. Forward Flux Sampling

The Forward Flux Sampling technique was developed by Allen et al. [13, 14, 15] in order to study *rare events* in soft matter and biophysical related problems. Here, we will limit ourselves to the original FFS scheme [13], and describe the way we applied it in studying nucleation processes in appendix C. An exhaustive discussion on various versions of FFS, all based upon this idea [13], can be found in [14] and [15]). Considering a rare transition between two regions of the phase space, A and B, Forward Flux Sampling is a technique that allows to compute both the crossing rate between the two states, and analyse the features of the pathways connecting A to B. In what follows, we present the FFS technique in a "step-by-step" manner.

1. First of all, it is necessary to introduce an order parameter Q, function of the phase space coordinates, to define both states A and B and relevant to describe the phase transition from A to B. It is important to mention that the results coming from the FFS runs do not depend on the choice of Q (see ref. [13]). When studying crystal nucleation, we select the number of solid particles in the biggest cluster n as the order parameter Q;

2. hence, by means of Q, we define the system being in state A whenever $Q < \lambda_0$, where λ_0 is state A boundary, or being in state B whenever $Q > \lambda_n$, where λ_n is state B boundary;

3. since transitions from A to B, and vice versa, are rare, most of the time Q will either be smaller than λ_0 or larger than λ_n. The key idea of FFS is to use a series of hypersurfaces in the phase space, also called *interfaces*, each one identified by a value of the order parameter Q ($Q = \lambda_0, Q = \lambda_1, \ldots, Q = \lambda_{n-1}, Q = \lambda_n$) to drive the system from state A to state B in a ratchet like manner;

4. once the interfaces are known, the next step is to perform a conventional brute-force simulation in one of the stable states, say state A. Each time the system crosses the interface λ_0 during this simulation, the coordinates of the phase space point are stored. At the end of this simulation, one has a distribution of state points at the first interface, λ_0 (as indicated in sketch (a) in fig. 2.8);

5. this distribution is then used to fire off a set of trajectories from the first interface λ_0. Each trajectory is continued until the system either reaches the next interface, λ_1, or arrives in state A again, i.e. crosses λ_0 (as indicated in sketch (b) in fig. 2.8). This procedure generates a distribution of state points at λ_1;

6. by repeating the same operation for the subsequent interfaces, one has for each interface i an estimate of the probability $P(\lambda_i|\lambda_{i+1})$, which is the probability that given that a trajectory is at interface i and has come from A, it reaches λ_{i+1} before it returns to state A (as indicated in sketch (c) in fig. 2.8). Figure 2.8(d) shows the last step: when a trajectory is originated at the last interface, it can either reach state B by crossing its boundary λ_n, or go all the way back to state A.

According to FFS, the nucleation rate is computed as a product of two terms: the flux at which stochastic trajectories starting at the initial state cross its boundary λ_0, times the probability that these trajectories can reach the final state of the transition. The rate constant R can then be obtained from [44] by

$$R = \Phi_{A\to 0} \cdot P_{0\to B} = \Phi_{A\to 0} \prod_{i=0}^{n-1} P_{i\to i+1} \tag{2.53}$$

Here, $\Phi_{A\to 0}$ is the steady-state flux of trajectories crossing state A boundary, which is the number of crossings of λ_0 per unit time and volume ($N_{A\to 0}$), and $P_{0\to B}$ is the overall probability that trajectories, initially at the first interface, manage to reach the final state B.

2.3.2.1. Numerical computation of the steady-state flux

In practise, the flux can be obtained from a first, brute-force simulation in state A:

$$\Phi_{A\to 0} = \frac{N_{A\to 0}}{t \cdot V} \tag{2.54}$$

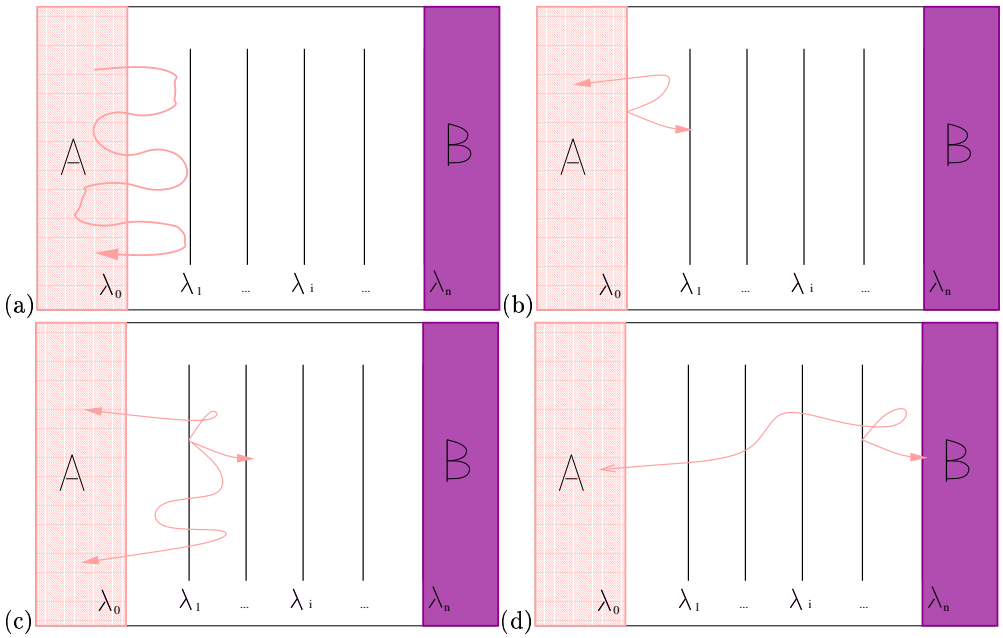

Figure 2.8.: (a) Flux of stochastic trajectories across the first interface, (b) fired off from the i^{th} interface (c), and from the last interface (d). Every time, a trajectory is considered to be successful if it reaches the next interface, unsuccessful if it goes all the way back to the initial A state.

where V is the volume of the simulation box and t is the average time the system spends in A before crossing $N_{A\to 1}$ times the first interface (see fig. 2.8(a)). While computing the flux, we collect N_0 configurations at the first interface λ_0.

In practise, to measure the flux, we collect the configurations crossing the interface λ_0, and measure the total time spent by the system in the A state, neglecting the time spent at λ_0.

2.3.2.2. Numerical computation of $P_{0\to B}$

The N_0 configurations collected at the first interface are used as starting points to shoot for each of them M_0 stochastic trajectories. The M_0 runs differ from each other in the different random seed of the random number generator. A trajectory is then considered to end

- either if it succeeds to reach the next interface (the second interface λ_1, in this case),
- or if it fails by going all the way back to the initial state A.

Hence, the probability to go from interface λ_0 to interface λ_1, $P_{0\to 1}$, is the ratio between the number of successful trajectories that reach interface 1 ($N_{0\to 1}^{succ}$) and the total number of trial

trajectories ($M_0 \cdot N_{A\to 0}$):

$$P_{0\to 1} = \frac{N_{0\to 1}^{succ}}{M_0 \cdot N_{A\to 0}}. \tag{2.55}$$

In the next step, the $N_{0\to 1}^{succ}$ configurations can be used as starting points to compute the probability to go from interface λ_1 to interface λ_2, $P_{1\to 2}$, and so on until we reach the final state B. Thanks to the fact that configurations have been stored at each interface, it is possible therefore to analyse the pathways to nucleation,

Acknowledgements

Concerning this chapter, I would like to thank E. Sanz for a patient and careful reading, together with J. A. van Meel and R. Hawkins.

Appendix A: Order parameter used to study homogeneous crystal nucleation

In order to quantify the progress of crystal nucleation from a metastable super-cooled liquid, we choose an order parameter that has the following general features:

1. it is sensitive to the differences between solid and liquid structures;
2. it does not depend on the orientation or position in space of the solid;
3. in case the system presents a rich phase diagram, characterised by several solid structures, the order parameter should not bias any of them.

The order parameter on one side detects only few particles as solids in the metastable liquid phase, on the other side it recognises "almost" all particles as solid-like in the stable solid phase.

In all our works, every time we have studied crystal nucleation, we used a so-called *local bond-order* parameter. The bond-order parameters were initially introduced by Steinhardt et al. [64] to describe the orientational order in liquids. They have been first used by van Duijneveldt et al. [11] to estimate the free energy as a function of the overall crystallinity in a metastable liquid of soft and repulsive spheres ($v(r) = \epsilon(\frac{\sigma}{r})^{12}$). Later on, ten Wolde el al. [103, 65] studied crystal nucleation from a super-cooled Lennard-Jones liquid, by means of the same bond-order parameters. More recently, ten Wolde el al. [29] and Auer et al. [66] analysed crystal nucleation from, respectively, metastable Lennard-Jones and hard-spheres fluid employing a *local* bond-order parameter.

Whenever studying homogeneous crystal nucleation, we have exploited the same local bond-order parameters to identify the *biggest crystalline cluster*, whose size we consider to be the relevant order parameter to follow the liquid-to-solid phase transition. In practise, we start by distinguishing between liquid-like and solid-like particles, and then use a cluster-algorithm to group neighbouring solid-like particles into crystalline clusters. The last step consists of selecting the biggest cluster, which size is going to be our local order parameter. In order to compute it:

1. we define the neighbour list of each particle i, as the set of all particles j within a cut-off distance of $r_{ij} \leq r_c$[6]. The cut-off radius r_c corresponds to the first minimum of the radial distribution function of the thermalised solid state;
2. now, we look at the spatial orientational correlation of vectors joining neighbouring atoms. For every particle i, we compute the *local* spatial orientation $\vec{q}_{lm}(i)$, which is a $(2l+1)$-dimensional complex vector, whose components are given by

$$q_{l,m}(i) = \frac{\frac{1}{N_b(i)} \left(\sum_{j=1}^{N_b(i)} \Upsilon_{l,m}(\theta_{ij}, \phi_{ij}) \right)}{\left(\sum_{m=-l}^{l} |\vec{q}_{l,m}(i)|^2 \right)^{1/2}}, \qquad m = [-l, l] \qquad (2.\mathrm{A}.1)$$

[6] In what follows, we denote with $\vec{r}_i$ the positional vector of particle i. $\vec{r}_{ij} = \vec{r}_j - \vec{r}_i$ is the distance between two particles i and j, whose modulus is $r_{ij} = |\vec{r}_{ij}|$, and $\hat{r}_{ij} = \vec{r}_{ij}/r_{ij}$ the unit vector pointing in the direction of $\vec{r}_{ij}$.

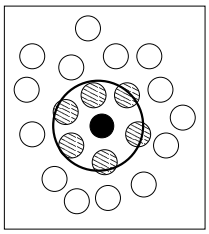

Figure 2.A.1.: The two-dimensional sketch indicates particle i (black at the centre) surrounded by its neighbours j (striped particles) within the cut-off radius r_c.The remaining particles (white) are not i's neighbours.

where $N_b(i)$ is the number of neighbours of the particle i, and $\Upsilon_{l,m}(\theta, \phi)$ are the order l spherical harmonics, obtained from the polar representation of $\hat{r}_{ij}$ (see fig. 2.A.2);

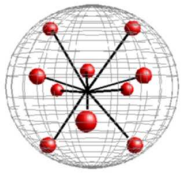

Figure 2.A.2.: Three-dimensional representation of a typical arrangement of a particle surrounded by neighbours. The orientations of the vectors linking the central particle (i) with any of its neighbours j define θ_{ij} and ϕ_{ij}, used to compute the order l spherical harmonics in eq. 2.A.1.

3. in order to distinguish liquid-like from solid-like particles, Ten Wolde et al. [29] proposed a rotationally invariant function $d_l(i,j)$ [7], i.e. the dot product between $\vec{q}_{l,m}$ computed at particle i, and the same complex vector computed for each of its neighbours:

$$d_l(i,j) = \sum_{m=-l}^{l} \vec{q}_{l,m}(i) \cdot \vec{q}^{*}_{l,m}(j). \tag{2.A.2}$$

   $d_l(i,j)$ is a normalised quantity correlating the local environments of neighbouring particles, it is a real number and is defined in the range $-1 \leq d_l(i,j) \leq 1$. The value of l is chosen depending on the symmetry of the growing cluster;

4. once $d_l(i,j)$ is computed for every particle i, it is possible to define a criterion to distinguish between liquid-like and solid-like particles. After calculating the probability

[7] A rotationally invariant order parameter doe not depend on the chosen reference frame.

distribution $P(d_l(i,j))$ both in the metastable liquid and in the solid (see fig. 2.A.3) for a generic system [8], two neighbouring particles i and j are defined as "connected", if $d_l(i,j)$ exceeds a certain threshold d_c. d_c is an *ad hoc* cut-off, corresponding to

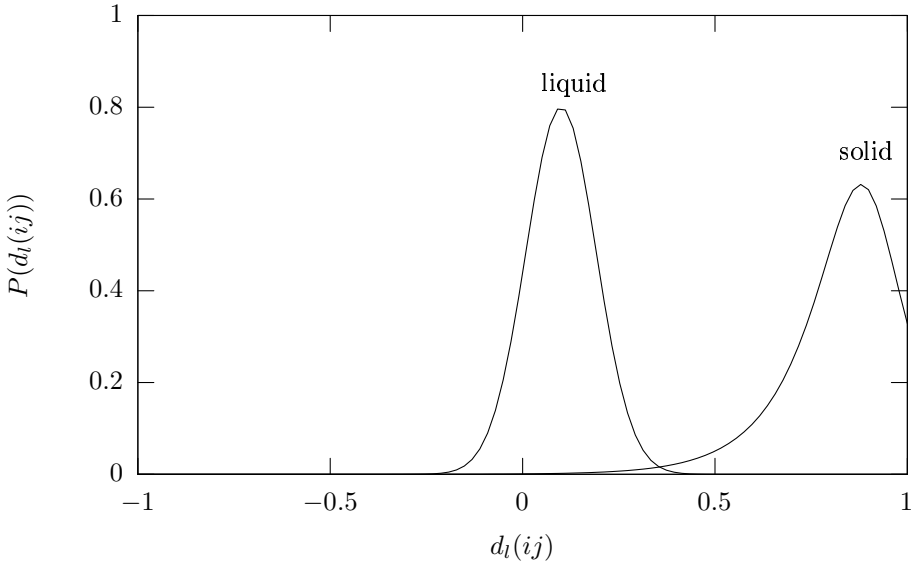

Figure 2.A.3.: Probability distribution $P(d_l(i,j))$ of a metastable liquid (on the left hand-side) and a thermalised solid (on the right hand-side) of a generic system. Two particles are "connected", when $d_l(i,j) \geq d_c$, where $r_c \approx 0.3$. (Courtesy of J. A. van Meel)

the smallest value of $d_l(i,j)$ where the probability that particle i is embedded in a solid-like environment is not zero. However, it appears clear from fig. 2.A.3 that at $d_l(i,j) = d_c$ the two probability distributions overlap, and there is a finite probability for particle i to be in a liquid-like environment, not connected to particle j;

5. thus, to enforce the above-mentioned criterion, Ten Wolde suggested a second criterion to identify a particle in a solid-like environment, by counting the number of connections of particle i

$$n_{con}(i) = \sum_{j=1}^{N_b(i)} H(d_l(i,j) - d_c), \tag{2.A.3}$$

where $N_b(i)$ is the number of neighbouring particles, H is the Heaviside step function and d_c the connection threshold. n_{con} is the total number of scalar product d_l with respect to particle i that overcomes the imposed threshold d_c.

[8] In a metastable liquid $P(d_l(i,j))$ is a distribution peaked at a small but positive value of $d_l(i,j)$. Whereas in a thermalised solid $P(d_l(i,j))$ is a broader distribution peaked around a value close to one, value, the latter, the distribution assumes in a ideal lattice.

By looking at the probability distribution of n_{con} per particle $P(n_{con})$ (fig. 2.A.4), it turns out that in a liquid the number of connections is fairly low, whereas typical values for solids are higher: $n_{con} = 12$ for a fcc crystal, $n_{con} = 8$ for a bcc crystal and $n_{con} = 6$ for a simple cube (NaCl crystal). The fact that there is no overlap between the two n_{con} distributions, allows a clear distinction between liquid-like and solid-like environment. Thus, a particle is considered to be solid (or in a solid-like environment) if its number of connections exceeds an assigned threshold n_{con}^c (in fig. 2.A.4, $n_{con}^c = 6$ is a reasonable cut-off);

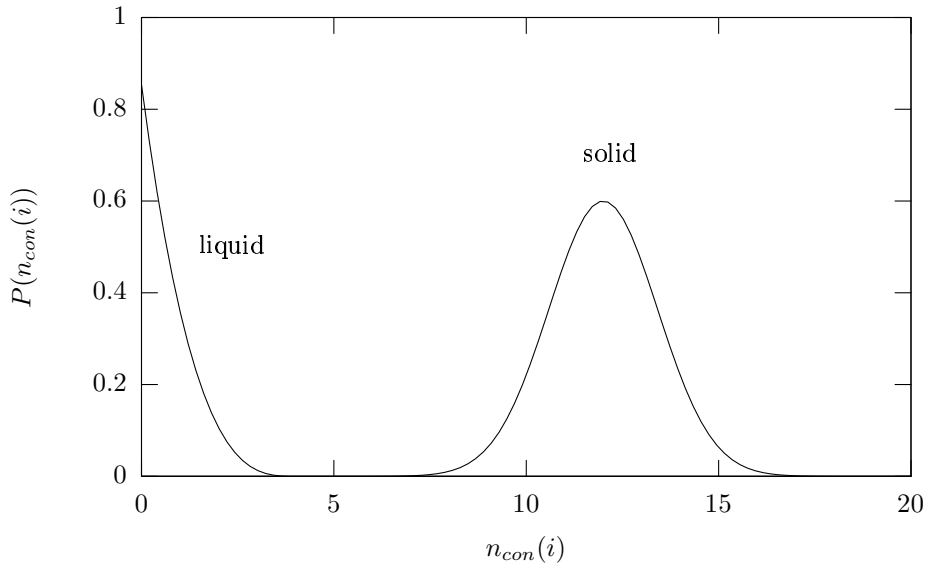

Figure 2.A.4.: Probability distribution of the number of connections per particle for a metastable liquid and for a solid for a generic system. (Courtesy of J. A. van Meel)

6. once all the solid particles are identified in the system, a cluster-algorithm can be used to check which particles belong to the same solid clusters: starting from a solid particle i, if particle j is a solid neighbour closer than a cut-off $r_c^{cluster}$, then i and j belong to the same solid cluster. The procedure is iterated over all the solid particles, that are labelled in a similar way if they belong to the same clusters;

7. at last, the biggest of those clusters is selected as *the* order parameter to describe the liquid-solid phase transition. In all our studies, the *biggest cluster size* is indicated with n.

The global bond-order parameter

From equation 2.A.1, it is possible to construct the *global bond-order* parameters used by van Duijneveldt [11] and ten Wolde [29]. After computing the average of $q_{l,m}$ over all the bonds, the global order parameter is defined as

$$\bar{Q}_{l,m} = \frac{\sum_{i=1}^{N} N_b(i) q_{l,m}(i)}{\sum_{i=1}^{N} N_b(i)}, \qquad m = [-l, l] \tag{2.A.4}$$

and its rotationally invariant version

$$Q_l = \left(\frac{4\pi}{2l+1} \sum_{m=-l}^{l} |\bar{Q}_{l,m}|^2 \right)^{1/2}. \tag{2.A.5}$$

It has been proved by Ten Wolde et al. [29] that the use of a global bond-order parameter can cause a spontaneous breaking of the pre-critical clusters into many small crystallites due to entropic reasons.

Appendix B: Landau free energy

The use of order parameters to construct phenomenological theories of phase transitions was pioneered by Landau [67]. In this approach, the order parameter Q is chosen based on physical concept in the Landau theory of continuous phase transitions, and can also be used to discuss first order phase transitions. The Landau free energy $\mathbf{G}$ is defined as It is defined as

$$\mathbf{G}(Q_0) = -k_B T \ln(P(Q_0)) = -k_B T \ln \int \exp^{-\beta(H_0+PV)} \delta(Q - Q_0) d\Gamma + constant, \tag{2.B.1}$$

where $P(Q_0)$ is the probability per unit interval to find the order parameter at a given value Q_0, H_0 is the Hamiltonian of the system, V its volume, P the external pressure, k_B denotes Boltzmann constant, and Γ indicates that the integral is over the phase space.

Let us assume that Q is an order parameter, function of the $3N$ system coordinates, relevant for the liquid (L) to solid (S) phase transition. In such a transition, we expect that above the freezing temperature $P(Q)$ is a distribution peaked at a low value of Q_L, corresponding to the liquid state. A peak in $P(Q)$ matches a minimum in the Landau free energy. At the freezing temperature the distribution gets double-peaked, the second peak at higher Q_S values corresponding to the solid state. The fact that $\mathbf{G}(Q)$ has two minima (L and S) means that there are two possible stable phases at Q_L and Q_S, respectively. At the thermodynamic coexistence point, the probabilities to find the system in each phase are equal, while at a given super-saturation one of the two peak becomes less stable, corresponding to a metastable minimum in $\mathbf{G}(Q)$. The lifetime of the system trapped in this metastable minimum depends on the height of the free-energy barrier separating it from the stable minimum.

The Gibbs free energies of each of the two phases (minima) can be written as

$$G_L = -k_B T \log \int_L \exp^{-\beta(H_0+PV)} d\Gamma, \tag{2.B.2}$$

obtained integrating over the phase space occupied, respectively, by phase L, and phase S (G_S). Therefore, the Gibbs free energy difference between the two phases is

$$G_L - G_S = -k_B T \ln(P_L/P_S), \tag{2.B.3}$$

where $P_L(P_S)$ is the probability to find the system in phase $L(S)$. Being $P_L \sim \exp -\beta \mathbf{G}(Q_L)$, eq. 2.B.3 becomes

$$G_L - G_S = \mathbf{G}(Q_L) - \mathbf{G}(Q_S) + O(Q^2) \tag{2.B.4}$$

$\mathbf{G}(Q_L)$ and $\mathbf{G}(Q_S)$ are the values of the Landau free energies at the two minima, and the second term is a small correction that depends on the curvature of these minima (assumed to be the same). In order to calculate $\mathbf{G}(Q)$, Lynden-Bell et al. [60] used standard Monte Carlo sampling, augmented with Umbrella Sampling to facilitate the sampling of those parts of the free-energy landscape that would be inadequately sampled in standard Metropolis sampling.

Appendix C: Details on the FFS calculations

Motivated by computational issues, to study nucleation processes we have applied the FFS scheme in a slightly different manner than the one presented in the original scheme [13], and [14], making sure to obtain the same results in both schemes. The way we have structured our calculations is the following:

1. as FFS prescribes, we fire off M_{i-1} stochastic trajectories from the N_{i-1} configurations collected at λ_{i-1}. This corresponds to $N_{i-1} \times M_{i-1}$ trials to get to the next interface λ_i. We decide to run all trial shootings starting from each configuration on the same computer cluster node. In this way we use as many processors as starting configurations;

2. assuming that the trajectories produce $N^{succ}_{i-1\to i}$ configurations at the next interface λ_i, we then use these configurations as starting points for trajectories shot towards the next interface λ_{i+1};

3. if $N^{succ}_{i-1\to i}$ is bigger than the number of computer cluster nodes available, we randomly select some of the configurations ($N^{sel}_{i-1\to i}$) to keep the computational time under control, and shoot M_i times the $N^{sel}_{i-1\to i}$ configurations using $N^{sel}_{i-1\to i}$ nodes in our computer cluster.

We iteratively repeat the shooting scheme until the last interface is reached.

Computation of $P_{0\to B}$
Thus, the probability to reach interface λ_{i+1} from interface λ_i becomes

$$P_{i\to i+1} = \frac{N^{succ}_{i\to i+1}}{(M_i \times N^{sel}_{i-1\to i})}, \tag{2.C.1}$$

and eq. 2.53 can be written as:

$$R_{AB} = \Phi_{A\to 0} \frac{N_{0\to 1}^{succ}}{M_0 \times N_{A\to 0}} \prod_{i=1}^{n-1} \frac{N_{i\to i+1}^{succ}}{(M_i \times N_{i-1\to i}^{sel})}. \qquad (2.C.2)$$

In order to test the validity of these calculations, we study homogeneous nucleation in a two-dimensional Ising model, and compare the nucleation rate computed by means of eq. 2.C.2 with the one obtained using the original FFS scheme of ref. [14]: we obtain $(6.3\pm2.5)\times10^{-13}$ MC step^{-1} spin^{-1}, in very good agreement with the value of $R_{AB} = 2.8 \pm 0.3 \times 10^{-13}$ MC step^{-1} spin^{-1} computed according to ref. [14] (see also chapter 3) and with the value 3.3×10^{-13} MC step^{-1} spin^{-1} computed for the same system by Sear et al.[68].

Location of the interfaces

In order to locate the first interface, also boundary of the A state, , λ_0, we employ the cumulative distribution function of the order parameter n in the A basin.

$$F(n) = \sum_{n_i \le n} P(n_i), \qquad (2.C.3)$$

where $F(n)$ is the probability that the biggest cluster has size less or equal than n.

The procedure we follow is:

1. we extract a random number, r from a random number generator uniformly distributed between 0 and 1;
2. we compare r with the values of the cumulative distribution $F(n)$, starting from $n = 0$;
3. we find which value of n corresponds to an $F(n)$ bigger than r, and set λ_0 at the corresponding value of n;
4. in this procedure, we define an upper boundary for the numerical values r can assume: if r is at least 0.995 or bigger, the value of λ_0 is located at the value n assumes when $F(n)$ is 0.995.

The position of λ_0 can be either chosen before starting the FFS runs, or every time we check if a trajectory shot from λ_i to λ_{i+1} is coming back to the initial state A.

To locate the other interfaces λ_i, we execute a "trial" FFS simulation, and select each λ_i as soon as it is reached by "at least" few percent of the trajectories coming from the previous λ_{i-1} interface. It is important to add that the FFS results do not depend on the position chosen for the interfaces. We have checked this statement using a different set of locations of the interfaces, and obtaining the same nucleation rate.

Appendix D: Tips for beginners

The aim of this appendix is to give few tips for newcomers in the field of computer simulations of nucleation of a stable phase B from a metastable parent phase A.

NPT or NVT ensemble?

In what follows, we give reasons why an NPT ensemble is more suited to study homogeneous nucleation than an NVT one. If we perform numerical experiments on condensation (vapour-to-liquid phase transition), we observe that at the top of the free-energy barrier the critical liquid cluster coexists in an unstable equilibrium with the surrounding vapour, while the vapour pressure decreases. However, as the clusters concentration is relatively small, the change in vapour pressure is negligible, and we can argue that the pressure in the system is constant during the nucleation process. In an NPT ensemble, whenever a cluster starts growing, the volume of the system adjusts in order to keep the vapour pressure constant. Whereas, in order to simulate the same process in an NVT ensemble, one would need a very large number of vapour particles to keep the vapour pressure constant. This implies a very large system. Moreover, real life nucleation experiments are carried out at constant temperature and pressure.

Different super-saturations of the system

Before tackling a nucleation study, knowledge of the "degree" of super-saturation to impose to the system is required. The super-saturation is measured in terms of the chemical potential difference between the nucleating and the parent phase: $\Delta\mu = [\mu_B(P) - \mu_A(P)]$. Depending on the super-saturation, we observe different scenarios:

1. if the super-saturation is almost zero, the system is still close to the coexistence region, where the free-energy barrier to nucleation is almost infinite. The critical cluster would be too large and finite size problems would arise;

2. if the super-saturation is very high, the system is in a region of the phase diagram where the free-energy barrier to nucleation is very small. In a vapour-liquid phase transition, when the barrier becomes zero, the system rapidly separates into the two different phases by means of a *spinodal decomposition* mechanism [9]. This mechanism is kinetically different from the nucleation one in the binodal region [69];

3. at last, if the super-saturation is moderate, there is a reasonably high free-energy barrier the system has to overcome in order to nucleate the new stable phase. What happens is that the system spends long time in the initial metastable state A, and *eventually* a ¨rare¨ density fluctuation happens, leading the system at the final stable B state.

Knowing the phase diagram of the chosen material makes it possible to quantify the amount of super-saturation. In all our simulations we study systems at moderate super-saturations.

System size and Periodic boundary conditions

In order to simulate a bulk system, we accommodate N particles in a cubic box, and periodically repeat the box in all three directions [70, 71]. In this way none of the particles is at the boundaries or close to the surface, as there are no surfaces in any direction.

[9] For solids, the spinodal picture is not appropriate [8]

A criterion to choose the appropriate system size is based on Classical Nucleation Theory. By means of eq. 2.13 it is indeed possible to estimate the critical cluster size: the system has to be large enough to accommodate (at least) the critical cluster. This means, in particular, that correlations induced in the parent phase due to the presence of the cluster (such as layering of particles in the liquid close to the cluster surface, anisotropy in the particles orientation close to the cluster surface, etc.) must decay on a length scale shorter than half of the the box length. Otherwise the cluster might interact with its own periodic images, leading, as a consequence, to spurious finite size effects.

Part II.

Forward Flux Sampling technique applied to nucleation phenomena

3. Computing stationary distributions with FFS[1]

... E' una via crucis.
Motto alpino

We present a method for computing stationary distributions for activated processes in equilibrium and non-equilibrium systems using Forward Flux Sampling (FFS). In contrast to most approaches to study rare events, the stationary distributions can be obtained directly from the rate-constant calculations for the forward and backward reactions; it is thus not necessary to perform one series of calculations for the stationary distribution and a separate one for the rate constant. We apply the method to the rare event problem proposed by Maier and Stein, and to nucleation in a two-dimensional Ising system.

3.1. Introduction

In the field of soft-condensed matter physics a number of simulation schemes have been developed in recent years, which makes it possible to zoom in on the rare events themselves. Techniques such as Umbrella Sampling allow the calculation of free-energy barriers separating the stable states [12, 11], while schemes such as the Bennet-Chandler method [10] and Transition Path Sampling [72, 41] also allow the computation of rate constants. Indeed, these techniques have now been widely applied to study ion permeating through membranes, protein folding, and nucleation. However, these schemes require previous knowledge of the phase space density.

For systems that are in thermodynamic equilibrium—systems that obey detailed balance and microscopic reversibility—the phase space density is known: it is given by the Boltzmann distribution. In contrast, for systems that are out-of-equilibrium, the phase space density is usually not known.

Hence, most numerical techniques for simulating rare events are limited to equilibrium systems only, and thus exclude a host of important rare-event problems in non-equilibrium systems, such as polymer collapse under flow, crystal nucleation under shear, and rare events in biology, such as protein trans-location and switching events in biochemical networks. A recently developed numerical technique, called Forward Flux Sampling (FFS), makes it

[1] Work carried out in collaboration with R. J. Allen, M. Morelli and P. R. ten Wolde.

possible to compute rate constants in both equilibrium and non-equilibrium systems with stochastic dynamics.

In this chapter, we show how, by performing an FFS calculation for the transition from the initial A to the final B state, and one for the reverse transition, not only the rate constants, but also the stationary distributions can be directly obtained.

The method can be used for both equilibrium and non-equilibrium systems. For equilibrium systems the advantage is that from an FFS simulation not only the rate constant, but also directly the free energy can be obtained. For non-equilibrium systems in steady-state, this approach is, to our knowledge, the first that allows the computation of stationary distributions.

The method is conceptually similar to that used in TIS and PPTIS to compute free-energy barriers, in the sense that the stationary distribution is obtained by matching the forward and backward trajectories [43, 41, 40].

In the next two section, we discuss the method to obtain the stationary distributions. We then illustrate the method using a symmetric and asymmetric double-well potential system (section 3.4.1), and both an equilibrium and non-equilibrium two-dimensional Maier-Stein system (section 3.4.2). Finally, in section 3.4.3, we apply the method to calculate the free-energy barrier for nucleation in a two-dimensional Ising system.

3.2. Stationary distributions: the theory

We are interested in computing the stationary distribution $\rho(Q)$, which is the probability per unit interval to find the order parameter Q at given values.

The key idea of the proposed scheme to obtain stationary distributions using FFS is to write $\rho(Q)$ as a sum of two contributions

$$\rho(Q) = \phi_A(Q) + \phi_B(Q). \tag{3.1}$$

Here $\phi_A(Q)$ is the contribution to $\rho(Q)$ at a given Q from those trajectories that come from region A and have not yet reached state B or state A again, and $\phi_B(Q)$ is the analogous contribution from the backward transition (see fig. 3.1). The forward FFS simulation harvests trajectories from A back to A (pathway I in fig. 3.1) and from A to B (pathway II in fig. 3.1), while the backward FFS simulation harvests trajectories from B back to B (pathway III in fig. 3.1), or from B to A (pathway IV in fig. 3.1).

Since transitions from A to B are rare, trajectories that are initiated at interface λ_0 tend to rapidly return to state A; the same holds for trajectories initiated at interface λ_n, that return to state B. FFS employs a series of interfaces to generate the Transition Path Ensemble "step by step". In this procedure, at each step an ensemble of paths is generated by firing off trajectories from points at an interface that have been obtained in the previous step; each trajectory is terminated as soon as it either reaches the next interface or λ_0 (see section 2.3.2).

We now can consider all the different kinds of trajectories represented in fig. 3.1 (I,II,III and IV), as independent parts of a longer (ideally infinite) trajectory connecting A and B: this allows us to write eq. 3.1, and to define an average over the ensemble of trajectories.

As we will describe below, the distribution function $\phi_A(Q)$ can be obtained by performing an FFS simulation for the transition from A to B, while $\phi_B(Q)$ can be computed using an

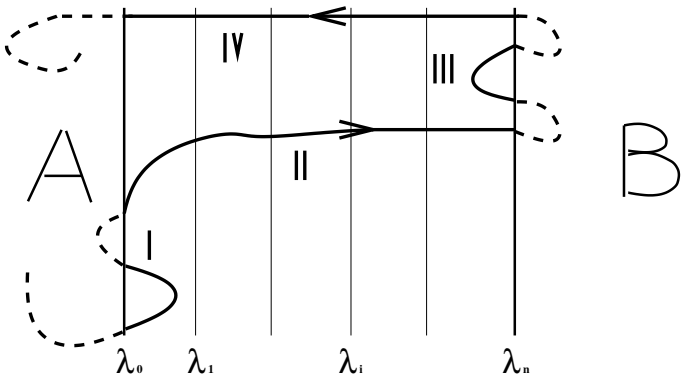

Figure 3.1.: Sketch of all kinds of trajectories that contribute to the stationary distribution $\rho(Q)$ (see eq. 3.1). I denotes a trajectory coming from A and going back to A; II is a trajectory coming from A and going to B; III is a trajectory coming from B and going back to B; IV is a trajectory coming from B and going to A. The figure also represents the interfaces $\{\lambda_0, \lambda_1, \ldots, \lambda_{n-1}, \lambda_n\}$ used in the FFS (introduced in chapter 2).

FFS simulation on the reverse transition, from B to A. For equilibrium systems, once $\rho(Q)$ is known, the free energy can be obtained from $\Delta G \sim -k_B T \ln[\rho(Q)]$.

We now describe $\phi_A(Q)$ and $\phi_B(Q)$. The function $\phi_A(Q)$ is given by

$$\phi_A(Q) = p_A \Phi_A \bar{t}(Q; \lambda_0), \tag{3.2}$$

and $\phi_B(Q)$

$$\phi_B(Q) = p_B \Phi_B \bar{t}(Q; \lambda_n), \tag{3.3}$$

Here, $p_A(p_B)$ is the probability that the system is at the beginning in state $A(B)$, $\Phi_A(\Phi_B)$ is the flux of trajectories leaving state $A(B)$ and crossing its boundary $\lambda_0(\lambda_n)$, and $\bar{t}(Q; \lambda_0)(\bar{t}(Q; \lambda_n))$ is the time a trajectory coming from $A(B)$ and not yet in $B(A)$ or in $\lambda_0(\lambda_n)$, spends at a certain value of Q (averaged over the ensemble of paths starting at $\lambda_0(\lambda_n)$).

We now focus on $\bar{t}(Q; \lambda_0)$, as $\bar{t}(Q; \lambda_n)$ can be analogously computed. $\bar{t}(Q; \lambda_0)$ is expressed as

$$\bar{t}(Q; \lambda_0) \quad = \quad \int \mathcal{D}[x(t)] \quad \cdot \quad \mathcal{P}[x(t)] \left[\int_{t_i}^{t_f} d\tau \delta \left(Q - Q[x(\tau)] \right) \right], \tag{3.4}$$

where x is a point in the multi-dimensional phase space, and $[x(t)]$ is the ensemble of trajectories starting at λ_0, and ending either at λ_0 or at λ_n [1]. The integral is run over the entire

[1] It is also important to notice that $[x(t)]$, the ensemble of trajectories, depends on the dynamics used to study the rare event: depending whether the system evolves according to a Langevin or a Monte Carlo dynamics, $[x(t)]$ will differ.

ensemble of trajectories ($\mathcal{D}[x(t)]$). $\mathcal{P}[x(t)]$ is the properly normalised probability associated to the trajectory $x(t)$ of the ensemble starting at λ_0: $\mathcal{P}[x(t)]$ is the conditional probability sampled by means of FFS in section 2.3.2. For equilibrium systems, the contributions to the average are weighted according to the Boltzmann distribution, while for non-equilibrium systems in steady-state they are weighted according to the steady-state phase space density. From eq. 3.4, we see that $\left[\int_{t_i}^{t_f} d\tau \delta\left(Q - Q[x(\tau)]\right)\right]$ is the average residence time of a trajectory $x(t)$ at a certain value of q, averaged over all the trajectories going either from λ_0 to λ_n or back to λ_0; it also indicates the contribution of the over-mentioned path starting at time t_i and ending at time t_f to each value of the order parameter q[2]. We emphasise also that the contribution to $\bar{t}(Q;\lambda_0)$ not only comes from trajectories that reach B from A, but also from trajectories starting in A, but ultimately returning back to A before reaching B. We underline the fact that eq. 3.4 is dimensionally correct, as $\mathcal{P}[x(t)]$ has dimensions of $[1/(\mathcal{D}[x(t)])]$, τ of time and δ of the inverse of the order parameter ($[1/Q]$): therefore, $\bar{t}$ will have dimensions of $[t/Q]$, i.e. a time divided by the order parameter.

Now that we know the way to compute $\bar{t}$, the flux of trajectories leaving state A and crossing the surface λ_0, Φ_A, is obtained from the forward FFS calculations. The same holds for Φ_B, computed in the reverse FFS.

In order to compute $\rho(Q)$, we also need to evaluate p_A and p_B. In steady-state,

$$p_A R_{AB} = p_B R_{BA}, \tag{3.5}$$

where R_{AB} and R_{BA} are the forward and backward rate constants measured in the forward and backward FFS, respectively, and $p_A(p_B)$ is the probability the system is initially in state $A(B)$. Since we assume a two state system (ignoring intermediate states), we can choose a normalisation such that $p_A + p_B = 1$, meaning that the system, at the beginning, can only be either in A or in B, but nowhere in between. This leads us to the following expressions for p_A and p_B:

$$p_A = \frac{R_{BA}/R_{AB}}{1 + R_{BA}/R_{AB}}, \tag{3.6}$$

and

$$p_B = \frac{1}{1 + R_{BA}/R_{AB}}. \tag{3.7}$$

This choice of normalisation can be corrected at the end of our calculations, such that $\rho(Q)$ in eq. 3.1 becomes a properly normalised probability distribution.

3.3. Stationary distributions: the method

As already mentioned, to obtain the stationary distribution $\rho(Q)$ we perform an FFS simulation for the transition from A to B and one for the reverse transition from B to A. For details on the computation of the fluxes Φ_A and Φ_B, as well as the rate constants R_{AB} and R_{BA}, we refer to section 2.3.2 and ref. [14].

[2] The paths are thus not necessarily of equal length—the number of steps per path does vary.

Here, we discuss a "step by step" procedure to compute $\bar{t}(Q;\lambda_0)$ and $\bar{t}(Q;\lambda_n)$. We only consider $\bar{t}(Q;\lambda_0)$, as $\bar{t}(Q;\lambda_n)$ is obtained similarly.

1. Having collected N_0 trajectories at λ_0. We fire a total of M_0 trial runs, each one terminated either when the next interface λ_1 is reached, or when it goes back to the initial A state;

2. every time the fired trajectory evolves, we update $\bar{t}(Q;\lambda_0)$: when trajectories come from the first interface λ_0, the contribution to each value of Q has the form of

$$t_0 = \frac{\Delta t_0}{\Delta h(Q) M_0}, \tag{3.8}$$

where $\Delta h(Q)$ is the bin size chosen to sample the order parameter space, M_0 is the total number of trial runs starting at λ_0, and Δt_0 is

$$\Delta t_0 = \sum_{i=1}^{M_0} \Delta t_i, \tag{3.9}$$

being Δt_i the simulation time steps (that are all the same in a Monte Carlo run). In order to avoid double counting, the contribution coming from the starting interface, should not be taken into account.

3. As FFS prescribes, after firing M_0 trial runs, we estimate the probability p_{01} of reaching λ_1 from λ_0 by

$$p_{01} = \frac{N_s^{(1)}}{M_0}, \tag{3.10}$$

where $N_s^{(1)}$ is the number of trials that successfully reached λ_1.

4. We then proceed to the next interface λ_2. The end points of the successful trajectories from λ_0 form a new collection of starting configurations at λ_1 ($N_s^{(1)}$). We now fire M_1 total trial runs, which either go to λ_2 or go back, beyond λ_0. Each of these trial runs, contributes to $\bar{t}(Q;\lambda_0)$ with

$$t_1 = \frac{\Delta t_1 \; p_{01}}{\Delta h(Q) \; M_1} \tag{3.11}$$

being

$$\Delta t_1 = \sum_{i=1}^{M_1} \Delta t_i \tag{3.12}$$

The factor p_{01} in eq. 3.11 arises from the fact that we have “forced” the system to be at $\lambda = \lambda_1$, and shows that in a brute force simulation, trajectories starting from λ_1 would be less probable than those starting from λ_0 by a factor p_{01}. We therefore have to include it to get the correct weighting for trial runs starting from λ_1, relative to those that started from λ_0.

Following the same procedure for all subsequent interfaces, $\bar{t}(Q;\lambda_0)$ is properly updated. More in general, for a generic interface i, the contribution of $\bar{t}(Q;\lambda_0)$ at each value of Q can be computed as

$$t_i = \frac{\Delta t_i \ \prod_{j=0}^{i-1} p_{j,j+1}}{\Delta h(Q) \ M_i}, \tag{3.13}$$

where $\prod_{j=0}^{i-1} p_{j,j+1}$ is the probability of finding a trajectory starting from λ_i in a brute force simulation, relative to that of finding one starting from λ_0, and

$$\Delta t_i = \sum_{j=1}^{M_i} \Delta t_j. \tag{3.14}$$

t_i is then the average residence time at Q of the trajectory that starts at λ_i and ends at either λ_{i+1} or λ_0, weighted with the probability of being at λ_i. At the end of the FFS sampling all the t_i's lead to the numerical estimate of $\bar{t}(Q;\lambda_0)$. Note that this quantity should not be normalised, since it is not a probability distribution.

In order to compute $\phi_B(\lambda)$, we repeat the same FFS algorithm, but going in the backward direction, i.e. from B to A. We first sample the B region, and then compute $\bar{t}(Q;\lambda_n)$.

Having obtained $\bar{t}(Q;\lambda_0)$ and $\bar{t}(Q;\lambda_n)$, we use them in eq. 3.1, to estimate $\rho(Q)$ in the region between λ_0 and λ_n: now the stationary probability can be properly normalised.

For equilibrium systems, it is possible to compute the free-energy barrier between A and B, as $\Delta G = -k_B T \ln \rho(Q)$, including the information on both states A and B. This is done by matching the stationary probabilities collected in A and B to the ones collected between the two states.

3.4. Results

We present our results in the following paragraphs.

3.4.1. Testing on a one-dimensional system

As an initial test, we have applied the method to a single particle moving with Brownian Dynamics in a one-dimensional double-well potential

$$V(x) = -bx^2 + cx^4, \tag{3.15}$$

with $b = 2$ and $c = 1$. Distances are measured in units of x_0, while time is measured in units of t_0. The stationary distribution function, as a function of the x-coordinate, is the Boltzmann distribution:

$$\rho(x) \sim e^{-V(x)/k_B T}. \tag{3.16}$$

The system is symmetric, so that $p(A) = p(B)$. According to the Langevin equation, the particle's velocity is:

$$v(t) = \frac{D}{k_B T} f(t) + \xi(t), \tag{3.17}$$

where f is the instantaneous force, D the diffusion constant, T the absolute temperature, k_B the Boltzmann constant, and ξ a random velocity, chosen from a Gaussian distribution with zero mean and variance $\langle \xi(t)\xi(0)\rangle = 2Ddt$ [71]. In our simulations, we use the following values: $D = 0.01x_0^2/t_0$, $k_BT = 0.1$ and the time step is $dt = 0.05t_0$.

We have carried out FFS simulations with 8 interfaces and $N_1 = 10000$ starting configurations at λ_0 as shown in table 3.1, where the value of the interfaces is set at specific values of x.

i	λ_i	$M(\lambda_i)$	i	λ_i	$M(\lambda_i)$
0	-0.8	100000	4	-0.1	25000
1	-0.7	250000	5	0.1	12000
2	-0.5	17000	6	0.3	10000
3	-0.3	70000	7	0.5	10000

Table 3.1.: Position of the interfaces and number of trials for the FFS sampling of the symmetric one-dimensional double-well potential.

From the calculations, we obtain a forward rate constant of $R_{AB} = (3.87 \pm 0.05) \times 10^{-6}t_0^{-1}$ (repeating twice to obtain the error bar). Because of the symmetry of the problem, it is not necessary to carry out separate FFS calculations for the backward transitions: the backward probability distribution can be obtained from the forward one by a simple coordinate inversion. The stationary distribution obtained from the FFS calculation is then compared to the expected Boltzmann distribution in fig. 3.2.

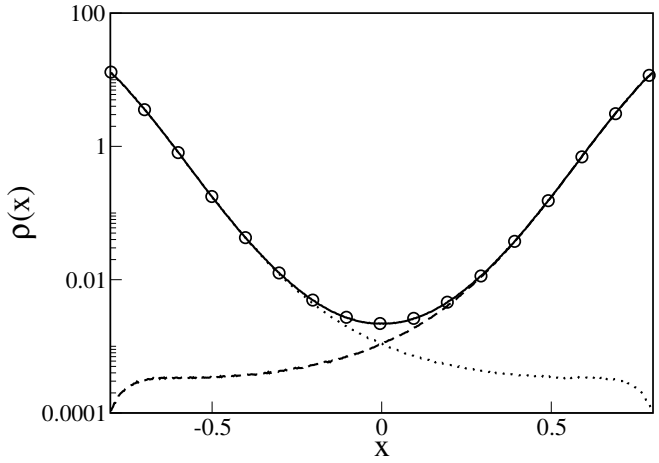

Figure 3.2.: Stationary distribution (solid line) obtained using the procedure described above, compared to the normalised Boltzmann distribution (circles) for a symmetric double-well potential. The dotted and dashed lines show $\bar{t}(x;\lambda_0)$ and $\bar{t}(x;\lambda_n)$, respectively.

We have also considered the asymmetric case, in which we include a term linear in x in

eq. 3.15:

$$V(x) = ax + -bx^2 + cx^4, \tag{3.18}$$

with $a = 0.25$, $b = 2$, $c = 1$, $D = 0.01x_0^2/t_0$, $k_BT = 0.1$ and $dt = 0.05t_0$. In this case, as $p(A) \neq p(B)$, it is necessary to carry out FFS sampling in both directions. We perform FFS simulations with 8 interfaces and $N_1 = 10000$ starting configurations. For the forward transition, we use $\lambda = x$, and for the backward transition, $\lambda = -x$. For both the forward and backward transitions, the parameters for the FFS runs are as shown in table 3.2. The

i	λ_i	$M(\lambda_i)$	i	λ_i	$M(\lambda_i)$
0	-0.8	100000	4	-0.1	50000
1	-0.7	560000	5	0.1	20000
2	-0.5	430000	6	0.3	12000
3	-0.3	170000	7	0.5	10000

Table 3.2.: Position of the interfaces and number of trials for the FFS sampling of the asymmetric one-dimensional double-well potential.

forward and backward rate constants are calculated to be $R_{AB} = (3.03 \pm 0.06) \times 10^{-7} t_0^{-1}$ and $R_{BA} = (3.96 \pm 0.03) \times 10^{-5} t_0^{-1}$, and the fluxes across the A boundary are $\Phi_A = (0.1526 \pm 0.0007) t_0^{-1}$ and $\Phi_B = (0.3648 \pm 0.0001) t_0^{-1}$, respectively. On the left side in fig. 3.3 we show $\bar{t}(x; \lambda_0)$ and $\bar{t}(x; \lambda_n)$, while on the right side we show $\rho(x)$ calculated from eq. 3.1 and properly normalised. Excellent agreement is obtained with the expected Boltzmann distribution.

3.4.2. Testing on the two-dimensional Maier-Stein system

We now compute the stationary distributions both in and out of equilibrium in a two-dimensional system moving according to an over-damped Brownian motion in the force field proposed by Maier and Stein [74]:

$$\begin{cases} \dot{x} = f_x(\mathbf{x}, t) + \xi_x(t) \\ \dot{y} = f_y(\mathbf{x}, t) + \xi_y(t), \end{cases} \tag{3.19}$$

where $\mathbf{x} = (x, y)$ is the particle's position, $\mathbf{v} = (\dot{x}, \dot{y})$ its velocity, $\mathbf{f} = (f_x, f_y)$ the time-independent force field, given by

$$\begin{cases} f_x = x - x^3 - \alpha x y^2 \\ f_y = -\mu y (1 + x^2), \end{cases} \tag{3.20}$$

being α and μ adjustable parameters, and $\xi = (\xi_x, \xi_y)$ the stochastic force, resulting from a δ-function-correlated white noise with variance ϵ

$$\langle \xi_i(t) \rangle = 0 \; ; \; \langle \xi_i(t) \xi_j(0) \rangle = \epsilon \, \delta_{ij} dt, \tag{3.21}$$

being $i = x, y$. In our simulations, we use $\epsilon = 0.1$. This system is bistable: the stable points are at $(\pm 1, 0)$ and the saddle point at $(0, 0)$. When $\alpha = \mu$, the force field can be expressed as

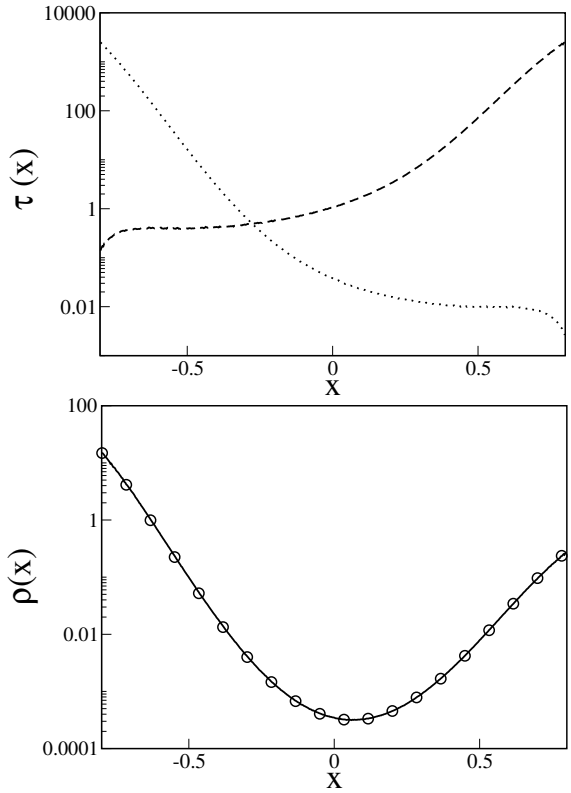

Figure 3.3.: Asymmetric double-well potential: on the right side, $\bar{t}(x;\lambda_0)$ (dotted line) and $\bar{t}(x;\lambda_n)$ (dashed line). On the left side, final result for $\rho(x)$ obtained from eq. 3.1 (solid line) compared to the expected Boltzmann distribution (circles).

the gradient of a potential energy function and the system is "in equilibrium". However, when $\alpha \neq \mu$, the force field cannot be expressed as the gradient of a potential energy function, and the system is intrinsically "out-of-equilibrium".

We set λ at fixed values of x and calculate the stationary distribution for $-0.8 < \lambda < 0.8$. For the FFS calculations, we use 8 interfaces and $N_1 = 100000$ initial configurations at λ_0. The parameters used are listed in table 3.3.

Equilibrium case

We initially consider the equilibrium case, with $\alpha = \mu = 1$ and $\epsilon = 0.1$: a particle moves in the potential field $\phi(x,y) = \frac{y^2(1+x^2)}{2} - \frac{x^2}{2} + \frac{x^4}{4}$. Figure 3.4 both on the left-side and on the right-side show the stationary distribution $\rho(x,y)$, as a function of x for $y = -0.39$, $y = -0.19$ and $y = 0.01$, and as a function of y for $x = -0.312$, $x = -0.152$ and

i	λ_i	$M(\lambda_i)$	i	λ_i	$M(\lambda_i)$
0	-0.8	1000000	4	0.2	200000
1	-0.6	500000	5	0.4	120000
2	-0.4	300000	6	0.6	100000
3	-0.2	250000	7	0.8	100000

Table 3.3.: Position of the interfaces and number of trials for the two-dimensional Maier-Stein system.

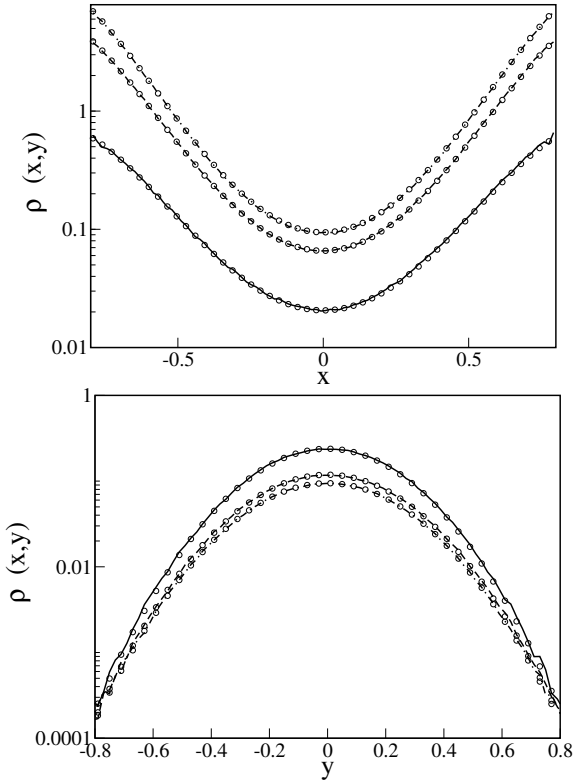

Figure 3.4.: Equilibrium case. On the left-side: $\rho(x, y)$ as a function of x for $y = -0.39$ (solid line), $y = -0.19$ (dashed line) and $y = 0.01$ (dot-dashed line) (from bottom to top), compared to the expected Boltzmann distribution (indicated by circles) for the Maier-Stein system with $\epsilon = 0.1$ and $\alpha = \mu = 1$. On the right-side: $\rho(x, y)$ as a function of y for $x = -0.312$ (solid line), $x = -0.152$ (dashed line) and $x = 0.008$ (dot-dashed line) (from top to bottom).

$x = 0.008$. In both panels, the results are in excellent agreement with the expected Boltzmann distribution (shown by circles).

Out-of-equilibrium case

We next discuss the non-equilibrium case ($\alpha \neq \mu$), taking $\alpha = 6.67$, $\mu = 2.0$ and $\epsilon = 0.1$. Fig. 3.5 shows equivalent results to fig. 3.4, but this time the FFS calculations are compared to stationary distributions computed from long brute-force simulations. The brute-force simulation results are normalised over the entire space. Even in this case, very good agreement is observed.

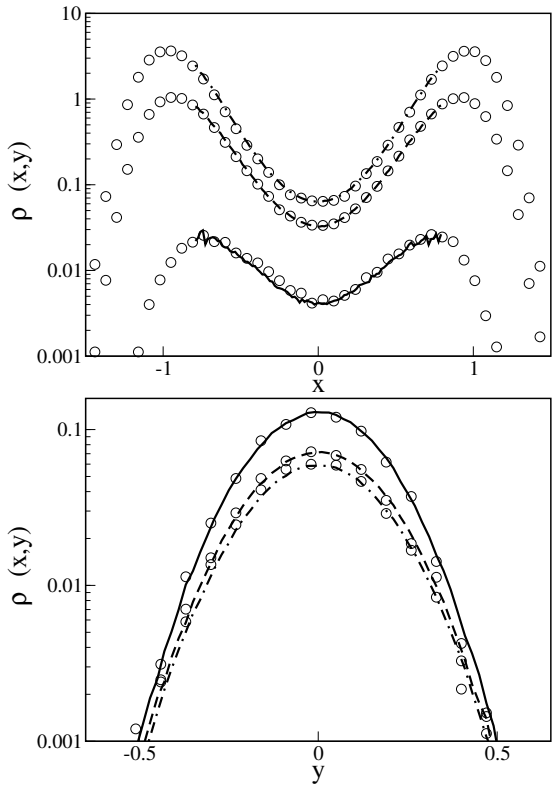

Figure 3.5.: Out-of-equilibrium case. On the left-side: $\rho(x, y)$ as a function of x for $y = -0.39$ (solid line), $y = -0.19$ (dashed line) and $y = 0.01$ (dot-dashed line) (from bottom to top), compared to the long brute force simulations (indicated by circles). On the right-side: $\rho(x, y)$ as a function of y for $x = -0.312$ (solid line), $x = -0.152$ (dashed line) and $x = 0.008$ (dot-dashed line)(from top to bottom).

3.4.3. Homogeneous nucleation in a two-dimensional Ising model

We now address a rare event problem in a more complex system: homogeneous nucleation in a two-dimensional Ising model. For now, we confine ourselves to an equilibrium system

without any external shear; non-equilibrium nucleation in an Ising model with an external shearing field will be considered in chapter 10. The two-dimensional Ising model consists of an $L \times L$ square lattice of spins with nearest neighbour interactions and periodic boundary conditions. Its Hamiltonian is

$$H = -J \sum_{ij}{}' \sigma_i \sigma_j - h \sum_i \sigma_i, \tag{3.22}$$

where J is the coupling constant between neighbouring spins ($\sigma_i = \pm 1$) and h the external magnetic field [75]. The prime indicates a sum over first nearest neighbour interactions only. We simulate a system with $N = 45 \times 45 = 2025$ spins, a positive magnetic field ($\beta h = 0.05$) and a positive coupling constant ($\beta J = 0.65$) above the critical point ($\beta J_c = 0.44$). The thermodynamically stable state is therefore the ferromagnetic state with net positive magnetisation, meaning that the system tends to have the majority of spins in the up state. However, if the system is initially in a state with an overall negative magnetisation (i.e. spins predominantly in the down state), it is metastable and remains in that state for a significant time. We aim to compute the free-energy barrier, as well as the rate constant, for transitions from this metastable down state to the thermodynamically stable up state. We begin our simulations in the down state and consider the formation of a cluster of up-spins, under conditions of moderate super-saturation (these conditions are identical to those used by Sear [68]). All our simulations are performed using a Metropolis Monte Carlo algorithm, in which we attempt to flip each spin once, on average, during each Monte Carlo cycle.

According to Classical Nucleation Theory [6], the free-energy cost of forming a square cluster of edge L is given by the sum of a line energy and a surface energy:

$$\Delta G = 4\gamma L - 2hL^2, \tag{3.23}$$

where γ is the inter-facial free energy between a cluster made of up-spins and the neighbouring down-spins, h is the driving force for nucleation (the external magnetic field), and (-$2hL^2$) is the energy cost of flipping the whole square cluster with area L^2. Therefore, using eq. 3.23, the nucleation free-energy barrier height is given by

$$\Delta G^* = \frac{2\gamma^2}{h}. \tag{3.24}$$

Plugging in numbers, if we compute the inter-facial free energy according to Onsager [76, 68], $\beta\gamma = 0.74$, the barrier height as predicted by Classical Nucleation Theory is $\Delta G^* \sim 22$ $k_B T$.

We compute the free-energy barrier using two simulation techniques: Umbrella Sampling and Forward Flux Sampling (both described in chapter 2). In both cases, we characterise the extent of the transition using a global order parameter, S, the total number of up-spins in the system. The free-energy barrier is then defined as $\beta\Delta G(S) \equiv -\ln[\rho(S)/N]$, where $\rho(S)$ is the probability of observing S up-spins in the stationary state, and N is the total number of spins in the system, such that $\rho(S)/N$ is now an intensive quantity. For the Umbrella Sampling calculations, we use an harmonic potential in S to bias the sampling of phase space

along the phase transition [12, 11], and use 25 windows to cover the range of $0 \leq S \leq 300$, with an overlap between neighbouring windows of 11 spins. We sample each window for 500000 MC cycles, and fit the resulting histograms together using a least-squares fitting procedure to obtain the free-energy profile in the same range. We do not attempt to calculate the barrier for values of S greater than 300, since once the top of the barrier is crossed, the system is expected to evolve rapidly and we cannot rely on the assumption of local thermodynamic equilibrium anymore. Moreover, when S is larger than half of the simulation box, the growing cluster is likely to interact with its own periodic images in neighbouring cells, making the results highly system-size dependent.

Concerning the FFS simulations, the interfaces λ are also defined in terms of the order parameter S, and are located, both for the forward and backward sampling, at values of S given in table 3.4, where we also list the number of trials performed at each interface.

i	λ_i	M_i	i	λ_i	M_i	i	λ_i	M_i
0	30	1000	9	250	1000	18	500	1000
1	50	1000	10	280	1000	19	550	1000
2	70	1000	11	300	1000	20	600	1000
3	100	1000	12	330	1000	21	650	1000
4	130	1000	13	350	1000	22	700	1000
5	150	1000	14	380	1000	23	750	1000
6	180	1000	15	400	1000	24	800	1000
7	200	1000	16	430	1000	25	850	1000
8	230	1000	17	450	1000	26	950	1000

Table 3.4.: Position of the interfaces and number of trials per interface for the FFS sampling of the two-dimensional Ising nucleation problem.

To calculate the free-energy barrier using FFS, we need to be able to sample the reverse transition, from the thermodynamically stable up state to the metastable down state. In general, this is very difficult in a nucleation problem, since the final thermodynamic state is much more stable than the metastable state, and there is a very high free-energy barrier for the system to overcome to return to the initial down state, making the reverse transition difficult to sample even with FFS.

In order to solve this problem, we construct a reflecting wall beyond the top of the nucleation barrier at a value of S indicated by B' in fig. 3.6. This wall is incorporated via a constraint on the system dynamics: each trial move that leads to $S > S_{B'}$ is simply rejected [3].

Since we are only interested in the free-energy profile of the region between A and the top of the barrier, we are allowed to perturb the free-energy landscape outside this region as we need. This fact, which is also exploited in Umbrella Sampling, depends on the system being in equilibrium - for a system driven out-of-equilibrium, we would not be able to

[3]The use of the reflecting wall greatly facilitates the FFS calculation for the reverse transition—it is possible to carry out the reverse FFS calculations without the wall, but this is rather laborious as it requires an incredibly large number of interfaces.

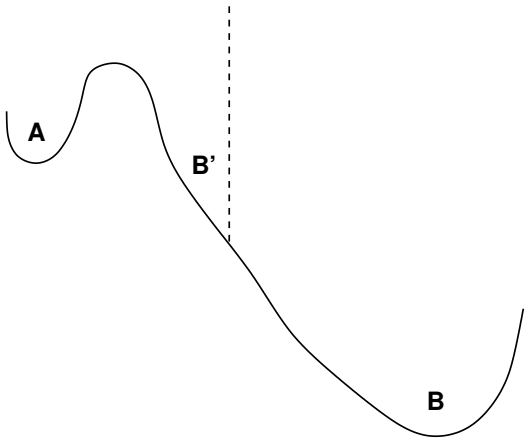

Figure 3.6.: Schematic view of the free-energy landscape. A is the metastable initial down state, B is the real thermodynamically stable final state, and $B^{'}$ is the "artificial" stable state, constructed by introducing a reflecting wall at $S = S_{B'} = 1050$.

use this approach. In general, in equilibrium systems the flux between any two state points is zero in steady-state. While for non-equilibrium systems this need not be the case, as in non-equilibrium systems the stationary distribution depends upon the full history of the trajectories, prohibiting the introduction of artificial boundaries. The reflecting wall, located at $S = S_{B'} = 1050$, replaces the B state as an artificial stable state $B^{'}$ (see fig. 3.6). In this way, the free-energy barrier for the $B' \rightarrow A$ transition is then much lower than that for the $B \rightarrow A$ transition, and the shape of the free-energy barrier on the A side remains unchanged. Before starting our calculations, we have also verified that the location of the reflecting wall is indeed well beyond the top of the free-energy barrier, which is estimated to be for $200 < S < 280$. The initial state A is defined by the first interface $\lambda_0 = 30$, i.e. when $0 < S < 30$ the system is in the A state. While the final state B' has its boundary in $\lambda_n = 1000$, i.e. when $1000 < S < 1050$ the system is in the B' state. In our FFS calculations, we consider $N_1 = 50$ configurations at the first interface.

The FFS calculations of the forward transition from A to $B^{'}$ is straightforward. The flux Φ_A through λ_0 of trajectories coming from A is $\Phi_A = 1.5 \times 10^{-5}$ MC step^{-1} spin^{-1} and the forward rate constant $R_{AB'} = (2.8 \pm 0.3) \times 10^{-13}$ MC step^{-1} spin^{-1}, in good agreement with the value of 3.3×10^{-13} MC step^{-1} spin^{-1} computed by Sear et al. [68]. We also check that the computed forward rate constant does not depend on the reflecting wall position $S_{B'}$. In the reverse direction, we use the same interfaces and sample from λ_n to λ_0. We obtain the flux $\Phi^{'}_B = 1.4 \times 10^{-6}$ MC step $^{-1}$ spin^{-1} and the backward rate constant $R_{B'A} = (2.0 \pm 0.2) \times 10^{-19}$ MC step^{-1} spin^{-1}. Combining the rate constants as in eqs. 3.6 and 3.7, we obtain $p_A = 7 \times 10^{-7}$ and $p_{B'} = 0.999$. By means of eqs. 3.1 and 3.2 we finally compute $\rho(S)$ for $30 < S < 1000$ that, fitted together with the distribution obtained by conventional sampling in A (as described in section 3.2), gives us the free-energy barrier

as $-\ln[\rho(S)/N]$.

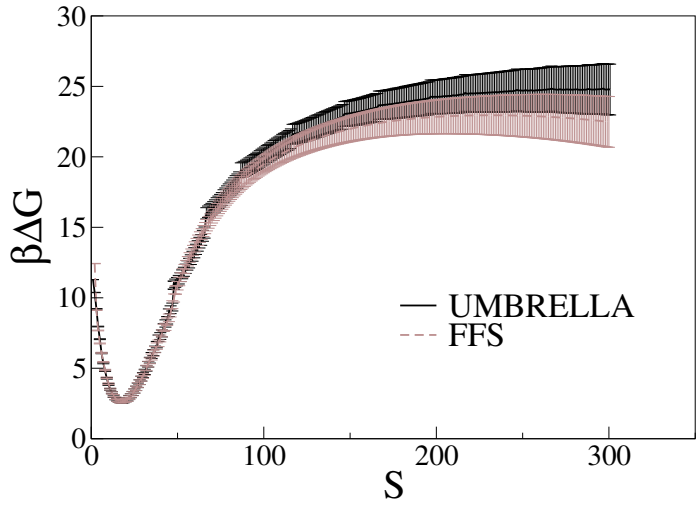

Figure 3.7.: Free-energy barrier of the two-dimensional Ising model for $\beta J = 0.65$ and $\beta h = 0.05$ calculated using FFS (dashed line; grey) and Umbrella Sampling (continuous line; black). Error bars are shown for both calculations.

Figure 3.7 shows the nucleation barrier $\beta\Delta G(S)$ in the range $0 < S < 300$. The free-energy minimum at $S \approx 20$ indicates that at this super-saturation, the system has a finite number of up-spins even in the down state.

The top of the free-energy barrier, as obtained by Umbrella Sampling and FFS, is $\Delta G^{\mathrm{US}} = 24.5 k_B T$ and $\Delta G^{\mathrm{FFS}} = 23 k_B T$, respectively. These values coincide within the error bars, which for both schemes are on the order of $k_B T$. The computed barrier heights also agree remarkably well with the CNT prediction of $22 k_B T$ at the same super-saturation.

3.5. Conclusions

The key concept used here to obtain the stationary distribution in the unstable region between two states A and B is to add the contributions from the trajectories that start in A and go to B or return to A, and those that start in B and go to A or return to B (see fig. 3.1). These contributions can be obtained by performing FFS calculations starting in state A and calculations starting in state B. For many rare event problems this is entirely possible - however, for systems where one state is very much more stable than the other, sampling the reverse transition ($B \rightarrow A$) may be computationally difficult, even with FFS. We have encountered this problem in the Ising nucleation example. For equilibrium systems, this problem is overcome by imposing an artificial stable state, as demonstrated here for the case of nucleation in an Ising system. However, this trick is not applicable for non-equilibrium

systems. As already mentioned, in general, in equilibrium systems the flux between any two state points is zero in steady-state, while in non-equilibrium systems this need not be the case. In these non-equilibrium systems, the stationary distribution depends upon the full history of the trajectories. This, in general, prohibits the introduction of artificial boundaries. In particular, while for equilibrium systems detailed balance and microscopic reversibility dictate that the forward and backward transition paths have to occupy the same region in state space, for systems that are out of equilibrium the backward and forward trajectories do not have to coincide; indeed, in these systems cycles in state space can occur. If the forward and backward transition paths form a cycle in state space, then it is conceivable that the artificial stable state "short cuts" the cycle and generates a wrong ensemble of points from which trajectories are initiated in the reverse direction.

For the computation of free-energy barriers in equilibrium systems a wide range of numerical techniques is available. The advantage of the scheme proposed here is that the free energy can be directly obtained from an FFS simulation, giving simultaneously the rate constant, transition paths and free-energy landscape. This is important because both the calculation of the rate constants and the evaluation of the free-energy barriers are computationally demanding, especially for large and complex systems.

It has long been appreciated that free-energy barriers are critical quantities for understanding rare events in equilibrium systems, such as nucleation and protein folding. However, the "barriers", or minima in the stationary probabilities, that separate steady-states in non-equilibrium systems are equally important, because the rate of switching from one steady-state to the next is proportional to the probability of being at the top of the "barrier" [73].

To our knowledge, this technique is the first to be proposed for efficient computation of stationary distributions for rare events in non-equilibrium systems. This should prove useful for enhancing our understanding of a range of important non-equilibrium rare event processes, as well as improving the efficiency of computation of free-energy landscapes in equilibrium systems.

Acknowledgements

Concerning this work, I would like to thank S. Tanase for very useful discussions.

Part III.

Ionic systems

4. Rate of homogeneous crystal nucleation in molten NaCl[1]

...Galeotto fu 'l libro e chi lo scrisse:
quel giorno più non vi leggemmo avante.
Dante Alighieri, Quinto canto, Inferno, Divina Commendia.

We report a numerical simulation of the rate of crystal nucleation of sodium chloride from its melt at moderate super-cooling. In this regime nucleation is too slow to be studied with "brute-force" Molecular Dynamics simulations. The melting temperature of ("Tosi-Fumi") NaCl is ~ 1060K. We studied crystal nucleation at both 800K and 825K. We observe that the critical cluster formed during the nucleation process has the crystal structure of bulk NaCl. Interestingly, the critical cluster is clearly faceted: the clusters have a cubical shape. We have computed the crystal-nucleation rate using two completely different approaches, one based on an estimate of the rate of diffusive crossing of the nucleation barrier, the other based on the Forward Flux Sampling method. We find that the two methods yield the same result to within an order of magnitude. However, when we compare the extrapolated simulation data with the only available experimental results for NaCl homogeneous nucleation, we observe a discrepancy of nearly 5 orders of magnitude. We discuss the possible causes for this discrepancy.

4.1. Introduction

Crystallisation of salts is a phenomenon of great practical relevance. In fact, it is one of the most important industrial separation processes. But it also plays a crucial role in geological processes that occur on an altogether different time scale.

It is clearly important to be able to predict the rate of nucleation of salts and – at a later stage – to understand the factors that influence nucleation. In the present chapter we aim to demonstrate that, with current simulation techniques and currently available force-fields, it is indeed possible to compute the rate of nucleation of a real salt crystal (in the present case NaCl from its melt). This opens the way to "ab-initio" predictions of nucleation rates of many ionic substances.

Under experimental conditions, nucleation is infrequent on the time scale of typical molecular processes. Yet, when it happens, it proceeds rapidly. This makes it difficult to study the

[1] Work carried out in collaboration with E. Sanz.

structure and dynamics of crystal clusters of atoms or small molecules in experiments. In the case of NaCl, the experiments are also complicated by the fact that crystallisation occurs at high temperatures. This may explain why there is a scarcity of experimental data on the nucleation of NaCl. To our knowledge, the only data are those of Buckle and Ubbelhode [77, 78] from the 1960's. In these experiments, crystallisation in NaCl micro-droplets was observed visually. As the droplet size (($\mathcal{O}(3\mu)$) and time window for the measurement (1–30 seconds – after which the droplets sedimented out of view) – were fixed, the nucleation rate could be determined at one temperature only (905 K). At this temperature, the nucleation rate was such that, on average, one cluster would form during the observation time ($\mathcal{O}(10s)$) in a droplet with a volume of order $10^{-17}m^3$, leading to an experimental nucleation rate per unit volume of $O(10^{16})\ m^{-3}s^{-1}$.

For experimental nucleation rates of this order of magnitude, brute-force MD simulations are out of the question. The average time it would take for clusters to form spontaneously in a system consisting of several thousands of particles is of order of 10^{20} seconds. Clearly, this is beyond the scope of MD simulations. The standard solution to circumvent this problem is to perform simulations at much larger super-cooling than used in the experiments. Huang et al. [79] performed MD simulations of melting and freezing of a droplet composed of 216 NaCl ions in vacuum: to this end, they performed temperature quenches down to 550K (i.e. approximately half the melting temperature) and found nucleation rates of the order of $O(10^{36})m^{-3}s^{-1}$, which is 20 orders of magnitude higher than the experimental rate at $905K$.

Another effort to study nucleation at less severe super-cooling was made by Koishi et al. [80]. These authors performed an MD simulation of 125000 ions system in vacuum, at temperatures of 740K (i.e. approximately 0.7 the melting temperature T_m) and 640K (i.e. approximately 0.6 the melting temperature T_m). Both free and periodic boundary conditions were used. The estimated nucleation rate at $740K$ was $O(10^{35})m^{-3}s^{-1}$, which is virtually the same value as the one found by Huang et al. [79] at a much larger super-cooling. This is surprising because nucleation rates tend to depend very strongly on temperature, and suggests that, at least at the lowest temperatures, the barrier for crystal nucleation is negligible. More in general, crystal nucleation under extreme super-cooling need not to proceed following the same path as under moderate super-cooling [6].

In the present work we study homogeneous crystal nucleation in the Tosi-Fumi NaCl model at two different temperatures, viz. T_1=800K and T_2=825K, corresponding to 25% and 22% super-cooling, respectively. For this system, we compute the nucleation barrier, examine the structure and shape of the critical cluster and calculate the nucleation rate.

4.2. Simulations details

The Tosi-Fumi rigid-ion two-body interaction potential for NaCl is of the following form [81],

$$U_{ij}(r) = A_{ij}e^{[B(\sigma_{ij}-r)]} - \frac{C_{ij}}{r^6} - \frac{D_{ij}}{r^8} + \frac{q_i q_j}{r}, \tag{4.1}$$

where i, j indicates Na or Cl, and the parameters have the values given in table 4.1.

	A_{ij} $[kJ/mol]$	B $[\dot{A}^{-1}]$	C_{ij} $[\dot{A}^6 kJ/mol]$	D_{ij} $[\dot{A}^8 kJ/mol]$	σ_{ij} $[\dot{A}]$
Na-Na	25.4435	3.1546	101.1719	48.1771	2.340
Na-Cl	20.3548	3.1546	674.4793	837.0770	2.755
Cl-Cl	15.2661	3.1546	6985.6786	14031.5785	3.170

Table 4.1.: Potential parameters for NaCl.

This pair potential is written as the sum of a Born-Mayer repulsion term, two attractive van der Waals contributions and a Coulomb interaction term.

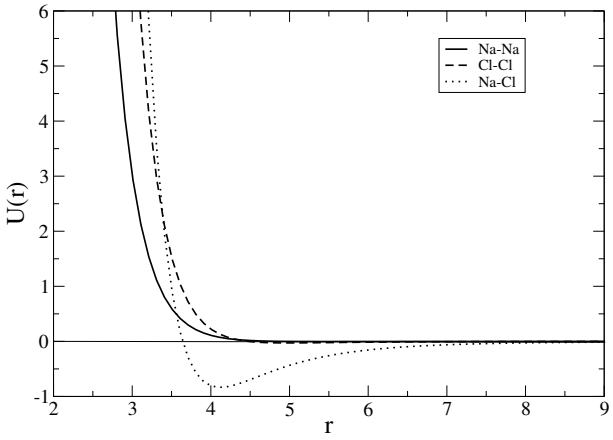

Figure 4.1.: Tosi Fumi potential.

In our simulations, we calculate the Coulomb interactions using the Ewald summations method [82, 83] with a real space cut-off of 10 $\dot{A}$ and a real space damping parameter of 0.25 $\dot{A}^{-1}$ [1]. We truncate the Van Der Waals part of the potential at 9 $\dot{A}$, assuming the $g(r) = 1$ beyond this cut-off, and take care of the truncation when computing the total energy of the system (see appendix A). The computed number density in the bulk solid at 800K and 825K and ambient pressure (10^5 Pa) is $0.041\dot{A}^{-3}$, in agreement with the experimental one [84]. The number density in the super-cooled liquid at the same temperature and pressure is $0.034\dot{A}^{-3}$. We prepare under cubic periodic boundary conditions a system of $(12)^3$ NaCl ion pairs at ambient pressure, and we super-cool it down below its melting temperature. For the present model, Anwar et al. [85] computed the value of the melting temperature: T_M=(1064 ± 14)K, which is very close to the experimental melting temperature (T_M^{exp}=1072K).

Using constant number of particles, pressure, temperature (NPT) Monte Carlo simula-

[1] In order to tune the Ewald's parameters, we numerically compute both the Madelung constant and the lattice energy of a perfect NaCl lattice (the Madelung constant is 1.7476 and the lattice energy (-766 kJ/mol)).

tions, we cool the system down to the temperatures where we want to study nucleation: T_1=800K and T_2=825K, corresponding to 25% and 22% super-coolings. Note that the experiments on NaCl nucleation were performed at a somewhat higher temperature (905K, or 16% super-cooling). The reason why we could not perform simulations at these high temperature is that at this condition the critical cluster would be about twice the size of the cluster that could be studied without spurious finite-size effects for the system sizes that we employ [86]. We also notice that at temperatures below $T_{min} = 750$K, spontaneous nucleation occurs during simulations. Therefore, when choosing the temperatures to study nucleation, we thermalise the system at $T_i > T_{min}$ ($i = 1, 2$), as we are interested in studying the nucleation mechanism at moderate super-coolings.

In what follows, we use the technique of refs. [11, 87, 88] based on a combination of Umbrella Sampling (to determine the barrier height) and a dynamical simulation (to determine the crossing rate) (see chapter 2). The computing time required for this scheme does not scale exponentially with the nucleation barrier, but it does increase with increasing cluster size, therefore the system size. We also compute the nucleation rate using an algorithm based on Forward Flux Sampling [13, 14] (see chapter 2) and compare it with the one obtained using the method previously mentioned. Once computed the nucleation rate per unit time and volume, we compare the results with those obtained using Classical Nucleation Theory (see equation 2.32).

The order parameter used to follow the phase transition from the liquid to the solid state, is the biggest solid cluster size (n): this is based on a local bond order parameter already mentioned in chapter 2 and hereby described in appendix B.

4.3. Results

We compute the free-energy barrier to crystal nucleation at ambient pressure and two different temperatures T_1=800K and T_2=825K, corresponding to $\beta\Delta\mu_1$=0.54 and $\beta\Delta\mu_2$=0.48. We numerically estimate $\beta\Delta\mu$ by means of thermodynamic integration from the coexistence temperature T_M and the free energies reported by Anwar et al. [85] (see appendix C).

Fig. 4.2 shows the computed nucleation barriers as a function of n. As expected, $\beta\Delta G$ decreases with increasing super-saturation. Around T$\leq$750K the barrier gets sufficiently low that spontaneous nucleation can take place on the time scale of a simulation.

We estimate the size of the critical cluster, n_c, by computing the value of n corresponding to the maximum of a fit of the functional form of the CNT free energy: $n_c \approx 120$ ions at T_1 and $n_c \approx 150$ ions at T_2 [2]. Koishi et al. [80] estimated $n_c = 120 - 130$ ions at 640K and 740K, which is surprising in view of the CNT prediction that the size of the critical cluster scales as $(\gamma/|\Delta\mu|)^3$, where γ is the liquid-solid surface free energy per unit area, $\Delta\mu$ is the difference in chemical potential between the solid and the super-cooled liquid. If we make

[2] We make sure that our simulations are not biased by finite size effects, that can result in spurious interactions between periodic images of the critical cluster. Firstly, we visually check that the critical cluster does not show a preferred spacial orientation in the simulation box, and that the minimum distance between repeated images is bigger than half box. Secondly, we calculate the Debye-Huckle screening length, and find that it is smaller than 1 $\AA$: this illustrates that not even electrostatic interactions are present between the critical cluster and its own periodic images.

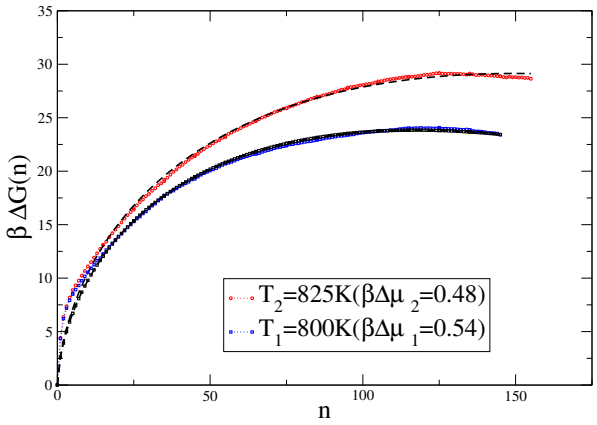

Figure 4.2.: free-energy barriers ΔG as a function of the cluster size n for T_1=800K($\beta\Delta\mu_1 = 0.54$) and T_2=825K($\beta\Delta\mu_2 = 0.48$). Error-bars on $\beta\Delta G$ are of the order of 1 k_BT. The dashed curves are fits to the functional form given by CNT.

the usual assumption [6, 89] that $\gamma \sim \Delta h$ and $\Delta\mu \approx (\Delta h/T_M)(T - T_M)$, where Δh is the entropy of fusion per ion pair, then we would expect that $n_c \sim (1 - T/T_M)^{-3}$, and predict that the critical cluster at 640K should contain a quarter as many particles as those at 800K. Next, we consider the structure and shape of the critical cluster.

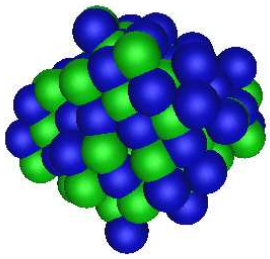

Figure 4.3.: Snapshot of the critical cluster at T_2=825K.

Fig. 4.3 shows a snapshot of the critical cluster at T_2=825K. Note that the crystal presents rudimentary low-index facets. In experiments [77, 90] the existence of such facets was postu-

lated, as they may act as sites for subsequent heterogeneous nucleation. Moreover, as can be seen from the figure, the critical cluster already shows the charge-ordered rock-salt structure of the bulk phase, exhibiting the morphology of macroscopic NaCl crystals [91]. fig. 4.3 also shows that, in the temperature range we studied, the critical cluster is non-spherical.

In order to better analyse the structure inside the crystallites, we have compared the radial distribution function ($g(r)$) of the solid particles inside the cluster with the one of the bulk solid at the same thermodynamic conditions. Figure 4.4 shows the comparison for a 135 solid-particles cluster obtained in a typical FFS nucleation pathway. From the figure it is evident that the crystallites have the same structure as the bulk solid NaCl, showing the peaks at the same positions. This indicates that, at least for NaCl, nucleation does not proceed via an intermediate metastable phase, as Ostwald's step rule implies [92].

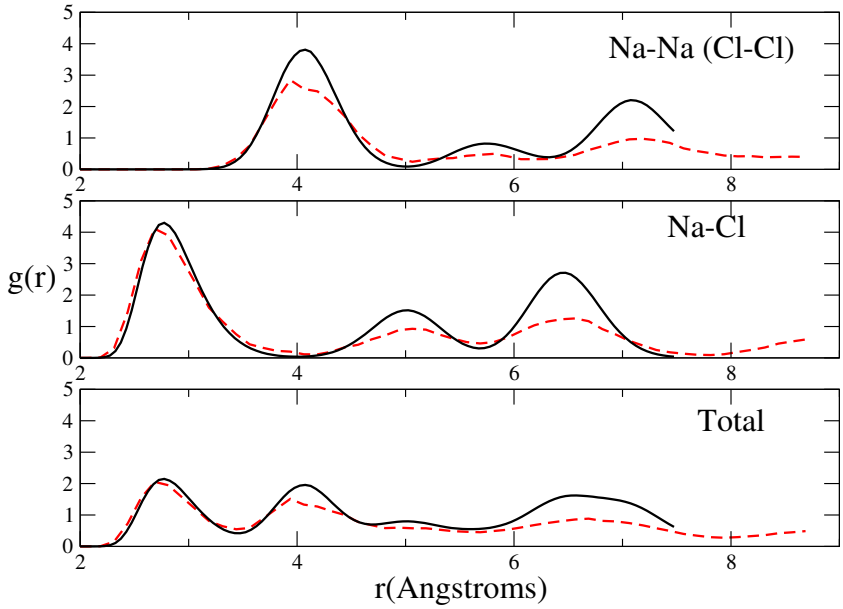

Figure 4.4.: Radial distribution function of a 135 particles cluster at 800 K and 1 atm (dashed line), compared with that of the bulk solid (solid line) at the same temperature and pressure. The g(r) of the ions belonging to the cluster is not normalised and has been multiplied by a factor of 10 in order to compare it visually with that of the bulk.

Using the computed height of the nucleation barrier and the values of $\Delta\mu$ as input, we can estimate the liquid-solid surface free energy γ. To this end, we make use of the CNT expression for the barrier height (eq. 2.10). However, this expression assumes the critical cluster being spherical. It is easy to derive the corresponding expression for a cubical cluster (see eq. 2.15) and express γ for different cluster shapes.

As already discussed chapter 2, eqns. 2.15 allows us to compute the liquid-solid inter-facial free energy for a pre-defined cluster shape. In our simulations, the computed number density

in the bulk solid at ambient pressure and at both T_1 and T_2 results to be 0.041 Å^{-3}: thus, the specific volume is $v_{1,S} \approx v_{2,S} = 24.4$ Å^3. The super-saturation of the system is $\beta\Delta\mu_1$=0.54 and $\beta\Delta\mu_2$=0.48. As the free-energy barrier heights are $\beta\Delta G_1 = 24$ and $\beta\Delta G_2 = 29$, by means of eq. 2.16 we get $\gamma_{\rm LS} \approx 100$ mJ m^{-2} for a spherical cluster and $\gamma_{\rm LS} \approx 80$ mJ m^{-2} for a cubic one, values that are reasonably close to the experimental measurement reported in the literature [77] (84 mJ m^{-2} for a spherical cluster and 68 mJ m^{-2} assuming a cubical shape). The results for both estimates of γ are summarised in table 4.2.

T[K]	γ_{sphere}	γ_{cube}
800	98 ± 2	80 ± 1
825	99 ± 1	79 ± 1
905	84.1^{exp}	67.8^{exp}

Table 4.2.: Surface free-energy density (in mJ m^{-2}) assuming spherical and cubic critical clusters. At 905K we report the experimental value [77]. The entry in the lower right-hand corner is based on the experimental estimate, but assuming a cubic cluster.

There exist experimental estimates of γ at 905K [77]. These estimates are based on a somewhat questionable CNT expression for the nucleation rate. Moreover, in ref. [77] it is assumed that the critical cluster is spherical. The experimental estimate of γ (γ_{exp}=84.1 mJ m^{-2}) is therefore not based on a direct determination. Nevertheless, in the absence of other experimental data, this is the only number we can compare to. As the table shows, there is a fair agreement between simulation and experiment. Again, the experimental estimate for γ is based on the assumption that the critical cluster is spherical. If cubic, one would obtain the number in the lower right-hand corner. In view of the many uncertainties in the analysis of the experimental data, it is impossible to tell whether the discrepancy between simulation and experiment is significant. An estimate of γ based on the experimental enthalpy of fusion following Turnbull would yield $\gamma \approx 115$ mJ m^{-2} (see e.g. ref [79]). Huang et al. [79] estimated the liquid-solid surface free energy of NaCl from the computed nucleation rate at 550K. To achieve this, Huang implied the validity of the CNT expression for the nucleation rate. Under those assumptions, they obtained: γ= 119.6 mJ m^{-2} for a spherically shaped cluster.

In the present work, we compute absolute nucleation rates making the assumption that the barrier crossing is a diffusive process and the Zeldovitch pre-factor is well approximated by the form presented in eq.2.33. The Zeldovitch factors are found to be respectively Z_1=0.016 at T_1 and Z_2=0.013 at T_2[3]. From our simulations, we compute $k_{+,{\rm n}^*}$ i.e. the attachment rate of particles to the critical cluster, according to eq. 2.52. In practise, we start with generating 120 uncorrelated configurations at the top of the free barrier, and carry out NVT MD simulations using the DLPOLY package [93] with a time-step of 0.5 fs [4]. Then, we measure the average mean square displacement of n ($\langle\langle(\Delta n^*)^2(t)\rangle\rangle$), and plot it as a function of $2t$: for long times the slope is proportional to the attachment rate. Thus, our results

[3]The true Zeldovitch factor may be slightly different, but, in any event, it is expected to be of $\mathcal{O}(10^{-2})$.

[4]Importantly, we make sure that the time it takes the initial velocities to equilibrate is shorter than

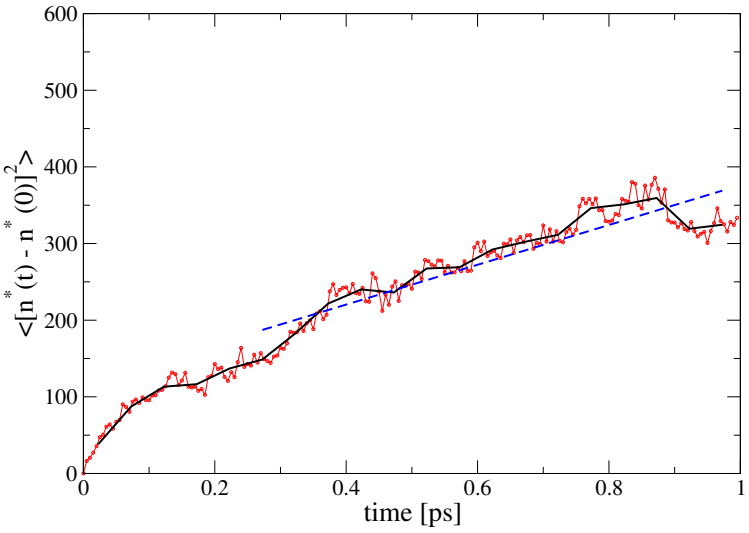

Figure 4.5.: Computation of the attachment rate k_{+,n^*} at T_1.

are k_{+,n^*}=0.013 ps^{-1} at T_1 and k_{+,n^*}=0.033 ps^{-1} at T_2. We can then compute the kinetic pre-factor (eq. 2.35): $\kappa(T_1)$= 6.9$\times 10^{36}$ $m^{-3}s^{-1}$ and $\kappa(T_2)$= 1.5$\times 10^{37}$ $m^{-3}s^{-1}$. As it is to be expected, the kinetic pre-factor depends only weakly on temperature. Using eq. 2.32 we finally calculate the nucleation rates: $R(T_1)$= $O(10^{26\pm1})$ $m^{-3}s^{-1}$ and $R(T_2)$= $O(10^{24\pm1})$ $m^{-3}s^{-1}$. These rates are about ten orders of magnitude higher than the estimated experimental rate at 905K ($O(10^{16})m^{-3}s^{-1}$). Such a difference is hardly surprising because the nucleation rate is expected to increase rapidly with increasing super-cooling.

We have also computed the nucleation rate at T_1 using an algorithm based on the path-sampling technique of ref. [13], Forward Flux Sampling, as we describe in details in chapter 2. Table 4.3 illustrates the chosen interfaces and number of trials for each of them, when studying crystal nucleation from molten sodium chloride. λ_0 is the boundary of the

interface	λ_i	M_i	**interface**	λ_i	M_i
0	20	30	5	62	45
1	26	40	6	85	15
2	33	40	7	115	5
3	40	40	8	900	-
4	48	40	–	–	–

Table 4.3.: Position of the interfaces, and number of trials to study homogeneous nucleation from molten sodium chloride at 800 K and 1 atm (see chapter 4).

the time the system diffuses away from the top of the free-energy barrier.

metastable liquid state, while whenever $\lambda_n > 900$ the system is in the solid state basin of attraction. The location of λ_0 is chosen according to the cumulative function presented in fig. 4.6.

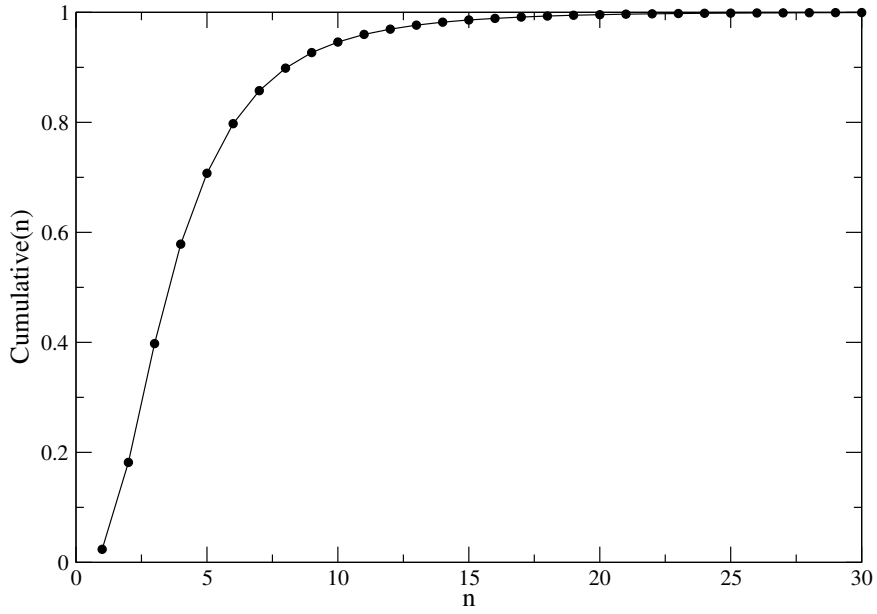

Figure 4.6.: Cumulative distribution of the biggest cluster size n in a super-cooled molten sodium chloride at $800K$ and 1 atm (see chapter 4 for the crystal nucleation study in this system).

The value obtained is $R_{FFS}(T_1) = O(10^{27\pm2})\ m^{-3}s^{-1}$, which agrees surprisingly well with the one computed using the diffusive barrier-crossing approach. As FFS does not depend on the choice of the order parameter and does not require prior knowledge of the phase space density, we can conclude that the diffusive barrier-crossing method based on the free energy calculation gives us a good estimate for the nucleation rate.

A summary of our numerical results for the nucleation barriers and rates is given in table 4.4.

T[K]	$\beta\Delta\mu$	$\beta\Delta G^*$	k_{+,n^*}	$R[m^{-3}s^{-1}]$	$R_{FFS}[m^{-3}s^{-1}]$
800	0.54	24	0.013	$3\times10^{26\pm1}$	$10^{27\pm2}$
825	0.48	29	0.033	$4\times10^{24\pm1}$	$--$

Table 4.4.: Summary of the simulation results for the calculation of the free-energy barrier and the nucleation rate for Tosi-Fumi NaCl.

We can also compare our calculated nucleation rate at $800K$ to the rate estimated with

CNT. In order to do that, we need to compute the kinetic pre-factor κ that, using the CNT approximations, is given by eq. 2.37. We compute the self-diffusion coefficient with MD simulations using the DLPOLY package in the super-cooled liquid at T_1=800K[5] , and find $D_S^{Na} = 3.4 \times 10^{-5} cm^2 s^{-1}$, in good agreement with an estimate based on extrapolation of the available experimental data of ref. [94] to the same temperature: $D_S^{Na} = 2.3 \times 10^{-5} cm^2 s^{-1}$ (since $D_S^{Na}/D_S^{Cl} \approx 1$, we only consider the self-diffusion of the Na^+ ions). We estimate λ as a fitting parameter from the kinetic pre-factor numerically calculated, and obtain $\lambda(T_1) = 10^2 \dot{A}$. However, considering that the ion size is $\sigma_{Na} \sim 1.1\ \dot{A}$, this value for the jump distance seems to be unphysical ($\lambda \sim 100\sigma$). Typically, one would expect λ to be of the order of a mean free path: in a molten salt, the mean free path of an ion is certainly less than a particle diameter. This discrepancy also suggests that the CNT picture is inadequate to describe crystal nucleation of NaCl.

To conclude, we have also computed the nucleation rate at 750 K, by means of the FFS scheme. The computed nucleation rate is $O(10^{35})\ m^{-3}s^{-1}$, the same order of magnitude as the nucleation rate obtained by Koishi et al. [80] using "brute-force" MD. At this temperature it is not possible to use the diffusive barrier-crossing approach, as the barrier is too low to avoid spontaneous nucleation to occur during long runs. However, if we assume that the kinetic pre-factor, the surface free energy, and latent heat of fusion do not vary too much with temperature, we can use CNT to extrapolate the nucleation rate from $800K$ to $750K$: $R_{CNT} = O(10^{30}\ m^{-3}s^{-1}$ which is considerably lower than the results of the FFS direct calculations. This suggests that an extrapolation procedure based on CNT is not reliable.

A similar problem occurs if we try to extrapolate our numerical data obtained at $800K$ and $825K$ to the experimental temperature of ref. [77]. At $905K$ the chemical potential difference between liquid and solid is $\beta\Delta\mu$=0.3. By means of CNT, we obtain an estimated nucleation rate of the order of $O(6 \times 10^{11}) m^{-3}s^{-1}$. This is some nearly five orders of magnitude less than the experimentally observed rate. In order to resolve the discrepancy between simulation and experiment, we make few assumptions:

1. There might be an appreciable (but unspecified) error in the experimental estimates (e.g. due to residual heterogeneous nucleation).

2. The estimated error in the computed melting temperature of the Tosi-Fumi model is of the order of 20K [85]. Such an uncertainty, again, easily translates into a variation of the nucleation rate by several orders of magnitude.

3. In view of the extreme sensitivity of nucleation rates to the details of the inter-molecular potential (see, e.g. [95]), the Tosi-Fumi interaction potential may be inadequate to model nucleation in NaCl, even though it can reproduce the static properties of the solid and liquid NaCl [18].

4. Finally, it is not quite correct to assume that the kinetic pre-factor, the surface free energy and the latent heat of fusion are temperature-independent quantities.

[5] We also use DLPOLY to test our NPT Monte Carlo code, by measuring, for instance, the average total energy and the density of both liquid and solid bulk phases.

4.4. Conclusions

In summary, we have computed the crystal nucleation rate of sodium chloride from the melt using two independent methods: one based on calculations of the free-energy barrier and the diffusive barrier-crossing and another based on Forward Flux Sampling.

We have found that, to within an order of magnitude, the two approaches yield the same value for the nucleation rate. As FFS does not depend on the choice of the order parameter and does not require prior knowledge of the phase space density, we conclude that the diffusive barrier-crossing method based on the free-energy calculation function of the biggest cluster size, gives a good estimate for the nucleation rate.

When we use Classical Nucleation Theory to extrapolate our numerical data to lower temperatures, we observe serious discrepancies with the results of direct calculations. At the same time, when we extrapolate to higher temperatures, we find serious discrepancies with the nucleation rates found in experiments. Several factors may contribute to this discrepancy but, at present, it is not yet known which factor is the most important.

Acknowledgements

Concerning this work, I want to thank A. Cacciuto, R. Allen, G. Boulougouris and J. Pámies for valuable discussions and suggestions.

Appendix A: Tail corrections of the total energy

Whenever we truncate the interaction potential at a certain cut-off (r_c), we need to compute the tail corrections of the thermodynamic properties of the system, such as the total energy: if the inter-atomic potential is not zero for distances larger than the cut-off ($r \geq r_c$), we have to add a tail correction to the total energy. In the case of NaCl, the total energy can be written as

$$U_{tot} = U_{TF} + U_{LT} \tag{4.A.1}$$

where U_{TF} is the Tosi-Fumi potential (eq. 4.1), and U_{LT} are the long tail corrections to it [70],

$$\begin{aligned} U_{LT}(r) &= \frac{1}{2}\int_{r_c}^{\infty} 4\pi r^2 \rho U_{TF}(r) dr \\ &= \frac{1}{2}\int_{r_c}^{\infty} 4\pi r^2 \rho \left(A e^{[B(\sigma - r)]} - \frac{C}{r^6} - \frac{D}{r^8} \right) \end{aligned} \tag{4.A.2}$$

where we omit the subscript i and j indicating the particle species. We do not consider the Coulomb interactions, as this will be treated separately by means of the Ewald summations method. Computing each contribution of eq. 4.A.2, we find

$$\begin{aligned} 2\pi\rho \int_{r_c}^{\infty} \left(A \exp^{B(\sigma - r)} \right) r^2 dr &= 2\pi\rho \frac{A \exp^{B\sigma}}{B \exp^{Br_c}} \left[rc^2 + \frac{2}{B} r_c + \frac{2}{B^2} \right] \\ 2\pi\rho \int_{r_c}^{\infty} \left(-\frac{C}{r^6} \right) r^2 dr &= 2\pi\rho \frac{C}{3} \frac{1}{r_c^3} \\ 2\pi\rho \int_{r_c}^{\infty} \left(-\frac{D}{r^8} \right) r^2 dr &= 2\pi\rho \frac{D}{5} \frac{1}{r_c^5}. \end{aligned} \tag{4.A.3}$$

By summing them up, we obtain the tail corrections U_{LT} to the total energy of the Tosi-Fumi NaCl interaction potential.

Moreover, when calculating the total energy of the system, we should also take into account that NaCl is a binary mixture, where the total number of particles is $N = N_{Na} + N_{Cl}$. Therefore, the fraction of particles of each species is $x_{Na} = \frac{N_{Na}}{N}$ and $x_{Cl} = \frac{N_{Cl}}{N}$. Eq. 4.A.2 then becomes

$$\begin{aligned} U_{LT} &= \sum_{i,j}^{Na,Cl} x_i x_j U_{LT}(r_{ij}) \\ &= (x_{Na} x_{Na})\, U_{LT}(r_{NaNa}) + (x_{Cl} x_{Cl})\, U_{LT}(r_{ClCl}) + 2\,(x_{Cl} x_{Na})\, U_{LT}(r_{NaCl}). \end{aligned} \tag{4.A.4}$$

As $x_{Na} = x_{Cl} = \frac{1}{2}$, eq. 4.A.4 becomes

$$U_{LT} = \frac{1}{4} U_{LT}(r_{NaNa}) + \frac{1}{4} U_{LT}(r_{ClCl}) + \frac{2}{4} U_{LT}(r_{NaCl}). \tag{4.A.5}$$

Differently from an NVT simulation, where the density is constant, in an NPT, as the density changes, we have to update the tail corrections every time the volume is changed.

Appendix B: Crystalline clusters in NaCl

To distinguish between solid-like and liquid-like particles, and identify the solid-like particles belonging to the biggest cluster, we use the local bond order parameter presented in chapter 2, where the complex $\vec{q}$ vector in eq. 2.A.1, and its thresholds are optimised for the cubic symmetry of NaCl:

1. according to the radial distribution function computed in the bulk liquid and solid, we identify a cut-off radios r_c of $4\dot{A}$, corresponding to the first minimum in the Na-Cl $g(r)$ (see fig. 4.B.1);

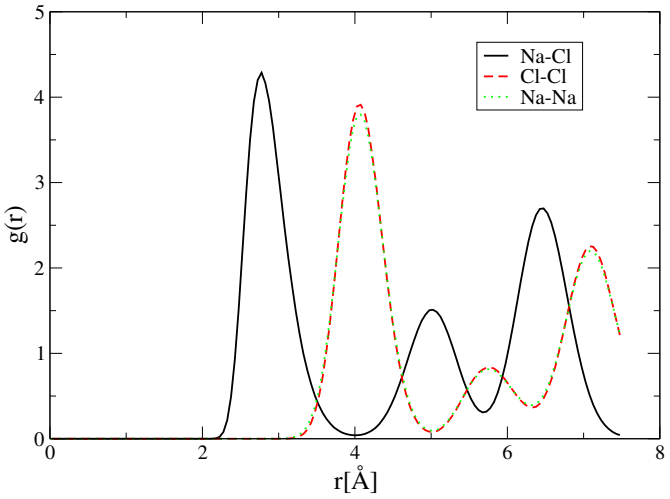

Figure 4.B.1.: Radial distribution function of the bulk solid at 800 K and 1 atm.

2. we compute the normalised complex vector in eq. 2.A.1 at $l = 4$ for every particle i. Each component m of this vector is given by:

$$q_{4,m}(i) = \frac{\frac{1}{N_b(i)} \sum_{j=1}^{N_b(i)} \Upsilon_{4,m}(\theta_{i,j}, \phi_{i,j})}{(\sum_{m=-4}^{4} |q_{4,m}(i)|^2)^{1/2}}, \qquad m = [-4, 4], \qquad (4.B.1)$$

where $N_b(i)$ is the number of neighbours of particle i within r_c , and $\Upsilon_{4,m}$ is the order 4 spherical harmonics;

3. we then compute the scalar product $d_4(i, j)$ (eq. 2.A.2) at $l = 4$ between every particle i and each of its neighbouring particle j: a connection is satisfied whenever $d_4(i, j)$ is bigger than a threshold of $d_c = 0.35$ (value beyond which there is a non-zero probability that particle i is in a solid-like environment, as shown in fig. 4.B.2);

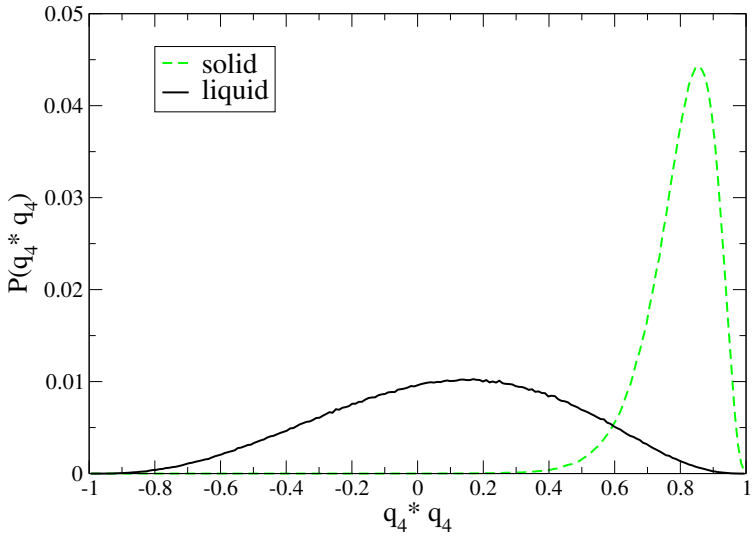

Figure 4.B.2.: Probability distribution of d_4 of both bulk liquid and solid at T_1.

4. however, at $d_c = 0.35$, there is a finite probability for particle i to be in a liquid-like environment, as it is evident by observing the two probability distributions in fig. 4.B.2 overlapping around d_c. Therefore, we compute the number of connections (eq. 2.A.3) for each particle i, and state that particle i is solid-like when $d_4(i,j) > d_c$ *AND* the number of connections overcomes the chosen threshold of $n^c_{con} = 6$ (see fig. 4.B.3);

5. the cut-off chosen for the cluster analysis is $r_c^{cluster}$=3.4 $\dot{A}$.

Appendix C: Computing $\beta\Delta\mu$

In order to calculate the super-saturation imposed to the system ($\beta\Delta\mu$), we compute the temperature dependence of the difference between the molar enthalpy of the super-cooled liquid and the one of the stable crystal at constant pressure (Δh), and then evaluate $\Delta\mu$ by means of thermodynamic integration from the melting point [70]. In an NPT ensemble

$$\left(\frac{d(\beta\mu)}{d\beta}\right)_{P,N} = h \tag{4.C.1}$$

where μ is the chemical potential of one phase, $\beta = 1/k_BT$ (k_B the Boltzmann constant, T the temperature), and h the enthalpy per particle. Note that $h = u + Pv$, where P is the pressure of the system, u the internal energy per particle and v the specific volume, a quantity easily sampled in a (e.g. Monte Carlo) simulation. We now integrate eq. 4.C.1 in each phase

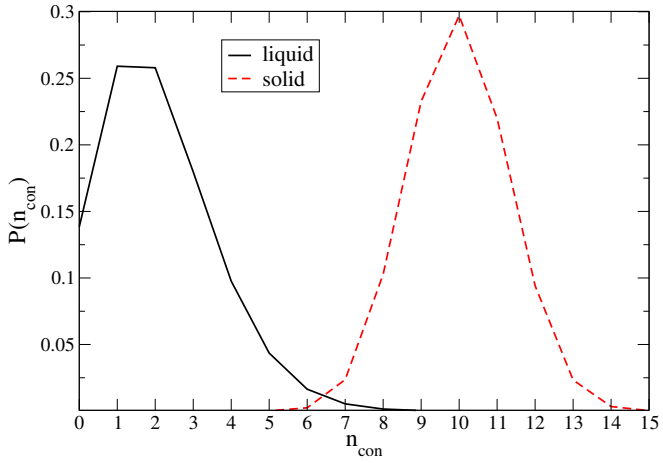

Figure 4.B.3.: Probability distributions of n_{con} of both the liquid and the solid at T_1.

along an isobar at 1 atm from the coexistence point ($\beta_{\rm M} = 1/(k_B T_{\rm M})$) to the temperature of the selected state points below coexistence (T_1 and T_2, respectively). At T_1, for instance, we find that

$$\begin{aligned}[\beta_1\mu_S(\beta_1) - \beta_M\mu_S(\beta_M)] - [\beta_1\mu_L(\beta_1) - \beta_M\mu_L(\beta_M)] \quad &= \\ [\beta_1\mu_S(\beta_1) - \beta_1\mu_L(\beta_M)] = \Delta(\beta_1\mu), \qquad &(4.C.2)\end{aligned}$$

being $\beta_M(\mu_S(\beta_M) - \mu_L(\beta_M)) = 0$ at coexistence; thus eq. 4.C.2 can be numerically computed by integrating eq. 4.C.1:

$$\Delta(\beta_1\mu) = \int_{\beta_M}^{\beta_1} \langle [h^S(\beta) - h^L(\beta)] \rangle_P \, d\beta. \qquad (4.C.3)$$

5. Out-of-equilibrium crystal nucleation in suspensions of oppositely charged colloids[1]

Parigi si, Parigi no...

We report a numerical study of the rate of crystal nucleation in a binary suspension of oppositely charged colloids. Two different crystal structures compete in the thermodynamic conditions under study. We find that the crystal phase that nucleates is metastable and, more surprisingly, its nucleation free-energy barrier is not the lowest one. This implies that, during nucleation, there is insufficient time for sub-critical clusters to relax to their lowest free-energy structure. Such behaviour is in direct contradiction with the common assumption that the phase that crystallises most readily is the one with the lowest free-energy barrier for nucleation. The phenomenon that we describe should be relevant for crystallisation experiments where competing solid structures are not connected by an easy transformation.

5.1. Introduction

Liquids often must be cooled substantially below the freezing temperature before spontaneous crystallisation occurs in the bulk. The reason is that the system has to overcome a free-energy barrier when moving from the metastable liquid to the stable solid phase. When the two phases are separated by a high free-energy barrier, spontaneous fluctuations that would result in the formation of the stable phase are unlikely and therefore rare. Most fluctuations will result in the formation of ephemeral "sub-critical" crystal clusters that redissolve spontaneously. Only occasionally a crystal cluster will form that exceeds the critical size needed for spontaneous subsequent growth [6]. The crystal nucleation rate is defined as the number of post-critical clusters that form per unit time in a unit volume.

In Classical Nucleation Theory (CNT), it is assumed that sub-critical clusters are in quasi-equilibrium with the parent phase [6]. This assumption is reasonable if the time it takes to establish an equilibrium distribution of sub-critical clusters is short compared to the time needed to nucleate a crystal.

If the nucleation rate is low, the steady-state distribution of sub-critical clusters of size n is (nearly) proportional to $\exp(-\beta\Delta G(n))$, where $\Delta G(n)$ is the free energy associated with

[1] Work carried out in collaboration with E. Sanz and M. Dijkstra.

the formation of a crystalline cluster of size n in the metastable liquid. The CNT expression for the nucleation rate per unit volume is given in eq. 2.35.

It was already pointed out by Ostwald [92] that often, during crystal nucleation, a solid phase forms that is not the thermodynamically most stable one. Stranski and Totomanow [16] have rationalised this observation in the language of CNT by suggesting that the phase that nucleates is the one separated from the parent phase by the lowest free-energy barrier - and this need not be the most stable solid phase. Implicit in this explanation is the assumption that the kinetic pre-factor κ is similar for different nucleation routes, and that hence the relative nucleation rates are exclusively determined by the heights of the nucleation barriers. Unfortunately, the assumptions underlying the Stranski-Totomanow (ST) rule cannot easily be tested in experiments. Here we present simulations where we compute independently the rate of crystal nucleation and the height of the free-energy barriers separating a metastable liquid from two more stable solid phases.

5.2. Simulation details

In order to study rare events such as liquid-to-solid nucleation by simulation, one has to resort to special simulation techniques, precisely because a typical nucleation event does not occur within the time scale of a conventional simulation. The only alternative is to use very large system sizes [96] and long simulation times [97]. But even then the metastable system has to be prepared in a state deeply super-saturated before spontaneous nucleation can be observed [79].

Here, we use the Forward Flux Sampling (FFS) method of Allen et al. to compute the rate of crystal nucleation (see chapter 2, appendix G in chapter 4 and ref. [13, 14, 15]). This method was designed to study rare events both *in* and *out* of equilibrium systems. It can be used under conditions where brute-force simulations become impractical. FFS has been used to calculate the rate of crystal nucleation in molten salts (see chapter 4 and [98]) and the nucleation rate of an Ising model in pores [99].

To compute the free-energy barriers for crystal nucleation, we use the Umbrella Sampling scheme (see chapter 2). This method has been used before to compute the free-energy barriers for the nucleation of crystals [100, 101] and liquids [87]. The Umbrella Sampling approach determines the variation of the free energy of the system with an order parameter that measures the progress of the transformation from the liquid to the crystalline phase (or from the vapour to the liquid phase). It should be noted that, whereas the nucleation rate is an observable quantity, the height of the free-energy barrier for crystal nucleation may depend somewhat on the choice of the order parameter.

Making use of the information obtained using both methods we will show below that crystal nucleation in a mixture of oppositely charged colloids is incompatible with the ST conjecture.

In our simulations, we study a 1:1 binary mixture of mono-disperse, oppositely charged colloids. The screened Coulomb interaction between two colloids of diameter σ and charge

Ze is approximated by a Yukawa potential:

$$U(r)/k_BT = \begin{cases} \infty & r < \sigma \\ \pm\frac{Z^2}{(1+\frac{\kappa\sigma}{2})^2}\frac{\lambda_B}{\sigma}\frac{e^{-\kappa(r-\sigma)}}{r/\sigma} & \sigma \le r < r_c \\ 0 & r \ge r_c, \end{cases} \tag{5.1}$$

where the sign is positive for equally charged and negative for oppositely charged colloids, $\lambda_B = e^2/\epsilon_s k_B T$ is the Bjerrum length (ϵ_s is the dielectric constant of the solvent) and $\kappa = \sqrt{8\pi\lambda_B\rho_{salt}}$ is the inverse Debye screening length (ρ_{salt} is the number density of added salt). A hard core prevents colloids from overlapping. The total energy of the system is the sum of the pair interactions. The cut-off radius, r_c, is 3.5σ. We define the reduced temperature $T^* = (1+\kappa\sigma/2)^2\sigma/Z^2\lambda_B$ as the inverse of the contact energy, the reduced pressure as $P^* = PT^*\sigma^3/k_BT$, and the packing fraction as $\eta = \pi\sigma^3 N/6V$.

The phase diagram of this potential for $k\sigma = 6$ reproduces the solid structures that are found experimentally in mixtures of oppositely charged colloids [17]. In this system, two solid phases can coexist with the fluid. At high temperatures, the liquid phase coexists with a substitutionally charge disordered face-centred-cubic colloidal crystal (disordered fcc). At low temperatures the stable solid at coexistence has a CsCl structure, where the charges are ordered on a bcc lattice (fig. 5.1).

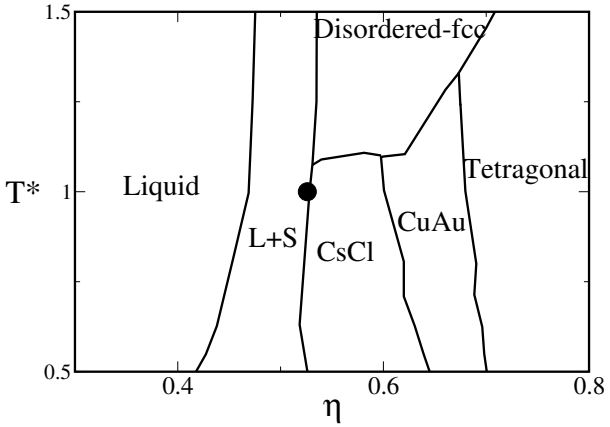

Figure 5.1.: Phase diagram of the system under study in the $T^* - \eta$ plane, where η is the packing fraction ($\eta = \pi\sigma^3 N/6V$) [17]. $L+S$ stands for liquid-solid coexistence region. The filled circle indicates the state point of the metastable liquid chosen to study crystal nucleation (T^*=1, P^*=15, η=0.526). The disordered fcc-liquid-CsCl triple point temperature is T^*=1.07.

This system is a suitable candidate to test the Stranski-Totomanow conjecture as two distinct solid phases may form during crystal nucleation. In contrast to systems that have been studied earlier [63, 102] these two solids are not connected by an "easy" (e.g. martensitic)

transformation. Besides, we study nucleation close to the coexistence temperature between both solids (The disordered fcc-liquid-CsCl triple point temperature being T^*=1.07).

In order to test the ST conjecture, i.e. the assumption that sub-critical clusters are in quasi-equilibrium, we make use of a *charge swap* move, described in appendix A.

Both for the FFS calculations and for the calculation of the free-energy barrier separating liquid and solid, we need an order parameter that measures the progress of the nucleation process. In the present study, we use n, the number of particles in the biggest solid cluster (see appendix B, chapter 2 and ref. [103]). We stress that the order parameter in the FFS scheme is only used to measure the progress of the crystal growth –it does not favour one crystal structure over another [13, 14].

As already described in chapter 2 (see eq. 2.53), the FFS technique expresses the nucleation rate from the metastable liquid to the crystal, R_{LS}, as the product of two factors:

$$R_{LS} = \Phi_{Lj} P_{jS}, \tag{5.2}$$

where Φ_{Lj} is the rate at which spontaneous fluctuations lead to the formation of a small crystallite consisting of j particles, whilst P_{jS} denotes the probability that such a cluster will grow to form a bulk solid, rather than redissolve. The probability P_{jS} is computed as a product of probabilities:

$$P_{jS} = P_{jk} P_{kl} ... P_{tS}, \tag{5.3}$$

where P_{jk} is the probability that a trajectory that starts with a cluster of size j, will grow to size K rather than redissolve. This probability can be estimated by starting a number of trajectories from a cluster of size j and dividing the number of those that arrive at k by the total number of trials. The successful trajectories provide starting configurations for the next step, namely, the calculation of the probability that cluster k will grow to size t, rather than redissolve. The FFS method only works if the dynamics of the system is not fully deterministic. In the present case, different kinetic Monte Carlo (MC) stochastic trajectories (with maximum displacement of 0.04 σ) are generated from the same configuration by changing the seed of the random number generator.

In what follows, we will ignore the effect of hydrodynamic interactions and estimate Φ_{Lj} using a kinetic Monte Carlo algorithm in an NPT ensemble [1] with a maximum displacement of 0.01 σ [63, 66, 105]. When computing the flux Φ_{Lj}, we should respect the *real* kinetics of the system. Therefore, as we will discuss later, we are not going to use the charge swap moves in the calculation of Φ_{Lj}.

5.3. Results

In this work, we have studied the crystallisation of the metastable liquid phase in a system of 1000 particles at $T^* = 1$ and P^*=15 ($P^*/P^*_{\rm coex} \approx 1.7$). The packing fraction of the liquid

[1] Cichocki et al. [104] suggested that in the limit of small maximum particle displacement, trajectories generated by means of Monte Carlo simulations resemble stochastic trajectories obtained from the Smoluchowski equation. Therefore, the MC algorithm is considered to approach the Brownian Dynamics.

at the coexistence pressure, $P^*_{\text{coex}} = (8.8 \pm 0.1)$, is $\eta = (0.471 \pm 0.005)$. At $T^* = 1$ and $P^* = 15$, the packing fraction of the metastable liquid is (0.526 ± 0.005).

At $P^* = 15$, no spontaneous nucleation is observed even after $3 \cdot 10^6$ MC cycles (a cycle consists of a trial move per particle and a volume move). However, the nucleation rate can be computed at $P^* = 15$ using the FFS method. We find that the probability that a crystalline cluster of 5 particles will continue to solidify is $10^{-28\pm2}$. The rate at which spontaneous fluctuations in the metastable liquid result in the formation of crystalline clusters of 5 particles is equal to $10^{-4\pm1} D_0 \sigma^{-5}$ (where D_0 denotes the diffusion coefficient at infinite dilution) [2]. Therefore, the nucleation rate is estimated to be $10^{-32\pm3} D_0 \sigma^{-5}$.

We observe the growth of a rather compact solid cluster in the metastable liquid. When the crystalline cluster has reached a size of $n = (120 \pm 15)$, it has a 50% probability of redissolving: this is our operational definition of the critical cluster size. To identify the crystal structure of the solid cluster, we analyse the radial distribution function $g(r)$ of the particles that belong to the cluster. This provides a convenient way to distinguish between disordered fcc and CsCl structures.

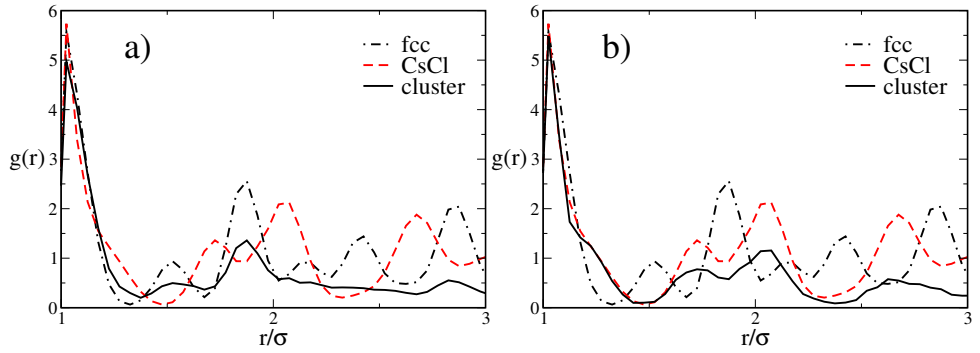

Figure 5.2.: Radial distribution function of an 80 particles cluster obtained in a typical FFS path at $T^* = 1$ and $P^* = 15$, compared with the $g(r)$ of the CsCl and disordered fcc solid structures. (a) without charge swap moves, (b) with charge swap moves. The structure of the clusters varies with the way in which the configurational space is sampled. The unnormalised $g(r)$ of the clusters have been multiplied by a factor of 20 in order to compare with the bulk radial distribution functions.

Fig. 5.2(a) shows the comparison of the radial distribution function for a cluster of 80 particles with that of the bulk solid phases. From the figure, it is evident that the arrangement of the particles in the growing solid cluster is fcc-like even though the stable solid phase at $T^* = 1$ and $P^* = 15$ is CsCl.

[2] D_0 is computed according to the Stokes-Einstein's relation [83]

$$D_0 = \frac{\langle \Delta x^2_{max} \rangle}{6}, \tag{5.4}$$

since we know that as soon as $\Delta x_{max} \to 0$, the simulation time becomes infinitely long. [105]

The formation of crystal clusters of a metastable solid phase can be interpreted as a manifestation of the Ostwald step rule. According to the conjecture of Stranski and Totomanow[16], the free-energy barrier for the formation of disordered fcc should then be lower than the one for the formation of a CsCl cluster. The ST conjecture relies on the assumption that sub-critical clusters are in quasi-equilibrium. However, as we will show, this turns out not to be the case.

We can test this by repeating the FFS scheme with a different kinetic Monte Carlo scheme that includes an additional trial move: the swap of positive and negative particles (see appendix A). If the system is already in equilibrium, or in quasi-equilibrium, the introduction of additional MC moves will not change the structure of the sub-critical clusters.

However, when we perform FFS simulations including 20% charge swap moves, we observe the formation of charge-ordered clusters with a CsCl structure (fig. 5.2(b)). Not only the structure of the sub-critical clusters has changed, but also the size of the critical cluster: it now contains (65 ± 15). Moreover, the probability that a solid cluster of 5 particles will transform into a bulk crystal has increased to $10^{-15\pm1}$.

The fact that the pathway for crystal nucleation can be altered by artificially improving the sampling of the configurational space indicates that local equilibrium is not established during the natural nucleation dynamics (without swaps). This observation is in direct contradiction to the key assumption underlying the Stranski-Totomanow conjecture. Our simulations suggest that the time it takes a cluster to grow from a small size to the critical size is too short to allow for efficient sampling of the accessible configurational space – as a result, it gets *kinetically trapped* in a metastable structure. We expect that such behaviour will be common when there is no "easy" kinetic route (e.g. martensitic transformation) from the metastable to the stable crystal phase.

At higher pressures ($P^* = 18$), where the probability of forming a post-critical cluster is higher and no FFS is needed to observe the transition, the same phenomenology is reproduced: in a kinetic Monte Carlo simulation without swap moves, a substitutionally disordered fcc lattice is formed. In contrast, when swap moves are included, the liquid transforms into a substitutionally ordered lattice.

Interestingly, as we can selectively prepare fcc or CsCl clusters by changing our kinetic Monte Carlo scheme, we can now separately compute with Umbrella Sampling [11] the free energies of these two different types of clusters. In Umbrella Sampling simulations, the minimum free-energy path is sampled along a given order parameter. Nevertheless, when the calculation is carried out without swap moves, the growth of CsCl clusters is dramatically slowed down, instead, fcc clusters are formed and persist for long time in the system. If the simulation is run long enough, the structure of the clusters changes into CsCl, suggesting that CsCl clusters have indeed lower free energy. By including swap moves in the Umbrella Sampling scheme, clusters grow directly in their lowest free-energy state (CsCl), yielding a different free-energy barrier.

Fig. 5.3 shows the barriers for both types of calculations.

As can be seen from the figure, the free-energy barrier for the nucleation of fcc clusters is higher than that for CsCl clusters. Snapshots of two typical critical clusters (disordered fcc (a) and CsCl (b)) are shown in figure 5.4.

This observation has direct implication for the interpretation of experiments on charged

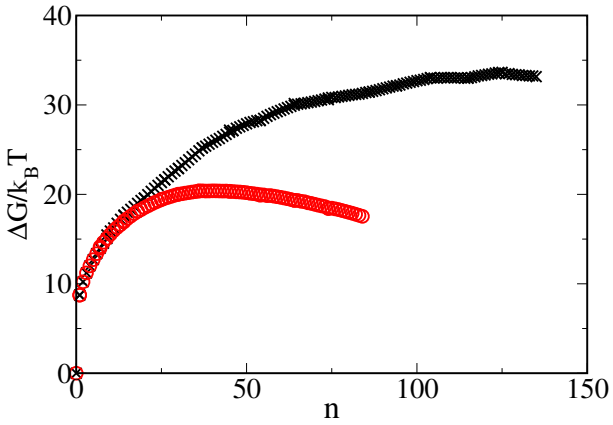

Figure 5.3.: Free-energy barriers calculated with Umbrella Sampling at T^*=1 and P^*=15 in an 8000 particles system. The CsCl clusters have lower free energy, but unless unphysical Monte Carlo moves are used in the sampling, the system remains *kinetically trapped* in a disordered fcc route of higher free energy.

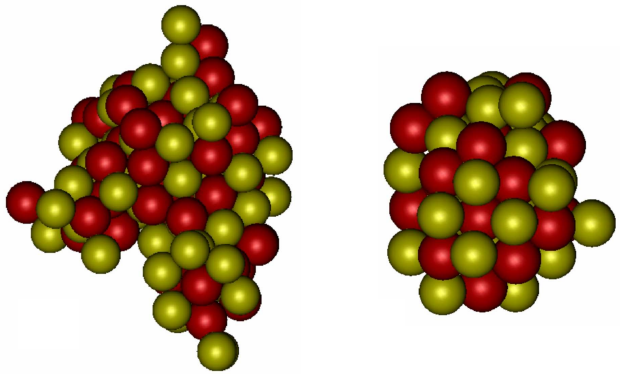

Figure 5.4.: Snapshot of a typical critical cluster with disordered fcc structure (a) and CsCl structure (b). Note that the disordered critical cluster is bigger than the ordered one.

colloids [106, 107]. The dynamics of real binary crystals of charged colloids is best described by the kinetic Monte Carlo scheme (i.e. without any unphysical swap move). Hence we should expect that in charged colloidal systems, crystallisation proceeds through a sequence of *non-equilibrium* sub-critical crystal clusters. In experiments on crystallisation in binary charged colloids [17], both substitutionally ordered (CuAu-like) and substitutionally disordered (fcc-like) crystallites have been observed. The simultaneous observation of both phases could be explained thermodynamically if the experimental conditions fortuitously

happened to correspond to coexistence. The present work suggests another explanation: non-equilibrium nucleation of the fcc phase precedes a subsequent, slow transformation to the substitutionally ordered crystal phase.

5.4. Conclusions

Our work conjecture that *non-equilibrium* nucleation of the metastable phase precedes a slow transformation to the stable phase. At first sight, it might seem that the present results, although at odds with the Stranski and Totomanow conjecture, are not incompatible with CNT. After all, within that theory, preferred nucleation of the crystal structure with the higher nucleation barrier is possible if a large kinetic pre-factor in eq. 2.35 compensates the effect of the higher nucleation barrier. Yet, the existing versions of CNT do not correctly describe this effect: in CNT the kinetic pre-factor describes the rate at which clusters grow due to the attachment and detachment of single particles to a pre-existing crystallite, and the rate of addition and removal of particles is hardly different for fcc and CsCl clusters. What seems to happen is that small clusters have a disordered fcc structure, but this structure cannot act as a template for subsequent CsCl growth, whilst a structural phase transition inside the clusters is kinetically inhibited. A crystal cluster could change its internal structure by a succession of particle additions and removals, but in practise this would mean that a disordered fcc cluster would have to redissolve almost completely before it can form a CsCl cluster. The "success" of the small sub-critical disordered fcc clusters blocks the subsequent formation of the more stable CsCl clusters. This phenomenon is reminiscent of the "self-poisoning" of small crystallites during the rapid growth of post-critical crystal clusters [108]. The difference is that, in the present case, the self-poisoning already takes place with sub-critical clusters.

The present results imply that, at least to predict crystal nucleation, there are situations where it is not enough to compute the free-energy barrier that separates the parent phase from resultant solid structures - beyond a certain cluster size, the formation of the lowest free-energy clusters may be kinetically inhibited. The fast growth of the clusters results in the breakdown of the local equilibrium assumption for sub-critical clusters.

Acknowledgements

Concerning this work, I would like to thank J. van Meel and R. Allen for a critical reading of the work, and M. Leunissen, A. P.Hynninen and A. van Blaaderen for useful discussions.

Appendix A: Charge swap move

In order to sample more efficiently the configurational space, we introduce another trial move, that respects the detailed balance and follows the Metropolis acceptance rule:

1. we calculate the internal energy of the system;
2. we select two particles at random in the system (they do not have to be neighbours): one has to be positively and the other negatively charged;
3. we swap the particles positions (see fig. 5.A.1);
4. we now compute the internal energy of the trial configuration, and accept or reject the move according to the Metropolis criterion.

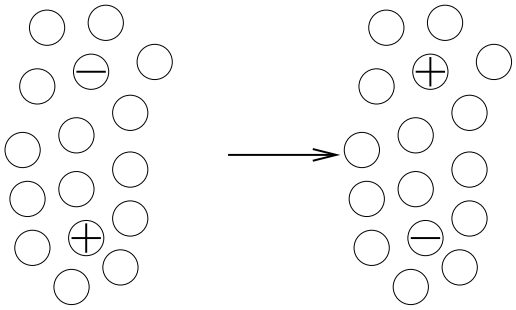

Figure 5.A.1.: Charge swap move. On the left-side, we select two oppositely charged particles at random. On the right-side, we swap their positions.

Appendix B: The order parameter for the Yukawa binary mixture

The order parameter we use to study this phase transition is the local bond-order parameter with $l = 6$ (d_6), already introduced in chapter 2. This order parameter, though being capable to distinguish between liquid and solid particles, is not sensitive to the structure of the crystalline lattice. In fact, at the thermodynamic conditions under study ($T^* = 1$, $P^* = 15$), every particle in either the disordered fcc or the CsCl-like solid phase is identified as crystalline. On the contrary, in the metastable liquid phase, less than five out of 1000 particles are identified as solid-like. The parameters used are the followings:

- the cut-off to identify two particles as being neighbours is set to $r_c = 1.33\sigma$, corresponding to the first minimum of the radial distribution function of both bulk crystalline structures, disordered fcc and CsCl;

- after computing d_6, we check whether it overcomes an earlier defined threshold of $d_c = 0.7$. This threshold is chosen according to the d_6 probability distributions of both liquid and solid: beyond d_c, there is a finite probability for particle i to be embedded in a solid-like environment;
- thus, if $d_6(i,j) \geq d_c$, particles i and j are considered to be connected;
- to enforce this criterion, we also count the number of connections, and establish that a particle is solid-like when $n_{con} > n_{con}^c = 9$;
- finally, two solid-like particles are considered to belong to the same crystalline cluster, if they are closer than $r_c^{cluster} = 1.3\sigma$.

Part IV.

Covalent systems: the Carbon case

6. Local structure of liquid carbon controls diamond nucleation[1]

Giu' fino a Scandolo!

Diamonds melt at temperatures above 4000 K. There are no measurements of the steady-state rate of the reverse process: diamond nucleation from the melt, because experiments are difficult at these extreme temperatures and pressures. Using numerical simulations, we estimate the diamond nucleation rate and find that it increases by many orders of magnitude when the pressure is increased at constant super-saturation. The reason is that an increase in pressure changes the local coordination of carbon atoms from three-fold to four-fold. It turns out to be much easier to nucleate diamond in a four-fold coordinated liquid than in a liquid with three-fold coordination, because in the latter case the free-energy cost to create a diamond-liquid interface is higher. We speculate that this mechanism for nucleation control is relevant for crystallisation in many network-forming liquids. On the basis of our calculations, we estimate the conditions under which homogeneous diamond nucleation is likely in carbon-rich stars and planets.

6.1. Introduction

Most liquids can be cooled considerably below their equilibrium freezing point before crystals start to form spontaneously in the bulk. This is caused by the fact that microscopic crystallites are thermodynamically less stable than the bulk solid. Spontaneous crystal growth can only proceed when, due to some rare fluctuation, one or more micro-crystallites exceed a critical size (the "critical cluster"). An estimate of the rate at which critical clusters form in a bulk liquid can be obtained from Classical Nucleation Theory (CNT) (see chapter 2). This theory relates R, the number of crystal clusters that form per second per cubic meter, to ΔG^*, the height of the free-energy barrier that has to be crossed to nucleate a crystal (see eq. 2.30). CNT assumes that $\Delta G(N)$, the Gibbs free-energy difference between a metastable liquid containing an N-particle crystal cluster and a pure liquid, is given by $\Delta G(N) = S(N)\gamma - N|\Delta\mu|$, where $S(N)$ is the area of the interface between an N-particle crystallite and the metastable liquid, γ is the liquid-solid surface free energy per unit area, and $\Delta\mu$ is the difference in chemical potential between the solid and the super-cooled liquid. The surface area $S(N)$ is given by $c(N/\rho_S)^{2/3}$, where the factor c depends on the shape and

[1] Work carried out in collaboration with L. M. Ghiringhelli and E. J. Meijer.

the geometry of the cluster (e.g. $c = 16\pi/3$ for a spherical cluster). From our simulations, we can only determine the product $c\gamma$: it is this quantity and the degree of super-saturation ($\Delta\mu$), that determine the the top of the free-energy barrier, and hence the nucleation rate.

The nucleation rate depends strongly on the height of the nucleation barrier. CNT predicts the following expression for the height of the nucleation barrier (see eq. 2.10 for the spherical case):

$$\Delta G^* = c\frac{\gamma^3}{\rho_S^2|\Delta\mu|^2}, \tag{6.1}$$

where ρ_S is the number density of the crystalline phase. As the nucleation rate depends exponentially on ΔG^*, a doubling of γ may change the nucleation rate by many orders of magnitude. Because of the extreme conditions under which homogeneous diamond nucleation takes place, there have been no quantitative experimental studies to determine its rate. Moreover, there exist no numerical estimates of $\Delta\mu$ and γ for diamond in super-cooled liquid carbon. Hence, it was thus far impossible to make even an order-of-magnitude estimate of the rate of diamond nucleation.

6.2. Simulation details

In this chapter, we calculate the diamond nucleation rate R in a liquid carbon of 2744 atoms at two state points $\{P = 85$ GPa, $T = 5000$ K$\}$ and $\{P = 30$ GPa, $T = 3750$ K$\}$ (points A and B in the carbon phase diagram shown in fig. 6.2). The phase diagram was computed by means of the LCBOPI$^+$ semi-empirical potential (see appendix A). At both state points, the liquid is super-cooled by $(T_m - T)/T_m \approx 25\%$ below the melting curve of diamond, with T_m the melting temperature and $T_m^A = 6600$ K and $T_m^B = 5000$ K, respectively. Simulations studies of the diamond melting curve have been reported for pressures up to 400 GPa [109], 1400 GPa [110], and 2000 GPa [111]. The last two studies were carried out by using "ab-initio" Molecular Dynamics. However, it would be prohibitively expensive to study nucleation using such an approach. We therefore use a semi-empirical many-body potential that has been fit to experimentally measured and "ab-initio" calculated properties of both carbon solid phases and liquid [112] (see appendix A). We use this model to study diamond nucleation in a system of 2744 particles in the "low-pressure" (P $<$ 100 GPa) region of the phase diagram. In this pressure-range, the calculated melting line of refs. [109], [110] and [111] are in reasonable agreement. In particular, all the three calculations predict a melting temperature of about 7000 K at 100 GPa.

In order to compute the nucleation free energy, we need an order parameter that quantifies the progress of the transformation from liquid to crystal. Our order parameter to study the nucleation phenomenon is the size of the biggest solid cluster in the system: in order to identify solid-like particles, we analyse the local environment of a particle using a criterion based on a spherical-harmonics expansion of the local bond order (see chapter 2). However, the present bond-order parameter is based on invariants constructed out of rank three spherical harmonics. This order detector can unambiguously identify solid particles in the liquid, without the need to distinguish between a graphite and a diamond lattice. Thus, the growing cluster can have a diamond, or a graphite, or a mixed structure. Only after nucleation has

taken place, we distinguish between diamond and graphite structures among the solid particles belonging to the biggest cluster by using a bond-order parameter based on second rank spherical harmonics. We extensively test our local order detector in samples of thermalised graphite and diamond and in liquid samples containing dissolving clusters. For more details, see appendix B.

In the present work, we compute the free-energy barrier ΔG^* to form a critical cluster, by means of the Umbrella Sampling technique, already mentioned in the chapter 2. In order to equilibrate the growing clusters, we implement a "parallel tempering" algorithm similar to the one described in ref. [113]. To ensure that the biggest cluster, when growing to its critical size, does not interact with its own periodic images, we make sure that the radius of a crystal cluster is always less than 25% of the box diameter L. When computing the kinetic pre-factor to get the nucleation rate, we have to consider the fact that for our model potential, LCBOPI$^+$, only a Monte Carlo code is available. In order to evaluate the self-diffusion coefficient needed to compute the CNT kinetic pre-factor (see chapter 2), we propagate a 128 carbon atoms system via Car-Parrinello Molecular Dynamics (as implemented in the CPMD code [114]) starting from a configuration equilibrated with LCBOPI$^+$. Data for the high pressure state point come from simulations used in ref. [115], while data for the low pressure state point come from a new simulation, with the same technical details as reported in [115]. For more details, see appendix C.

6.3. Results

As we know the free-energy barrier ΔG^* to form a critical cluster at state point A from ref. [116] (ΔG^*_A = 25 k_BT for a critical cluster size of $N_A = 110$), after measuring the kinetic pre-factor, we compute the crystal-nucleation rate at state point A: $R_A = 10^{30} m^{-3} s^{-1}$ (see appendix D). From the calculated ΔG^*_A and the number density of the solid ($\rho_A = 0.191$ Å^{-3}), we can estimate the surface free energy per unit area at state point A using equation(6.1). Assuming that the critical cluster is effectively spherical, we find $\gamma_A \approx 0.27\ k_BT$/Å^2 = 1.86 J m^{-2}. We stress that, in what follows, we do not make use of this estimate: rather, we always employ the combination $c\gamma$ that follows directly from the simulations. $\Delta\mu$ is evaluated by thermodynamic integration from the melting point. We find: $|\Delta\mu_A/k_BT| = 0.60$ and $|\Delta\mu_B/k_BT| = 0.77$, respectively (see appendix E).

In state point B we cannot follow the same procedure, as a system of 2744 particles is too small to accommodate a critical cluster . We therefore have to resort to an indirect way, based on CNT, to estimate ΔG^* (see appendix F for more details on this calculation). In order to estimate γ_B, we prepare a rod-like crystal in a system with a slab geometry (a flattened box containing $N \sim 4000$ particles, with lateral dimensions that are some four times larger than its height). The crystal rod is oriented perpendicular to the plane of the slab. It spans the height of the simulation box and is continued periodically. The cross section of this crystal rod is lozenge shaped, such that its [111]-faces are in contact with the liquid. [1]. We then use

[1] The [111] planes are the most stable for the diamond lattice. In fact, macroscopic natural diamonds have often an octahedral shape, with eight [111] exposed surfaces. Indeed we find stable [111] surfaces in all but the smallest diamond clusters that we studied. At 85 GPa clusters grow by

Umbrella Sampling to determine the Gibbs free energy of such a crystallite as a function of its size, both at state points A and B. In this way we estimate the ratio of the surface free energies at A and B. We find that $c\gamma_B/c\gamma_A = \gamma_B/\gamma_A \sim 2.5$. Since we know γ_A from the height of the nucleation barrier in state point A for a spherical cluster, we deduce the corresponding γ_B for a spherical cluster. Using our estimate, $\gamma_A \approx 1.86$ J m^{-2}, we find $\gamma_B \approx 0.68\ k_BT/\text{Å}^2 = 3.5$ J m^{-2}. As $\Delta\mu$ and ρ_B are known ($\rho_B = 0.17$ Å^{-3}), we can now use CNT to estimate ΔG^* in state point B. It turns out that, mainly because γ_B is 2.5 times larger than γ_A, the nucleation barrier in B is more than ten times higher than in point A, thereby hugely suppressing the nucleation rate ($R_B \sim 10^{-80}$ s^{-1}m^{-3}).

To understand the microscopic origin for the large difference in nucleation rates in state points A and B, it is useful to compare the local structure of the liquid phase in both state points. It turns out that the liquid structure in state points A and B is markedly different (see also refs. [115, 117]): liquid carbon is mainly four-fold coordinated at state point A (20% three-fold and 80% four-fold), while at the lower temperatures and pressures of point B, the coordination in the liquid resembles that of the graphite and is mainly three-fold coordinated (5% two-fold, 85% three-fold and 10% four-fold). Apparently, it is less favourable to create an interface between a diamond and a graphitic liquid than between a diamond and a four-fold coordinated liquid. The destabilising effect of the graphitic liquid on the diamond clusters is most pronounced for small clusters (large surface-to-volume ratio). In fact, in state point B, clusters containing less than 25 particles tend to be graphitic in structure, with a small number of four-fold coordinated particles linking the different graphite planes. Clusters containing up to 60 particles show a mixed graphite-diamond structure, whereas larger clusters have a diamond bulk like structure, but the surface remains graphitic in nature (see appendix B and fig. 6.1). The unusual surface structure of the diamond cluster is an indication of the poor match between a diamond lattice and a three-fold coordinated liquid.

There are many network-forming liquids that, upon changing pressure and temperature, undergo profound structural changes or even liquid-liquid phase transitions [118]. Experiments on a completely different class of materials, viz. liquid metals [119], suggest that the local structure, in particular, local icosahedral packing, may interfere with direct nucleation of crystals. What is interesting about the present simulations is that we show that the ease of homogeneous crystal nucleation from one-and-the-same meta-stable liquid can be tuned by changing its pressure, and thereby its local structure. The thermodynamic conditions we discuss are relevant for experiments that study nucleation in compressed, laser-melted carbon. In addition, homogeneous nucleation of diamond may have taken place in carbon-rich white dwarf [120]. It has also been suggested that diamonds could also have formed in the carbon-rich middle layer of Uranus and Neptune [121]. The present work allows us to make a rough estimate of the conditions that are necessary to yield appreciable diamond nucleation on astronomical timescales. Neither white dwarfs nor planets consist of pure carbon. Nevertheless, it is useful to estimate an upper bound to the diamond nucleation rate by considering the rate at which diamonds would form in a hypothetical environment of pure carbon. To this end we use our numerical data on the chemical potential of liquid carbon and diamond and our numerical estimate of the diamond-liquid surface free energy, to estimate the nucleation

the addition of [111] layers. Note that when graphite and diamond structures compete at 30 GPa (see fig. 6.1), the [001] graphite sheets transform into [111] diamond planes.

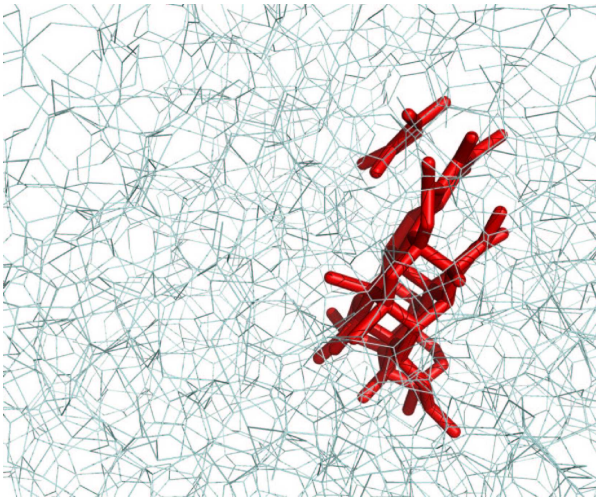

Figure 6.1.: Typical snapshot of a small crystalline cluster of $\sim$ 75 particles obtained at 30 GPa and 3750 K (state point B), surrounded by mainly three-fold coordinated liquid particles. The figure shows both three/four-fold coordinated particles (upper half). The grey lines surrounding the cluster indicate bonds between liquid carbon atoms.

barrier of diamond as a function of temperature and pressure. We then use CNT to estimate the rate of diamond nucleation (see appendix G for details). The results are shown in fig. 6.2. The figure shows that there is a region of some 1000K below the freezing curve (continuous red line) where diamond nucleation is less than 10^{-40} $m^{-3}s^{-1}$. If the rate is lower than this number, not a single diamond could have nucleated in a Uranus-sized body during the life of the universe. As can be seen from the figure, our simulations for state point B are outside the regime where observable nucleation would be expected.

However, this figure provides just an upper bound to the rate of diamond nucleation. In practise, the carbon concentration is somewhat less in carbon-rich stars ($\sim$50%) [120], and much less (1-2% [121]) in Uranus and Neptune. In fig. 6.3, we show how dilution affects the regime where diamond nucleation is possible. To simplify this figure, we do not vary pressure and temperature independently but assume that they follow the adiabatic relation that is supposed to hold along the isentrope of Uranus [122]. We make the assumption that nucleation takes place from an ideal mixture of C, N,O and H [123]. In practise we extend our results by making use of the relation: $\beta\Delta\mu = \beta\Delta\mu_0 + \beta ln([C])$, where $\beta\Delta\mu_0$ is the chemical potential of the pure substance (C) and $[C]$ is the concentration of carbon in the mixture. Not surprisingly, fig. 6.3 shows that dilution of the liquid decreases the driving force for crystallisation to the extent that no diamond phase is expected for C concentrations of less than 8%. As before, there is a wide range of conditions where diamonds could form in principle, but never will in practise. Assuming that, for a given pressure, the width of this region is the same as in the pure C case (almost certainly a serious underestimate), we

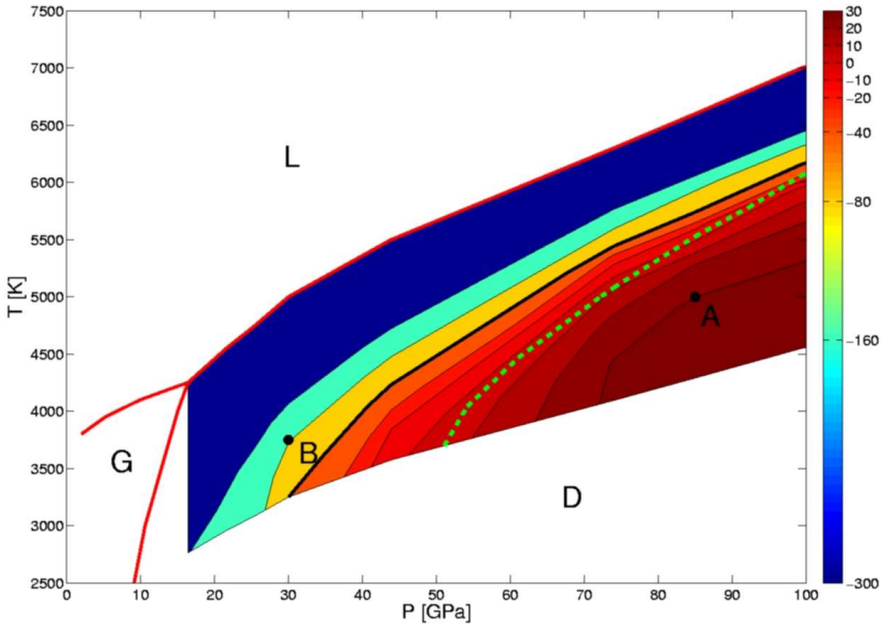

Figure 6.2.: The figure shows part of the carbon phase diagram from ref. [109] and the iso-nucleation rate zones. The solid red lines represent the coexistence lines from ref. [109]. State point A is at $P_A = 85$ GPa, $T_A = 5000$ K, and state point B is at $P_B = 30$ GPa, $T_B = 3750$ K. In the text, we give estimates for the nucleation rate at points A and B. Along the green dashed curve the ratio of 3-fold and 4-fold coordination in the liquid is 1:1. The colour code used in the plot is the following: the numbers on the right indicate the order of magnitude of the crystal nucleation rate from the molten carbon (expressed in $m^{-3}s^{-1}$). The continuous black curve indicates the boundary of the region where the nucleation rate is negligible ($< 10^{-40}m^{-3}s^{-1}$).

arrive at the estimate in fig. 6.3 of the region where nucleation is negligible (i.e. less than one diamond per planet per life-of-the-universe). From this figure, we see that quite high Carbon concentrations (over 15%) are needed to get homogeneous diamond nucleation. Such conditions do exist in white dwarfs, but certainly not in Uranus or Neptune.

6.4. Conclusions

We conclude that is less favourable to create an interface between a diamond and a graphitic liquid than between a diamond and a four-fold coordinated liquid. The destabilising effect of

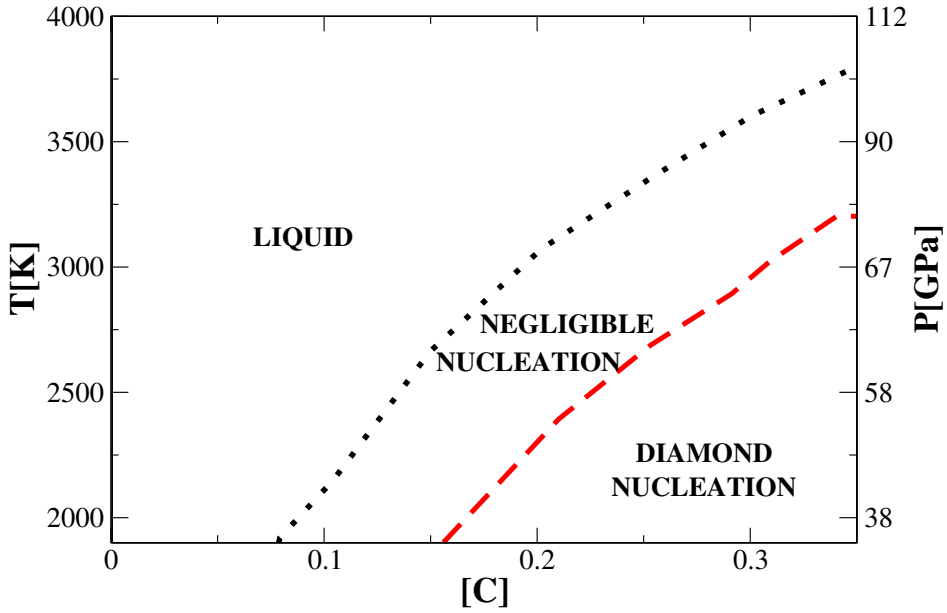

Figure 6.3.: Diamond nucleation boundary as a function of carbon concentration: in the plot, the rate is zero (no thermodynamic driving force to nucleation) in the top region (liquid), it is negligible ($< 10^{-40} m^{-3} s^{-1}$) in the middle region and non-negligible ($> 10^{-40} m^{-3} s^{-1}$) in the bottom-right region. We call the nucleation rate negligible if it corresponds to less than one cluster per Uranus-sized planet over a period of 10^{10} years. The left hand y-axis represents the temperature; the right-hand y-axis indicates the corresponding pressure for a Uranus-like isentrope (see ref. [121]).

the graphitic liquid on the diamond clusters is most pronounced for small clusters, where the surface to volume ratio is larger. The unusual surface structure of the biggest cluster at state point B demonstrate the bad match between a diamond structure and a 3-fold coordinated liquid. Moreover, our work indicates that quite high Carbon concentrations are needed to get homogeneous diamond nucleation. Therefore, it is extremely unlikely that diamonds could ever have nucleated in the carbon-rich middle layer of Uranus and Neptune [121], while the appropriate thermodynamic conditions to diamond nucleation are present in carbon-rich white dwarfs.

Acknowledgements

Concerning this work, I would like to thank S. Iacopini, E. Sanz, P. R. ten Wolde and H. L. Tepper for helpful suggestions.

Appendix A: $LCBOPI^+$

$LCBOPI^+$ [124] is a *bond order* potential good to describe both solid and liquid structures of carbon in a broad range of temperatures and pressures. This potential was modelled in order to be capable to deal with the *conjugation of the* π *bond*, i.e. the coupling between the free orbitals of neighbouring carbon atoms with less than four first neighbours, that can lead to hybridisation effects. The family of $LCBOPI^+$ potentials [124] include both *bonded* and *non bonded* interactions, such as

$$V(r_{ij}) = \frac{1}{2}\sum_{i,j}^{N}(f_c V^{SR}(r_{ij}) + (1-f_c)V^{LR}(r_{ij})) \qquad (6.A.1)$$

where r_{ij} is the distance between atom i and j, f_c is a cut-off function, V^{SR} is the short range *bonded* part and V^{LR} is the long range *non bonded* part. The short range part of the potential only accounts for covalent and metallic bonds, and can be explicitly written as $V^{SR} = V_R(r_{ij}) - b_{ij}V_A(r_{ij}$, where b_{ij} is the angular dependent term, function of the local environment of i and j, also called *bond order*, $V_R(r_{ij}) = A\exp^{-\alpha r_{ij}}$ stands for all the repulsive inter-atomic interactions and $V_A(r_{ij}) = B_1\exp^{-\beta_1 r_{ij}} + B_2\exp^{-\beta_2 r_{ij}}$ for the attractions, being $A, \alpha, B_1, \beta_1, B_2, \beta_2$ parameters specific for the atom species.

Whereas V^{LR} is the long range *non bonded* part, that was introduced for the need of taking into account the week coupling of the π orbitals between the graphite sheets. It has to be long range as the inter-planar distance is ~ 0.34 nm, whereas the first and second neighbours are at ~ 0.14nm and ~ 0.25 nm, respectively (while the same distance in the diamond lattice is $\sim$0.15 nm). Numerically, V^{LR} comes from a best fit to the Density Functional data at the Local Density Approximation level for the inter-planar energies in graphite, and has the shape of $V^{LR}(r) = \Theta(r_0 - r)V_1^M(r) + \Theta(r - r_0)V_2^M(r)$, being $V^M(r)$ a Morse-like potential. For further details, we refer to ref. [116]. Therefore $LCBOPI^+$ contains the isotropical non bonded term, and the short range term, both fitted to match the reference data in the range where both contributions (bonded and non bonded) are present.

$LCBOPI^+$ was computed at zero Kelvin and pressures of the order of TPa for solid structures, like simple cubic and face centred cubic, and fitted by means of *ab initio* calculations. At finite temperatures (of the order of thousands Kelvin), this interaction potential was tested for both solid and liquid structures using Car-Parrinello Molecular Dynamics. For liquid structures available experimental data (like the coexistence line between graphite and diamond) were also adopted to validate the fits. Some of us estimated the region of validity of $LCBOPI^+$ to be up to 15000 K and 4000 GPa. At a certain point, beyond 4000 GPa, the liquid is expected to become mainly 5 and 6 fold coordinated [110, 111]: features that $LCBOPI^+$ does not reproduce.

Appendix B: Order parameter to study diamond nucleation from molten carbon

The local order parameter we use to detect the biggest crystal cluster from molten carbon is the biggest cluster size n, already described in chapter 2. However, due to the symmetry of the diamond crystal, this time the local bond order parameter is chosen to be a function of order three spherical harmonics (Y_{3m}). This choice allows us to identify the tetragonal symmetry of the diamond structure, as already described in ref. [116], and is also perfectly suited to find particles in a graphite-like environment. We consider an odd order of the spherical harmonics, as both diamond and graphite are not invariant upon inversion of coordinates. To define the local order parameter, we start with computing

$$q_{3,m}(i) = \frac{1}{Z_i} \sum_{j \neq i} S^{down}(r_{ij})\ Y_{3m}(\hat{\mathbf{r}}_{ij}) \tag{6.B.1}$$

for each value of m, where the sum extends over all particle i neighbours. $S^{down}(r_{ij})$ is a smooth cut-off function, introduced in the context of $LCBOPI^{+}$[124, 116]

$$S^{down}(r_{ij}) = \begin{cases} 1 & \text{for} \quad 0 < r_{ij} \leq 1.7 \\ (1-x)(1+2x+3x^2)(1-x)^2 & \text{for} \quad 1.7 < r_{ij} \leq 2.2 \\ 0 & \text{for} \quad 2.2 < r_{ij}, \end{cases} \tag{6.B.2}$$

where $x = \left(\frac{r_{ij}-1.7}{2.2-1.7}\right)$, and Z_i is the *coordination* of particle i , i.e. the fractional number of neighbours around it ($Z_i = \sum_{j \neq i} S^{down}(r_{ij})$). Normalising eq. 6.B.1, we get

$$q^{'}_{3,m}(i) = \frac{q_{3,m}(i)}{(\sum_{m=-l}^{l} q_{3,m} \cdot q^{*}_{3,m})^{1/2}}, \tag{6.B.3}$$

being $q^{*}_{3,m}$ the complex conjugate of $q_{3,m}$. According to eq. 2.A.2, we calculate $d_3(i,j)$, i.e. the dot product between the normalised function $q^{'}_{3,m}$ of particle i and the same function computed for each of its first neighbours, and sum them up over all the m values:

$$d_3(i,j) = \sum_{m=-l}^{l} q^{'}_{3,m}(i) \cdot q^{'*}_{3,m}(j) S^{down}(r_{ij}), \tag{6.B.4}$$

d_3 is a real number defined between -1 and 1: it assumes the value of -1 when computed for both the graphite and diamond ideal structures. Two neighbouring particles i and j are considered to be connected whenever $d_3(i,j) \leq d_c = -0.87$, as shown in ref. [116]. By counting the total number of connections (n_{con}) and plotting the probability distribution of n_{con}, we define a threshold for the number of connections needed to neatly distinguish between a liquid-like and a solid-like environment: we assume that whenever $n_{con} > n^{c}_{con} = 3$ a particle is considered to be solid-like. By means of a cluster algorithm we then define all the solid-like AND *connected* particles as belonging to the same crystal cluster. After computing the size of each cluster, we select the biggest as the local order parameter to describe the phase transition. At this stage, we do not specify any nature of the particle's crystallinity, whether diamond-like or graphite-like.

Diamond vs graphite analysis at state point B

Only after the nucleation process, we try to differentiate graphite-like from diamond-like particles. In an *a posteriori* analysis, we use another order parameter, this time function of the order two spherical harmonics, particularly sensitive to the graphite planar geometry: being $q_{2m}(i)$ the linear combination of spherical harmonics computed for each particle i

$$q_{2m}(i) = \frac{1}{Z_i} \sum_{j \neq i} S^{down}(r_{ij})\, Y_{2m}(\hat{\mathbf{r}}_{ij}) \tag{6.B.5}$$

where the sum extended over all particle i neighbours. We then sum over all the m values and calculate the modulus, $|q_2|$. The $|q_2|$ probability distribution for both A and B is represented in fig. 6.B.1.

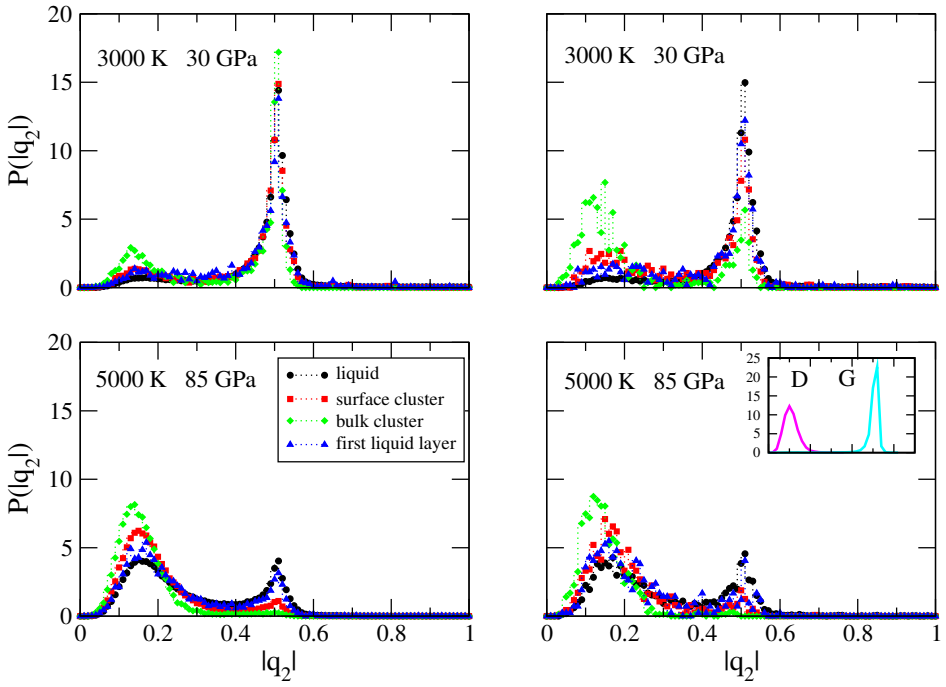

Figure 6.B.1.: The top-left side represents clusters of ~ 20 and the top-right side clusters of ~ 75 at state point B. Whereas the bottom-left side clusters of ~ 20 and the bottom-right side clusters of ~ 250 particles at state point A. The used code is: circles=liquid particles, squares=particles belonging to the biggest cluster's surface, diamonds=particles within the bulk cluster, triangles= particles belonging to the first liquid layer surrounding the biggest cluster. The inset shows the $|q_2|$ probability distribution for an equilibrated bulk diamond (D) (left-hand side) and graphite (G) (right-hand side).

The figure depicts the features of both the smallest (~ 20 in both state points A and B)

and the biggest clusters ($\sim$ 250 in A and $\sim$ 75 in B). Later, we distinguish among: liquid-like particles (circles), particles belonging to the biggest cluster's surface [2] (squares), particles within the bulk cluster (diamonds) and particles belonging to the first liquid layer surrounding the biggest cluster (triangles). To neatly distinguish between a diamond-like or a graphite-like environment, we use as a reference the $|q_2|$ probability distribution for both bulk diamond (D) and graphite (G), delineated in the inset of fig. 6.B.1. At state point A, it is clear that bulk particles belonging to the both small clusters (bottom-left side) and big clusters (bottom-right side) are mainly diamond-like, as well as particles belonging to the surface of the clusters. While at state point$B$, bulk particles belonging to the small clusters (top-left side) show both graphite-like and diamond-like finger-prints. By visual inspection, we note that when clusters reach a bigger size (around 75 particles), particles at the surface tend to be mainly 3-fold coordinated, while bulk particles stay 4-fold coordinated, as shown in the top-right side of fig. 6.B.1. Concerning the particles belonging to the first liquid layer surrounding the cluster, they usually display the same behaviour as the ones belonging to the surface, coherently with the uncertainty in distinguishing a surface-particle from a first-liquid-layer particle.

It is also important to notice that the metastable liquids in A and B are structurally different. In A the liquid is mainly 4-fold coordinated (diamond-like), while in B the percentage of 3-fold coordinated liquid is dominant: in this region, even though the diamond is energetically more stable, both diamond and graphite crystal structures can compete in the nucleation process. In fact, it has been shown in ref. [125, 126] that a simple path exists to transform graphite into diamond, i.e. via the buckling of the graphite plane at several thousand Kelvins into the 111 diamond plane.

Appendix C: Self-diffusion coefficient

In order to compute the self-diffusion coefficient, we use the fact that molten carbon is an Arrenhius-like liquid: therefore, once the activation energy is known, we compute the viscosity as a function of temperature and by means of the Stokes-Einstein relation obtain the diffusion coefficient. Earlier on, Kanter [127] measured the liquid carbon activation energy, getting E_A =683 $\frac{kJ}{mol}$. Later, Fedosayev [128] reported a measurement of the molten carbon viscosity: η = 5 $\times 10^{11}$ poise at $T = 1860K$. From the Stokes-Einstein relation [83], we can estimate the self-diffusion coefficient at the same temperature:

$$D = \frac{k_B T}{\eta a} \tag{6.C.1}$$

where $a = 1.54\dot{A}$ and k_B is the Boltzmann's constant: $D(1860K) = 3.3 \times 10^{-17}$ cm^2/s. As we assume that molten carbon is an Arrenhius-like fluid [129],

$$D(T) = D_0 \exp^{-\frac{E_A}{k_B T}}, \tag{6.C.2}$$

we can calculate D_0: $D_0 = 470$cm^2/s, and then extrapolate the diffusion coefficient for different temperatures. In order to make sure that our extrapolations are correct, we use a

[2] According to our definition, particles belonging to the surface of the cluster, are those *connected* to a solid-like particles, but not solid-like themselves.

Car-Parrinello Molecular Dynamics [114] to calculate the self-diffusion coefficient by means of the mean square displacement: at state point A $D = 2.3 \times 10^{-5}$cm^2/s, that match really well with the diffusion coefficient estimated by means of the Arrhenius law, $D = 3.5 \times 10^{-5}$ cm^2/s.

Hence, we are allowed to extrapolate the values of D for a broad range of temperatures (see fig. 6.C.1).

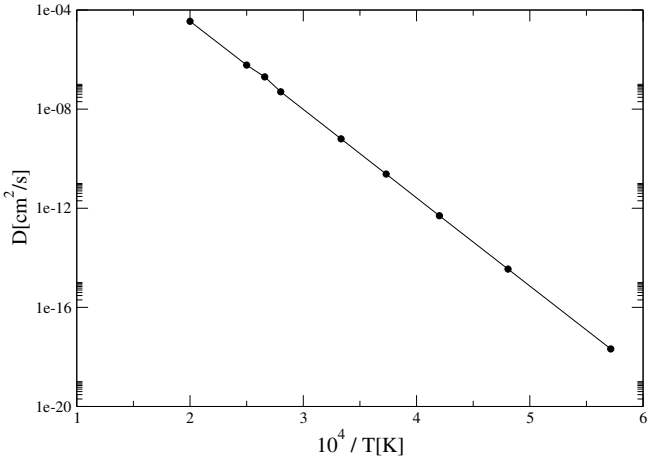

Figure 6.C.1.: Arrhenius plot for the super-cooled liquid carbon. The activation energy is $E_A = 7$eV from ref.[127].

T[K]	**D**$[\dot{A}/s^2]$	**T[K]**	**D**$[\dot{A}/s^2]$
1750	2.1×10^{-2}	3000	6.3×10^{6}
2080	3.5×10^{1}	3300	7.6×10^{7}
2380	5.0×10^{4}	3570	5.0×10^{8}
2680	2.4×10^{5}	3760	2.0×10^{9}

Table 6.C.1.: Self diffusion coefficient as a function of temperature.

At state point A $D_A = 3.5 \times 10^{-5}$ cm^2/s, while at state point B $D_B = 2 \times 10^{-7}$ cm^2/s.

Appendix D: Computation of the crystal nucleation rate at state point A and B

In our computer simulations, we have also calculated the crystal nucleation rate at both state points A and B by means of the FFS technique (see chapter 2 and ref. [13, 14]). At state point A we obtain $R_A \sim 10^{33}$ m^{-3} s^{-1}. However, due to the time-consuming empirical potential

used ($LCBOPI^+$), we only sample few tens of trajectories crossing the top of the nucleation free-energy barrier: this leads to a poor statistics of the estimated rate. Comparing R_A to the crystal nucleation rate in a Lennard-Jones system at the same under-cooling, $R_{LJ} \sim 10^{30}$ m^{-3} s^{-1} [29], we conclude that molten carbon nucleates faster than Lennard-Jones, leading to the formation of many small diamond crystallites. However, comparing R_A to the crystal nucleation rate of sodium-chloride (see chapter 4) ($R_{NaCl} \sim 10^{24}$ m^{-3} s^{-1}), we conclude that NaCl nucleates into a big crystal with a much slower rate than molten carbon.

Fig. 6.D.1 represents the critical cluster obtained in the FFS simulations: it contains around

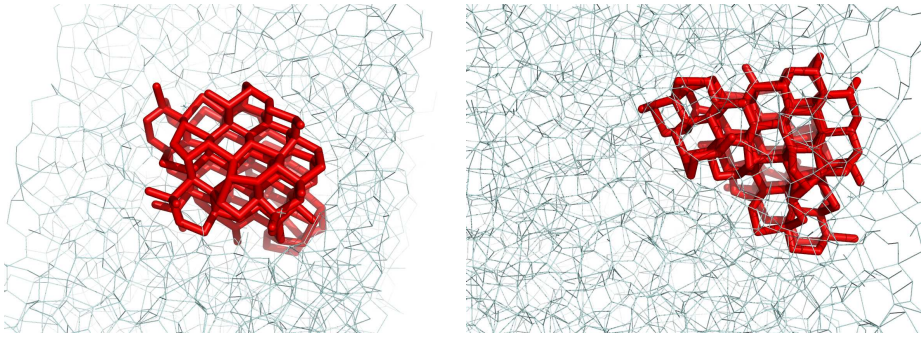

Figure 6.D.1.: Two views of the biggest cluster at state point A containing around 110 particles, surrounded by mainly 4-fold coordinated liquid particles.

110 particles surrounded by mainly 4-fold coordinated liquid particles. The pictures shows two different views of the same cluster: all particles within the bulk are diamond-like, while the surface particles are less *connected*, but still mainly 3-4 fold coordinated.

At state point B, it is not possible to nucleate any crystal cluster bigger than 75 particles, even though we try to shoot several hundreds stochastic trajectories: this leads to a nucleation rate of $R_B \sim 0$ $s^{-1}m^{-3}$. As already shown in fig. 6.1, a 75 particles cluster presents 3-fold coordinated surface particles surrounding the 4-fold coordinated bulk particles, while embedded in a 2-3 fold coordinated liquid.

Appendix E: Computing the super-saturation

In order to study the liquid-to-solid phase transition, we start by simulating in a Monte Carlo scheme a metastable liquid by means of the semi-empirical potential $LCBOPI^+$ (see appendix A) deeply described in refs. [124, 116]. The liquid is made metastable in an NPT ensemble, by cooling it down, while keeping pressure fix, to a temperature below the coexistence temperature (T_{coex}), both at pressure of 85 GPa (state point A) and 30 GPa (state point B). Defining the amount of super-cooling as $(T - T_{coex})/T_{coex}$, we have that the super-cooling in A is 24% while in B is 25%, being $T_{coex,A}$ =6600K and $T_{coex,B}$ =5000K. Following the same procedure as the one described in appendix C in chapter 4, we obtain that $\beta\Delta\mu$ =0.60 in state point A and $\beta\Delta\mu$ =0.77 in state point B.

Appendix F: Inter-facial free-energy estimate via the free-energy barrier

According to Classical Nucleation Theory (CNT) (thoroughly discussed in chapter 2), the crystal nucleation rate depends exponentially on the top of the free-energy barrier (see eq. 2.10). The latter is a function of the inter-facial free energy (γ) cube and inversely proportional to the super-saturation ($\Delta\mu$) square. Since the super-saturation is quite similar in both cases ($\beta\Delta\mu_A$ =0.60 and $\beta\Delta\mu_B$ =0.77 that are the same if expressed in Joule), we deduce that the inter-facial free energy might play a major role. Thus, in what follows, we calculate γ in both state point A and B, while keeping in mind that the structures of the metastable liquids in A and B are utterly dissimilar.

In order to calculate the inter-facial free energy γ we use CNT. Thus, to practically get the value of γ:

1. we compute the free-energy barrier as a function of the biggest cluster size n using the Umbrella Sampling scheme;

2. we select only the first part of the nucleation curve given by eq. 2.7. The first part results to be mainly dominated by the surface term $A(n)\gamma$;

3. we fit the slope of the free-energy barrier curve to a polynomial function, while imposing the value of the super-saturation ($|\Delta\mu|$);

4. from the coefficient of the fit, we extract the value of γ, once having assumed the shape of the growing cluster ($A(n)$).

We start with computing γ at state point A (γ_A). The free-energy barrier as a function of the biggest cluster size was already computed in ref. [116] by means of Umbrella Sampling. Assuming a spherical shape for the nucleating cluster, we obtain eq. 2.12, where $\rho_B = \rho_S$, the solid number density. By fitting the first part of eq.2.12 we obtain that the inter-facial free energy is $\gamma_A = 0.27 k_B T/\text{Å}^2 \sim 1.86$ J m^{-2}. Same value of the inter-facial free energy is obtained from the top of the free-energy barrier (eq. 2.10): $\Delta G^* = 25 k_B T$, being $\beta\Delta\mu$ =0.60 and $\rho_S = 0.191$ Å^{-3}. By means of eq. 2.13, we can estimate the size of the critical cluster: at state point A is n^* ∼85, corresponding to the value observed at the top of the free-energy barrier in ref. [116] (n^* ∼110), within the error bars. At the chosen thermodynamic conditions, there are no finite size effects, caused by *spurious* interaction of the critical cluster with its own periodically repeated image. [3] Knowing the inter-facial free energy in A, and assuming the validity of CNT, we estimate the crystal nucleation rate by means of eq. 2.32, where we use eq. 2.35 to compute the kinetic pre-factor (the diffusion coefficient being discussed in appendix C and the atomic jump distance λ being of the order of the diamond bond distance 1.54Å): $R_A^{CNT} \sim O(10^{30})$ s^{-1}m^{-3}. This value is three order of magnitude smaller than the one computed by means of FFS. Nevertheless, if we consider that the standard deviation corresponding to γ is around 10% of its measured value, we conclude that the nucleation rate

[3] The bulk system of 2744 atoms is simulated using periodic boundary conditions, repeating along the x,y and z directions a cubic box whose edge was 18Å.

is $O(10^{30\pm3})$ s^{-1}m^{-3}. Moreover, as already pointed out in appendix D, another source of error can be the poor statistics used to compute the nucleation rate by means of FFS.

We now attempt to explain the results of our simulations at state point B. As by means of FFS we are not able to reach the critical cluster, we conclude that a system of 2744 particles might be too small to accommodate a spherical critical cluster. Therefore, we resort to an indirect way to estimate the free-energy barrier ΔG^* to grow a spherical critical cluster. In order to measure the free-energy barrier, as we know the solid number density ($\rho_S = 0.177$ Å^{-3}) and the chemical potential difference between the liquid and the solid ($\beta\Delta\mu_B$ =0.77), we only need to calculate the inter-facial free energy. Nevertheless, as we cannot accommodate a spherical critical cluster in our simulation box, we reduce the dimensionality of the problem. We compute γ for a rod-like crystal in a system with a slab geometry (containing around 4000 particles): the crystal is oriented perpendicular to the plane of the slab and has a parallelepiped-like shape spanning the height of the simulation box with the [111] faces exposed to the liquid. Fig. 6.F.1 represents the top side view at state point B (30 GPa and 3750

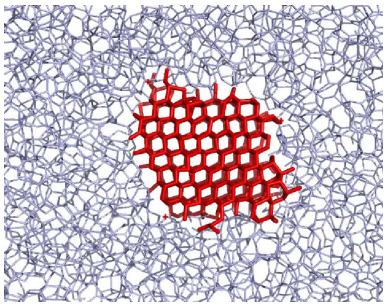

Figure 6.F.1.: Top side view of a rectangular parallelepiped formed by four [111] faces and two [1-10] lozenge bases with acute angle θ=70.52 degrees at 30 GPa and 3750 K.

K) of a rod-like crystal, formed by four [111] faces and two bases as [1-10] lozenge with the acute angles of θ=70.52 degrees. We then rewrite eq. (2.7) for a rectangular parallelepiped having four [111] faces and two basis [1-10] as lozenges with acute angle of $\theta = 70.52$

$$\Delta G = 4\sqrt{\frac{h}{\rho \sin\theta}}\gamma^l n^{1/2} - |\Delta\mu| n, \tag{6.F.1}$$

where h is the slab's height. We then use the Umbrella Sampling technique to compute the slope of the first part of the free-energy barrier. As $h = 10$ Å, we obtain from fitting eq. 6.F.1 that the inter-facial free energy for the lozenge-shaped cluster is $\gamma^l_B = 0.91 k_B T/$Å$^2 \sim 4.70$ J m^{-2}. By computing the inter-facial free energy of the rod-like crystal at state point A, we obtain $\gamma^l_A = 0.37 k_B T/$Å$^2 \sim 2.55$ J m^{-2}, considering the same slab's height and the same angle θ. Now that we know the inter-facial free energies of the lozenge-shaped clusters at the state points A and B, we estimate the ratio between them: we find that $c\gamma_B/c\gamma_A = \gamma_B/\gamma_A \sim 2.5$. As we compare clusters having the same shape, this ratio turns out to be independent on the assumed cluster shape. Therefore, we claim that at state point B the early stage of the

crystalline clusters is mainly dominated by the inter-facial free-energy term, that obstacles the clusters to grow further and, consequently, the liquid to wet the surface. Since we know γ_A of the spherical cluster and the ratio between the two γ's, we can infer γ_B of a cluster with the same spherical shape: $\gamma_B = 0.68 k_B T/\text{Å}^2 \sim 3.50$ J m^{-2}.

If we now estimate the size of a critical spherical cluster at state point B, by knowing the lozenge-shaped parallelepiped critical cluster, we can indeed show that we would have needed a much larger system in order to accommodate such a cluster at the thermodynamic conditions simulated in B. From eq. 6.F.1, we calculate the critical cluster size for the lozenge-shaped parallelepiped n_l^* and use it to estimate the critical spherical cluster n_s^* in B. As

$$n_l^* = \frac{4h}{\rho_S \sin\theta} \frac{(\gamma)^2}{(\Delta\mu)^2}. \tag{6.F.2}$$

At state point B n_l^* ∼330 particles. Expressing n_s^* of a spherical cluster as a function of the lozenge-shaped parallelepiped one, we get

$$n_s^* = \frac{8}{3}\pi \frac{\gamma \sin\theta}{\rho_S \Delta\mu h} \times n_l^*, \tag{6.F.3}$$

where ρ_S the solid density ($\rho_B = 0.17$ Å^{-3}), $\Delta\mu$ the chemical potential difference between the solid and the super-cooled liquid ($|\Delta\mu_B/k_BT| = 0.77$), and h is the height of the slab (10 Å). Eq. 6.F.3 corresponds to a spherical cluster of $n_s^* \sim 1700$ particles at state point B. Thus, one would need a system of at least 17000 particles to contain such critical cluster and avoid finite size effects. Such a system size is beyond our present computational capacity. [4] In contrast, in the slab geometry we find that the free energy of a lozenge-shaped crystal goes through a maximum at a size of ∼ 340 particles, which is much less than the system size (4000 particles). Now that we know γ_B, we can estimate the nucleation rate according to CNT. The free-energy barrier height of a spherical cluster is $\Delta G^* \sim 280 k_B T$, roughly 11 times higher than the free-energy barrier in A, and the nucleation rate is $R_B \sim 10^{-80}$ s^{-1}m^{-3}, confirming our consideration that the growth is intrinsically more difficult at state point B.

Appendix G: Estimating the nucleation rates throughout the region of the phase diagram between T_A and T_B

In order to extrapolate our results to thermodynamic conditions that are proper of planets like Uranus and Neptune and carbon-rich stars, we extend the estimate for the nucleation rate from the triple point pressure up to 100 GPa, from the melting temperatures to 35 % undercooling (at which our samples stopped diffusing) by means of eq. 2.32, 6.1, and 2.35. The state point

[4] To guarantee that the critical cluster does not interact with its own periodic images, its radius should always be less than 25% of the box diameter L. A spherical cluster with a radius of 0.25 L occupies ∼ 7 % of the volume of the box and, as the solid is denser than the liquid, it contains about 10 % of the total number of particles.

dependent quantities are the solid and liquid densities ρ_L and ρ_S, the self-diffusion coefficient D_S, the surface free energy γ, the difference in chemical potential between the liquid and the solid $\Delta\mu$, and the critical cluster size N^*. We estimate them in the following way:

- the densities are directly measured after the MC simulations of the solid and the liquid;
- for the self diffusion coefficient, we assume an Arrhenius behaviour, where the activation energy is the bonding energy per particle;
- concerning the chemical potential difference, we extrapolate the values calculated via eq. **??** at 30 and 85 GPa to all pressures: in practise, $\Delta\mu$ at a certain (P, T) point is estimated by linearly combining the values at 30 and 85 GPa *at the same under-cooling*;
- in view of the strong dependence of γ on the atomic coordination in the liquid phase, we assume that $\gamma(P, T)$ depends linearly on c_4, the equilibrium concentration of 4-fold coordinated atoms at the selected state point. This quantity is easily measured during the MC simulations of the liquid;
- we assume that the height of the nucleation barrier is given by the CNT expression of eq. 6.1 and we that the factor c is the same for all clusters.

Part V.

Bubble nucleation

7. Perturbation-theory estimates of liquid-solid and liquid-vapour γ for Lennard-Jones[1]

A husband is a suitcase with legs.
Chinese proverb.

The most naive perturbation method to estimate inter-facial free energies is based on the assumption that the interface between coexisting phases is infinitely sharp. Although this approximation does not yield particularly accurate estimates for the liquid-vapour surface tension, we find that it works surprisingly well for the interface between a dense liquid and a solid. As an illustration we estimate the liquid-solid inter-facial free energy of a Lennard-Jones system with truncated and shifted interactions and compare the results with numerical data that have been reported in the literature. We find that the agreement between theory and simulation is excellent. In contrast, if we apply the same procedure to estimate the variation of the liquid-vapour surface tension for different variants of the Lennard-Jones potential (truncated/shifted/force-shifted), we find that the agreement with the available simulation data is, at best, fair. The present method makes it possible to obtain quick and easy estimate of the effect on the surface free energy of different potential-truncation schemes used in computer simulations.

7.1. Introduction

In computer simulations of classical many-body systems, the intermolecular potential is often truncated at a finite distance to reduce the numerical computational cost, which, inevitably, changes the system properties such as energy, pressure, etc. Standard "tail corrections" exist to compensate for the truncation errors in uniform systems with sufficiently short-ranged potentials (see e.g. ref. [70]). In contrast, in inhomogeneous systems, calculations of the tail corrections are not straightforward, and they might not be small compared to the reference values. In particular, expressions for the tail corrections of the liquid-vapour inter-facial free-energy density (γ) in Lennard-Jones systems were derived using the thermodynamic perturbation theory [130, 131, 132]. Chapela et al. [133] employed the Kirkwood-Buff-Fowler's

[1] Work carried out in collaboration with Z.J. Wang.

formula to compute the correction to the exact surface tension while postulating a hyperbolic tangent shape for the inter-facial profile, and their results were subsequently refined by Blokhuis et al. [134] and Mecke et al. [135]. These results were used in ref. [133, 134, 135] to compute the free energy of the liquid-vapour interface in a Lennard-Jones fluids with truncation of the intermolecular potential, adopting the full Lennard-Jones system as a reference.

Interestingly, this approach can also be used for a "rule-of-thumb" estimate of the liquid-solid inter-facial free energy, as we show in the present chapter. The following assumptions on the interface profile and the reference system seem to be in order in this case. The simplest inter-facial profile goes back to Laplace [136], who treated it as a step function in the density. Not surprisingly, it does not yield a particularly good estimate for the liquid-vapour surface tension, where the dividing surface is rough and not well defined, especially close to the critical point. However, one might expect this approximation to be much better for the sharp interface between crystal and dense (and rather incompressible [83]) liquid, where the role of fluctuations is much smaller. As a reference system the hard-sphere model can be exploited by means of the Weeks, Chandler and Andersen [137]'s approach. The hard-sphere system exhibits a liquid-solid interface under the appropriate conditions. This, again, simplifies situation in comparisons with the liquid-vapour interface, where the full Lennard-Jones system needs to be taken as a reference (the hard-sphere do not exhibit a liquid-vapour phase separation).

Thus, we use perturbation theory approach in the present chapter to estimate the surface free energy of truncated-force-shifted Lennard-Jones crystals in contact with its melt. For the sake of comparison, we employ the same approach to estimate the difference in the liquid-vapour surface tension of truncated and un-truncated LJ models. Although it is not particularly good in the latter case, we include the results for future reference, because the relevant simulation data appeared to be rather scattered in the literature.

7.2. Method

We aim to estimate the inter-facial free energy of particles interacting via a modified (truncated and (force)shifted) Lennard-Jones potential, using either the hard-sphere system (for liquid-solid) or the full Lennard-Jones model (for liquid-vapour) as the reference state.

$$\gamma_{LJ} = \gamma_{ref} + \gamma_P. \tag{7.1}$$

We assume that γ_{ref} is known. Below, we list the various contributions to the perturbation (γ_P). The overall perturbation is additive. In all cases we make the "Laplacian" assumption that the interface separating the two phases has a step profile. We consider three possible "perturbation" terms: $v_{P1}(r)$,$v_{P2}(r)$ and $v_{P3}(r)$ contributions to obtain the truncated and shifted interaction potential:

1. $v_{P1}(r)$ is a constant term that is needed to shift a truncated potential to zero at the cut-off radius r_c:

$$v_{P1}(r) = \begin{cases} -v_{LJ}(r_c) & \text{for } r \le r_c \\ 0 & \text{for } r > r_c. \end{cases} \tag{7.2}$$

   It guarantees the continuity of the potential at r_c. v_{P1} is positive, as $v_{LJ}(r_c) < 0$.

2. $v_{P2}(r)$ is the perturbation that removes the long-range part of the LJ potential (for $r \geq r_c$):

$$v_{P2}(r) = \begin{cases} 0 & \text{for } r < r_c \\ -4\epsilon \left[\left(\frac{\sigma}{r}\right)^{12} - \left(\frac{\sigma}{r}\right)^{6} \right] & \text{for } r \geq r_c. \end{cases} \tag{7.3}$$

3. Finally, only in the truncated and force-shifted potential, we also use $v_{P3}(r)$, a term that ensures the continuity of the first derivative of the potential at r_c

$$v_{P3}(r) = \begin{cases} -(r - r_c) v'_{LJ}(r_c) & \text{for } r \leq r_c \\ 0 & \text{for } r > r_c, \end{cases} \tag{7.4}$$

where $v'_{LJ}(r)$ is $\left(24\epsilon \frac{\sigma^6}{r} \left[\frac{1}{r^6} - \frac{2\sigma^6}{r^{12}}\right]\right)$. $v_{P3}(r)$ is also positive, as the first derivative is positive for $r > r_c$.

We can now easily estimate the contributions of these three perturbations to the surface free energy, that follows Rowlinson and Widom's prescription [130]. We start our procedure, by considering a system (I) where particles interact via a full Lennard-Jones potential (v_{LJ}). As shown in the left side of fig. 7.1, we divide it into two sub-systems: one half is in the liquid phase (phase 1), and the other half is the solid phase (phase 2), for instance. The two halves are separated by a dividing surface (S). We then consider a second system (II) divided the same way as system I in two halves containing phase 1 and 2 (right side of fig. 7.1): here particles interact via a full Lennard-Jones plus a long range perturbation potential ($v_{LJ} + v_P$), for instance a truncated and force shifted interaction potential.

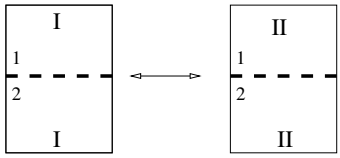

Figure 7.1.: On the left, phase 1 and phase 2 of a system where particles interact via v_{LJ}. On the right, the same phases 1 and 2 of a system where particles interact via $v_{LJ} + v_P$.

Being ρ_1 the phase 1 density and ρ_2 the phase 2 density, $\Delta\rho = (\rho_2 - \rho_1)$ is the density difference between the two phases separated by the dividing surface S: $\Delta\rho$ will have the same value in both systems I and II.

We now consider the energy at the dividing surface S between phase 1 and 2 in system I (ϵ_I^{1-2}), and the same quantity estimated in system II (ϵ_{II}^{1-2}). We then compute the difference between ϵ_I^{1-2} and ϵ_{II}^{1-2}, defined as $\Delta\epsilon$: this difference corresponds to the contribution to the inter-facial energy in S due to the perturbation terms. We notice that we can evaluate $\Delta\epsilon$ either starting from phase 1 or from phase 2, and we use a subscript to indicate it: accordingly, we obtain $\Delta\epsilon_1$ and $\Delta\epsilon_2$. Therefore, both $\Delta\epsilon_1$ and $\Delta\epsilon_2$ only depend on the contribution coming from the long range perturbations v_P.

As the inter-facial free energy is defined as the energy at the dividing surface per unit area, we express the corrections γ_P to the inter-facial free energy of the unperturbed system, as the total $\Delta\epsilon$ at the dividing interface S per unit area:

$$\gamma_P = \frac{\Delta\epsilon_1 + \Delta\epsilon_2}{S} \tag{7.5}$$

where $\Delta\epsilon_i$ is the inter-facial energy difference between phase 1 and 2 in both system I and II, starting from 1 and 2, respectively (i=1,2), and S is the area of the interface between the two phases. Therefore, in order to compute γ_P we start by evaluating $\Delta\epsilon_1$ and $\Delta\epsilon_2$. Then we use eq. 7.1 to get the liquid-solid inter-facial free energy in a truncated and force shifted Lennard-Jones system.

In order to compute $\Delta\epsilon_1$, we consider the interaction zone of a particle P located in phase 1 nearby the surface dividing the two phases (S). Fig. 7.2 shows the particle P interaction zone.

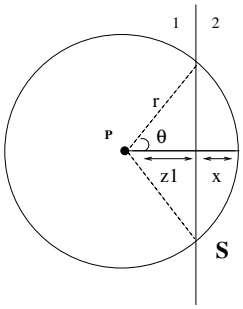

Figure 7.2.: Interaction zone of a particle P located in phase 1 nearby the dividing surface S. The interaction zone includes a spherical cap in phase 2, where z_1 is the distance between P and the dividing surface, θ is the contact-angle, x is the height of the cap, and r the P interaction radius.

For any particle P in phase 1 nearby the dividing surface S, the interaction zone in phase 2 can be described as a spherical cap, where z_1 is the distance between P and S, θ is the contact-angle, x is the height of the cap, and r the P interaction radius. Being

$$x \quad = \quad r - z_1 = r - r\cos\theta = r\left(1 - \frac{z_1}{r}\right), \tag{7.6}$$

the area of the spherical cap is a function of r and z_1:

$$S(r, z_1) = 2\pi r \cdot x = 2\pi(r^2 - z_1 r). \tag{7.7}$$

Hence, the contribution at P coming from phase 2 to the inter-facial energy difference $\Delta\epsilon_1$ is a function of $S(r, z_1)$. In order to estimate the total contribution to the inter-facial energy due to phase 2, we integrate the energy in r deeply into phase 2, from z_1 to ∞. To conclude, to calculate the inter-facial energy not only in P but due to all the particles in phase 1, we

integrate the energy previously calculated in z_1 over all phase 1 from 0 to ∞, i.e. within phase 1.

In practise, using the first order in Zwanzig's perturbation theory [138], as suggested by Abraham [139], in the limit of a sharp dividing surface of zero thickness, and assuming that the liquid is homogeneous on the length scale of the interaction potential (the radial distribution function $g(r) \rightarrow 1$) (see ref. [130]), we get

$$\Delta\epsilon_1 = \frac{1}{2}\rho_1(\rho_2 - \rho_1)S\int_0^\infty dz_1 \int_{z_1}^\infty dr\ v_P(r)\ S(r, z_1) \tag{7.8}$$

where ρ_1 is the phase 1 density, ρ_2 the phase 2 density, and the subscript 1 indicates that we have started our calculations from in phase 1.

Repeating the same calculation for the symmetric case, where we start from particles in phase 2, we obtain

$$\Delta\epsilon_2 = \frac{1}{2}\rho_2(\rho_1 - \rho_2)S\int_0^\infty dz_1 \int_{z_1}^\infty dr\ v_P(r)\ S(r, z_1). \tag{7.9}$$

Now that we know the energy at the dividing surface, we introduce eq. 7.8 and 7.9 into eq. 7.5, and obtain

$$\begin{aligned}\gamma_P &= \frac{\Delta\epsilon_1 + \Delta\epsilon_2}{S} \\ &= -\frac{1}{2}(\Delta\rho)^2\int_0^\infty dz_1 \int_{z_1}^\infty dr\ v_P(r)\ S(r, z_1)\end{aligned} \tag{7.10}$$

In what follows, we separately calculate each contribution to the correction due to the different perturbation terms: γ_{P1}, γ_{P2} and γ_{P3}, respectively. In all our calculations, we choose $r_c = 2.5\sigma$ as a cut-off. Three-body and higher order terms are not included in the energy calculations. The total energy of the system is assumed to be pairwise additive. All the variables are expressed in reduced units: σ and ϵ are length and energy units, respectively; the reduced temperature is $T^* = \frac{k_B T}{\epsilon}$, (where k_B is the Boltzmann's constant), the reduced density $\rho^* = \frac{N\sigma^3}{V}$ and the reduced inter-facial free energy $\gamma^* = \frac{\gamma\sigma^2}{\epsilon}$. In what follows, we express both γ and ρ omitting the asterisks, but always refer to variables in reduced units.

1. The contribution due to $v_{P1}(r)$, is denoted by γ_{P1} and given by:

$$\begin{aligned}\gamma_{P1} &= -\frac{1}{2}(\rho_2 - \rho_1)^2\int_0^{r_c} dz_1 \int_{z_1}^{r_c} dr(-v_{LJ}(r_c))\left(2\pi(r^2 - z_1 r)\right) \\ &= \frac{\pi}{8}v_{LJ}(r_c)r_c^4(\Delta\rho)^2.\end{aligned} \tag{7.11}$$

For $r_c = 2.5\sigma$, $v_{LJ}(r_c) \approx -0.0163\epsilon < 0$, and we obtain: $\gamma_{P1} = -0.25(\Delta\rho)^2$.

2. γ_{P2}, the contribution due to $v_{P2}(r)$ is:

$$\begin{aligned}\gamma_{P2} &= -\frac{1}{2}(\rho_2-\rho_1)^2\int_0^\infty dz_1\int_{z_1}^\infty dr\left\{-4\epsilon\left[\left(\frac{\sigma}{r}\right)^{12}-\left(\frac{\sigma}{r}\right)^{6}\right]\right\}(2\pi(r^2-z_1r))\Theta(r-r_c)\\ &= 2\pi\epsilon\left[\frac{\sigma^{12}}{8r_c^8}-\frac{\sigma^6}{2r_c^2}\right](\Delta\rho)^2. \qquad (7.12)\end{aligned}$$

For $r_c = 2.5\sigma$, we obtain: $\gamma_{P2} = -0.50(\Delta\rho)^2$.

3. Finally, γ_{P3} (the contribution due to $v_{P3}(r)$) is:

$$\begin{aligned}\gamma_{P3} &= -\frac{1}{2}(\rho_2-\rho_1)^2\int_0^{r_c} dz_1\int_{z_1}^{r_c} dr\left[-(r-r_c)v_{LJ}^{'}(r_c)\right](2\pi(r^2-z_1r))\\ &= -\frac{\pi}{40}v_{LJ}^{'}(r_c)r_c^5(\Delta\rho)^2. \qquad (7.13)\end{aligned}$$

For $r_c = 2.5\sigma$, $v_{LJ}^{'}(r_c) \approx 0.039\frac{\epsilon}{\sigma} > 0$, and $\gamma_{P3} \approx -0.3(\Delta\rho)^2$.

7.3. Results

We present our results in the following paragraphs.

7.3.1. Calculation of the liquid-solid inter-facial free energy

A numerical calculation of the liquid-solid inter-facial free energy of a Lennard-Jones system (more precisely: truncated and force-shifted LJ (TSF)) was reported in 1986 by Broughton and Gilmer [140] and, more recently, by Davidchack and Laird [141]. Both sets of authors considered the [100], [110] and [111] surfaces. In addition, Davidchack and Laird computed the inter-facial free energy for the same faces of a hard sphere crystal. It so happens that the reduced density difference between solid and liquid for the TSF-LJ system at the triple-point temperature considered in both refs [140, 141] is very nearly equal to that of the hard-sphere system, making the system an ideal target for the liquid-solid flat-interface version of the Fowler-Kirkwood-Buff theory.

The TSF-LJ potential has the following form:

$$v_{TSF-LJ}(r) = \begin{cases} 4\epsilon\left[\left(\frac{\sigma}{r}\right)^{12}-\left(\frac{\sigma}{r}\right)^{6}\right]+c_1 & \text{for } r \le 2.3\sigma \\ c_2\left(\frac{\sigma}{r}\right)^{12}+c_3\left(\frac{\sigma}{r}\right)^{6}+c_4\left(\frac{\sigma}{r}\right)^{-2}+c_5 & \text{for } 2.3\sigma < r \le 2.5\sigma \\ 0 & \text{for } r > 2.5\sigma, \end{cases} \qquad (7.14)$$

where $c_1 = 0.16132\epsilon$, $c_2 = 3.1366\times10^3\epsilon$, $c_3 = -6.8069\times10^1\epsilon$, $c_4 = 0.083312\epsilon$, and $c_5 = 0.74689\epsilon$ (see ref. [140]). For the perturbation-theory estimate of the inter-facial free energy, we use the full Lennard-Jones as the reference system. To compute its contribution, as

suggested by Weeks, Chandler and Andersen [137], we separate the LJ interaction potential in a repulsive term (hard-sphere-like, v_R)

$$v_R(r) = \begin{cases} \infty & \text{for} \quad r \leq 2^{1/6}\sigma \\ 0 & \text{for} \quad r > 2^{1/6}\sigma \end{cases} \tag{7.15}$$

and an attractive perturbation term (v_A)

$$v_A(r) = \begin{cases} -\epsilon & \text{for} \quad r \leq 2^{1/6}\sigma \\ 4\epsilon \left[\left(\frac{\sigma}{r}\right)^{12} - \left(\frac{\sigma}{r}\right)^{6} \right] & \text{for} \quad r > 2^{1/6}\sigma \end{cases} \tag{7.16}$$

To map the repulsive LJ system onto a hard -sphere system, we use the Barker-Henderson rule [142] to compute the equivalent hard-sphere radius of continuous repulsive potential:

$$\sigma_{HS} = \int_0^\infty [\exp^{-\beta v_R(r)} - 1] dr, \tag{7.17}$$

where σ denotes the effective hard-sphere diameter of particles interacting via the Lennard-Jones potential, and $\beta = \epsilon/(k_B T) = 1/T^*$ assuming ϵ and k_B equal to 1. As is obvious from eq. 7.17, σ_{HS} is a function of temperature, but not of the density. Calculating eq. 7.17 at $T^* = 0.617$, the temperature where Broughton and Gilmer computed γ, we find that $\sigma_{HS} = 1.032\sigma$. We then compute the LJ liquid-solid inter-facial free energy by adding to the hard-sphere term the perturbation coming from the attractive part of the potential, and estimate the inter-facial free energy of the TSF-LJ potential by including the perturbation terms computed according to eq.7.14.

Table 7.1 contains the values of the hard-sphere liquid-solid inter-facial free energy computed by Davidchack [143] (first column: in units of $[k_B T/\sigma_{HS}^2]$, second column: in units of $[\epsilon/\sigma^2]$); our estimate for γ based on the perturbation theory, assuming a step profile in the density (γ_{TSF-LJ}); at last, the numerical data for the TSF-LJ potential reported by Davidchack and Laird [141] and by Broughton and Gilmer [140]. As can be seen from the table, the perturbation-theory results are in rather good (2-3%) agreement with the numerical data. Interestingly, the variation of the surface free energy with the crystal face appears to be largely due to the corresponding variation in the hard-sphere reference system.

Below, we use the same approach to estimate the difference in surface free energy of various Lennard-Jones-like models (un-truncated, truncated and shifted, truncated and force-shifted). In this case, we do *not* use a hard-sphere reference system (as this system has no liquid-vapour interface). Rather we use the full (un-truncated) LJ system as our reference system.

7.3.2. Calculation of the liquid-vapour surface tension

According to the expressions given in the Method section, the correction to the full Lennard-Jones surface tension due to truncation and shifting of the potential (γ_{TS-LJ}) at $r_c = 2.5\sigma$ is of the order of $\gamma_{P1} + \gamma_{P2} = -0.75(\Delta\rho)^2$ (for a cut-off of $r_c = 2.5\sigma$). Considering the full Lennard-Jones as the reference system of our perturbation calculation, we summarise our

$\gamma_{HS}[k_BT/\sigma_{HS}^2]$[143]	$\gamma_{HS}[\epsilon/\sigma^2]$	γ_{TSF-LJ}	γ_{TSF-LJ}[141]	γ_{TSF-LJ}[140]
0.546	0.316	0.342	0.347(3)	0.35(2)
0.557	0.323	0.349	0.360(3)	0.36(2)
0.574	0.333	0.359	0.371(3)	0.34(2)
0.559	0.324	0.35	0.359	0.35

Table 7.1.: Liquid-solid inter-facial free energy of difference crystalline orientations for hard-sphere [143], present perturbation-theory estimate of γ_{TSF-LJ}, estimate of γ_{TSF-LJ} by Davidchack and Laird [141], estimate of γ_{TSF-LJ} by Broughton and Gilmer [140]. The first line represents the calculation at the [111] surface, the second at the [110], the third at the [100]. The bottom line of the table, is γ average over the different orientations.

resulting predictions for the truncated and shifted Lennard-Jones potential in the following tables, where we also show the numerical data, where available.

The data for the full (or "almost full") Lennard-Jones potential (table 7.3) are taken from Potoff and Panagiotopoulos [144], Errington [145], Trokhymchuk and Alejandre [146] (truncated Lennard-Jones with $r_c = 5.5\sigma$), Holcomb, Clancy and Zollweg [147](truncated Lennard-Jones with $r_c = 6.3\sigma$), Mecke, Winkelmann and Fischer [135](truncated Lennard-Jones with $r_c = 6.5\sigma$), and Nijmeijer, Bakker and Bruin [148] (truncated Lennard-Jones with $r_c = 7.33\sigma$). These data are all considered to be un-truncated, as the effect of truncation for these large values of r_c is negligible.

The data for the truncated and shifted Lennard-Jones potentials are taken from Haye and Bruin [149], Holcomb, Clancy and Zollweg [147], Nijmeijer, Bakker and Bruin[148], Trokhymchuk and Alejandre [146], Adams and Henderson [163] and Mecke et al. [135]. It is evident that the perturbation-theory with the sharp dividing surface estimate, that works well for the TSF-LJ liquid-solid interface, fails rather badly in the case of the liquid-vapour interface. Although the latter observation is not new, we have included tables 7.2-7.3, as they contain data that are rather scattered in the literature.

The data of table 7.2 have been plotted in fig. 7.3, where the full Lennard-Jones data from table 7.3 are fitted to a polynomial function. We estimate the surface tension as a function of $\Delta\rho = \rho_L - \rho_V$ (fig. 7.3) for the full Lennard-Jones potential ($T_c = 1.312$ ref.[151]), and for the truncated and shifted LJ potential ($T_c = 0.935$ ref. [152]).

The figure clearly shows that the step-profile perturbation theory estimate is not particularly accurate and gets worse as we approach the critical temperature: so much so that for small $\Delta\rho$, γ_{TS-LJ} would become negative. However, there is also considerable spread between the various numerical data. It has been noted before (already in ref. [153]) that the discrepancy between the discontinuous-interface approximation and the simulation results is due to the fact that the L-V interface gets more and more diffuse as T_c is approached. The step-profile approximation is then not justified (see ref. [134]).

$\Delta\rho$	ρ_l	ρ_v	T	γ_{LJ}	γ_{TS-LJ}	Source
0.46±0.02	0.5794	0.1030	1.0	-	0.082±0.008	[146]
0.46±0.02	0.5694	0.0987	1.0	-	0.076±0.002	[149]
0.46±0.02	0.565	0.103	1.0	-	0.088±0.007	[148]
0.46±0.02	0.580	0.100	1.0	0.124±0.001[a]	-0.004 [d]	
0.55±0.02	0.6213	0.0068	0.95	-	0.154±0.003	[149]
0.55±0.02	0.618	0.0068	0.95	0.224±0.001[b]	-0.003 [d]	
0.59±0.01	0.6505	0.0518	0.92	-	0.197±0.016	[146]
0.59±0.01	0.645	0.055	0.94	0.343±0.002[c]	0.08 [d]	
0.62±0.02	0.6619	0.0454	0.90	-	0.223±0.003	[149]
0.62±0.02	0.662	0.0439	0.90	-	0.224±0.009	[148]
0.62±0.02	0.671	0.040	0.90	-	0.23±0.02	[163]
0.62±0.02	0.6644	0.0444	0.90	-	0.227±0.016	[146]
0.62±0.02	0.666	0.046	0.90	0.46±0.03[a]	0.17 [d]	
0.67±0.03	0.6973	0.0307	0.85	-	0.303±0.003	[149]
0.67±0.03	0.706	0.027	0.85	-	0.29±0.07	[163]
0.67±0.03	0.699	0.029	0.745	0.56±0.02[a]	0.22 [d]	
0.71±0.01	0.7306	0.0196	0.80	-	0.408±0.018	[146]
0.71±0.01	0.7315	0.195	0.80	-	0.39 ±0.01	[148]
0.71±0.01	0.731	0.02	0.80	-	0.39 ±0.07	[163]
0.71±0.01	0.7287	0.02	0.80	-	0.388 ±0.04	[149]
0.71±0.01	0.730	0.020	0.75(0.705)	0.61±0.01[a]	0.23 [d]	
0.74±0.01	0.7580	0.0132	0.75	-	0.480±0.003	[149]
0.74±0.01	0.761	0.014	0.75	-	0.46±0.05	[163]
0.74±0.01	0.754	0.0142	0.75	0.679[b]	0.27 [d]	
0.77±0.01	0.7749	0.0088	0.72	-	0.544±0.018	[146]
0.77±0.01	0.777	0.009	0.72	-	0.55	[147]
0.77±0.01	0.7764	0.0093	0.72	-	0.55 ±0.01	[148]
0.77±0.01	0.787	0.006	0.72	-	0.57 ±0.04	[163]
0.77±0.01	0.777	0.007	0.72	0.837±0.002[c]	0.39 [d]	

Table 7.2.: Comparison with literature data for the surface tension of various Lennard-Jones models for $0.42 \leq T^* \leq 0.62$. $\Delta\rho$ (in reduced units) is the density difference between ρl (liquid) and ρv (vapour). T is the temperature for each $\Delta\rho$. $\gamma_{TS-LJ} = \gamma_{LJ} + \gamma_{LR1} + \gamma_{LR2}$. The numerical data for γ of the full Lennard-Jones potential come from ref.[144] (super-script a) ref.[146] (super-script b), and [145] (super-script c). Our data are indicated by in super-script d.

7.4. Conclusions

Concerning the computation of the liquid-solid inter-facial free energy, we think that the agreement found between simple perturbative calculations and simulations might be caused

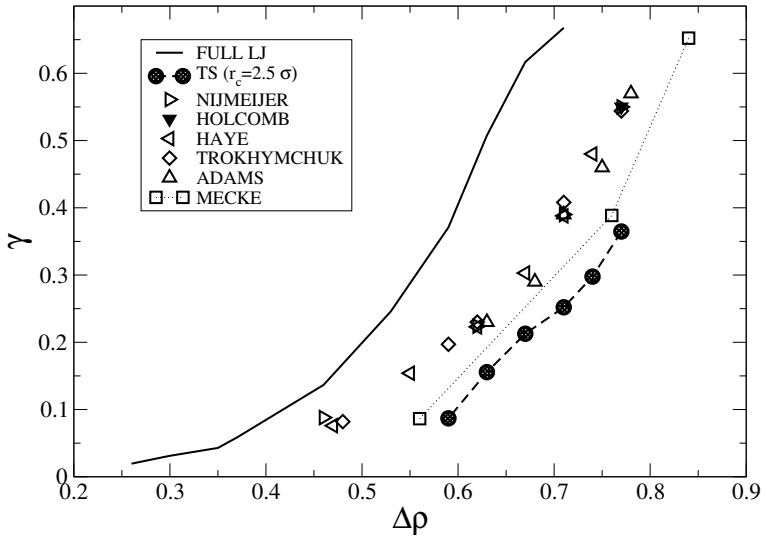

Figure 7.3.: Surface tension as a function of the liquid-vapour density difference for a truncated and shifted Lennard Jones at $r_c = 2.5\sigma$. The perturbation-theory estimates for the TS-LJ model are represented by filled , and obtained considering the full Lennard-Jones as the reference system. The simulation data are represented as follows: ref. [149] ($\triangleleft$), ref .[147] ($\bigtriangledown$), ref. [148] ($\triangleright$), ref. [146] ($\Diamond$), and ref. [163] ($\bigtriangleup$).

by some cancellation of errors - on one side, an assumption of a infinitely sharp interface (typically, the dividing surface is about one particle diameter thick), and, on the other side, the disregard of the dense liquid layering in proximity of the interface with the solid.

However, in the liquid-vapour case, the perturbation theory approach with the sharp interface seems to be too simplistic, possibly due to the fact that for liquid and vapour at coexistence, the interface is fairly rough and not well defined, especially close to the critical point. In view of the rather poor performance of the perturbation-theory estimate for the liquid-vapour interface, the success in the case of the liquid-solid interface is encouraging and, in fact, somewhat surprising.

Acknowledgements

Concerning this work, I would like to thank F. Diotallevi and K. Shundyak for very helpful discussions and a critical reading of this chapter.

$\Delta\rho$	ρ_l	ρ_v	T	γ_{LJ}	Source
0.165	0.401	0.236	1.310	0.0000786	[144]
0.187	0.412	0.225	1.305	0.0019575	[144]
0.211	0.424	0.213	1.300	0.00429	[144]
0.217	0.4271	0.2096	1.300	0.005	[145]
0.234	0.436	0.202	1.295	0.0068635	[144]
0.256	0.447	0.191	1.290	0.009933	[144]
0.276	0.458	0.182	1.285	0.0132355	[144]
0.295	0.468	0.173	1.280	0.017408	[144]
0.31	0.476	0.166	1.275	0.019635	[144]
0.323	0.483	0.160	1.270	0.024638	[144]
0.334	0.488	0.154	1.265	0.03036	[144]
0.348	0.497	0.149	1.260	0.036288	[144]
0.368	0.509	0.141	1.250	0.04875	[144]
0.4644	0.564	0.0996	1.200	0.1236	[144]
0.5311	0.605	0.0739	1.150	0.21965	[144]
0.5484	0.6147	0.0663	1.127	0.224	[146]
0.5646	0.6236	0.059	1.100	0.2853	[135]
0.586	0.6410	0.05485	1.100	0.343	[145]
0.587	0.642	0.055	1.110	0.33855	[144]
0.6316	0.672	0.0404	1.050	0.462	[144]
0.6631	0.694	.0309	1.000	0.45	[146]
0.6716	0.701	0.0294	1.000	0.56	[144]
0.709	0.730	0.0210	0.950	0.608	[144]
0.715	0.7358	0.0208	0.920	0.629	[146]
0.721	0.739	0.018	0.920	0.61	[147]
0.722	0.740	0.018	0.920	0.63	[148]
0.7311	0.7458	0.0147	0.900	0.679	[146]
0.7608	0.7698	0.009	0.850	0.7527	[135]
0.7664	0.776	0.009611	0.850	0.837	[145]
0.7875	0.7927	0.0052	0.800	0.854	[146]
0.8235	0.8254	0.0019	0.720	1.042	[146]
0.8355	0.8375	0.002	0.700	1.075	[135]
0.84	0.8424	0.001992	0.700	1.182	[145]

Table 7.3.: Liquid-vapour surface tension in reduced units as a function of temperature and reduced density difference for the full Lennard-Jones ($T_c = 1.312$ [151]). The data are taken from: Potoff and Panagiotopoulos [144] (here we express the surface tension in reduced units), Holcomb, Clancy and Zollweg [147](truncated Lennard-Jones with $r_c = 6.3\sigma$), Nijmeijer, Bakker and Bruin,[148] (truncated Lennard-Jones with $r_c = 7.33\sigma$), Trokhymchuk and Alejandre [146] (truncated Lennard-Jones with $r_c = 5.5\sigma$), Errington [145] and Mecke, Winkelmann and Fischer [135](truncated Lennard-Jones with $r_c = 6.5\sigma$).

Appendix A: Comparison with Fowler's expression

Recently, Mulero et al.[154] considered the Fowler's formula [132] of the liquid-vapour surface tension including also the contribution of the vapour density:

$$\gamma = \frac{\pi(\rho_L - \rho_V)^2}{8} \int_0^\infty r^4 u^{'} g(r) dr \tag{7.A.1}$$

this corresponds to the Fowler's expression with the Laplace approximation of a sharp interface, and it is also equivalent to the result obtained by Rowlinson and Widom [130] for $\rho_V = 0$. By means of the mean field approximation, that considers the liquid homogeneous on the length scale of the potential, ($g(r) = 1$), it is possible to recover the Laplace's equation for the surface tension, as shown in Rowlinson and Widom [130].

Considering only the $(\sigma/r)^6$ term in the Lennard-Jones potential, it is also possible to compute the tail corrections for a truncated and shifted potential at a certain cut-off r_c, by integrating from r_c to infinite eq. 7.A.1 with the above-mentioned approximations, obtaining :

$$\gamma_{tail} = \frac{3}{2}\pi(\Delta\rho)^2 \frac{\epsilon}{r_c^2} \tag{7.A.2}$$

Hence, for $r_c = 2.5\sigma$, eq. 7.A.2 becomes $\gamma_{tail} = 0.75(\Delta\rho)^2$.

At this point, we want to demonstrate that our calculations recover eq. 7.A.2, that is also the zero thickness limit of Blokhuis's expression [134]. We start by describing Blokhuis's equation for the liquid-vapour surface tension of a flat interface of a truncated and shifted Lennard-Jones potential. Blokhuis used the Kirkwood-Buff[131] expression for the surface tension

$$\begin{aligned} \gamma &= \frac{1}{4}\int_{-\infty}^{\infty} dz_1 \int d\mathbf{r}\ \ u^{'}(r) r (1 - 3s^2) \rho^{(2)}(z_1, z_2, r) \\ &= \frac{\pi}{4}(\rho_L - \rho_V)^2 \int_{-1}^{1} ds \int_0^\infty dr\ \ u^{'}(r) r^4 (3s^3 - s) g(r) \coth\left(\frac{sr}{2\xi}\right), \end{aligned} \tag{7.A.3}$$

where $\mathbf{r} \equiv |\mathbf{r_1} - \mathbf{r_2}|$, $s \equiv \cos\theta_{12}$, $z_2 \equiv z_1 + sr$, $u^{'}(r)$ is the derivative of the potential, and ξ is the thickness of the interface. The second equation is obtained from the first integrating over z_1, after approximating the pair density by the product of the density and the pair correlation function in the uniform liquid, assuming $g(r) \sim 1$, the first derivative of the potential equal to $24r^{-7}$ in Lennard-Jones units (neglecting the repulsive part of the potential), and the density profile through the inter-facial region with a $\tanh$ profile with finite thickness. Performing the integration in eq. 7.A.3 over r from the cut-off r_c in case of a Lennard-Jones interaction

$$\gamma_{tail} = 12\pi(\rho_L - \rho_V)^2 \int_0^1 ds \int_{r_c}^\infty dr \left(\frac{1}{r}\right)^3 (3s^3 - s) \coth\left(\frac{2sr}{\xi}\right) \tag{7.A.4}$$

that is Blokhuis's expression for the tail corrections of the truncated Lennard-Jones interaction potential. Considering the limit of zero thickness, eq. 7.A.4 recovers the result in eq. 7.A.2.

We now show that our calculations of the tail corrections correspond to eq. 7.A.2 (and therefore eq. 7.A.4). Computing the contribution due to the overall perturbation by means of our analytical calculation we obtain: γ_{P1}+γ_{P2}=-0.75 $(\Delta\rho)^2$ perfectly matching the absolute value of the previous result. Our result has the opposite sign as Blokhuis's one, as we have slightly different approaches.

1. We compute the tail correction for the surface free energy.
2. We add it to the reference system;

while Blokhuis and Mecke

1. compute the surface free energy for the truncated potential, and
2. add the tail corrections in order to recover the surface free energy for the full Lennard Jones.

We underline the fact that in our analytical approach we do not assume *a priori* the nature of phase 1 and 2.

8. Homogeneous Bubble Nucleation in the Lennard-Jones fluid.[1]

Katanga, la cinese frusciante.
Italian imagination.

We present a numerical study of homogeneous bubble nucleation in a super-heated Lennard-Jones liquid. For the first time, we employ Forward Flux Sampling in combination with a Molecular Dynamics simulation to estimate the rate of bubble nucleation and investigate its pathway. In contrast to earlier work by Shen and Debenedetti [155], we find that explosive boiling starts with compact, rather than with ramified bubbles. We find that the bubble-nucleation rate coincides with the one expected on the basis of Classical Nucleation Theory, assuming the surface tension γ equal to 0.08. However, the CNT result is extremely sensitive to the precise value of the surface tension of the bubble. Hence, a precise value of γ for the truncated potential used is needed in order to make a correct comparison.

8.1. Introduction

Anyone who has ever sprinkled water droplets into a pan with hot frying oil is familiar with the phenomenon of explosive boiling: the liquid water will be heated far above its equilibrium boiling point before the vapour phase nucleates suddenly and violently. As this example illustrates, explosive boiling is very common, and usually undesirable in practical situations. In addition to explosive boiling itself [156], application areas include the study of cavitation erosion [157], sonochemistry [158] and the design of high-efficiency heat exchangers [159]. In spite of the practical relevance of these phenomena, the mechanism by which the vapour phase nucleates in a homogeneous, super-heated liquid is still under debate. The standard model to describe bubble nucleation is based on Classical Nucleation Theory (CNT). In 1975, Blander and Katz [160] wrote a review on this topic in which they concluded that the measured bubble-nucleation rates of a large number of organic compounds were consistent with the prediction of Classical Nucleation Theory (CNT) [161, 162, 6]. However, the picture is not always that simple. Bubble nucleation in $n-nonane$ (C_9H_{20}) was investigated using a variety of different techniques: fast expansion cloud chamber [163], two-piston cloud chamber [164] and upward thermal diffusion cloud chamber [165]. The resulting rates extended over 14 order of magnitudes, from 10^{-4} to 10^{10} cm^{-3} s^{-1}. The analysis of Hung

[1] Work carried out in collaboration with Z.J. Wang.

et al. [164] showed that CNT failed to predict the temperature dependence of the bubble nucleation rate, yet correctly predicting the variation of nucleation rate with super-saturation. The same observation applies to bubble nucleation in water [166, 167], toluene [168], and n-alcohols [169, 170]: the predicted CNT nucleation rates were too low at low temperatures, and too high at high temperatures, with error bars of several orders of magnitude.

As bubble nucleation is a rare event, its mechanism depends crucially on the processes that lead to the formation of microscopic "embryonic" bubbles that can subsequently grow to macroscopic size. Unfortunately, at this stage there are no experiments that probe the incipient bubbles directly, although such experiments should be possible in colloidal systems. In recent years, theory and numerical simulation have proved to be valuable tools to explore the microscopic and initial phases of nucleation phenomena, both for coalescence [103] and for cavitation [155] . Zeng and Oxtoby [171] studied the liquid-to-vapour phase transition in a Lennard-Jones fluid by means of Density Functional Theory, and found that CNT underestimated the nucleation rate by more than 15 orders of magnitude. Classical Nucleation Theory has been widely criticised in the past. On the one hand, Oxtoby and co-workers [172] pointed out the fact that CNT, based on the capillary approximation, ignored the effect of curvature on the surface free energy. On the other hand, both Cahn and Hilliard [69, 173] and Oxtoby and Evans [7] illustrated the failure of the theory in predicting a finite barrier while approaching the spinodal curve- a topic that remains controversial to this day [174]. Delale et al. [175] attempted to derive the minimum work of bubble formation in a phenomenological way, using the data of the experimental super-heating. With this phenomenological approach they then estimated the steady-state bubble nucleation rate, and found the same discrepancy between computed and measured rates already observed when comparing the nucleation rates with the CNT predictions. More recently, Shen and Debenedetti [155] reported the first direct Monte Carlo simulations to estimate the free-energy barrier for bubble nucleation in a simple model system (truncated and shifted Lennard-Jones potential). These authors computed the free-energy barrier using Umbrella Sampling. The progress of the bubble nucleation was monitored using a global order parameter based on the density of the system. A geometric analysis of the resulting vapour phase suggested that the critical cluster had a web-like, system-spanning structure rather than a spherical shape as CNT would predict. This finding is puzzling, as nucleation is expected to be a highly localised event.

The work reported in the present chapter was prompted by the findings of ref. [155]. However, rather than using the Umbrella Sampling scheme (which, after all, makes assumptions about the quasi-equilibrium and Markovian nature of the nucleation process), we decide to study bubble nucleation of the same truncated force shifted Lennard-Jones potential, using Forward Flux Sampling, a technique also suited to simulate nucleation events proceeding in a distinctly non-equilibrium manner.

8.2. Simulation details

To follow the process of bubble nucleation, we simulate a system consisting of 3375 particles interacting via a truncated and force-shifted (TSF) Lennard-Jones potential:

$$v_{TSF}(r) = v_{LJ}(r) - v_{LJ}(r_c) - \left|\frac{dv_{LJ}}{dr}\right|_{r_c} (r - r_c). \tag{8.1}$$

where v_{LJ} denotes a 12-6 Lennard-Jones potential truncated at $r_c = 2.5\sigma$ (σ is the particle diameter), the second term ensures the continuity of the potential and the third term the continuity of its first derivative at r_c. The reason to use a truncated and shifted potential, rather than the full LJ potential is related to the fact that, when a bubble nucleates, the system becomes spatially inhomogeneous: this does not allow the use of energy and pressure tail corrections, employed when simulating a a homogeneous system. We equilibrate this system using constant-NPT Molecular Dynamics simulations with a Nosé thermostat [176, 70] and an Andersen barostat [177] (see appendix A) [1]. In order to integrate the equations of motion, we use a leap-frog algorithm [178]. The integration time step is fixed at $\delta t^* = 0.00046$: using the Lennard-Jones parameters for Argon, this corresponds to a time-step of 1 femto-second. In our simulations, we adopt periodic boundary conditions. As a test of our MD code, we first reproduce the (known) liquid-vapour phase diagram of the TSF-LJ model (see appendix B and ref. [152]). In what follows, we express all variables in Lennard-Jones units; σ, m, ε, and $\sqrt{m\sigma^2/\varepsilon}$ are, respectively, the length, mass, energy, and time units, i.e. $r^* = r/\sigma$, $m^* = 1$, $e^* = e/\varepsilon$, and $t^* = t/\sqrt{m\sigma^2/\varepsilon}$.

When bubble nucleation happens, we expect that the volume of the simulation box expands quite rapidly, especially once the bubble size exceeds the "critical" value, growing essentially without bound. In our simulations we check for finite-size effects, to avoid spurious interactions of the bubbles with their own periodic images. The choice of the system size has to be balanced with the choice of the super-saturation, as if the super-saturation is too low, the critical bubble becomes too large, thus implying a large system, whereas if the super-saturation is too high, the system may become absolutely unstable: boiling does not proceed anymore through bubble nucleation but through spinodal decomposition. In order to get a rough estimate of the super-saturation, we make use of Classical Nucleation Theory. Assuming that the pressure in the critical bubble is the same as the vapour pressure at the imposed temperature, the critical bubble size is given by eq. 2.11, where the Laplace pressure is $\Delta P^* = P_V^*(T) - P^*$ with P^* the imposed pressure of the liquid and $P_V^*(T)$ the equilibrium vapour pressure at temperature T^*. Shen and Debenedetti [155] studied at the saturation pressure of $P^* = 0.046$, the same system at different super-heatings S (defined as S=$(T^* - T_{sat}^*)/T_{sat}^*$, where T_{sat}^* is the vapour-liquid coexistence temperature at the given pressure). Among others, ref. [155] considered S=9% , in which case CNT predicts a free-energy barrier height of about $20k_BT$. To accommodate a critical cluster in our 3375 particles system, we super-heat the system by the same amount as in ref. [155], but imposing

[1] To study bubble nucleation, we use Molecular Dynamics, as capturing the kinetics of the system is an important issue: the collective motions of the liquid particles may not be adequately reproduced in Monte Carlo simulations.

a lower saturation pressure, $P^* = 0.026$. At $P^* = 0.026$ the coexistence temperature is $T^*_{sat} = 0.785$. At $T^* = 0.785$ and $P^* = 0.026$, the equilibrium liquid and vapour densities are, respectively, $\rho^*_L = 0.668$ and $\rho^*_V = 0.043$. Therefore, we super-heat the liquid at constant pressure up to $T^* = 0.855$, that corresponds to $0.91T^*_c$ (where $T^*_c = 0.935$ estimated by Errington et al [152]) and to a super-saturation of S=9%. By super-heating the liquid up to $T^* = 0.855$ keeping the external pressure constant, the liquid density becomes $\rho^*_L = 0.58$. At the coexisting state point of $T^*_{sat} = 0.855$ and $P^*_{coex} = 0.046$, the liquid density is $\rho^*_L = 0.598$, and the vapour one $\rho^*_V = 0.083$.

In order to follow the progress of a bubble nucleation event, we compute the size (volume) of the biggest bubble present in the system, and use this quantity as the order parameter. As we impose a moderate super-saturation to the system, we assume that, at any given time, the system contains at most one very big bubble. Due to spontaneous density fluctuations happening in the system, there may be many regions where, locally, the density is low. Even though these fluctuations might not be important for the formation of a localised bubble, they do contribute to the total void volume in the system. Indeed, if we consider a very big simulation box, the local density fluctuations will completely dominate the total void volume. Shen and Debenedetti, in their study, employed a global order parameter based on the overall density of the system. However, as it was already pointed out by ten Wolde et al. [29], a global order parameter probes the total void volume, rather than the void volume concentrated in one bubble. Moreover, the entropic factors that favour a homogeneous distribution of void volume bubbles are indeed more pronounced for big systems.

In what follows, we describe the *step-by-step* procedure to identify vapour bubbles as the biggest domain of low-density (*non-liquid-like*) volume:

1. following the approach of ref. [179], we superimpose a three-dimensional grid with unit cell mesh of $(0.5\sigma^{*3})$ on the system;

2. as in ref. [180], we use Stillinger's cluster criterion [181] to identify all the nearest neighbours j of each particle i. A particle j is considered to be a neighbour of a given particle i if it is located within a cut-off distance of $r^*_c = 1.6$, that corresponds to the first minimum of the radial distribution function of the liquid. Using this criterion, we compute the probability distribution of the number of neighbours of each particle N in both the liquid and the vapour phases;

3. we identify a particle as *liquid-like* if it has more than five neighbours. This choice of this threshold is dictated by the fact that essentially all vapour-like particles have less neighbours than the liquid-like ones (see fig. 8.1);

4. we define a spherical volume with radius r^*_c around every liquid-like particle: all grid cells that are included in a sphere with radius r^*_c around a liquid-like particle are labelled as "liquid";

5. the grid cells that are not identified as *liquid-like* constitute the *vapour-like* volume;

6. we now perform a cluster analysis on the vapour-like cells: bubbles are defined as compact clusters of vapour-like cells;

7. finally we select the biggest bubble;

8. once we have the biggest bubble, the order parameter that measures the bubble nucleation process is defined as the volume of the biggest bubble W_b, expressed in units of $\Delta V^* = 0.1{\sigma^*}^3$.

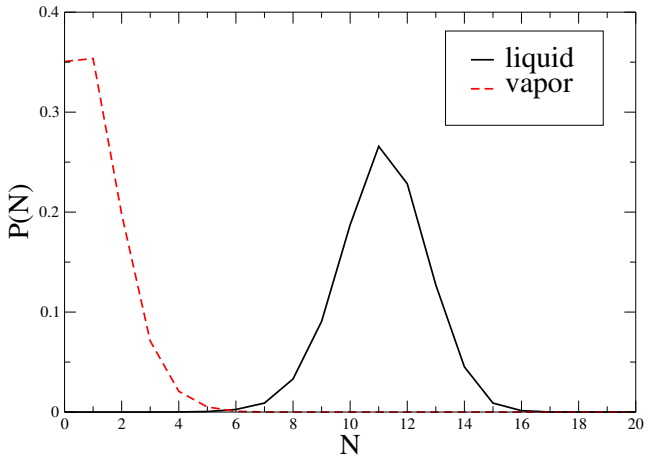

Figure 8.1.: Probability distribution of the number of neighbours N for both liquid and vapour at coexistence $T^* = 0.785$ and $P^* = 0.026$. Two particles are neighbours whenever their distance is smaller than $r_c^* = 1.6$.

In our simulations, we use the Forward Flux Sampling (FFS) technique (already introduced in chapter 2) to study the cavitation phenomenon: by means of FFS, we measure the bubble nucleation rate and analyse the pathways to nucleation at $T^* = 0.855$ and $P^* = 0.026$. To our knowledge, the present study is the first example where FFS is used in combination with a Molecular Dynamics simulation. The FFS technique can only be used for systems that present a time evolution at least partially stochastic. A normal Molecular Dynamics (NVE ensemble) simulates deterministic events, thus unsuited to be used together with FFS. In the present work instead, we use constant NPT Molecular Dynamics simulations, and employ the stochastic nature of the thermostat. In particular, together with a Nosé thermostat, we combine a Lowe-Andersen thermostat as a noise generator [182]. In doing so, we ensure a "tunable" dynamical instability in the evolution of the trajectories in the phase space [183], whilst preserving a realistic dynamics of the system, obtained by monitoring the diffusion coefficient with and without the noise generator, and tuning the thermostat parameters in order not to affect the diffusivity of the system (see appendix C).

8.3. Results

As mentioned above, at $T^* = 0.855$ and $P^* = 0.026$, the average density of the metastable liquid is $\rho_L^* = 0.58$, thus the average volume of the 3375 particles system is $V^* = N/\rho_L^* \sim 5820$. We locate the boundary of the metastable liquid basin at $W_b = 25$ and collect $O(10^2)$ configurations at this interface. The complete set of location of the interfaces at $T^* = 0.855$ and $P^* = 0.026$ is:

i	$(W_b)_i$	M_i	i	$(W_b)_i$	M_i	i	$(W_b)_i$	M_i
1	25→ 37	100	6	180→ 240	25	11	700→ 820	10
2	37→ 57	100	7	240→ 300	20	12	820→ 950	11
3	57→ 92	100	8	300→ 400	15	13	950→ 1200	10
4	92 → 120	60	9	400→ 550	15	14	1200→ 1900	10
5	120→ 180	30	10	550→ 700	12	15	1900	3500

Table 8.1.: Position of the interfaces and number of trials per interface for the FFS sampling of the Lennard-Jones cavitation study.

We fix the boundary of the stable vapour state at W_b =3500, a value where the probability a bubble is committed to completely phase transform and fill the system is almost one. We estimate that the critical bubble has size W_b around 950. However, there is a considerable variation in the sizes of the critical bubbles. In our simulations, we do not allow the bubble to grow bigger than W_b =3500, as this would correspond to infinitely large an expansion of the box size.

We compute the bubble nucleation rate at $T^* = 0.855$ and $P^* = 0.026$ to be $R = 9 \times 10^{-15\pm1}\sigma^{*-3}\tau^{*-1}$, in CGS units (assuming the Lennard-Jones parameters for Argon) $R = 10^{19}\text{cm}^{-3}\text{s}^{-1}$. We cannot directly compare these numbers with experimental data for Argon. However, we note that the computed bubble-nucleation rate is much higher than the one measured experimentally for a number of volatile organic liquids at $0.89T_c^*$. For these systems, Blander and Katz [160] reported a bubble nucleation rate of the order of $10^4 - 10^6\text{cm}^{-3}\text{s}^{-1}$.

Comparison with Classical Nucleation Theory

A CNT-based theoretical estimate of the bubble nucleation rate was given by Katz (eq. 12 in ref. [30]):

$$R_{CNT} = N\left[\frac{2\gamma}{\pi m B}\right]\exp -\beta\Delta G, \tag{8.2}$$

where the pre-factor ($N\left[\frac{2\sigma}{\pi m B}\right]$) contains the number density of the liquid (N) and the Zeldovitch factor ($\left[\frac{2\sigma}{\pi m B}\right]$), m is the mass of a molecule, γ the liquid-vapour surface tension, and B a term that takes into account the mechanical equilibrium of the bubble: in cavitation experiments, B is always equal to unity. $\beta\Delta$ G is the free-energy barrier to form a critical bubble, assumed to be spherical: $\frac{-16\pi\gamma^3}{3[P_V - P_L]^2}$, where $P_V - P_L$ is the Laplace pressure.

As a first approximation, we consider the value of the liquid-vapour surface tension computed for the truncated and shifted Lennard-Jones potential by Haye et al. [149] at the same $\Delta\rho^* = \rho_L^* - \rho_V^* = 0.54$ as our simulations : $\gamma^* = 0.154$, even though this value of the liquid-vapour surface tension over-estimates the γ^* of the interaction potential we use, thus of the free-energy barrier. Nevertheless, computing the free-energy barrier by means of CNT, we obtain $\beta\Delta G \sim 180$ and $R_{CNT} \sim O(10^{-81})\sigma^{*-3}\tau^{*-1}$. However, if we assume a value of γ^* around 0.08, we get $\beta\Delta G \sim 25$ and a nucleation rate comparable with the one computed by means of FFS, $R_{CNT} \sim O(10^{-12})\sigma^{*-3}\tau^{*-1}$.

Bubble nucleation pathways

Figure 8.2 shows a generic pathway we observe in the bubble nucleation simulations, from a super-heated liquid at $T^* = 0.855$ and $P^* = 0.026$: the top left snapshot is the initial stage of the bubble, while the bottom right snapshot is the critical bubble corresponding to the top of the free-energy barrier. The growing bubble does not exhibit a ramified, system-spanning structure, not even the critical bubble. In this respect, our findings differ qualitatively from those reported in ref. [155]. We speculate that, on the one hand, the percolation of the vapour phase observed by the authors is the result of the use of a global order parameter. On the other hand, we believe the authors were fairly close to the critical point, thus inducing a spinodal instability to the system. Their chosen super-saturation was around 9% at $P^* = 0.046$, where the coexistence temperature is $T^*_{sat} = 0.855$. Therefore the temperature where the authors studied the nucleation phenomenon was $T^* = 0.93$, very close to T^*_c. Even though our results seem promising, we have to point out a possible drawback of our "local" order parameter. It can happen that a bubble is formed by two sub-bubbles attached by a narrow *non-liquid-like* volume (only one or two grid cells). This results in sudden jumps of W_b (see fig. 8.3 top and bottom). However, as the Forward Flux Sampling technique does not depend on the choice of the order parameter, we believe this effect should not compromise the calculation of the rate.

8.4. Conclusions and future work

Using Forward Flux Sampling and the volume of the biggest bubble as a local order parameter, we have studied cavitation in a Lennard-Jones liquid. We have compared the computed bubble-nucleation rate with the value estimated using CNT. In order for the simulations and the CNT prediction to match, we have to assume a value for the surface tension of the TSF-LJ fluid a relatively low value of the surface tension. However, an exact calculation of γ^* is needed for a precise comparison.

We have observed that nucleation takes place via the formation of compact bubbles. In contrast, Shen et al.[155] observed the formation of ramified, percolating void spaces. We argue that this discrepancy may be partly due to the use of a global order parameter in ref. [155] and, more pertinently, that the simulations in ref. [155] were carried out at a state point that is very close to the liquid-vapour spinodal of the FTS-LJ model.

Analysing the nucleation pathways, we have observed that the bubbles are fairly compact.

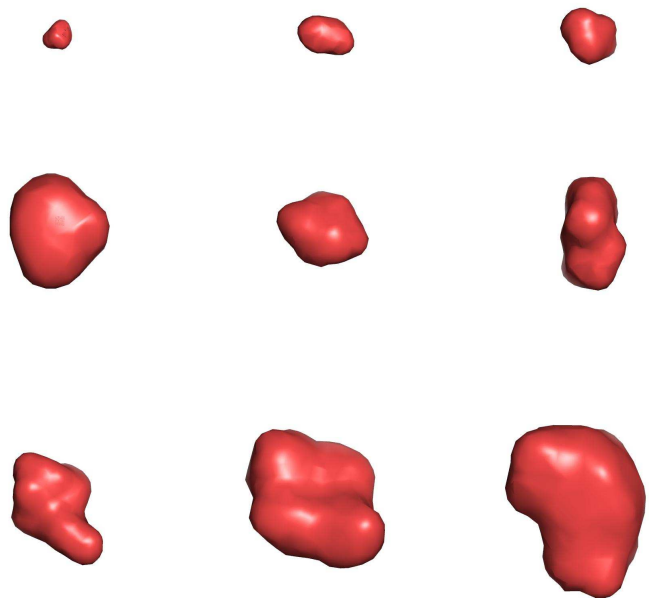

Figure 8.2.: Nucleation pathway of the growing biggest bubble from a super-heated liquid at $T^* = 0.855$ and $P^* = 0.026$. The bottom right snapshot is the bubble corresponding to the top of the free-energy barrier, i.e. the critical cluster.

However, we have also detected bubbles with different topologies (work in progress), proving that small bubble are strongly fluctuating objects. We plan to attempt a systematic characterisation of the topology of the bubbles, as we believe it might play an important role in the cavitation process.

In addition, we also think that the propensity to nucleate a bubble is related to the local structure of the liquid. However, if we consider the reverse process, bubble collapse – in particular in the extreme case of sonoluminescence – we should expect that the local temperature at the site of an emerging bubble may have a strong influence on the propensity for bubble nucleation. Further work is needed to clarify this issue.

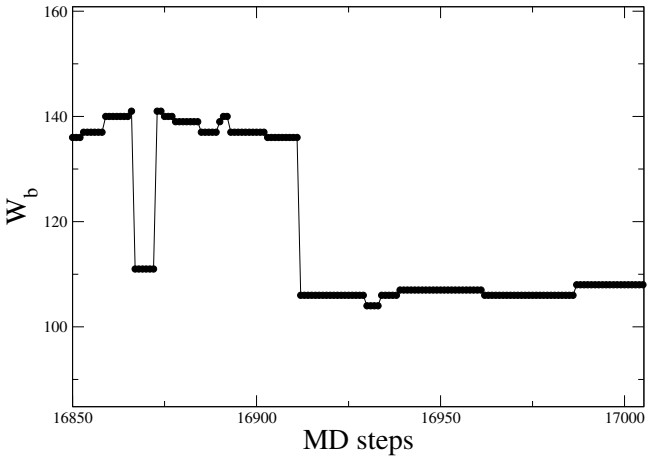

Figure 8.3.: Fluctuations of the order parameter as a function of MD time steps for a generic FFS-interface at $T^* = 0.855$ and $P^* = 0.026$. The " nonphysical" effect due to due anomalous conformation of the bubble, made of two sub-bubbles attached by a narrow *non-liquid-like* volume, results in a jump of W_b.

Acknowledgements

Concerning this work, I would like to Z. Wang for a careful reading of the chapter.

Appendix A: Details on the thermostat and the barostat

In our Molecular Dynamics simulations we choose a time step of $\delta t^* = 0.00046$. To select reasonable relaxation times for both the thermostat and barostat in our NPT ensemble, we perform different trial runs at different temperatures and pressures. On the basis of the results of these runs, we select $\tau_T^* = 0.093$ for the thermostat and $\tau_P^* = 1.39$ for the barostat. Fig. 8.A.1 illustrates the (kinetic) temperature fluctuations and the (virial) pressure fluctuations in the Lennard-Jones fluid during an NPT simulation using the above-mentioned relaxation times, with $\langle T^* \rangle = 0.9$ and $\langle P^* \rangle = 0.064$. In order to choose the proper mass of the

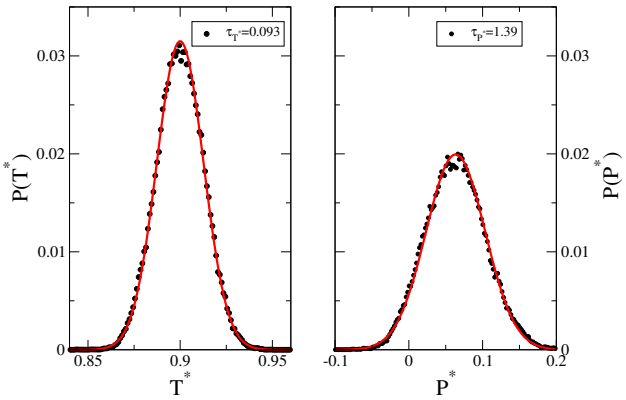

Figure 8.A.1.: Fluctuations distribution of both thermostat (on the right-hand side) and barostat (on the left-hand side) (dotted line), compared to a Gaussian distribution with the same width (continuos line).

piston, we accord the volume fluctuations in the system on a time scale of around 1 ps, that corresponds to the simulation box edge ($V^{*1/3}$) divided by the speed of sound in the liquid (900÷1500 m/s at room temperature) [177].

Appendix B: TSF-LJ liquid-vapour phase diagram

It is well known that many thermodynamic properties depend sensitively on the details of the long-range part of the potential. A truncation of the full Lennard-Jones interaction potential can severely affect both the location of the critical point and the value of the surface tension.

The location of the critical point in a Lennard-Jones system was studied by several authors using a combination of theory and computer simulation. For the full Lennard-Jones, a prediction of the critical point based on the equation of state by Nicolas et al. [184] and Levesque et al. [185], resulted in a critical temperature of T_c^*=1.35 and a critical density of ρ_c^*=0.35. However, by fitting Nicolas's results to a density scaling law, and assuming the three-dimensional

Ising critical exponent ($\beta = 0.32$), Smit obtained T_c^*=1.316 and ρ_c^*=0.304 [186] . More recently, Potoff and Panagiotopoulos, using the histogram re-weighting method and mixed-field-finite-size-scaling techniques within a Grand Canonical Monte Carlo simulations, obtained T_c^*=1.312 and ρ_c^*=0.316 [151]. Wilding [187], with the same techniques as Potoff but imposing a truncation at $r_c = 2.5\sigma$, computed T_c^*=1.19 and ρ_c^*=0.32.

The truncated but un-shifted Lennard-Jones critical point at $r_c = 2.5\sigma$, was estimated by Finn and Monson via an isobaric-isothermal Monte Carlo scheme [188]: they corrected the full Lennard-Jones equation of state of Nicolas, because of the discontinuity of the potential in r_c and the absence of long tail corrections, and found T_c^*=1.23 and ρ_c^*=0.32.

The truncated and shifted Lennard-Jones critical point at $r_c = 2.5\sigma$ was estimated by Smit using Gibbs ensemble Monte Carlo and a version of the Nicolas equation of state, corrected for the long tail of the potential [186]: from his calculations, T_c^*=1.085 and ρ_c^*=0.317.

Smit and Frenkel [189] used Gibbs ensemble Monte Carlo simulations to show that in a two-dimensional Lennard-Jones system both the critical point and the overall shape of the liquid-vapour coexistence curve, was strongly dependent on the long range part of the interaction. The same observations apply to the three-dimensional Lennard-Jones system [186]. The overall effect of truncation of the full Lennard-Jones potential is a (substantial) shift of T_c^* to lower temperatures.

By adding a truncation and shift of the forces to the Lennard-Jones potential (TSF-LJ), Errington et al. [152] computed the liquid-vapour phase diagram by means of Monte-Carlo simulations. Fig. 8.B.1 represents the liquid-vapour phase diagram for a Lennard-Jones sys-

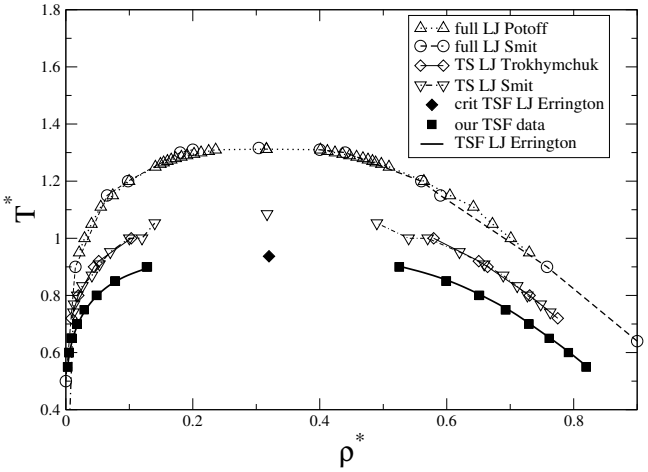

Figure 8.B.1.: Liquid-vapour phase-diagram in the temperature-density plane. The filled squares are our data, all other symbols are data from the literature of the full, truncated and shifted (TS) and truncated and force shifted (TSF) Lennard Jones.

tem: the full Lennard Jones data are from Potoff et al. [144] and Smit [186], the truncated and shifted Lennard-Jones at $r_c = 2.5\sigma$ from Smit [186] and Trokhymchuk et al. [146], and

the truncated-shifted-force Lennard Jones ($r_c = 2.5\sigma$) from Errington et al. [152]; in the same figure, we also plot our simulation data, perfectly matching Errington's results. From fig. 8.B.1 it is evident that truncation and shifting of the potential have a considerable effect on the phase behaviour and on the critical properties. In fig. 8.B.2, we plot the phase diagram in the pressure-temperature plane. The continuous line and the triangle (critical point) are from the Monte Carlo simulations in reference [152], while crosses and circles our data for the liquid and the vapour: the critical point being at $T^*_{c,TSF}$=0.937 and $\rho^*_{c,TSF}$=0.320.

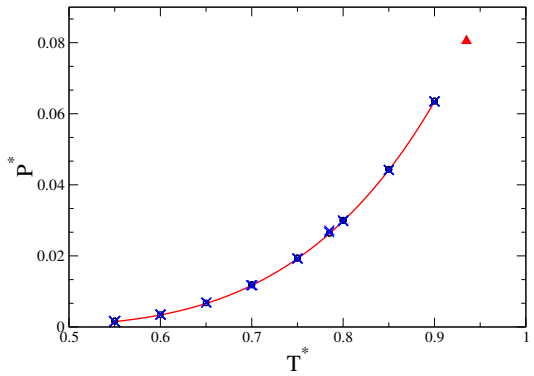

Figure 8.B.2.: Phase diagram of the TSF Lennard-Jones fluid in the pressure-temperature plane. Continuous line and triangle (critical point) are from ref. [152], while crosses and circles our data for the liquid and the vapour.

Appendix C: Lowe-Andersen thermostat and the FFS scheme

The Lowe-Andersen (LA) thermostat is a momentum conserving and Galilean invariant analog of the Andersen thermostat. It works as follows:

1. we compute the relative velocity between two particles, knowing each particle's velocity from the MD runs;
2. we extract from a Gaussian distribution a "new" relative velocity with probability $\nu^*\Delta t^*$ where Δt is the MD time step ($1fs$ in our case) and ν the LA tunable parameter indicating the strength of the coupling between the system and the thermostat [182]: the smaller the ν^*, the weaker the coupling;
3. we then compute the "new" velocity of each particle from the relative velocity.

ν^* is the tunable parameter of the LA thermostat: the dynamical properties of the system can be tuned by properly choosing ν^*. In fig. 8.C.1 we show the self-diffusion coefficient

computed for different values of ν^*: when $\nu^* \leq 100$, the diffusion of the system with the LA thermostat is indistinguishable from the one obtained in a system without this thermostat. In fact, there is little change in the diffusion coefficient as long as $\nu^* \leq 1000$. However, when $\nu^* \geq 10000$, the thermostat clearly affects the dynamics.

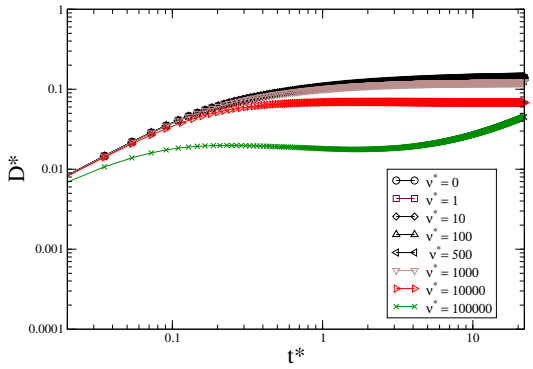

Figure 8.C.1.: Diffusion coefficients as a function of time. The ν^* corresponds to the curves from top to bottom.

In order to use the FFS combined with our Molecular Dynamics simulation, we need to generate stochastic trajectories. This means that, on the one hand we need to add enough "stochasticity" to the system to have a proper sampling of distinct trajectories, on the other hand, we need to keep the dynamics of the system close to Newtonian. We find that when $\nu^* = 500$ (see fig. 8.C.2), the stochasticity of the trajectories is sufficient to be used in FFS under the chosen thermodynamic conditions ($T^* = 0.855$ and $P^* = 0.026$), and the "real" dynamics of the system is preserved, as shown in fig. 8.C.1.

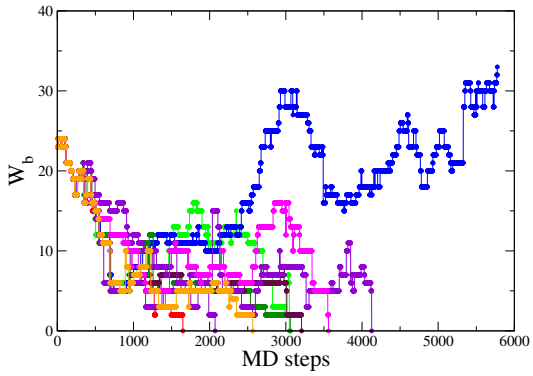

Figure 8.C.2.: Stochastic trajectories in W_b from the first to the second interface ($\nu^* = 500$).

Part VI.

The γ mystery

9. Irreducible finite-size effects in surface free energies from crystal-nucleation data[1]

Le orecchie degli elefanti.

In this chapter we report a simulation study in which we compare the liquid-solid inter-facial free energy of NaCl at coexistence with the value that follows from the height of the homogeneous nucleation barrier. We find that the two estimates differ by more than 100%.

Similar, although smaller discrepancies are found for crystals of hard-sphere colloids and of Lennard-Jones ("Argon") particles. We consider a variety of possible causes for this discrepancy and are forced to conclude that it is due to a finite-size effect that cannot be corrected for by any simple thermodynamic procedure. Importantly, we find that the surface free energies that follow from real nucleation experiments should be subject to large finite size effects. Taking this into account, we obtain quantitative agreement between the simulation data and the surface free energy of NaCl that follows from nucleation experiments. Our finding suggests that virtually all published liquid-solid surface free energies will have to be revised.

9.1. Introduction

The study of homogeneous crystal nucleation is of interest because it provides information about the pathway by which crystalline order emerges from the disordered parent phase. However, such experiments are also of considerable practical importance, as they are used to estimate the magnitude of the liquid-solid inter-facial free energy. Classical Nucleation Theory (CNT, see chapter 2) provides the route by which experimental nucleation rates are related to surface free energies. CNT relates the number of crystal clusters that form per second per cubic meter (denoted by R) to ΔG^*, the height of the free-energy barrier that has to be crossed to nucleate a crystal, as already shown in eq. 2.32. As already mentioned in chapter 2 (and eq. 6.1), CNT predicts the height of the nucleation barrier ΔG^* as a function of γ the liquid-solid surface free energy per unit area, $\Delta\mu$ the difference in chemical potential between the solid and the super-cooled liquid, and ρ_S the number density of the crystalline phase. As already discussed in chapter 6, c is a constant that depends on the shape of the

[1] Work carried out in collaboration with T. Zykova-Timan, E. Sanz and E. Tosatti.

cluster, e.g. $c = 16\pi/3$ for a spherical crystal cluster. As the nucleation rate depends exponentially on ΔG^*, the rate is a very sensitive function of the surface free-energy density γ.

A crucial assumption underlying CNT is that the bulk and surface properties of a small crystal cluster are the same as those of a macroscopic crystal. However, it has been long realised that this assumption is questionable, as a critical crystal cluster often contains only a few hundred molecules. Indeed, in his review on crystal nucleation, Kelton writes: "...while the precise meaning of [γ] is uncertain, it constitutes a parameter that can be determined for each element and profitably used to make predictions of the nucleation behaviour". In other words: the γ determined from nucleation experiments can only be used to predict the outcome of other nucleation experiments, thus severely limiting the predictive value of CNT. A similar conclusion about the limitations of CNT was drawn by Harrowell and Oxtoby [190] on the basis of their Density Functional Theory calculations of crystal nucleation barriers. Nevertheless, surface energies that derive from nucleation experiments are often used in the literature as if they pertain to macroscopic surfaces.

Increasingly accurate simulation techniques allow us to probe both the free energy of small clusters and the surface free energies of planar crystal-liquid interfaces. A case in point is the system NaCl in contact with its melt. Ref. [191] reports the surface free energy of a NaCl [100] interface in contact with the coexisting liquid phase: $\gamma \approx 36 \pm 6$ mJ m^{-2}. However, as already shown in chapter 4 and ref. [98], the effective surface free energy that follows from the NaCl crystal-nucleation barrier at 800 K is $\gamma = 80 \pm 1$ mJ m^{-2} assuming that the cluster has a cubic shape. In addition, nucleation experiments at 905K [77] provided an experimental estimate of $\gamma \approx 68$ mJ m^{-2}. Another example of a large difference between γ derived from the nucleation barrier and from coexistence data comes from hard-sphere colloids: a comparison of simulations at coexistence [192] and in the super-saturated regime [88] indicate that the value of γ estimated on the basis of the nucleation barrier is some 30% larger than the value for a planar interface at coexistence. A similar discrepancy ($\mathcal{O}(20\%)$) exists between the surface free energy for the planar interface and the crystal cluster of the (truncated and (force-)shifted) Lennard-Jones potential [140, 141, 100] (see table 7.1 in chapter 7).

It is clearly of considerable interest to understand the origin of the discrepancy between the nucleation data and the results for γ at coexistence, as this might facilitate the interpretation and analysis of experimental nucleation data. In what follows, we will indicate the liquid-solid inter-facial free-energy with γ_{LS}.

9.2. Simulation details

In this section, we report a systematic study of the finite-size effects in the surface free energy of NaCl crystals in contact with their melt. We choose this system because it shows the largest discrepancy of all examples listed above. As in refs. [191, 98] we use the Tosi-Fumi rigid-ion-pair interaction potential [81] to model the inter-ionic interactions in NaCl. In the first method we describe, the liquid-solid inter-facial free energy was obtained via the Young's equation by Zykova-Timan et al. [191]:

$$\gamma_{\mathrm{LS}} = \gamma_{\mathrm{SV}} - \gamma_{\mathrm{LV}} \cos\theta_{LV}, \tag{9.1}$$

where θ_{LV} is the contact angle at the interface between the liquid and the vapour, and $\gamma_{\rm SV}$, $\gamma_{\rm LV}$, $\gamma_{\rm LS}$ are, respectively, the solid-vapour, liquid-vapour and liquid-solid inter-facial free energies. To find $\gamma_{\rm LS}$, $\gamma_{\rm LV}$ and θ_{LV} the authors carried out Molecular Dynamics simulations. After having computed

1. $\gamma_{\rm LV}$ by means of the Kirkwood-Buff formula [131];
2. and $\gamma_{\rm SV}$ by means of thermodynamic integration;
3. they performed a computer experiments of spreading a liquid nanodroplet on the [100] NaCl solid surface in the vicinity of the melting point.

They observed that the droplet settled down on the surface forming a finite contact angle θ_{LV} of ($50^\circ \pm 5^\circ$); by substituting in eq. 9.1 θ_{LV}, $\gamma_{\rm LV}$ is then 104 mJ/m^2 and $\gamma_{\rm SV}$ is 103 mJ/m^2. Thus $\gamma_{\rm LS}$=(36$\pm$6) mJ/m^2, an unusually large value for the liquid-solid inter-facial free energy in comparison with other materials [193], that the authors justified because of the large differences between the NaCl solid and liquid bulk properties (see ref.[18]).

In the second method, already discussed in chapter 4 the estimation of the liquid-solid inter-facial free energy based on the cluster analysis, is developed by means of Monte Carlo simulations of the same model potential. We equilibrate a system of $(12)^3$ NaCl ion pairs in an NPT ensemble at 1 atm and three different temperatures: $T_1 = 800$ K, $T_2 = 825$ K and, differently from chapter 4, also at the coexistence temperature $(1060 \pm 10)\ K$. $T_{\rm coex}$=(1060$\pm$10) K. $T_{\rm coex}$ is reported in [191, 85], and it is close to the experimental value: $T^{exp}_{\rm coex}$=1072 K [84].

Due to the moderate super-saturation in T_1 and T_2, we claim our system to be in *quasi-equilibrium*, and compute the Gibbs free-energy barrier via an Umbrella Sampling technique (see chapter 2) at constant N, P and T, that uses the number of solid particles belonging to the biggest cluster (n) as an order parameter to study the liquid-to-solid phase transition. We then estimate the liquid-solid inter-facial free energy using the prescription of Classical Nucleation Theory, e.g. from the top of the free-energy barrier to grow a critical cubic-like cluster. In what follows, we will refer to the biggest cluster size as N_g instead of n.

9.3. Results

We note at the outset that it is imprecise to speak of *the* surface free-energy density of a small crystallite, as the value of γ depends on the choice of the dividing surface (equimolar dividing surface, equi-enthalpy dividing surface, surface of tension etc. - see ref. [130, 194]). For flat interfaces, the corresponding surface free energies are all the same, but this is not the case for strongly curved surfaces.

The surface free energy that enters into CNT is the one associated with the surface of tension [195]. One property of the surface of tension is that it is, to lowest order, independent of the choice of the dividing surface. We use this property to determine γ associated with the surface of tension. To facilitate the comparison with the data of ref. [191] that refer to a flat interface at coexistence, we deduce $\gamma_{\rm LS}$ from the size-dependence of the free energy of a small crystallite at coexistence. At coexistence, there is no difference in chemical potential

between the liquid and the bulk solid, hence the excess free energy of a small crystallite is entirely due to its surface.

As a first step, we determine the dependence of the free energy of small NaCl crystallites on the number of ions in the crystal. For this part of the calculation, we make use of Umbrella Sampling [11, 29]. These simulations yield the excess free energy of the biggest crystalline cluster in the system as a function of the number of particles in that cluster (N_g). We use a geometrical criterion (see chapter 4) to distinguish crystalline from liquid-like particles.

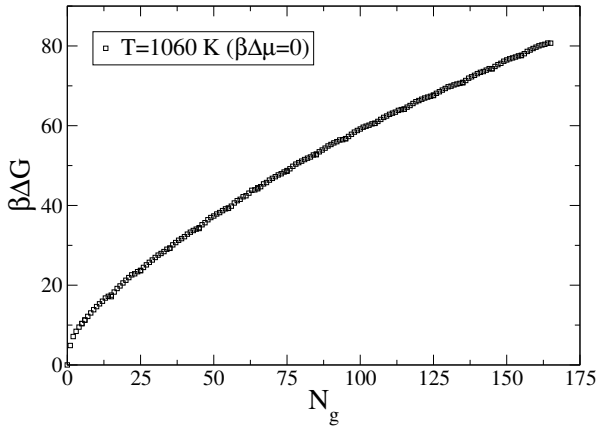

Figure 9.1.: Free-energy barrier ($\beta\Delta G$) as a function of N_g at coexistence T_{coex}. The error bars in $\beta\Delta G$ are comparable to the size of the symbols.

We can then deduce the surface free-energy density using eq. 2.7 where we assume that the growing cluster is either a cube or a sphere (see chapter 2). Although there are strong fluctuations in the shape of a small NaCl crystallite in contact with its melt, its average shape is fairly cubic (see fig. 9.2)[1]. Of course, we need not assume *a priori* that the cluster is cubic: we can use the average cluster shape from figure 9.2 to perform a Wulff construction (see e.g. [196] and appendix A) that yields the variation of the surface free energy with orientation. Assuming that the surface free energy of the $[100]$ interface equals the macroscopic value, we can then compute the average γ of the cluster. Leaving apart the question whether a Wulff construction is at all meaningful for clusters containing $\mathcal{O}(10^2)$ particles, we note that this procedure yields $\langle\gamma_{\mathrm{LS}}\rangle \approx 40$ mJ m^{-2}, which is within 10% of the value expected for a perfect cube. In what follows, we will therefore assume that small NaCl crystals have the same cubic morphology as macroscopic crystals.

From figure 9.1, we cannot yet deduce the surface free energy because there is no *a priori* reason to assume that the surface of this geometrical cluster has any thermodynamic meaning

[1] As the shape of such a small cluster fluctuates, we obtain the average shape by superimposing a large number of instantaneous configurations of the same mass, fixing their centre of mass, and the orientation of the crystal axes. We average over all 48 symmetry-related orientations. The surface is defined as the set of points where the average density equals the average of the solid and liquid densities. Only the crystalline particles inside this surface are shown.

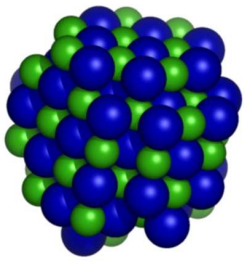

Figure 9.2.: Average shape of a NaCl crystallite consisting of 140 solid-like particles.

(see appendix B). We know, however, that in the thermodynamic limit, the ratio of N_g to N, the "thermodynamic" number of atoms in the crystal, should approach 1. We therefore make the ansatz:

$$N = (N_g^{1/3} + a)^3 \tag{9.2}$$

where a is an adjustable parameter that remains to be determined. To find the number of atoms within the surface of tension, we choose a value of a that minimises the variation of $\gamma_{\rm LS}$ with the size of the cluster. This analysis leads to a value of $a \approx 0$ at the surface of tension. Figure 9.3 shows that, over the range of cluster sizes studied, the resulting value of $\gamma_{\rm LS}$ is indeed almost independent of N for all but the smallest clusters.

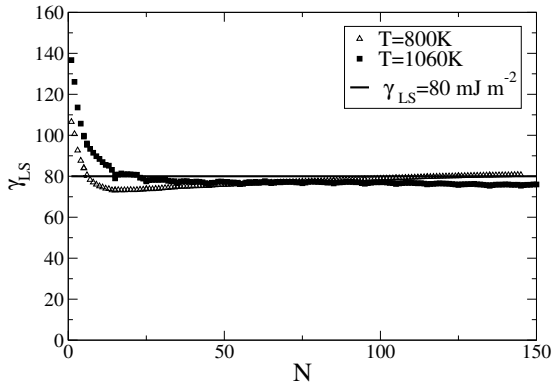

Figure 9.3.: Inter-facial free energy as a function of N computed at the surface of tension, assuming a cubic cluster with a=0.

More interestingly, we find that the resulting value of $\gamma_{\rm LS}$ is very close to the value $\gamma_{\rm LS} \approx 80$mJ m^{-2} that follows from the analysis of the nucleation barrier at 800K [98] (see figure 9.3 and chapter 4). Moreover, a similar analysis at 800 K, leads to the same estimate of $\gamma_{\rm LS}$. The internal consistency between the values of $\gamma_{\rm LS}$ derived from the nucleation barrier

and from the surface of tension would be encouraging, were it not for the fact that it does nothing to resolve the discrepancy with the value of 36 mJ m^{-2} found for a flat interface. Choosing another conventional dividing surface (e.g. the equimolar or the equi-enthalpy surface (see appendix C)) only makes matters worse: in both cases we find a negative value of a that results in an even larger value of $\gamma_{\rm LS}$ that is, moreover, strongly cluster-size dependent. Hence, we conclude that the discrepancy between the properties of a small crystal and a flat interface cannot be corrected for by choosing a better definition of the location of the liquid-solid interface.

The above discussion suggests that the conventional version of CNT cannot account for the observed discrepancy between the surface free energy of a flat interface and that of a small crystallite. However, even within a thermodynamic approach, one can introduce corrections to Classical Nucleation Theory that would change the apparent value of the surface free energy. One such correction takes into account that the crystal cluster is compressible and that the surface free energy depends on the density of the crystal. To estimate the magnitude of this effect, we extend the analysis of Mullins [195] (see appendix D for more details on the calculation) to obtain:

$$r \approx \frac{(\gamma_{\rm LS}(\rho_S)/\gamma_{\rm LS}(\rho_S(0))^3}{\left(1-\Delta\mu\rho_S/(2B)-\frac{1}{2}B\epsilon^2/(\rho_S\Delta\mu)\right)^2}$$

where r is the ratio between the barrier height in the case of compressible clusters (with density ρ_S), compared to that for incompressible clusters (with density $\rho_S(0)$). B denotes the bulk modulus of the crystal and ϵ the elastic strain, compared to that of a solid at the same chemical potential as that of the parent liquid. From our simulations, we find that the density at the centre of the crystal cluster is some 6% lower than the reference value. Even with this rather extreme estimate of the strain in the cluster, we find a compressibility-correction to the apparent value of $\gamma_{\rm LS}$ that is no more than 10%. Hence, we conclude that compressibility effects cannot account for the observed discrepancy.

Thus far, we have not considered the effect of edges and vertexes on the surface free energy of a small cluster. This effect is certainly non-negligible. If, for instance, we consider a cubic NaCl crystal in vacuum at $T = 0K$ (see fig. 9.4), both the line energy of the edges and the vertex energy of the corners can be determined directly (see appendix E). The energy of an

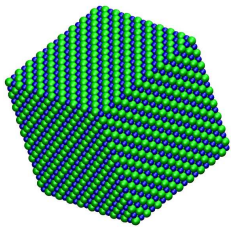

Figure 9.4.: Snapshot of a perfect cube at zero Kelvin made of 9 unit cells.

NaCl cube can be written as:

$$e = e_B\ell^3 + 6e_S\ell^2 + 12e_E\ell + 8e_C \tag{9.3}$$

where e is the total internal energy per particle, e_B, the energy per particle in a bulk crystal, e_S the energy of a particle belonging to the surface, e_E the energy of a particle belonging to an edge, e_C the energy of a particle belonging to a corner of the cube, and ℓ is the number of atoms per edge. Computing this energy for a crystal of 64, 216 and 512 atoms [198], we find that $e_E/e_S = 0.22$ and $e_C/e_s = 1.2$. The effect of these edge and vertex contributions is to increase the apparent surface energy by 13% for a crystal of 216 particles. Of course, these numbers do not apply to a hot NaCl crystal in contact with its melt and it is not at even obvious how to define the various terms in that case, as not only the magnitude but even the sign of e_E and e_C depend on the precise choice of the dividing surface. This means that, within the macroscopic framework imposed by CNT, we cannot reliably estimate the edge and corner contributions to the surface free energy. We are therefore forced to conclude that the large apparent value of $\gamma_{\rm LS}$ of small crystallites is due to a finite-size effect that is not easily accounted for by within a "thermodynamic" theory. Rather, the free energy of small clusters must be computed using a molecular approach, either theoretically (as in DFT [190]) or numerically, as illustrated in the present work.

In the present chapter, and in ref. [98], we compute the free energy of relatively small clusters (up to 200 solid particles). However, under the experimental conditions for crystal nucleation of NaCl (T=905K), the critical cluster is expected to contain $\mathcal{O}(6 \times 10^2)$ particles. Calculations for larger clusters would be feasible, but expensive. We therefore use the Tolman ansatz [199], namely that the leading correction to surface free energy is proportional to $1/R^*$, where R^* is the radius of the critical cluster [2]. As $1/R^* \sim \Delta\mu$, we assume that the variation in $\gamma_{\rm LS}$ is of the form: $\gamma_{\rm LS}(\Delta\mu) = \gamma_{\rm LS}^{\rm M} + b\Delta\mu$(see appendix F). We can determine b from the simulation data of refs [191, 98]. Inserting the value $\Delta\mu = 0.3kT$ at T=905K, we predict that under the condition of the nucleation experiments of ref. [77], the effective value of $\gamma_{\rm LS}$ should be 67 mJ m^{-2}, in almost embarrassing agreement with the experimental data ($\gamma_{\rm LS}$=68 mJ m^{-2}). Although this good agreement is almost certainly fortuitous, it does support our conjecture that the surface free energies measured in nucleation experiments are subject to very large finite size corrections (in this case: more than 80%). If we take this strong $\Delta\mu$-dependence of $\gamma_{\rm LS}$ seriously, it would mean that for strongly faceted crystals (al-

[2] The Tolman length (δ) measures the extent by which the surface tension of a small liquid droplet embedded in a vapour deviates from a planar interface[130, 199]. It is defined as the leading order correction in an expansion of the Laplace pressure ΔP in $1/R$ (with $R = R_e$ the equimolar radius of the liquid droplet, and ΔP the pressure difference between the bulk pressure of the liquid inside the droplet and the vapour pressure outside).

$$\Delta P = \frac{2\gamma}{R}\left(1 - \frac{\delta}{R} + ...\right) \tag{9.4}$$

being γ the surface tension of a planar interface. However, The Tolman length is also related to the surface of tension, located at R_s

$$\Delta P = \frac{2\gamma_s}{R_s} \tag{9.5}$$

where, this time γ_s is the surface tension at the surface of tension. The location of the surface of tension and of the the Gibbs equimolar dividing surface are related by means of the Tolman length:

$$\delta = \lim_{R_s \to \infty}(R_e - R_s) \tag{9.6}$$

though not for NaCl), the nucleation barrier could start to rise again at large super-saturations. This should be experimentally observable, as it would lead to an increase in the final crystallite size in fully crystallised samples [200, 197]. Interestingly – but we do not know if it is really relevant – the final crystallite size in hard-sphere crystallisation suddenly grows as the concentration is increased beyond a volume fraction of 58%. If the barrier is a monotonically decreasing function of the volume fraction, this should not happen.

9.4. Conclusions

In summary, our study of the free energy of NaCl crystallites indicates that the surface free energy is subject to large finite size corrections that cannot be accounted for within a thermodynamic theory. Based on the small number of examples where the relevant simulation data are available (NaCl, Lennard Jones, hard spheres), we speculate that the finite size effects are most pronounced for strongly faceted crystals, such as NaCl. The present results support the suggestion by Kelton that the large number of published surface free energies that are based on nucleation data are of little use to predict macroscopic surface free energies. Our work highlights the need for a simple, yet accurate molecular theory for crystal nucleation that properly accounts for the fact that crystal clusters are far from macroscopic.

Acknowledgements

Concerning this work, I would like to thank A. Arnold for the computation of the cubic NaCl crystal in vacuum at $T = 0K$, and H. Tepper for a careful reading of the chapter.

Appendix A: Averaged cluster shapes and numerical Wulff's construction

Analysing the instantaneous solid clusters, we observe that their shapes strongly fluctuates and is far from being spherical. In the framework of CNT, one should neglect these fluctuations and assume some average equilibrium shape for the clusters. Assuming we can neglect small clusters, it follows that

- the average shape will necessarily retain the symmetry of the bulk crystal;
- it should possess the lowest inter-facial free energy $\gamma_{\rm LS}$ among all possible shapes, given a fixed volume: this corresponds to the cluster shape obtained via the Wulff's construction.

In particular, if $\gamma_{\rm LS}$ does not depend on the orientation of the crystal, i.e. the cluster is isotropic, this shape should be spherical, as the ideal CNT predictions. In our calculations, we take into account both the increase of the inter-facial area with respect to the spherical shape, and its related anisotropy. Both effects enhance the value of the effective nucleation barrier, in particular the second one could be very large in the NaCl case, due to the presumable high cost of the presence of "charged" interfaces, such as the [111] one. Thus, the steps we take are the following:

1. we superimpose several clusters of the same size N_g, while keeping their centre of mass fixed;
2. we find the main crystalline directions of each cluster, by computing the maximum of the structure factor and orienting it along the x,y and z crystalline axis corresponding to the [100] plane. At this point, if the statistics is good enough, the surface profile averaged over these clusters, is the Wulff's profile we are looking for. However, as the number of clusters we can deal with is limited to few tens, the average cluster profile is rough and fairly asymmetrical;
3. in order to solve this problem, we consider the fact that the equilibrium shape should have a cubic symmetry and apply the correspondent symmetry operations to the larger clusters. A cubic symmetry belongs to the octahedral crystallographic symmetry group O_h. Thus, we apply all the 48 symmetry operations to every instantaneous cluster configuration: the identity E, the rotation by π around the axes x, y,z ($3\mathrm{C}_4^2$); the rotations by $\pm\pi/2$ around the axes x,y,z ($6\mathrm{C}_4$); the rotations by π around the bisectrices in the planes xy, yz, xz ($6\mathrm{C}_2$); the rotations by $\pm 2\pi/3$ around the four diagonals of the cube ($8\mathrm{C}_3$), and the combination of the inversion (I) with the above-mentioned 24 symmetry operations;
4. next, we compute the average cluster shape by means of a density distribution profile. We super-impose a three-dimensional cubic grid to the cluster, and compute the density distribution: the *surface part* of the cluster is defined whenever the number density is constant and is 1/2 ρ_S. We then cut the cluster along the surface, keeping in mind

that its volume is constrained to be equal to the averaged volume of the instantaneous clusters;

5. finally, the inter-facial free energy is obtained from an inverse Wulff's construction [196]. We following Nozieres's procedure, as sketched in fig. 9.A.1:
   a) we consider the centre of mass of the cluster as the origin (O);
   b) we compute the distance between a point (P) on a facet of the cluster's equilibrium shape and the centre (OP);
   c) OP is a catetus of a rectangular triangle, whose hypothenuse (OM) defines the inter-facial free energy ($OM = \gamma_{\rm LS}(\theta)$), and whose other catetus belongs to the plane tangent to a facet;
   d) the locus of all the M point is the polar plot of $\gamma_{\rm LS}(\theta)$ (the envelope passing for M plotted)in fig. 9.A.1;
   e) the inter-facial free energy $\gamma_{\rm LS}(\theta)$ of each facet is then directly proportional to OM and inversely proportional to the area of the facet;

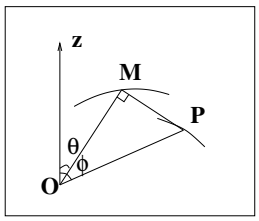

Figure 9.A.1.: Wulff construction. O is the centre of mass of the cluster, the polar plot of $\gamma_{\rm LS}$ is the envelope passing for M plotted, while the one passing for P indicates the equilibrium shape.

The $\gamma_{\rm LS}$-plot so obtained is analytically solvable only in case the cluster is rough in all directions (see the right-side of fig. 9.A.2): this happens when the shape is convex and has no mathematically flat facets (in the $\gamma_{\rm LS}$-polar plot this would lead to cusps). Fig.9.A.2 (left-hand side) shows the (faceted interpolated) shape for the $N = 140$ solid cluster, and the corresponding $\gamma_{\rm LS}$-polar plot is represented in the right side of the same figure. The averaged cluster shape has many [100] facets, possibly artificially made, that suggests a "flat" liquid-solid interface at coexistence. Most liquid-solid interfaces are rough at the melting point. Besides this fact, the overall shape is sufficiently rounded, and the $\gamma_{\rm LS}$-plot is not very anisotropic.

If we assume $\gamma_{\rm LS}$[100] equal to 36 mJ/m^2, then the maximum value obtained for the average-shape cluster is $\gamma_{\rm LS}^{max}$ = 69 mJ/m^2, while the value averaged over all possible facets is $\gamma_{\rm LS}^{av} \sim$ 40 mJ/m^2, still a factor 2 lower than the one previously computed from the CNT nucleation barrier. Conversely, accounting for a factor of about two would require an unrealistically high anisotropy — far higher than that of crystalline NaCl clusters,[201]. Therefore, it seems that this is not contributing to understand our discrepancy.

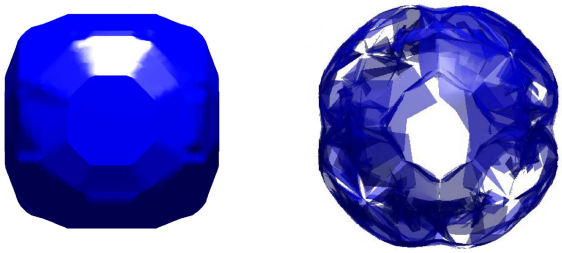

Figure 9.A.2.: Average shape (faceted interpolated) of the $N = 140$ solid cluster is shown on the left-hand side, whereas the corresponding γ_{LS}-polar plot on the right-hand side.

Appendix B: Thermodynamic versus geometric N

According to the CNT expression for the free-energy barrier, N is the thermodynamic number of solid particles of the biggest cluster in the system. However, as already shown in chapter 2, what we measure in our simulations, is the number of solid-like particles belonging to the biggest cluster identified by means of a local bond-order based geometrical criterion (N_g).

In principle, N_g is different from from N, and depends on the location of the liquid-solid dividing surface. In the thermodynamic limit, all choices of the dividing surfaces coincide, but at the small length scale of the cluster size, differences are indeed substantial.

In order to relate our simulation results of the inter-facial free-energy function of N_g, to the values depending on the thermodynamic N, we use a similar approach as Cacciuto et al.[202], and assume an explicit relation between N and N_g, that allows us to express the inter-facial free energy as a function of N, as presented in eq. 9.2.

Appendix C: Different choices of the dividing surface bring to different values of γ

We now estimate γ_{LS} as a function of N at the surface of tension, at the equimolar dividing surface and at the equi-enthalpy dividing surface. The inter-facial free energy for a spherical and a cubic cluster is expressed in terms of the thermodynamic number of particles N, being the radius of the surface of tension proportional to N:

$$\gamma_{SL}(N) = \frac{\Delta G(N) + N|\Delta\mu|}{(4\pi)^{1/3}} \left(\frac{\rho_s}{3}\right)^{2/3} N^{-2/3}; \gamma_{SL}(N) = \frac{\Delta G(N) + N|\Delta\mu|}{6} \rho_s^{2/3} N^{-2/3}. \tag{9.C.1}$$

The parameter a in eq. 9.2 is properly tuned for every dividing surface, by plotting

$$a = \frac{(N - N_g)}{3N_g^{2/3}} + O(N_g^{-1/3}). \tag{9.C.2}$$

as a function of N_g for relatively big clusters.

$\gamma_{\rm LS}$ at the surface of tension

The value of a that minimises the variation of $\gamma_{\rm LS}$ with the size of the cluster, is $a = 0$. By means of eq. 9.C.2 we find that when $a = 0$, $\gamma_{\rm LS}$ at the surface of tension does not depend on the radius of the cluster. For a spherical cluster $\gamma_{\rm LS}$ is presented in fig. 9.C.1 while for a

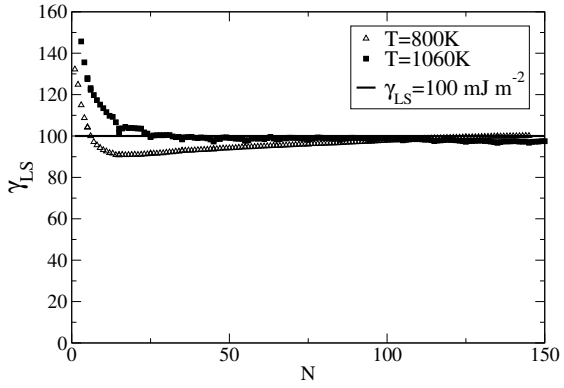

Figure 9.C.1.: $\gamma_{\rm LS}$ as a function of N at the surface of tension for a spherical cluster.

cubic cluster, we have already shown it in fig. 9.3. Even though for small clusters γ assumes really large values, its asymptotic limit for a spherical cluster is around 100 mJ m^{-2} and it does not depend on temperature.

γ at the Gibbs equimolar dividing surface

The equimolar dividing surface, according to Gibbs, is the surface that does not contain any excess particles and has no volume. The total volume of the system $\langle V\rangle$ is $\langle V\rangle = \langle v_L\rangle N_L + \langle v_S\rangle N_S$, being v_L and v_S the liquid and solid volume per particle, respectively. The total number of particles in the system (N_{tot}) is then equal to the sum of the overall solid (N_S) and liquid (N_L) particles, $N_{tot} = N_S + N_L$. The number of solid particles enclosed by the equimolar dividing surface N_S coincides with the thermodynamic number of solid particles N previously defined ($N_S = N$), and is equal to:

$$N = N_{tot}\frac{\langle v\rangle - \langle v_L\rangle}{\langle v_S\rangle - \langle v_L\rangle}, \tag{9.C.3}$$

where N_{tot} is 3456, $\langle v_S\rangle$ and $\langle v_L\rangle$ are the bulk solid and liquid average volumes per particle at coexistence ($\langle v_S\rangle = 25.66$Å^{-3} and $\langle v_L\rangle = 33.13$Å^{-3}), and $\langle v\rangle$ is the average volume per particle (in the NPT simulations) of the metastable liquid containing the biggest solid cluster N_g. Figure 9.C.2 illustrates the average volume per particle for the system at coexistence.

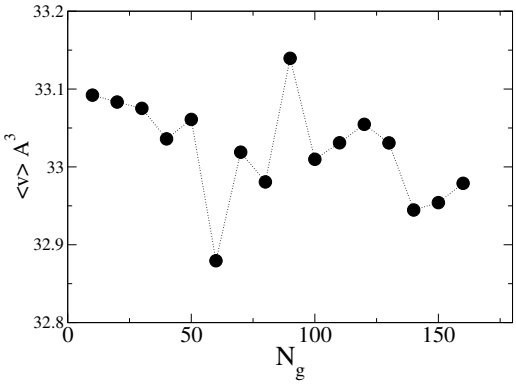

Figure 9.C.2.: Average volume per particle in an NPT simulations at coexistence. Each point represents a metastable liquid containing the biggest solid cluster with N_g ions.

In order to compute $\langle v \rangle$, we average over several configurations with the same N_g ranging from 100 to 160.

We thus obtain a set of values (N, N_g) for each cluster size, and assuming the same dependence as in eq. 9.C.2, we get an estimate of the parameter a, as it is shown in fig. 9.C.3 The inset in fig. 9.C.3 shows how, for clusters with less than 100 particles the value of a is quite noisy, whereas for sizes beyond 100 particles, a seems to fluctuate around an average value: by using eq. 9.C.2 a=-0.95 at the equimolar dividing surface.

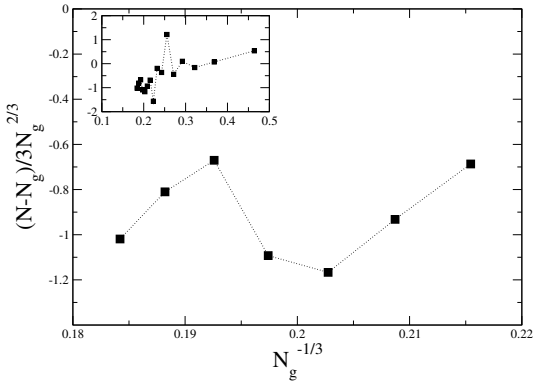

Figure 9.C.3.: Estimation of a at the Gibbs equimolar dividing surface for different cluster sizes ranging from 100 to 160 particles. In the inset, the x and the y axes represent the same variables.

We then plot the inter-facial free energy as a function of the thermodynamic number of solid particles N for the computed value of a (see fig. 9.C.4): the asymptotic limit (which should be equal to the one obtained for the surface of tension), is not nearly reached for the

studied cluster sizes, and the slow convergence is particularly obvious when the system is at coexistence.

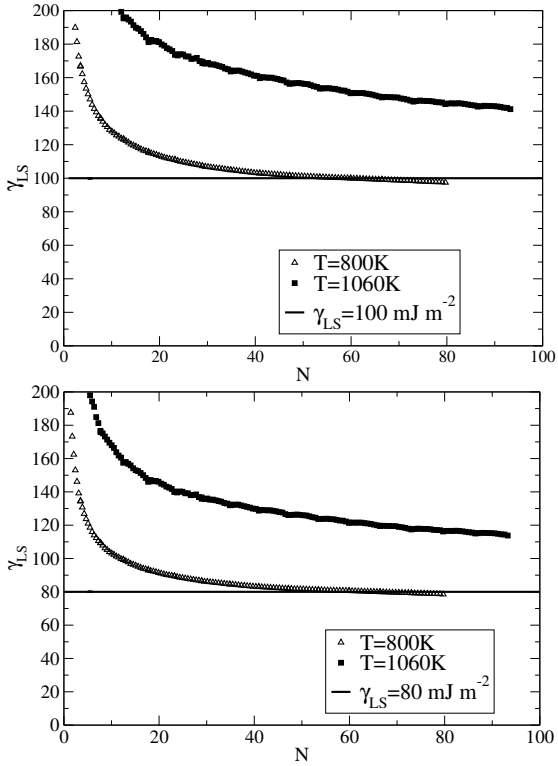

Figure 9.C.4.: Inter-facial free energy as a function of N at the Gibbs equimolar dividing surface, assuming a spherical (top) and cubic cluster (bottom).

From this analysis, we conclude that we the surface of tension's calculations give a better estimate of the asymptotic value of $\gamma_{\rm LS}$ than the result obtained with the equimolar dividing surface

γ at the equi-enthalpy dividing surface

We also estimate the inter-facial free energy associated with the equi-enthalpy dividing surface. The total enthalpy of the system is defined as $H = N_S h_S + N_L h_L$, where N_S and N_L are the total number of solid and liquid particles in the system and h_S, h_L are the liquid and solid enthalpies per particle, respectively. At the equi-enthalpy dividing surface, we assume that there are no excess particles and neglect possible contributions due to the interface. Since the total number of particles is $N_{tot} = N_S + N_L$

$$H = N_S h_S + N_L h_L = N_{tot} h_S + N_L \Delta h = N_{tot} h_L - N_S \Delta h \qquad (9.C.4)$$

where Δh is enthalpy of fusion per particle, available from both experimental and simulation data [84, 191]. The thermodynamic number of solid particles in the biggest cluster (N_S) is the number of solid particles enclosed by the equi-enthalpy dividing surface (N) and can be evaluated from eq. 9.C.4, where $N_{tot}h_L$ is the total enthalpy of the bulk liquid and H is the enthalpy we measure in an NPR simulation. We obtain that the enthalpy of fusion per particle is equal to $\Delta h = -1.59k_BT$, while the enthalpy per particle is $h_L^1 = -54.74k_BT$ at T_1, $h_L^2 = -52.98k_BT$ at T_2, and $h_L^{coex} = -40.66k_BT$ at coexistence. By means of eq. 9.C.2, we get an estimate of the parameter a at the equi-enthalpy dividing surface, considering N_g ranging from 100 to 160 particles, we obtain a = -0.35.

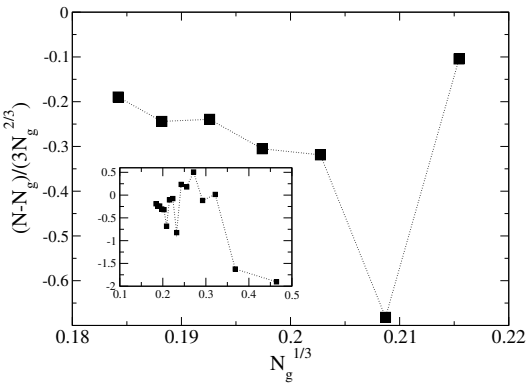

Figure 9.C.5.: Estimation of a at the equi-enthalpy dividing surface for different cluster sizes ranging from 100 to 160 particles. The inset shows that, for clusters smaller than 100 particles, the value of a is quite noisy. In the inset, the x and the y axes represent the same variables.

We then compute γ_{LS} as a function of N at the equi-enthalpy dividing surface for the estimated value of a (see fig. 9.C.6), and observe that in this case the asymptotic limit of γ_{LS} is reached faster than in the equimolar dividing surface case, in better agreement with the results previously obtained at the surface of tension.

Appendix D: Gibbsian droplet model and the compressibility effect

Another attempt we make is based on including the compressibility effect in the thermodynamics of the nucleating crystal clusters.

Gibbsian droplet model

In the Gibbsian droplet model of (liquid (phase B) from supersaturated vapour (phase A)) nucleation, the free-energy barrier for nucleation is computed by considering the effect of the Laplace pressure on the chemical potential of the critical cluster. At the top of the free energy

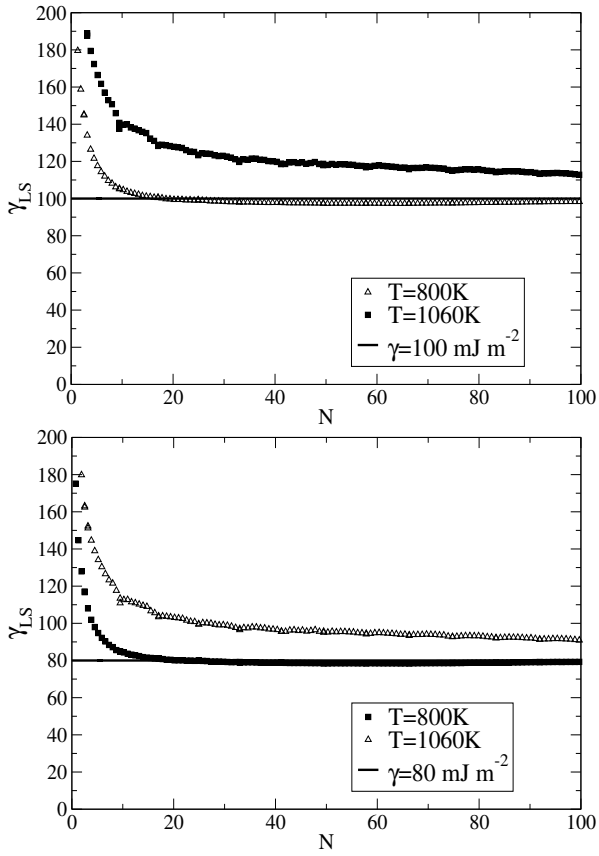

Figure 9.C.6.: Inter-facial free energy as a function of N at the equi-enthalpy dividing surface assuming a spherical (top) and cubic cluster (bottom).

barrier, the critical liquid cluster is in (unstable) equilibrium with the supersaturated vapour phase. Hence, the droplet and the vapour must have the same chemical potential. This is only possible if the pressure inside the cluster is higher than the pressure of the parent phase (see fig. 9.D.1). Therefore, there is a difference between the chemical potential $\mu_A(P_A)$ of the metastable phase and the chemical potential $\mu_B(P_A)$ that would correspond to the bulk stable phase B at this thermodynamic conditions. $\Delta\mu$ is a negative quantity given by $\mu_B(P_A) - \mu_A(P_A)$, and it constitutes the driving force to nucleation.

If we work within the CNT framework, we assume that the cluster is incompressible. This leads to $d\mu/dP = constant$: meaning that in CNT the curve representing the chemical potential (μ_B) in phase B is approximated by a straight line, as shown in fig. 9.D.1. Thus, the accuracy of the CNT approximation depends on the curvature of μ_B: if the curvature is high, the CNT approximation can lead to a different value of μ_B, hence of $\Delta\mu$.

In the droplet model, the pressure difference between the metastable vapour surrounding

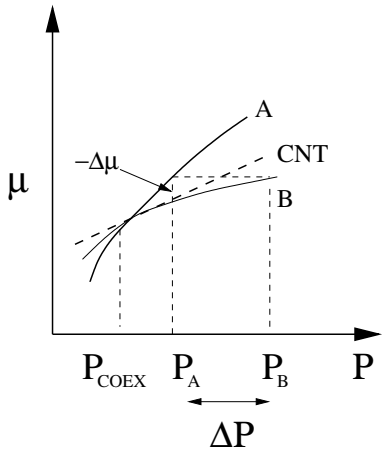

Figure 9.D.1.: Chemical potential curves as a function of pressure at constant temperature, for both phases A and B. ΔP is the Laplace pressure, and $-\Delta\mu$ the chemical potential difference between phase B and A at pressure P_A. As CNT assumes incompressibility of the growing phase, the chemical potential of phase B is represented as a straight line.

the droplet and the inside of the droplet needed to keep the same chemical potential difference, is the Laplace pressure of eq. 2.11, where R^* is radius of the critical cluster of the surface of tension, and γ the surface tension. Assuming that both γ and the pressure dependence of the chemical potential of both phases are known, we can then compute R^*, and the nucleation barrier itself, that for a spherical cluster will be

$$\Delta G = \frac{4}{3}\pi\gamma R^{*2} = \frac{2}{3}\Delta P R^{*3}. \tag{9.D.1}$$

In contrast to CNT, the droplet model allows for the *compressibility* of the phase that nucleates. As the Laplace pressure is always positive, the droplet model predicts that small clusters are denser than the corresponding bulk phase.

But as Gibbs already realised [20], the droplet model cannot be applied to crystallites because the excess pressure of crystals is not equal to the Laplace pressure $2\gamma/R^*$. For solid interfaces, we have to distinguish between the surface tension and the surface stress In Mullins's work [195], we find the correct expression for the excess pressure inside a critical crystal cluster of density ρ_S and radius R is:

$$\Delta P = \frac{2\gamma_{\mathrm{LS}} - 3\rho_S\left(\frac{\partial\gamma_{\mathrm{LS}}}{\partial\rho_S}\right)}{R^*}\,. \tag{9.D.2}$$

For materials with a large cohesive energy, the derivative $\left(\frac{\partial\gamma_{\mathrm{LS}}}{\partial\rho_S}\right)$ is large and positive. So much that ΔP can become negative. Therefore, it results that small crystal clusters can be very different from the bulk material.

Compressibility effect

For solid interfaces, one should distinguish between the surface tension and the surface stress. Therefore, it results that small crystal clusters can be very different from the bulk material. For materials with a large cohesive energy, the surface free energy will decrease strongly with the bulk density. This leads to a negative surface stress. As a result, small clusters may have a much lower density than the bulk at coexistence.

This will consequently have an effect on the nucleation barrier. If we use the expression for nucleation of a compressible crystal under conditions where the surface stress differs strongly from the surface free-energy density, we find that the effect of the surface stress is to:

- decrease the thermodynamic driving force for nucleation, and
- decrease the surface free energy.

Therefore, in order to get the same barrier height we should find a lower γ_{LS}.

We now demonstrate that an analysis of the nucleation barrier assuming incompressibility results in a systematic overestimation of the surface free energy. In what follows, we will define γ_{LS} as γ, and ρ_S as ρ.

Nucleation barrier considering the surface stress effect

To study the effect of surface stress on nucleation, we start by considering the generalisation of the Gibbs expression for the nucleation barrier in the fluid/fluid case

$$W^* = \frac{\gamma A}{3} \tag{9.D.3}$$

(where A is the surface area of the cluster and γ is the inter-facial free energy), and the Buff and Kondo [203, 204] equation

$$\omega_L - \omega_S = \frac{1}{R^2}\frac{\partial(R^2\Omega)}{\partial R} = \frac{2\Omega}{R} + \frac{\partial\Omega}{\partial R} \tag{9.D.4}$$

where ω_L/ω_S are the grand potentials per unit volume of the liquid and the nucleating solid spherical cluster, R is the radius of the spherical dividing surface (following Gibbs's procedure), and Ω represents the excess of gran potential associated with the dividing surface. Equation 9.D.4 holds at equilibrium for an arbitrary choice of the dividing surface radius R [3].

[3] Buff and Kondo's equation [205, 203] for a fluid(sphere)/fluid system is

$$(\omega^S - \omega^L) = \frac{\partial(A\Omega_A)}{\partial V^S} \tag{9.D.5}$$

where Ω_A is the excess of gran potential associated with the dividing surface, A is the area of the cluster, and V^S is the volume of the solid cluster. Equation 9.D.5 is valid at equilibrium for an arbitrary choice of the shape of the dividing surface, and can also be written without imposing any cluster shape. It appears then evident that Ω does not depend on the facets of the cluster: either it is the same for all facets, or all facets are identical.

At the surface of tension R_s $\left(\frac{\partial\Omega}{\partial R}\right)_{R_s} = 0$. We then define $\Omega(R_s) \equiv \gamma$ such that

$$\omega_L - \omega_S = \frac{2\gamma}{R_s} \tag{9.D.6}$$

where γ is the R-independent inter-facial free-energy density at the surface of tension.

When a fluid sphere is embedded in a different fluid [206], equation 9.D.6 becomes the Gibbs-Thomson equation: being $\omega_L = -P_L$ and $\omega_S = -P_S$

$$P_S - P_L = \frac{2\gamma}{R_s} \tag{9.D.7}$$

where $\Delta P = P_S - P_L$ is the so-called Laplace pressure. As we just mentioned, in the liquid phase the gran potential per unit volume is

$$\omega_L = -P_L \tag{9.D.8}$$

where P_L is the pressure of a liquid at coexistence. For a bulk solid at coexistence, $\omega_S = -P_S$, being P_S the pressure at which the bulk solid has the same chemical potential as the liquid at the same temperature but at pressure P_L.

However, for small clusters, $\omega_S \neq -P_S$ due to elastic deformations. In order to properly compute ω_S, we start by adopting Mullins's approach (eq. 40 and eq. 41 in ref. [195]): we consider both eq. 9.D.6 and

$$P_S - P_L = \frac{2f}{R_s} \tag{9.D.9}$$

where f is now the surface stress, defined as

$$f = \gamma + \frac{3}{2} v \frac{d\gamma}{dv} \tag{9.D.10}$$

eq. 9.D.9 indicates that f and not γ determines the pressure in the solid spherical cluster: $f \neq \gamma$ unless $\left(\frac{d\gamma}{dv} = 0\right)$ (see eq. 29 in ref. [195]).

In principle, it should be possible to simultaneously solve eq. 9.D.6 and 9.D.9 at a given T and μ for R_s and v, given the functions $P_L(T,\mu)$, $\omega_S(T,\mu,v)$ and $\gamma(T,\mu,v)$. Mullins obtained an approximate solution by expanding the latter two functions (ω_S and γ) to second order in powers of $\epsilon \equiv (v - v_S)/v_S \equiv \Delta v/v_S$, where v_S is the volume per unit cell of a bulk solid at T and μ, and $\Delta v = v - v_S$ indicates the density dependence of the inter-facial free energy. Therefore, ϵ measures the elastic strain of the solid cluster: assuming, for convenience, that the crystal is elastically isotropic, we argue that $\epsilon << 1$.

In what follows, whenever we use the super-script S, we indicate the bulk state. We can now express ω_S as (see eq. 43a in ref. [195])

$$\omega_S = -P_S + \frac{1}{2}B\epsilon^2 + O(\epsilon^2) \approx -P_S + \frac{1}{2}B\left(\frac{\Delta v}{v_S}\right)^2 \tag{9.D.11}$$

where P_S is the bulk solid pressure at T and μ, and B the bulk modulus $\left(B = -V\left(\frac{\partial P}{\partial V}\right)_T\right)$, that corresponds to a dilatation of the unit cell at constant T and μ. Equation 9.D.11 is lacking the linear term in ϵ, as we can see that the coefficient in front of the linear term is zero:

$$d\omega_S = d(\Omega_S/V_S) = -s_S dT - \rho_S d\mu - (\omega_S + P_S)dv/v_S = -s_S dT - \rho_S d\mu \quad (9.D.12)$$

being $\omega_S = -P_S$ for a fluid. Moreover, to the zero order in ϵ, ω_S in the spherical cluster assumes the bulk value.

According to Mullins, γ can be written as (see eq. 44 in ref. [195])

$$\gamma = \gamma_S + \gamma_1\epsilon + \frac{1}{2}\gamma_2\epsilon^2 \quad (9.D.13)$$

where γ_S is the inter-facial free energy of the bulk solid, γ_1 is

$$\gamma_1 = \left(\frac{2}{3}\right)(f_S - \gamma_S) \quad (9.D.14)$$

being f_S the surface stress of the bulk solid, and γ_2

$$\gamma_2 = \left(-\frac{10}{9}\right)(f_S - \gamma_S) + \left(\frac{2}{3}\right)\left(\frac{\partial f}{\partial v}\right)_S \quad (9.D.15)$$

All coefficients in eq. 9.D.11 and 9.D.13, and v_S , are functions of T and μ. Hence, Mullins obtains, by means of eq. 9.D.11 and 9.D.13, a cubic equation in ϵ, whose solution is given by the following term (see eq. 46 in ref. [195])

$$\epsilon = -\frac{3\gamma_1(P_S - P_L)}{2\gamma_S B} \quad (9.D.16)$$

Until this point, we have been written Mullins's results. While from here on, we will extend his results to obtain an expression of the nucleation barrier for compressible clusters.

We now rewrite eq. 9.D.16 as

$$\frac{v - v_S}{v_S} = -\frac{3\gamma_1(P_S - P_L)}{2\gamma_S B} \quad (9.D.17)$$

using eq. 9.D.7, we obtain that

$$\frac{v - v_S}{v_S} = -\frac{3\gamma_1}{R_s B} \quad (9.D.18)$$

by means of both eq. 9.D.14 and eq. 9.D.10, γ_1 becomes $\gamma_1 = v_S\left(\frac{d\gamma}{dv}\right)_S$. Therefore, we can write ϵ as

$$\frac{v - v_S}{v_S} = -\frac{3v_S}{R_s B}\left(\frac{d\gamma}{dv}\right)_S \quad (9.D.19)$$

In what follows, we will discuss two possible sub-cases: on one side, the case when the inter-facial free energy is constant (Case a), on the other side, when the inter-facial free energy differs from the surface stress (Case b).

Case a: The inter-facial free energy γ is constant

Let us first consider the case where γ is constant. Even then, eq. 9.D.3 and 9.D.6 are not equivalent to the corresponding equations within the CNT framework, because we are now including the cluster's compressibility.

We start by expressing the chemical potential of the solid cluster at the pressure of the surrounding liquid:

$$\mu_S(P_L) = \mu_S(P_S) + \left(\frac{\partial \mu_S}{\partial P}\right)_T (P_L - P_S) + \frac{1}{2}\left(\frac{\partial^2 \mu_S}{\partial P^2}\right)_T (P_L - P_S)^2 + \cdots \quad (9.D.20)$$

Being $\Delta P \equiv P_S - P_L$, and ignoring all terms higher than the quadratic one in ΔP, we get

$$\mu_S(P_L) = \mu_S(P_S) - v_S \Delta P - \frac{1}{2}\frac{v_S}{B}(\Delta P)^2 \quad (9.D.21)$$

where $\left(\frac{\partial \mu_S}{\partial P}\right)_T = -\frac{V_S}{N_S} = -v_S$ and $\left(\frac{\partial^2 \mu_S}{\partial P^2}\right)_T = v_S \kappa_T = \frac{v_S}{B}$, with κ_T the isothermal compressibility $\left(\kappa_T = -\frac{1}{V}\left(\frac{\partial V}{\partial P}\right)_T\right)$, and B the bulk modulus $(B = 1/\kappa_T)$.

As the critical solid cluster is in thermodynamic equilibrium with the liquid (at constant temperature)

$$\mu_S(P_S) = \mu_L(P_L) \quad (9.D.22)$$

Using the notation $\Delta\mu \equiv (\mu_L(P_L) - \mu_S(P_L))$, we see that

$$\frac{1}{2}\frac{v_S}{B}(\Delta P)^2 + v_S \Delta P - \Delta\mu = 0 \quad (9.D.23)$$

or

$$\begin{aligned} \Delta P &= B(\sqrt{1 + 2\Delta\mu/(B v_S)} - 1) \\ &= B(\sqrt{1 + 2\Delta\mu\rho_S/B} - 1) \end{aligned} \quad (9.D.24)$$

We now consider two examples: first when the solid is not very compressible, therefore the bulk modulus is large, next when the solid is highly compressible, therefore the bulk modulus is small.

LARGE BULK MODULUS B

If the solid is not very compressible (large bulk modulus B), we can write

$$\Delta P \approx B\left(1 + \frac{1}{2}\left(\frac{2\Delta\mu\rho_S}{B}\right) - \frac{1}{8}\left(\frac{2\Delta\mu\rho_S}{B}\right)^2\right) = \Delta\mu\rho_S\left(1 - \frac{\Delta\mu\rho_S}{2B}\right) \quad (9.D.25)$$

Combining this result with eq. 9.D.6, we get an expression for the Laplace pressure

$$\frac{2\gamma}{R_s} = \Delta\mu\rho_S\left(1 - \frac{\Delta\mu\rho_S}{2B}\right) \quad (9.D.26)$$

that implies a radius of the critical cluster of

$$R_s = \frac{2\gamma}{\Delta\mu\rho_S(1-\frac{\Delta\mu\rho_S}{2B})} \tag{9.D.27}$$

Therefore the height of the nucleation barrier, assuming a spherical cluster, is given by

$$W_{COMP} = \frac{16\pi}{3}\frac{\gamma^3}{(\Delta\mu\rho_S\left(1-\frac{\Delta\mu\rho_S}{2B}\right)\Big)^2}. \tag{9.D.28}$$

If we compare this with the result for the nucleation barrier of an incompressible solid W_{INCOMP}(see the CNT expression for the free-energy barrier in chapter 2), we find that

$$W_{COMP} = \frac{W_{INCOMP}}{\left(1-\frac{\Delta\mu\rho_S}{2B}\right)^2} \tag{9.D.29}$$

For solid clusters, this correction is usually small (a few percent).

However, in bubble nucleation, it can be very substantial. If a bubble is filled with an ideal gas, we know that $PV = Nk_BT$. In an isothermal transformation ($PV = const$) $d(PV) = PdV + VdP = 0$, that implies dV/V=-dP/P. So, being the bulk modulus $B = -dP/(dV/V)$, we get $B = P = \rho_G k_B T$, where ρ_G is the density of the vapour at the same thermodynamic conditions as the metastable liquid. The above relation then becomes:

$$W_{COMP} = \frac{W_{INCOMP}}{(1-\frac{1}{2}\frac{\Delta\mu}{k_BT})^2}. \tag{9.D.30}$$

that implies a larger contribution that eq. 9.D.29.

SMALL BULK MODULUS B

For highly compressible materials, we obtain a completely different expression for the nucleation barrier. For small B, we can write eq. 9.D.24 as

$$\Delta P = B(\sqrt{1+2\Delta\mu\rho_S/B}-1) \approx \sqrt{2\Delta\mu\rho_S B} \tag{9.D.31}$$

Therefore, the top of the free-energy barrier, assuming a spherical cluster, becomes

$$W_{COMP} = \frac{16\pi}{3}\frac{\gamma^3}{2\Delta\mu\rho_S B} \tag{9.D.32}$$

This expression is qualitatively different from the usual CNT expression as, it predicts that the nucleation barrier scales as $(\Delta\mu)^{-1}$, rather than as $(\Delta\mu)^{-2}$.

Case b: The inter-facial free energy differs from the surface stress and large bulk modulus

Next we consider the situation where the surface stress differs from the inter-facial free energy. The theoretical analysis of Mullins [195] shows that, to the lowest order in the crystal strain, the density change of a crystalline cluster is given by eq. 9.D.19, that here we rewrite for the sake of clarity:

$$\frac{v - v_S}{v_S} = -\frac{3v_S}{R_s B}\left(\frac{d\gamma}{dv}\right)_S \tag{9.D.33}$$

We now want to express eq. 9.D.33 in terms of $\rho = 1/v$.

$$\frac{v - v_S}{v_S} = \frac{\rho_S - \rho}{\rho} \tag{9.D.34}$$

if we introduce $\Delta\rho = \rho - \rho_S$

$$\frac{\rho_S - \rho}{\rho} = \frac{\Delta\rho}{\Delta\rho + \rho_S} = -R \tag{9.D.35}$$

where we introduce a parameter R. Therefore

$$\frac{\Delta\rho}{\rho_S} = \frac{-R}{1+R} \approx -R \tag{9.D.36}$$

assuming $R << 1$; this brings us to eq. 9.D.19 expressed as a function of ρ

$$\frac{\rho - \rho_S}{\rho_S} = -\left(\frac{\partial\gamma}{\partial\rho}\right)_S \frac{3\rho_S}{R_s B} \tag{9.D.37}$$

If we now insert this equation in eq. 9.D.11, we get

$$\omega_S = -P_S + \frac{1}{2}B\left(\frac{\rho_S - \rho}{\rho_S}\right)^2 = -P_S + \left(\frac{\partial\gamma}{\partial\rho}\right)^2 \frac{9\rho_S^2}{2R_s^2 B} \tag{9.D.38}$$

We only focus on the generalised Laplace equation when the inter-facial free energy differs from surface stress and the bulk modulus is large (see eq. 9.D.25). We insert eq. 9.D.8 and 9.D.38 into eq. 9.D.6 and get

$$\frac{2\gamma}{R_s} = \Delta\mu\rho_S\left(1 - \frac{\Delta\mu\rho_S}{2B}\right) - \left(\frac{\partial\gamma}{\partial\rho}\right)^2 \frac{9\rho_S^2}{2R_s^2 B} \tag{9.D.39}$$

Solving this equation for R_s, to the lowest order, in the incompressible case, $R_s \approx 2\gamma/(\Delta\mu\rho_S)$ and hence

$$\frac{2\gamma}{R_s} = \Delta\mu\rho_S\left(1 - \frac{\Delta\mu\rho_S}{2B}\right) - \left(\frac{\partial\gamma}{\partial\rho}\right)^2 \frac{9\rho_S^4\Delta\mu^2}{8\gamma^2 B} \tag{9.D.40}$$

$$= \Delta\mu\rho_S\left(1 - \frac{\Delta\mu\rho_S}{2B} - \left(\frac{\partial\gamma}{\partial\rho}\right)^2 \frac{9\rho_S^3\Delta\mu}{8\gamma^2 B}\right) \tag{9.D.41}$$

Therefore, the nucleation barrier in case of a not too compressible solid with a surface stress unequal to the inter-facial free energy is:

$$W_{COMP} = \frac{W_{INCOMP}}{\left(1 - \frac{\Delta\mu\rho_S}{2B} - \left(\frac{\partial\gamma}{\partial\rho}\right)^2 \frac{9\rho_S^3\Delta\mu}{8\gamma^2 B}\right)^2} \quad (9.D.42)$$

A more manageable form is obtained if we insert expression (9.D.37). Then

$$W_{COMP} = \frac{W_{INCOMP}}{\left(1 - \frac{\Delta\mu\rho_S}{2B} - \frac{1}{2}B\left(\frac{\epsilon^2}{\rho_S\Delta\mu}\right)\right)^2} \quad (9.D.43)$$

Comments on NaCl

First of all, we start noticing that the density of small NaCl clusters – both at coexistence and in the super-cooled regimes – is some 4% lower than the bulk density. This indicates a large negative surface stress, and it is consistent with our observations that the radius of the Gibbs equimolar dividing surface is smaller than the radius of the surface of tension that follows from the cluster analysis.

In particular, we can estimate the bulk modulus of NaCl through the volume fluctuations, obtaining $B \approx 15GPa$; the number density of the solid is $\rho_S = 0.0376$ Å^{-3} that in k_BT units is $\rho_s kT = 5\ 10^8 Pa$ at coexistence ($T_M = 1060K$). However, compressing a bulk solid to the pressure inside the cluster would increase its density by almost 2%. Hence, the value of ϵ that we should use in eq. 9.D.43 is almost 6%. Such a deformation results in an increase of the barrier height with respect to the incompressible case of about 25%!

Whilst this effect is non-negligible, it is not huge. It would correspond to an apparent increase in the inter-facial free energy of 16%. However, $\gamma_{\rm LS}$ would be decreased as the density of the cluster is lower than the bulk density. Roughly, this decreases $\gamma_{\rm LS}$ by 5%. Hence the net effect of the surface stress in NaCl is to increase the apparent $\gamma_{\rm LS}$ by 11%. This would corresponds to a $\gamma_{\rm LS}$ of around 70 erg/cm^2. This analysis is rather sensitive to the procedure we use to determine the density of the cluster. If we only look at the density within the core, we obtain the 4% expansion above mentioned. However, it may be more meaningful to compare the radius of the equimolar surface and the one of the surface of tension. If we do that, we get much larger values for ϵ.

Appendix E: Comparison with edge and corner free energies at 0 Kelvin

It is known that the surface energy at 0 Kelvin is different depending on the orientation of the surface itself. Wortis [201] computed, by means of analytical calculations, the energies of a [100], [110] and [111] surface for the Born-Mayer-Huggins[207] model potential (NaCl), obtaining 187, 349 and 659 mJ/m^2, respectively, showing that the cheaper surface was the [100]

one. However, the Wulff construction analysis on our clusters indicates that the influence of facets other than [100] on the overall inter-facial free energy is not relevant.

There obviously are directions other than [100] in the cluster surface: for a faceted cluster, that implies surface energy contributions coming from edges (where two facets meet) and corners (where three facets meet), not taken into account in the Wulff's construction analysis.

We start by analysing the surface energy dependence on the system size for a perfect cubic cluster in vacuum at zero Kelvin: we will consider a 2x2x2 crystal (64 atoms), 3x3x3 (216 atoms), 4x4x4 (512 atoms), and 9x9x9 (5832)(shown in fig.(9.4))

At these thermodynamic conditions, the total energy of a cubic shaped cluster is

$$e = e_B l^3 + 6e_S l^2 + 12e_E l + 8e_C \tag{9.E.1}$$

where e is the total internal energy per particle, e_S is the energy of a particle belonging to the surface, e_E the energy of a particle belonging to an edge, e_C the energy of a particle belonging to a corner of the cube, and l is the number of atoms per edge. The cube consists of 6 [100] facets.

To estimate e_B, we determine the energy per particle of an ideal periodic lattice with a unit cell spacing of 2.62Å, which minimises the total energy: we obtain $e_B = -64.5$ erg/atom [198]. For the calculation of e_S, e_E and e_C, we create a perfect cubic crystal of $2, 3, \ldots, 9$ unit cells and relax it. While the corner particles change their position significantly by about 0.5Å, the overall lattice spacing remains almost unchanged (5.59Å for the 2x2x2 crystal (64 atoms), 5.60Å for 3x3x3 (216 atoms) and 5.61Å for 4x4x4 (512 atoms) compared to 5.62Å for the bulk). This corresponds to a density change of less than 2%. To obtain e_S, e_E and e_C, we fit equation (9.E.1) to the measured relaxed energy, imposing e_B from the bulk crystal calculation. The difference of the fitted e to the measured one is less than 1%, and less than $.01\%$ for more than 4 unit cells. Expressing the surface energy in mJ/m^2, we find e_S=187

$e_S[10^{-13}$ erg/atom]	$e_E[10^{-13}$ erg/atom]	$e_C[10^{-13}$ erg/atom]	e_E/e_S	e_C/e_S
1.57	0.35	1.9	0.22	1.2

Table 9.E.1.: e_S is the energy of a particle belonging to the surface, e_E the energy of a particle belonging to an edge and e_C the energy of a particle belonging to a corner of the cube.

mJ/m^2, in perfect agreement with the calculation by van Zeggeren and Benson [208], that obtained e_S=188 mJ/m^2. Ignoring the edge and corner contributions does not change the surface energy significantly; to test this, we impose $e_E = e_C = 0$ in equation (9.E.1), and repeat the fits for e_S to obtain the apparent surface energy e'_S, that are shown in the following table(9.E.2) The 9x9x9 (5832) case can almost be considered a bulk system: there the system is so big that corners and edges do not play any role, differently from the 2x2x2 system. Moreover, the 9x9x9 result perfectly match the result obtained by Shi and Wortis[201] for the surface energy of the same system modelled with another interaction potential, the CDN I[209]. To conclude this analysis, we observe that for clusters of around 200 particles, typical cluster size that fits in our simulation box, these results indicate that the edge and corner contributions are negligible, as the cluster density changes by $\approx 1\%$ and the apparent surface energy differs by about 15% from that of a perfect surface.

unit cells	2	3	4	9
$e'_S[10^{-13}$ erg/atom]	1.90	1.78	1.72	1.62
e_S/e'_S	1.21	1.13	1.10	1.03

Table 9.E.2.: Surface energy of a particle with (e_S) and without (e'_S) edge and corners.

Appendix F: Comparison with experiments

As all the *microscopic* attempts to describe the crystallites have failed, we now try a different route. We expand $\gamma_{\rm LS}$ in terms of $1/R$, the curvature correction: the "effective" inter-facial free energy of a cluster of size N is then

$$\gamma_{LS,eff}(N) = \gamma_{LS,100} + \frac{c}{N^{1/3}} \tag{9.F.1}$$

where $\gamma_{LS,100}$ is the value numerically estimated by Zykova-Timan et al. [191] for a [100] flat NaCl surface by means of the Young's relation, and the second term is a correction due to the presence of edges in the cluster: here, c is a constant and N is the thermodynamic number of particles belonging to the cluster. As the surface of tension is the dividing surface where we observe the best convergence of our results to the asymptotic limit of infinite large cluster, in what follows we are going to use the surface of tension as the liquid-solid dividing surface. At the surface of tension $N = N_g$, being N_g the geometrical number of solid particles belonging to the biggest cluster. Therefore we can express eq. 9.F.1 in terms of N_g. If we now consider the value of $\gamma_{\rm LS}$ obtained at T_2=825K in chapter 4 as the effective inter-facial free energy at this super-saturation $\gamma_{LS,eff}(T_2) = 80$mJ/m^2, being N_g $\sim$125 particles, we find that $c = 220$. At last, we want to estimate the liquid-solid inter-facial free energy at the temperature where Buckle and Ubbelohde did the experiments [77]: $\gamma_{LS,eff}(T_{exp})$, where T_{exp}=905K. In order to estimate $\gamma_{LS,eff}$ we assume that clusters at T_2 and at T_{exp} have the same shape. Hence, as the critical cluster size is proportional to $\frac{\gamma_{\rm LS}^3}{(\rho_S \Delta\mu)^3}$, we can compute the number of particles a critical cluster would contain at T_{exp}:

$$\frac{N_1}{N_{exp}} = \frac{[\gamma_{LS,eff}(T_2)]^3}{(\rho_{S,2}\Delta\mu_2)^3} \frac{(\rho_{S,exp}\Delta\mu_{exp})^3}{[\gamma_{LS,eff}(T_{exp})]^3} \tag{9.F.2}$$

where $\rho_{S,2}$=0.0408 is the density of the solid, $\Delta\mu_2$=0.48 the super-saturation at T_2, $\rho_{S,exp}$=0.0402 the density of the solid and $\Delta\mu_{exp}$=0.3 the super-saturation at T_{exp}, and $\gamma_{LS,eff}(T_{exp})$=68 mJ/m^2 the experimental liquid-solid inter-facial free energy for a cubic critical cluster. Therefore, we obtain that N_{exp} $\sim$315. Considering the values of c and N_{exp} already computed, by means of eq. 9.F.1, we get that $\gamma_{LS,eff}(T_{exp})$=67 mJ/m^2, in prefect agreement with the experimental measurement. This founding corroborate our idea that γ_{LS} for a finite size cluster at coexistence should be higher than the one obtained by Zykova-Timan et al. [191] for a [100] flat NaCl surface by means of the Young's relation.

Part VII.

Homogeneous nucleation under shear

10. Study of homogeneous nucleation under shear in a 2D Ising model[1]

V'è fra gli uomini un detto antico molto,
che di nessuno tu potrai la vita conoscer mai, se fu felice o trista,
prima che muoia.
"Le Trachinie", Sofocle.

We report a numerical study of nucleation in a two-dimensional Ising model under shear. The system is studied using Forward Flux Sampling (FFS) and single-spin-flip Metropolis Monte Carlo dynamics. We find that the nucleation rate goes through a maximum and decreases for large shear rates. We argue that this behaviour is due to two competing effects: first of all, shearing a sub-critical cluster increases the number of kinks on its perimeter. The kinks are places where the growth of the cluster is favoured, therefore extra kinks increase the growth rate. This effect is essentially due to the discreteness of our system and appears to be linear for small values of the shear rate. Secondly, the nucleating cluster is deformed by the shear. This increases the perimeter-to-area ratio, and, therefore, the free-energy cost of nucleating a cluster of a given size. For geometric (symmetry) reasons this effect, which decreases the nucleation rate, is a symmetric function of the shear rate. We determine the transition state ensemble (TSE), and show that the TSE configurations exhibit a wide variation in surface and perimeter. This supports the view that the size of the biggest cluster is not a good reaction coordinate to study homogeneous nucleation under an external shear. We argue that the observed nucleation behaviour can be relevant for experiments on aggregation in viscous mixtures.

10.1. Introduction

The nucleation of a stable phase from a metastable one is a common process in nature. Already when the system is in *quasi*-equilibrium the nature of the metastable phase as well as the relaxation toward the stable phase is not so well understood. This mechanism results even less known in systems driven out of equilibrium such that the microscopic dynamics

[1] Work carried out in collaboration with R. J. Allen, S. Tănase-Nicola and P. R. ten Wolde.

do not satisfy detailed balance. In order to gain a better understanding of nucleation in non-equilibrium systems, we study this phenomenon in a two-dimensional Ising model under shear. The reason why we choose this system is that most of its equilibrium properties are known analytically. Moreover, it is computationally cheap.

Numerical studies of homogeneous nucleation in two and three-dimensional Ising systems without shear have been reported in the literature. In particular, Binder and Muller-Krumbhaar [210] obtained a detailed description of the nucleation process in a two-dimensional Ising system, and found that their simulations were incompatible with existing nucleation theories [211]. However, they found that a nucleation theory based on Fisher's cluster model [212] was consistent with both static and dynamic scaling results. Shneidman et al. [213, 214] investigated the kinetics of phase transitions of a two-dimensional Ising models on a triangular lattice. When they studied nucleation as a function of the degree of super-cooling, they found that a droplet-model based nucleation picture including the estimate of the kinetic pre-factor, was yielding good results at moderate under-coolings. Nucleation in the two-dimensional Ising model was simulated by Peters and Trout [215]. These authors showed that the "reaction coordinate" measuring the progress of the nucleation event, depends both on the size of the cluster and on the length of its perimeter. Interestingly, they found that a larger surface area increases the propensity a cluster in two dimensions grows but decreases it in three dimensions, presumably because a protrusion from a flat surface on the two-dimensional clusters tends to grow a new layer on the face, while for the three-dimensional system, a protrusion tends to disappear. Stauffer et al. [216] computed the nucleation rate in a three-dimensional Ising model as a function of super-saturation. Analysis of the results allowed them to estimate the surface tension of the droplets. Simulations at significantly lower temperatures than earlier numerical experiments [217] yielded good agreement with the predictions of Classical Nucleation Theory [218]. A similar conclusion was reached by Acharyya et al. [219], who analysed nucleation phenomena in the Ising system for various system sizes and dimensionalities. On the whole, their numerical results were consistent with the predictions of Classical Nucleation Theory. Brendel et al. [220] examined nucleation in the two-dimensional Ising model. In particular, they computed the free-energies barriers for nucleation. There results are consistent with the predictions of the Becker-Döring expression [5], provided the assumption of an effective surface tension that exceeds the macroscopic surface tension by up to 20%. Wonczak et al. [221] examined the same system and found good agreement with the Gibbs-Thomson relation for cubical instead of spherical clusters. Pan and Chandler [222] studied the three-dimensional Ising model by means of transition-path sampling [39] of single spin flip Monte Carlo dynamics. These authors analysed the transition state ensembles and showed that the critical clusters are rough and anisotropic. They also demonstrated that the cluster size and their surface area might not be enough to fully describe the nucleation phenomenon. All the above-mentioned authors considered the case of a two or three-dimensional Ising system in a uniform magnetic field and studied the nucleation of the stable phase (for instance up spins) from the metastable down-spins phase.

In the present study, we choose to drive the system out of equilibrium by applying an external, macroscopic, shear. This type of non-equilibrium dynamics is rather artificial in the context of the Ising model. However, it may be viewed as a rough description of the

experimental situations of droplet nucleation in emulsions [223]. In the present study, we use this model merely as a test case to study the basic features of activated processes in systems driven out of equilibrium.

Homogeneous nucleation is a *rare event*. We study this phenomenon using Forward Flux Sampling (FFS) [13] as this method can also easily be applied to systems that are driven out of equilibrium [224]. In contrast, algorithms based on Umbrella Sampling, transition-path sampling or (partial-path) transition-interface sampling, are limited to systems in thermodynamic (quasi)equilibrium.

In an earlier study (see chapter 3) we had shown that FFS can reproduce the known homogeneous nucleation behaviour of a two-dimensional Ising model without external driving fields. Below, we show that an applied shear strongly influences the nucleation pathways in the Ising system. As in the equilibrium case, the relaxation from the metastable phase takes place through the nucleation of a cluster of the stable state. However in the non-equilibrium case the nucleation rate has a non-trivial dependence on the shear rate.

10.2. Simulation details

We consider a two-dimensional Ising model consisting of an $L \times L$ square lattice of spins with nearest-neighbour interactions and periodic boundary conditions. The Ising Hamiltonian is

$$H = -J \sum_{ij}{}' \sigma_i \sigma_j - h \sum_i \sigma_i, \tag{10.1}$$

where J is the coupling constant between neighbouring spins ($\sigma_i = \pm 1$) and h the external magnetic field. The prime indicates that the sum is restricted to nearest-neighbour interactions.

All of our simulations are performed using a Metropolis spin-flip Monte Carlo dynamics, in which we randomly choose a spin and attempt to flip it. The spin flip is accepted or rejected according to the Metropolis rule. One Monte Carlo cycle corresponds to N attempts where N is the number of spins. We simulate a 65×65 lattice with periodic boundary conditions in the x and y directions. We use parameter values $h = 0.05 k_B T$ and $J = 0.65 k_B T$, above the critical coupling J_c. The thermodynamically stable state is therefore a ferromagnetic one with net positive magnetisation, meaning that the system tends to have the majority of its spins in the up-spins state. Hence, an initial state with an overall negative magnetisation (*i.e.* spins predominantly in the down-spins state) is metastable and a system prepared as such will remain in that state for a significant time.

In the absence of shear, this system is the same as the one investigated in chapter 3 and ref. [68], except that in the present work we use a larger box size. We chose a larger box size because we found that the nucleation rate is more sensitive to system size in the presence of shear. We find no evidence for finite-size effects in the $L = 65 \times 65$ spins system, at least, not for the shear rates used in this study. We apply a shear using a method based on the one proposed by Cirillo et al. [225] (see appendix A). As we consider rare fluctuations between two regions of state space A and B, being state A the initial metastable state mainly

characterised by down spins and B the final stable state with the overall *up* spins, we use FFS to study the transition fro A to B. According to the FFS prescription, the regions A and B are defined in terms of an order parameter $\lambda(x)$ (being x the phase space coordinates) such that the system is in state A if $\lambda(x) < \lambda_0$ (state A boundary), and it is in state B if $\lambda(x) > \lambda_n$ (state B boundary). For the system studied in this chapter, the λ parameter is chosen to be N_{up}, the total number of *up* spins. FFS calculations are carried out with 39 interfaces, defining the A state at $\lambda < \lambda_0$ where $\lambda_0 = 25$ *up* spins, and the B state at $\lambda > \lambda_n$ where $\lambda_n = 2005$ *up* spins. The rate constant R_{AB} can then be obtained as in eq. 2.53. By tracing back paths that successfully arrive at λ_n, we can sample the transition path ensemble for the rare event. Analysis of these paths can lead to insight into the mechanism by which the event occurs.

We use $N_1 = 1000$ points at the first interface and repeat the sampling 25 times to obtain the error bars. The positions λ_i of the interfaces and the number of trials M_i shot at each interface are given in table 10.1.

i	λ_i	M_i	i	λ_i	M_i	i	λ_i	M_i
0	25	6000	13	86	4000	26	171	3000
1	30	7000	14	91	4000	27	181	3000
2	35	8000	15	96	4000	28	191	3000
3	40	6000	16	101	3000	29	201	3000
4	44	7000	17	106	1300	30	302	3000
5	49	5000	18	111	3000	31	405	3000
6	53	6000	19	116	3000	32	605	3000
7	57	5000	20	121	3000	33	805	3000
8	61	5000	21	126	3000	34	1005	3000
9	66	5000	22	131	3000	35	1205	3000
10	71	5000	23	141	3000	36	1405	3000
11	76	4000	24	151	3000	37	1605	3000
12	81	4000	25	161	3000	38	1805	3000

Table 10.1.: Positions of the interfaces λ_i and the number of trials at each interface M_i used to study homogeneous nucleation in a two-dimensional Ising model under shear.

With FFS, it is possible to compute stationary distributions for activated processes, both in equilibrium and in driven systems. However, this method requires that one can simulate both the forward and backward reactions (see chapter 3).. We find that backwards reactions are extremely rare in the presence of shear. Rather, we compute the steady-state distribution for a system under shear with an *absorbing boundary*. That means that we terminate the simulation as soon as the final up-spins state is reached, and start a new one from the metastable down state.

10.3. Results

Fig. 10.1 shows the nucleation rate R as a function of the shear rate $\dot{\gamma}$. At zero shear rate, the value of R is in good agreement with the value of 3.3×10^{-13} per MC cycle per site obtained by Sear [68]. For small shear rates R appears to increase linearly with $\dot{\gamma}$ by an order of magnitude, before reaching a maximum value around $\dot{\gamma} = 0.06$. At that point, for an even larger shear rate, R starts decreasing again. Such behaviour may be qualitatively understood as follows:

1. first, shearing a sub-critical cluster increases the number of kinks on its perimeter. The kinks are places where the growth of the cluster is favoured, therefore extra kinks increase the growth rate. This effect is essentially due to the discreteness of our system and seems to be linear for small values of the shear rate;

2. at higher shear, the nucleating cluster becomes increasingly deformed. This increases the perimeter-to-area ratio, leading to an effective decrease of the nucleation rate: further growth of the cluster is strongly disfavoured, as growing clusters tend to be broken up by the shear.

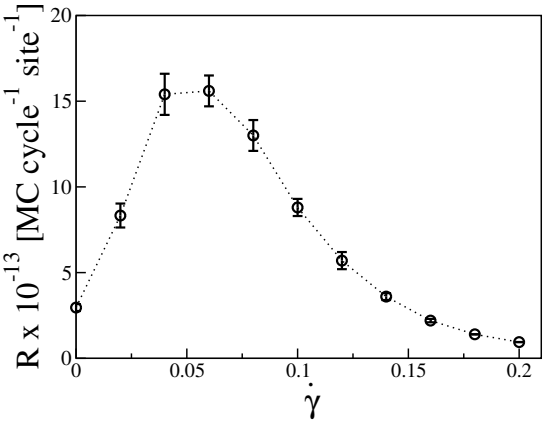

Figure 10.1.: Nucleation rate R per MC cycle and per lattice site for a range of values of $\dot{\gamma}$, for $\beta J = 0.65$, $\beta h = 0.05$ and $L_x = L_y = 65$.

In what follows, we analyse the transition path ensemble, using two order parameters: the size of the biggest cluster of up spins N_c and its perimeter P_c. We focus on three values of the shear rate: zero shear rate ($\dot{\gamma} = 0.0$), moderate shear rate ($\dot{\gamma} = 0.06$), before the maximum of the nucleation rate in fig. 10.1, and high shear rate ($\dot{\gamma} = 0.12$). Figure 10.2 shows a selection of configurations appearing on transition paths, for $\dot{\gamma} = 0$ and $\dot{\gamma} = 0.06$, plotted as a function of both N_c and P_c.

In panel (a), for the case of zero shear, the inset shows that P_c increases approximately as $N_c^{1/2}$, as expected for a shape that grows isomorphically by expansion in all directions:

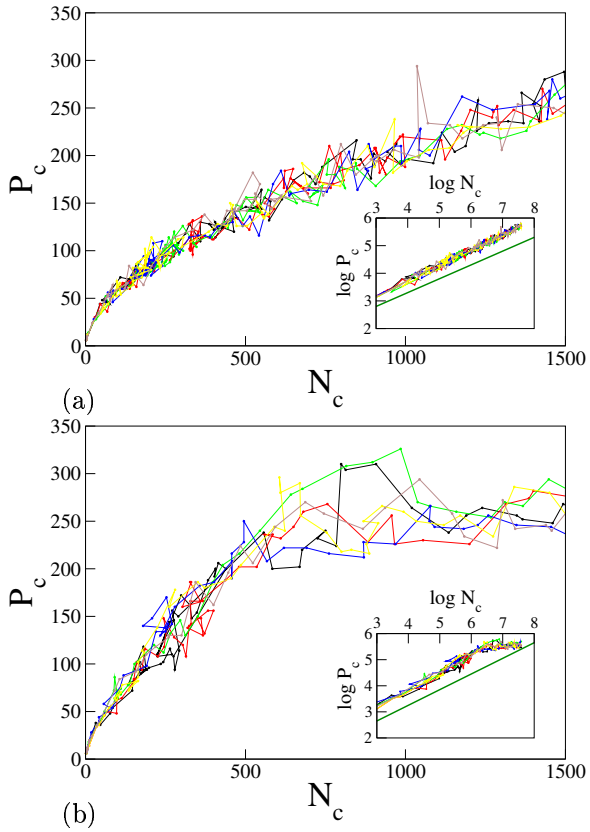

Figure 10.2.: Six transition paths as a function of the biggest cluster size N_c and its P_c for the no shear rate case $\dot{\gamma} = 0.0$ (panel a) and the shear rate corresponding to the maximum of the nucleation rate $\dot{\gamma} = 0.06$ (panel b). Each transition path is represented by a series of coloured dots and continuous line. The insets show paths as functions of $\log P_c$ and $\log N_c$ - the solid lines correspond to $P_c = N_c^{1/2}$.

Peters and Trout [215] observed the same scaling behaviour, that is also in agreement with Classical Nucleation Theory. In panel (b), we present the sheared system with $\dot{\gamma} = 0.06$. We observe that in this case the perimeter of the cluster grows more rapidly with N_c than for the zero shear case. This indicates that the perimeter is rougher and has more kinks. For $N_c > 750$, P_c reaches a plateau, meaning that at this point, the elongated cluster stretches right across the simulation box along the direction of shear (see figure 10.4).

We also measure the distributions of the lengths τ of the transitions paths, for the same $\dot{\gamma} = 0$, $\dot{\gamma} = 0.06$ and $\dot{\gamma} = 0.12$. Figure 10.3 shows the distribution of τ, expressed in MC cycles. The figure shows that the phase transition occurs much more rapidly in the presence of shear. Moreover, the distribution of path lengths gets narrower the higher the applied shear.

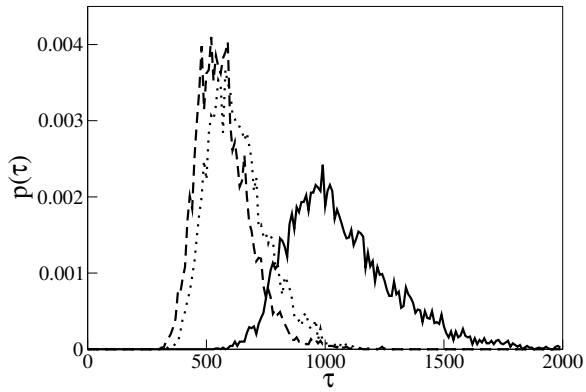

Figure 10.3.: Distribution of transition path lengths τ (in MC cycles) for $\dot{\gamma} = 0.0$ (solid line), $\dot{\gamma} = 0.06$ (dotted line) and $\dot{\gamma} = 0.12$ (dashed line).

To understand better the nucleation mechanism in the presence of shear, we have extracted members of the transition state ensemble (TSE) from the transition paths [1].

To determine the TSE, we follow the same procedure described by Pan and Chandler [222].

1. We check every 10Th configuration along each transition path, and then initiate a series of trajectories from that configuration.

2. After 11, 14, 17, 20, 25, 30, 35, 42, 49 and 100 trajectories, we check whether the ratio of trajectories ending in B to the total trajectories is 0.5, to within a 95% confidence interval.

3. If not, we terminate the procedure.

The purpose of this is simply to avoid firing a large number of unnecessary trajectories for configurations with P_B far from 0.5. Using this procedure, we obtain 3472 TSE configurations for $\dot{\gamma} = 0.0$, 959 for $\dot{\gamma} = 0.06$ and 6135 for $\dot{\gamma} = 0.06$. Fig. 10.4 shows typical snapshots from the transition-state ensemble, for zero shear rate $\dot{\gamma} = 0.0$, low shear rate $\dot{\gamma} = 0.06$ and high shear rate $\dot{\gamma} = 0.12$.

It is evident that the critical clusters become larger and more elongated in the presence of shear. Sheared clusters are also less compact (as illustrated by the branches in fig. 10.4c), which might explain the reason why P_c increases faster with N_c in the presence of shear in fig. 10.2. It is clear from the preceding analysis and especially from the snapshots of fig. 10.4

[1] These are the configurations X in the transition paths for which the probability of a path starting in X, to reach the state B before reaching the state A – called committor probability, P_B – is 50%. This means that if a large number of new trajectories are initiated from this point, on average half of them will reach the B state while the other half reach A.

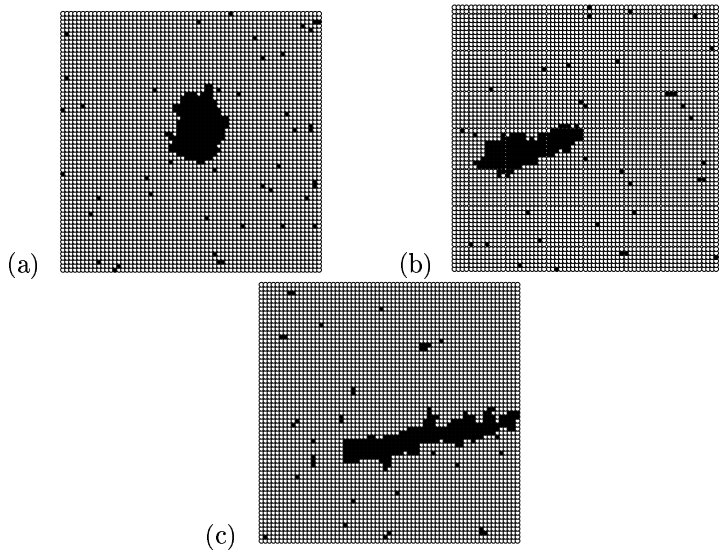

Figure 10.4.: Typical configurations from TSE. Panel (a) corresponds to $\dot{\gamma} = 0.0$, panel (b) to $\dot{\gamma} = 0.06$ and panel (c) to $\dot{\gamma} = 0.12$.

that shear causes the TSE configurations to both elongate and align in the direction of the shear.

In fig. 10.5, we plot the distribution of points in the TSE as a function of the size N_c and perimeter P_c of the biggest cluster for $\dot{\gamma} = 0.0$, $\dot{\gamma} = 0.06$ and $\dot{\gamma} = 0.12$. For $\dot{\gamma} = 0.0$, the TSE points are rather densely clustered, indicating that N_c is a useful order parameter to study the phase transition. It also indicates that the critical clusters all have similar shape. However, this picture changes dramatically in the presence of shear. The effect of shear is to smear out the TSE distribution. For $\dot{\gamma} = 0.12$, the TSE points cover a wide range of N_c and P_c, suggesting that these order parameters are no longer good order parameters to describe nucleation of an island of up spins in a see of down spins.

To try to characterise the mechanism for nucleation in the presence of shear, we plot the distribution of various order parameters over the TSE points in fig. 10.6.

Figure 10.6a shows the distribution of the biggest cluster sizes N_c for points in the TSE. We notice that the average critical cluster size varies non-monotonically with the shear rate. The width of the distribution, however, increases with $\dot{\gamma}$, indicating that while N_c may be a good descriptor of the transition mechanism for the zero shear case, it increasingly fails to characterise the mechanism as the shear rate increases. Figure 10.6b shows a similar characterisation of the perimeter P_c of the biggest cluster for the TSE configurations. The critical clusters are quite uniform in shape for the zero shear case, but become increasingly non-uniform as $\dot{\gamma}$ increases. The average perimeter of the biggest cluster monotonically increases, as it might be expected from the typical configurations shown in fig. 10.4. This

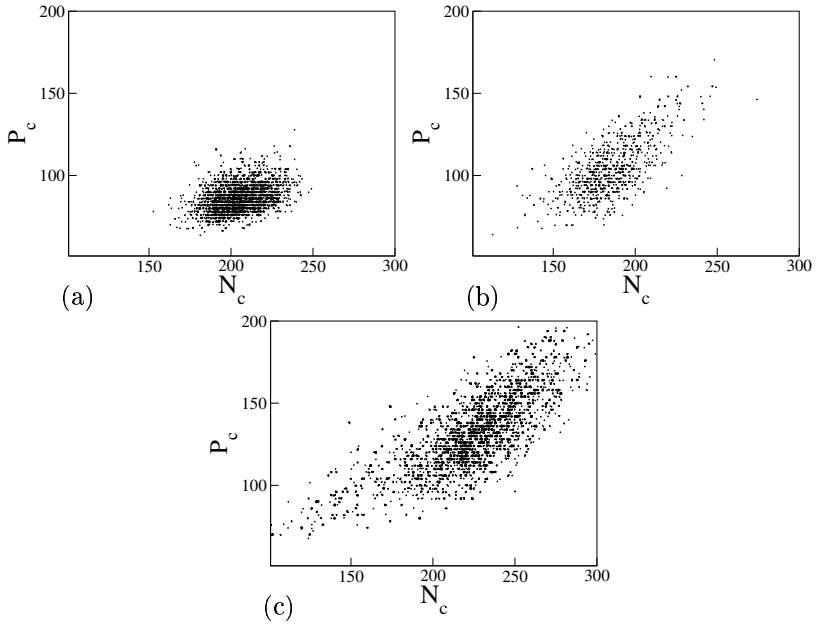

Figure 10.5.: Points in the TSE, projected onto N_c-P_c. Panel (a) corresponds to $\dot{\gamma} = 0.0$, panel (b) to $\dot{\gamma} = 0.06$ and panel (c) to $\dot{\gamma} = 0.12$.

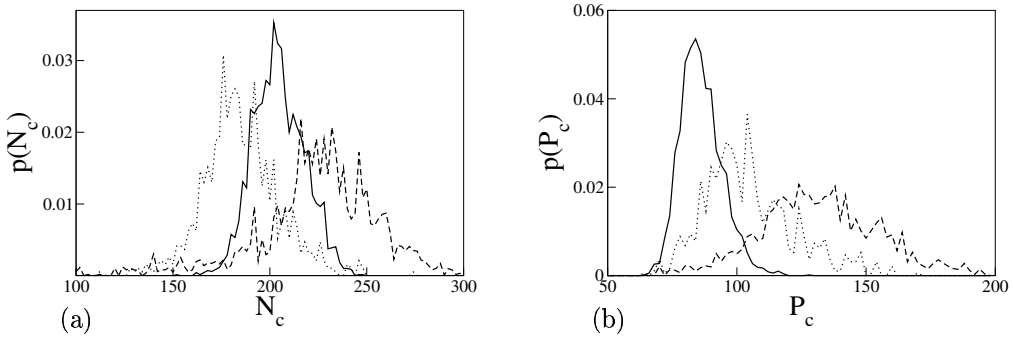

Figure 10.6.: Distributions of the biggest cluster sizes N_c (panel (a)) and perimeters P_c of the biggest cluster (panel(b)) for points in the TSE, for shear rates $\dot{\gamma} = 0.0$ (continuous line), $\dot{\gamma} = 0.06$ (dotted line) and $\dot{\gamma} = 0.12$ (dashed line).

indicates that a CNT-type analysis, in which the shape of the growing cluster is assumed to be circular, will certainly fail in the presence of shear.

In order to check the validity of the chosen order parameter, we have also used FFS to calculate stationary distribution functions $\rho(N_c, P_c)$ according to chapter 3 for a system with an "absorbing" boundary condition [2]. In figure 10.7, we plot $-\log \rho(N_c, P_c)$, and superimpose the scatter plots of fig. 10.5 for the TSE points, for the two cases of $\dot{\gamma} = 0$ and $\dot{\gamma} = 0.12$. Firstly, it is clear that $\rho(N_c, P_c)$ is strongly affected by the shear, being shifted toward clusters

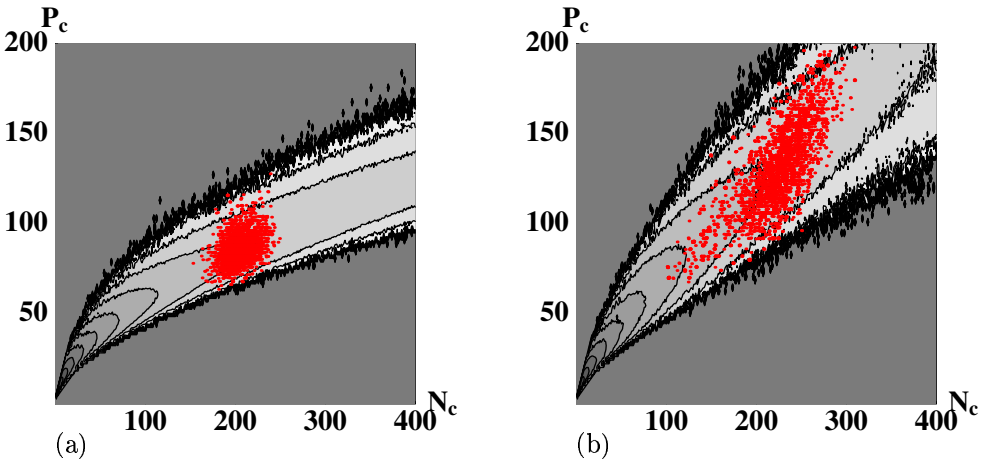

Figure 10.7.: $-\log \rho(N_c, P_c)$ (contour lines spaced at intervals of 2.5), together with members of the TSE (red dots). Panel (a) corresponds to $\dot{\gamma} = 0.0$, panel (b) to $\dot{\gamma} = 0.12$.

with larger perimeters. For $\dot{\gamma} = 0$, the TSE does appear to correspond quite closely to the main "exit channel" from the metastable state. However, for $\dot{\gamma} = 0.12$, although the TSE still lies within the "exit channel", it is very much more spread out and, moreover, is not longer oriented perpendicular to the contour lines of $-\log \rho(N_c, P_c)$. This seems to indicate either that N_c and P_c no longer provide enough information to describe the transition mechanism, not being *THE* relevant reaction coordinates for the transition, or that the transition paths do not follow the stationary distribution function in the presence of shear.

10.4. Conclusions

We have studied the nucleation in a two-dimensional Ising system with an imposed external shear using Forward Flux Sampling. This method is suited to simulate rare events systems in non-equilibrium steady-states.

We observe that for a large shear rate, the nucleation rate R decreases with the applied shear. This behaviour could be explained using an analogy with the equilibrium system. In figure 10.4 we can see that the shear deforms the growing cluster by imposing an elongation

[2] Such a calculation yields the average occupation of a region of phase space for trajectories that originate in the metastable down state and terminate upon entering the up-spins state.

along the shear direction. As a consequence, for the same number of spins in the cluster under shear, the perimeter is larger under a finite shear that at zero shear (when the cluster is more or less isotropic). Therefore the "free-energy barrier" will be larger under shear, thus decreasing the nucleation rate. This "macroscopic" deformation is independent of the direction of the shear, and has, for symmetry reasons, to depend on even powers of the shear rate.

Nevertheless, we can see from figure 10.2 that the perimeter of the growing cluster does not scale uniformly with its surface but somewhat faster. This indicates either an increased anisotropy or an increase of the roughness of the cluster's perimeter. A non-uniform perimeter would contain more kinks, or concave regions where down spins will have an advantage in flipping and thus increasing the size of the cluster. This effect would enhance the nucleation rate. Indeed, we observe that at low shear the nucleation rate increases. This interpretation is in agreement with all our results. To summarise:

1. for moderate shear rates we observe a positive and linear increase in the nucleation rate, as an effect of the discreteness of the system under study;

2. at moderate and high shear rates we observe an increased diffusion in the size of the clusters, therefore nucleation paths are shorter in time;

3. at moderate shear rates the increase of the perimeter of TSE clusters corresponds to a decrease of their size, as seen in fig. 10.6.

4. at high shear rates, the nucleation rate R decreases as the shear deforms the growing cluster, and this is independent of the direction of the shear.

We suggest that the clusters roughness (number of concave kinks in the growing clusters) might be a better order parameter together with the biggest cluster size to study the nucleation phenomenon. Indeed, with the additional driving from the kinks, the cluster should need less bulk "free energy" to commit to the up-spins phase. This additional parameter strongly influences the nucleation dynamics and could explain the increased spread of the TSE clusters in figures 10.5 and 10.7.

In conclusion, at moderated shear the nucleation rate increases due to a microscopic effect of kink creation. This effect has less to do with the macroscopic shear and corresponds more to a induced non-equilibrium microscopic disorder, more along the lines of the model of Hurtado [226, 227]. On the other hand the macroscopic shear increases the size of the critical cluster and the nucleation barrier, decreasing the nucleation rate, but only as a higher order effect in the shear rate.

It would be interesting to experimentally study the surface of the nucleating droplet, as we predict rougher droplets that could even increase the nucleation rate at low shear. We stress that our conclusions cannot be extended to crystal nucleation phenomena, as we have completely neglected the hydrodynamics interactions and we imposed an "artificial" shear to the system, such that it cannot respond to the external applied shear.

Acknowledgements

Concerning this work, I would like to thank R. Allen for most of the computation of this work.

Appendix A: Shear algorithm

The shear algorithm is characterised by two parameters, N_s and P_s, being N_s the number of steps and P_s the probability to shear, and it is described as follows:

1. after each Monte Carlo cycle, we carry out a series of $N_s \times L$ attempts to shear the system;
2. in each attempt, we carry out a "shearing step" with probability P_s;
3. in a shearing step, we choose a row j_s at random from the lattice, and all lattice sites with $j > j_s$ are then shifted to the right by **one** lattice site.
4. At the end of each shearing step we update the relevant part of the neighbour list [3].

The results of one row shift are illustrated in fig.10.A.1.

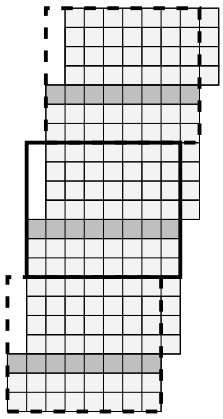

Figure 10.A.1.: Illustration of a row shift in the shearing algorithm. In this sketch, the box size is $L = 7$ (surrounded by a thick line) - $L = 65$ in the simulations. The row shaded grey is the one that is shifted. All rows above it are shifted to the right by one lattice site. The images of the system which lie above and below in the periodic lattice (shown with dotted borders) have been shifted forwards and backwards, respectively, by one lattice site.

In this scheme, rows that have larger j values will be shifted more often to the right; therefore the net result is a "velocity gradient" linear in y: the average number of times that row j is shifted per MC cycle is $N_s P_s j$, so that the shear rate is $\dot{\gamma} = N_s P_s$. In contrast to the work of Cirillo [225], we do not shift by more than one lattice site in any shear step, but instead use multiple shear steps per MC cycle to achieve high shear rates. [4]

[3] we should not only store the spins of all the lattice sites, but also information on the current state of the neighbour lists, since these are shifted by an amount that depends on the history of the shearing.

[4] The nucleation dynamics depends on the precise method used for implementing the shear. We have found that increasing the size of the shear step at constant shear rate decreases the nucleation

rate.

Bibliography

[1] D. B. Fahrenheit, *Phil. Trans. Roy. Soc.* **39**, 78 (1724).

[2] J. L. Gay Lussac, *Ann. de. Chemie* **87**, 225 (1813); *Ann. de. Chemie* **11**, 296 (1819).

[3] J. W. Gibbs, *Trans. Connect. Acad.* **3**, 108 (11878).

[4] M. Volmer and A. Weber, *Z. Phys. Chem.* **119**, 227 (1926).

[5] R. Becker and W. Döring, *Ann. Phys.* **24**, 719 (1935).

[6] K. F. Kelton, *Crystal Nucleation in Liquids and Glasses* **45**, 75-177, Academic Press, Boston (1991).

[7] D. W. Oxtoby and R. Evans, *J. Chem. Phys.* **89**, 833 (1988).

[8] D. Oxtoby, *Acc. Chem. Res.* **31**, 91 (1998).

[9] J. B. Anderson, *J. Chem. Phys.* **58**, 4684 (1973).

[10] D. Chandler, *J. Chem. Phys.* **68**, 2959 (1978); C. H. Bennett, *Algorithms for Chemical Computations*, ACS Symposium, Series No.46, Americal Chemical Society, Washington D.C. (1977).

[11] J. S. van Duijneveld and D. Frenkel, *J. Chem. Phys.* **96**, 4655 (1992).

[12] G. M. Torrie and J. P. Valleau, *Chem. Phys. Lett.* **28**, 578 (1974).

[13] R. J. Allen, P. B. Warren, and P. R. ten Wolde, *Phys. Rev. Lett.* **94**, 018104 (2005).

[14] R. J. Allen, D. Frenkel, and P. R. ten Wolde, *J. Chem. Phys.* **124**, 024102 (2006).

[15] R. J. Allen, D. Frenkel, and P. R. ten Wolde, *J. Chem. Phys.* **124**, 194111 (2006).

[16] I. N. Stransky and D. Totomanow, *Z. Phys. Chem.* **163**, 399 (1933).

[17] A. -P. Hynninen, M. E. Leunissen, A. van Blaaderen, and M.Dijkstra, *Phys. Rev. Lett.* **96**, 018303 (2006).

[18] T. Zykova-Timan, U. Tartaglino, D. Ceresoli, and E. Tosatti, *Surface Science* **566**, 794-798 Part 2 (2004).

[19] P. M. Chaikin and T.C. Lubensky, *Principles of Condensed Matter Physics*, Cambridge University Press, Cambridge (1995).

[20] J. W. Gibbs, **The Scientific Papers of J. Willard Gibbs**, Volume **I**: Thermodynamics, Ox Bow Press, Woodbridge (1993).

[21] J. D. Gunton, M. San Miguel P. S. Sahni, *Phase transitions and critical phenomena*, C. Domb and J. L. Lebowitz edition, Volume **VIII**, Academic Press, New York (1983).

[22] J. W. Cahn and J. E. Hilliard, *J. Chem. Phys.* **28**, 258 (1957).

[23] P. P. Wegener, *Acta Mech.* **21**, 65 (1975).

[24] R. C. Reid, *Amer. Sci.* **64**, 146 (1976).

[25] A. I. Berezhnoi, *Glass-Ceramics and Photo-Sitalls*, Plenum Press, New York (1970).

[26] L. Farkas, *Z. Phys. Chem.* **125**, 236 (1927).

[27] D. Turnbull and J. C. Fisher, *J. Chem. Phys.* **17**, 71 (1949).

[28] P. R.ten Wolde, M. J. Ruiz-Montero, and D. Frenkel, *J. Chem. Phys.* **104**, 9932 (1996).

[29] P. R. ten Wolde, M. J. Ruiz-Montero, and D. Frenkel, *Faraday Discuss.* **104**, 93 (1996).

[30] J. L. Katz, *Pure & Appl. Chem.* **64**, 1661 (1992).

[31] N. G. van Kampen, *Stochastic processes in Physics and Chemistry*, North Holland, Amsterdam (1981).

[32] D. W. Oxtoby, *J. Phys. Cond. Matt.* **4**, 7627 (1992).

[33] J. Zeldovitch, *J. Expr. Theor. Phys.* (Russia) **12**, 525 (1942).

[34] W. C. Swope and H. C. Andersen, *Phys. Rev. B* **41**, 7042 (1990).

[35] P. Bolhuis, C. Dellago, D. Chandler, and P. L. Geissler, *Transition Path Sampling*, *Advances in Chemical Physics*, Wiley, New York (2001); P. G. Bolhuis, D. Chandler, C. Dellago, and P. L. Geissler, *Ann. Rev. Phys. Chem.* **53**, 291 (2002).

[36] R. Du, V. Pande, A. Y. Grosberg, T. Tanake, and E. S. Shakhnovich, *J. Chem. Phys.* **108**, 334 (1998).

[37] P. G. Bolhuis, C. Dellago, and D. Chandler, *Proc. Nat. Ac. of Science* **97**, 5877 (2000).

[38] L. R. Pratt, *J. Chem. Phys.* **85**, 5045 (1986).

[39] C. Dellago, P. Bolhuis, F. Csajka, and D. Chandler, *J. Chem. Phys.* **108**, 1964 (1998); C. Dellago, P. Bolhuis, and D. Chandler, *J. Chem. Phys.* **108**, 9236 (1998); C. Dellago, P. G. Bolhuis, and P. L. Geissler, *Adv. Chem. Phys.* **123**, 1 (2002).

[40] D. Moroni, *Efficient sampling of rare event pathways*, University of Amtserdam (2005). It can be downloaded from:
$http://www.science.uva.nl/\ moroni/thesis.html$.

[41] T. S. van Erp, D. Moroni, and P. G. Bolhuis, *J. Chem. Phys.* **118**, 7762 (2003); T. S. van Erp and P. G. Bolhuis, *J. Chem. Phys.* **205**, 157 (2005).

[42] D. Moroni, T. S. van Erp, and P. G. Bolhuis, *Physica A* **340**, 395 (2004).

[43] D. Moroni, P. G. Bolhuis, and T. S. van Erp, *J. Chem. Phys.* **120**, 4055 (2004).

[44] D. Moroni, T. S. van Erp, and P. G. Bolhuis, *Phys. Rev. E* **71**, 056709 (2005).

[45] D. Moroni, P. R. ten Wolde, and P. G. Bolhuis, *Phys. Rev. Lett.* **94**, 235703 (2005).

[46] A. K. Faradjian and R. Elber, *J. Chem. Phys.* **120**, 10880 (2004).

[47] W. E, W. Ren and E. Vanden-Eijnden, *Phys. Rev. B* **66**, 052301 (2002).

[48] L. Maragliano, A. Fischer, and E. Vanden-Eijnden, *J. Chem. Phys.* **125**, 024106 (2006).

[49] E. A. Carter, G. Ciccotti, J. T. Hynes, and R. Kapral, *Chem. Phys. Lett.* **156**, 472 (1989).

[50] C. Ciccotti and M. Ferrario, *Mol. Sim.* **30**, 787 (2004).

[51] A. Laio, and M. Parrinello, *Proc. Nat. Ac. of Science* **99**, 12562 (2002); B. Ensing, A. Laio, M. Parrinello, and M. L. Klein, *J. Phys. Chem.* **109**, 6676 (2005).

[52] D. Donadio, P. Raiteri, and M. Parrinello, *J. Phys. Chem. B* **109**, 5421 (2005).

[53] F. Trudu, D. Donadio, and M. Parrinello, *Phys. Rev. Lett.* **97**, 105701 (2006).

[54] R. Radhakrishnan and B. L. Trout, *J. Am. Chem. Soc.* **125**, 7743 (2003).

[55] J. Wedekind, R Strey, and David Reguera, *J. Chem. Phys.* **126**, 134103 (2007).

[56] B. Peters and B. L. Trout, *J. Chem. Phys.* **125**, 054108 (2006).

[57] M. Chopra, M. Muller, and J. de Pablo, *J. Chem. Phys.* **124**, 134102 (2006).

[58] T. S. van Erp and P. G. Bolhuis, *J. Comp. Phys.* **205**, 157 (2005).

[59] M. J. Ruiz-Montero, D. Frenkel, and J. Brey, *Mol. Phys.* **90**, 925 (1997).

[60] R. M. Lynden-Bell, J. S. Van Duijvendelt, and D. Frenkel, *Mol. Phys.* **80**, 801 (1993).

[61] W. H Press, *Numerical recipes in FORTRAN : the art of scientific computing*, Cambridge University Press (1992).

[62] H. Flyvbjerg and H. G. Petersen, *J. Chem. Phys.* **91**, 461 (1989).

[63] S. Auer and D. Frenkel, *J. Phys. Cond. Matt.* **14**, 7667 (2002).

[64] P. J. Steinhardt, D. R. Nelson, and M. Ronchetti, *Phys. Rev. B* **28**, 784 (1983).

[65] P. R. ten Wolde, *Numerical studies of pathways for homogeneous nucleation*, University of Amsterdam (1998). It can be downloaded from: $http://www.amolf.nl/publications/theses/wolde/tenwolde\_begin\_p1\_8.pdf$.

[66] S. Auer and D. Frenkel, *Nature* **409**, 1020 (2001).

[67] L. Landau and E. Lifchitz, *Physique Statistique*, Volume **V**, MIR edition, Moscow (1984).

[68] R. P. Sear, *J. Phys. Chem. B* **110**, 4985 (2006).

[69] J. W. Cahn and J. E. Hilliard, *J. Chem. Phys.* **28**, 258 (1958).

[70] D. Frenkel and B. Smit, *Understanding Molecular Simulation. From Algorithms to Applications*, Academic Press, Boston (1996 1st Ed) (2002, 2nd Ed).

[71] M. P. Allen and D. J. Tildesley, *Computer Simulation of Liquids* , Oxford University Press, USA; reprint edition (February 11, 1988).

[72] C. Dellago, P. G. Bolhuis, and P. L. Geissler, *Adv. Chem. Phys.* **123**, 1 (2002).

[73] P. B. Warren and P. R. ten Wolde, *J. Chem. Phys.* **109**, 6812 (2005).

[74] R. S. Maier and D. L. Stein, *Phys. Rev. Lett.* **69**, 3691 (1992); R. S. Maier and D. L. Stein, *J. Stat. Phys.* **83**, 291 (1996); R. S. Maier and D. L. Stein, *Phys. Rev. E* **48**, 931 (1993).

[75] K. Binder, *Ising Model*, *Encyclopaedia of Mathematics*, SpringerLink (2001).

[76] L. Onsager, *Phys. Rev.* **65**, 117 (1944).

[77] E. R. Buckle and A. R. Ubbelohde, *Proc. R. Soc. London, Ser. A* **529**, 325 (1960);*Proc. R. Soc. London, Ser. A* **261**, 197 (1961).

[78] E. R. Buckle, *Proc. R. Soc. London, Ser. A* **261**, 189 (1961).

[79] J. Huang, X. Zhu and L. S. Bartell, *J. Phys. Chem. A* **102**, 2708 (1998).

[80] T. Koishi, K. Yasuoka, and T. Ebisuzaki, *J. Chem. Phys.* **119**, 11298 (2003).

[81] F. Fumi and M. Tosi, *J. Phys. Chem. Solids* **25**, 31 (1964); M. Tosi and F. Fumi, *J. Phys. Chem. Solids* **25**, 45 (1964).

[82] P. P. Ewald, *Ann. Phys.* (Leipzig) (**64**), 253 (1921).

[83] J. P. Hansen and I. R. Mc Donald, *Theory of simple liquids*, Academic Press (2006, 3rd Ed).

[84] G. J. Janz, *Molten Salt Handbook*, Academic Press, New York (1967).

[85] J. Anwar, D. Frenkel, and M. Noro, *J. Chem. Phys.* **188**, 728 (2003).

[86] J. D. Honeycutt and H. C. Andersen, *Chem. Phys. Lett.* **108**, 535 (1984).

[87] P. R. ten Wolde and D. Frenkel, *J. Chem. Phys.* **109**, 9901 (1998).

[88] S. Auer and D. Frenkel, *J. Chem. Phys.* **120**, 3015 (2004).

[89] D. Turnbull, *J. Chem. Phys.* **18**, 198 (1950);D. Turnbull, *J. Appl. Phys.* **21**, 1022 (1950).

[90] P. Balk and G. C. Benson, *J. Phys. Chem.* **63**, 1009 (1959).

[91] J. C. Heyraud and J. J. Métois, *J. Cryst. Growth* **82**, 269 (1987).

[92] W. Ostwald, *Z. Phys. Chem.* **22**, 289 (1897).

[93] W. Smith and T. Forester, *J. Mol. Graphics* **14**, 136 (1996).

[94] J. O. M. Bockris, S. R. Richards, and L. Nanis, *J. Phys. Chem.* **69(5)**, 1627 (1965).

[95] S. Auer, W. C. K. Poon, and D. Frenkel, *Phys. Rev. E* **67**, 020401 (2003).

[96] T. Koishi, K. Yasuoka, and T. Ebisuzaki, *J. Chem. Phys.* **119**, 11298 (2003).

[97] M. Matsumoto, S. Saito, and I. Ohmine, *Nature* **416**, 409 (2002).

[98] C. Valeriani, E. Sanz, and D. Frenkel, *J. Chem. Phys.* **122**, 194501 (2005).

[99] A. Page and R. Sear, *Phys. Rev. Lett.* **97**, 065701 (2006).

[100] P. R. ten Wolde, M. J. Ruiz-Montero, and D. Frenkel, *Phys. Rev. Lett.* **75**, 2714 (1995).

[101] S. Punnathanam and P. A. Monson, *J. Chem. Phys.* **125**, 024805 (2006).

[102] A. Cacciuto, S. Auer, and D. Frenkel, *Phys. Rev. Lett.* **93**, 166105 (2004).

[103] P. R.ten Wolde, M. J. Ruiz-Montero, and D. Frenkel, *J. Chem. Phys.* **104**, 9932 (1996).

[104] B. Cichocki and K. Hinson, *Physica A* **166**, 473 (1990).

[105] S. A. Auer, *Quantitative prediction of crystal nucleation rates for spherical colloids: a computational study*, University of Amsterdam (2002). It can be downloaded from:
$http://www.amolf.nl/publications/theses/auer$.

[106] P. Bartltett and A. I. Campbell, *Phys. Rev. Lett.* **95**, 128302 (2005).

[107] M. E. Leunissen, C. G. Christova, A. -P. Hynninen, C. P. Royall, A. I. Campbell, A. Imhof, M. Dijkstra, R. van Roij, and A. van Blaaderen, *Nature* **437**, 235 (2005).

[108] C. S.Towler, R. J. Davey, R. W. Lancaster, and C. J. Price, *J. Am. Chem. Soc.* **126**, 13347 (2004).

[109] L. M. Ghiringhelli, J. H. Los, E. J. Meijer, A. Fasolino, and D. Frenkel, *Phys. Rev. Lett.* **94**, 145701 (2005).

[110] X. Wang, S. Scandolo and R. Car, *Phys. Rev. Lett.* **95**, 185701 (2005).

[111] A. A. Correa, S. A. Bonev, and G. Galli, *Proc. Nat. Ac. of Science* **103**, 1204 (2006).

[112] The potential we use for the present study, labelled as LCBOPI$^+$, is fully described in Appendix A of: J. H. Los, L. M. Ghiringhelli, E. J. Meijer, and A. Fasolino, *Phys. Rev. B* **72**, 214102 (2005).

[113] S. Auer and D. Frenkel, *Ann. Rev. Phys. Chem.* **55**, 333 (2004).

[114] R. Car and M. Parrinello, *Phys. Rev. Lett.* **55**, 2471 (1985).

[115] L. M. Ghiringhelli, J. H. Los, E. J. Meijer, A. Fasolino, and D. Frenkel, *Phys. Rev. B* **69**, 100101(R) (2004).

[116] L. M. Ghiringhelli, *On the Nature of phase transitions in covalent liquids*, University of Amtserdam (2006). It can be downloaded from:
$http://dare.uva.nl/document/18341$.

[117] L. M. Ghiringhelli, J. H. Los, E. J. Meijer, A. Fasolino, and D. Frenkel, *J. Phys. Cond. Matt.* **17**, S3619 (2005).

[118] O. Mishima and H. E. Stanley, *Nature* **396**, 329 (1998); Y. Katayama, T. Mizutani, W. Utsumi, O. Shimomura, M. Yamakata, and K. Funakoshi, *Nature* **403**, 170 (2000); I. Saika-Voivod, F. Sciortino, and P. H. Poole, *Phys. Rev. E* **63**, 011202 (2000).

[119] K. F. Kelton, A. L. Greer, D. M. Herlach, and D. Holl, *M. R. S. Bullettin* **29**, 7931 (2004).

[120] S. E. Haggerty, *Science* **285**, 851 (1999); U. A. Jorgensen,*Nature* **332**, 702 (1988).

[121] J. I. Bergstrahl, E. D. Miner, and M. S. Matthews, *Uranus*, University of Arizona Press, Tucson (1991); M. Ross, *Nature* **292**, 435 (1981); S. Scandolo, G. Chiarotti, and E. Tosatti, *Physics World* **13**, 31 (2000); M. J. Kuchner and S. Seager, *Astr-phys/0504214*, preprint (2005).

[122] S. Scandolo and R. Jeanloz, *Am. Sc.* **91**, 516 (2003).

[123] J. L. Barrat, J. P. Hansen, and R. Mochkovitch, *Astronomy and Astrophysics* **199**, 15 (1988).

[124] J. H. Los, L. M. Ghiringhelli, E. J. Meijer, and A. Fasolino, *Phys. Rev. B* **72**, 214102 (2005).

[125] S. Fahy and S. T. Louie, and M. L. Cohen, *Phys. Rev. B* **34**, 1191 (1986).

[126] S. Scandolo, G. L. Chiarotti, and E. Tosatti, *Phys. Rev. Lett.* **74**, 4015 (1995).

[127] M. A. Kanter, *Phys. Rev.* **107**, 655 (1957).

[128] D. V. Fedosayev, B. V. Deryagin, and I. G. Varasavskaja, *Nauka* , Moscow (1984).

[129] P. G. Debenedetti, *Metastable Liquids*, Princeton University Press, New Jersey (1994).

[130] J. S. Rowlinson and B. Widom, *Molecular Theory of Capillarity*, Oxford University Press, New York (1982).

[131] J. G. Kirkwood and F. P. Buff, *J. Chem. Phys.* **17**, 338 (1949).

[132] R. H. Fowler, *Proc. R. Soc. A* **159**, 229 (1937).

[133] G. A. Chapela, G. Saville, S. M. Thompson, and J. S. Rowlinson, *J. Chem. Soc. Faraday Trans. II* **8**, 1133 (1977).

[134] E. M. Blokhuis, D. Bedeaux, C. D. Holcomb, and J. A. Zollweg, *Mol. Phys.* **85**, 665 (1995).

[135] M. M. Mecke, J. Winkelmann, and J. Fischer, *J. Chem. Phys.* **107**, 9264 (1997).

[136] Laplace, *Traite de Mechanique Celeste; Supplement au dixieme livre, Sur L'Action Capillaire*, Courcier, Paris (1806), and *Supplement a la Theorie de l'Action Capillaire*, reprinted in *Oeuvres complete de Laplace*, Volume **IV**, 349, Gauthiers-Villars, Paris (1880).

[137] J. D. Weeks, D. Chandler, and H. C. Andersen, *J. Chem. Phys.* **54**, 5237 (1971).

[138] R.W.Zwanzig, *J. Chem. Phys.* **22**, 1420 (1954).

[139] F.F.Abraham, *J. Chem. Phys.* **63**, 157 (1975).

[140] J. Q. Broughton and G. H. Gilmer, *J. Chem. Phys.* **79**, 5095 (1983); J. Q. Broughton and G. H. Gilmer, *J. Chem. Phys.* **84**, 5749 (1986).

[141] R. L. Davidchack and B. B. Laird, *J. Chem. Phys.* **118**, 7651 (2003).

[142] J. A. Barker and D. Henderson, *J. Chem. Phys.* **47**, 4714 (1967).

[143] R. L. Davidchack, J. R. Morris, and B. B. Laird, *J. Chem. Phys.* , **125** 094710 (2006).

[144] J. J. Potoff and A. Z. Panagiotopoulos, *J. Chem. Phys.* **112**, 6411,(2000).

[145] J. R. Errington, *Phys. Rev. E* **67**, 012102 (2003).

[146] A. Trokhymchuk and J. Alejandre, *J. Chem. Phys.* **111**, 8510 (1999).

[147] C. D. Holcomb,P. Clancy, and J. A. Zollweg, *Mol. Phys.* **78**, 437 (1993).

[148] M. J. P. Nijmeijer, A. F. Bakker, and C. Bruin,*J. Chem. Phys.* **89**, 3789 (1988).

[149] M. Haye and C. Bruin, *J. Chem. Phys.* **100**, 556 (1993).

[150] P. Adams and J. R. Henderson,*Mol. Phys.* **73**, 1383 (1991).

[151] J. J. Potoff and A. Z. Panagiotopoulos,*J. Chem. Phys.* **109**, 10914 (1998).

[152] J. R. Erringon and P. G. Debenedetti, *J. Chem. Phys.* **118**, 2256 (2003).

[153] K. S. C. Freeman and I. R. McDonald, *Mol. Phys.* **26**, 529 (1973).

[154] A. Mulero, C. Galan, and F. Cuarlos, *J. Phys. Cond. Matt.* **15**, 2285 (2003).

[155] V. K. Shen and P. G. Debenedetti, *J. Chem. Phys.* **111**, 3581 (1999).

[156] M. Shusser and D. Weihs, *International Journal of Multiphase Flow* **25(8)**, 1561 (1999).

[157] Y. L. Chen and J. Israelachvili, *Science* **252**, 1157 (1991).

[158] K. S. Suslick, *Science* **247**, 1439 (1990).

[159] V. K. Dhir, *Annual Review of Fluid Mechanics* **30**, 365 (1998).

[160] M. Blander and J. L. Katz, *AIChe Journal* **21**, 833 (1975).

[161] F. Abraham, *Homogeneous nucleation theory*, Academic Press, New York (1974).

[162] J. Frenkel, *Kinetic Theory of Liquids*, Oxford University Press, London (1955).

[163] G. W. Adams, J. L. Schmidt, and R. A. Zalabsky, *J. Chem. Phys.* **81**, 5074 (1984).

[164] C. Hung, M. J. Krasnopoler, and J. L. Katz, *J. Chem. Phys.* **90**, 1856 (1989).

[165] P. E. Wagner and R. Strey, *J. Chem. Phys.* **80**, 5266 (1984).

[166] M. A. Sharaf and R. A. Dobbins, *J. Chem. Phys.* **77**, 1982 (1982).

[167] E. Herbert, S. Balibar and F. Caupin, *Phys. Rev. E* **74**, 041603 (2006); F. Caupin, *Phys. Rev. E* **71**, 051605 (2005).

[168] J. L. Scgmitt, R. A. Zalabsky, and G. W. Adams, *J. Chem. Phys.* **79**, 4496 (1983).

[169] R. Strey, P. E. Wagner and T. Schmeling, *J. Chem. Phys.* **84**, 2325 (1986).

[170] F. Peters and B. Paikert, *J. Chem. Phys.* **91**, 5672 (1982).

[171] X. C. Zeng and D. W. Oxtoby, *J. Chem. Phys.* **94**, 4472 (1991).

[172] D. W. Oxtoby, V. Talanquer, and A. Laaksonen, *Nucleation: Measurements, Theory, and Atmospheric Applications*, *Annu. Rev. Phys. Chem.* **46**, 489 (1995); *Nucleation and Atmospheric Aerosols*, 21-29, Pergamon Press, New York (1996).

[173] J. W. Cahn and J. E. Hilliard, *J. Chem. Phys.* **31**, 688 (1959).

[174] N. P. Balsara, C. Lin, and B. Hammouda, *Phys. Rev. Lett.* **77**, 3847 (1996); A. C. Pan, T. J. Rappl, D. Chandler, and N. P. Balsara, *J. Phys. Chem. B* **110**, 3692 (2006).

[175] C. F. Delale, J. Hruby, and F. Marsik, *J. Chem. Phys.* **118**, 792 (2003).

[176] S. Nose, *J. Chem. Phys.* **81**, 511 (1984).

[177] H. C. Andersen, *J. Chem. Phys.* **72**, 2384 (1980).

[178] S. Melchionna, G. Ciccotti, and B. L. Holian, *Mol. Phys.* **78**, 533 (1993).

[179] Z. -J. Wang and D. Frenkel, *J. Chem. Phys.* **123**, 154701 (2006).

[180] P. R. ten Wolde, M. J. Ruiz-Montero, and D. Frenkel, *J. Chem. Phys.* **110**, 1591 (1999).

[181] F. H. Stillinger, *J. Chem. Phys.* **38**, 1486 (1963).

[182] P. Nikunen, M. Karttunen, and I. Vattulainen, *Comp. Phys. Comm.* **153**, 407 (2003).

[183] P. G. Bolhuis, *J. Phys. Cond. Matt.* **15**, S113 (2003).

[184] J. J. Nicolas, K. E. Gubbins, W. B. Street, and D. J. Tildesley, *Mol. Phys.* **37**, 1429 (1979).

[185] D. Levesque and L. Verlet, *Phys. Rev.* **182**, 307 (1969).

[186] B. Smit, *J. Chem. Phys.* **96**, 8639 (1992).

[187] N. B. Wilding, *Phys. Rev. E* **52**, 602 (1995).

[188] J. E. Finn and P. A. Monson, *Phys. Rev. A* **39**, 6402 (1989).

[189] B. Smit and D. Frenkel, *J. Chem. Phys.* **94**, 5663 (1991).

[190] P. Harrowell and D. W. Oxtoby, *J. Chem. Phys.* **80**, 1639 (1984).

[191] T. Zykova-Timan, D. Ceresoli, U. Tartaglino, and E. Tosatti, *Phys. Rev. Lett.* **94**, 176105 (2005).

[192] R. L. Davidchak and B. B. Laird, *Phys. Rev. Lett.* **94**, 086102 (2005).

[193] D. Turnbull, *J. Appl. Phys.* **21**, 1022 (1950); F. Di Tolla, *Interplay of Melting, Wetting, Overheating and Faceting on Metal Surface: Theory and Simulations*, SISSA Trieste (1995). It can be downloaded from: $http : //www.sissa.it/cm/phd.php$; V. Petrenko and R. W. Whitworth *Physics of Ice*, Oxford University Press (1999).

[194] D. Kashchiev, *J. Chem. Phys.* **118**, 9081 (2003).

[195] W. W. Mullins, *J. Chem. Phys.* **81**, 1436 (1984).

[196] P. Nozieres, *Solids far from equilibrium*, Cambridge University Press (1991).

[197] J. C. Heyraud and J. J. Métois, *J. Cryst. Growth* **84**, 503 (1987).

[198] These calculations were performed with the ESPResSo program package, see: H. - J. Limbach, A. Arnold, B. A. Mann, and C. Holm, *Comp. Phys. Comm.* **174**, 704 (2006).

[199] R. C. Tolman, *J. Chem. Phys.* **17**, 333 (1949) E. M. Blokhuis and J. Kuipers, *J. Chem. Phys.* **124**, 074701 (2006).

[200] A. Shi and M. Wortis, *Phys. Rev. B* **47**, 9804 (1993).

[201] A. Shi and M. Wortis, *Phys. Rev. B* **37**, 7793 (1988).

[202] A. Cacciuto, S. Auer, and D. Frenkel, *J. Chem. Phys.* **119**, 7467 (2003).

[203] F. P. Buff,*J. Chem. Phys.* **23**, 419 (1955).

[204] S. Kondo, *J. Chem. Phys.* **25**, 662 (1956).

[205] S. Ono and S. Kondo, *Encyclopedia of Physics*, SpringerLink, Berlin (1960).

[206] The Scientific Papers of J. Willard Gibbs. Volume **I**: Thermodynamics, Ox Bow Press, Woodbridge (1993): Eq. 500.

[207] J. E. Mayer, *J. Chem. Phys.* **1**, 270 (1933); M. L. Huggins and J. E. Mayer, *J. Chem. Phys.* **1**, 643 (1933).

[208] F. van Zeggeren and G. C. Benson, *J. Chem. Phys.* **26**, 1077 (1957).

[209] C. R. A. Catlow, K. M. Diller and M. J. Norgett, *J. Phys. C* **10**, 1395 (1977).

[210] K. Binder and H. Muller-Krumbhaar, *Phys. Rev. B* **9**, 2328 (1974).

[211] C. S. Kiang, D. Stauffer, G. H. Walker, O. P. Puri, J. D. Wise, and E. M. Patterson, *J. Atmos .Sci.* **28**, 1112 (1971); J. Feder, K. C. Russell, J. Lothe, and G. M. Pound, *Adv. Phys.* **15**, 117 (1966).

[212] M. E. Fisher, *Physics* **3**, 255 (1967).

[213] V. A. Shneidman, K. A. Jackson, and K. M. Beatty, *Phys. Rev. B* **59**, 3579 (1999).

[214] V. A. Shneidman, K. A. Jackson, and K. M. Beatty, *J. Chem. Phys.* **111**, 6932 (1999).

[215] B Peters and B. L. Trout, *J. Chem. Phys.* **125**, 054108 (2006).

[216] D. Stauffer, A. Coniglio, and D. W. Heermann, *Phys. Rev. Lett.* **49**, 1299 (1982).

[217] J. L. Lebowitz, J. Marro, and M. H. Kalos, *Acta Metall.* **30**, 297 (1982).

[218] F. F. Abraham, *Homogeneous Nucleation Theory*, Accademic Press, New York (1974).

[219] M. Acharya and D. Stauffer, *Eur. Phys. J. B* **5**, 571 (1998).

[220] K. Brendel, G. T. Barkema, and H. van Beijeren, *Phys. Rev. E* **71**, 031601 (2005).

[221] S. Wonczak, R. Strey, and D. Stauffer, *J. Chem. Phys.* **113**, 1976 (2000).

[222] A. C. Pan and D. Chandler, *J. Phys. Chem. B* **108**, 19681 (2004).

[223] T. G. Mason and J. Bibette, *Phys. Rev. Lett.* **77**, 3481 (1996).

[224] M. J. Morelli, R. J. Allen, and P. R. ten Wolde, in preparation (2007).

[225] E. N. M. Cirillo, G. Gonnella, and G. P. Saracco, *Phys. Rev. E* **72**, 026139 (2005).

[226] P. I. Hurtado, J. Marro, and P. L. Garrido, *Phys. Rev. E* **70**, 021101 (2004).

[227] P. I. Hurtado, J. Marro, and P. L. Garrido, *Phys. Rev. E* **74**, 050101 (2006).

[228] B. Smit, K. Esselink, and D. Frenkel, *Mol. Phys.* **87**, 159 (1996).

[229] C. Vega, J. L. F . Abascal, C. McBride, and F. Bresme, *J. Chem. Phys.* **119**, 964 (2003).

Summary

The focus of the research presented in this thesis is the study of nucleation pathways in a variety of different systems. To this end, we make use of existing and novel simulation techniques to study rare events, mainly the Umbrella Sampling [12, 11] (US) and a simulation method recently developed by Allen et al. [13, 14, 15] named Forward Flux Sampling (FFS). Differently from other path sampling techniques, FFS allows to evaluate *stationary distributions* for both equilibrium and non-equilibrium systems. We employ both US and FFS to compute the rate of nucleation in various systems. By means of FFS, we analyse the pathways taken by the system to nucleate a new thermodynamically stable phase from the metastable one, and through US, we compute free-energy nucleation barriers as a function of an order parameter relevant for the phase transition. Moreover, for the first time we numerically estimate free-energy barriers adopting the FFS technique (chapter 3).

Using FFS, we study crystal nucleation from the melt in charged systems. First, we explore *sodium chloride* (NaCl). Computing the nucleation rate by means of both US and FFS, we obtain the same results, thus validating the FFS scheme for the first time applied to crystal nucleation. We also observe that the critical cluster formed during the nucleation process has the crystal structure of bulk NaCl. Interestingly, the critical cluster is clearly faceted, presenting a cubical shape (see chapter 4). We then investigate a system made of oppositely charged colloids, and encounter a puzzling behaviour (chapter 5). Charged colloids show a "zoo" of crystal phases, as both Smit and Frenkel and Vega and coworkers [228, 229] have shown in the case of the Restricted Primitive model, and Hynninen et al. [17] in the case of a *Yukawa binary mixture*. By over-compressing the last system at constant temperature, we observe the growth of disordered fcc clusters of higher free energy than the ordered-CsCl counterparts, contradicting both the Stranski-Totomanow conjecture [16], and the Classical Nucleation Theory picture (CNT) [6]. Within CNT, preferred nucleation of the crystal structure with the higher nucleation barrier is possible when a large kinetic pre-factor compensates the effect of a higher barrier. However, in CNT, the kinetic pre-factor describes the rate at which clusters grow due to the attachment and detachment of single particles to a pre-existing crystallite, and the rate of addition and removal of particles is hardly different for fcc and CsCl clusters. What we believe happens instead, is that small clusters growing in the metastable liquid have a disordered fcc structure with higher probability. However, this structure cannot act as a template for subsequent CsCl growth, whilst a structural phase transition inside the clusters is kinetically inhibited.

We then carry on a study on the way crystal nucleation pathways change with thermodynamic conditions in *one-and-the-same* meta-stable liquid: *carbon*. Liquid carbon is fairly peculiar, as its local structure changes dramatically with temperature and pressure. At tem-

peratures of 5000K and pressures of 80GPa, it mainly manifests a *four-fold coordinated* structure, whereas at temperatures of 3800K and pressure of 30GPa it exhibits a *three-fold coordinated* structure. When studying nucleation in these two liquids, we observe that it is less favourable to create an interface between a crystallite with a diamond structure and a *graphitic-like* liquid than between the same crystallite and a *diamond-like* liquid. The unusual surface structure of the diamond cluster is an indication of the poor match between a diamond lattice and a graphitic-like liquid. We then extrapolate our results to carbon-rich planets and stars, and find that quite a high carbon concentration is needed to get homogeneous diamond nucleation: we conclude that it is extremely unlikely that diamonds can never have nucleated in the carbon-rich middle layer of planets such as *Uranus and Neptune*, while the appropriate thermodynamic conditions for diamond nucleation are present in *carbon-rich white dwarfs stars* (see chapter 6).

In chapter 7 we re-interpret and applied a standard thermodynamic *perturbation-based theory* to estimate both the liquid-vapour and the liquid-solid *inter-facial free energy* in a system with different truncations of the Lennard-Jones potential. We make the simplifying assumption (already made by Laplace) that the interface dividing the two phases is infinitely sharp, and find that on the one hand this approach is not correct for liquid and vapour at coexistence, as the dividing interface is fairly rough. On the other hand, to our surprise, the theory can be very useful in the case of estimating the liquid-solid inter-facial free energy of these truncated model potentials - this application is, to our knowledge, new.

Triggered by the work of Shen and Debenedetti [155], we also study the liquid-to-vapour phase transition, or *bubble nucleation*, from a Lennard-Jones fluid using the FFS scheme. To our knowledge, this is the first time Forward Flux Sampling is used in combination with a Molecular Dynamics simulation. We observe nucleation taking place via the formation of compact bubbles, contrary to the web-like-system-spanning critical clusters observed by Shen. We argue that the difference between the present results and those of ref. [155] are partly due to the use of a global order parameter by the authors but, more likely, because the simulations of ref. [155] were carried out at a state point relatively close to the liquid-vapour spinodal of the model system under study. We also compare the computed bubble-nucleation rate with the value estimated adopting CNT. We notice that in order for the simulations and the CNT prediction to match, we have to assume a relatively low value of the surface tension (γ) of the Lennard-Jones fluid. However, an exact calculation of γ is needed for a precise comparison (see chapter 8).

In chapter 9 we examine the differences between the liquid-solid *inter-facial free energy* measured by bulk properties and by Classical Nucleation Theory in *sodium chloride*. Zykova-Timan, Tosatti and coworkers [191] measured by means of computer simulations the liquid-solid inter-facial free energy of the Tosi-Fumi NaCl model at coexistence using the Young's equation in liquid droplet embedded in its vapour and deposited onto a NaCl [100] crystal plane. They obtained about one third of the value we got in chapter 4 employing CNT. In order to find the origin of this mysterious discrepancy, we thoroughly analyse the free energy of NaCl clusters obtained at melting conditions where liquid and solid coexist, and conclude that the surface free energy is subject to quite large finite size corrections that cannot be accounted for within a thermodynamic theory. Therefore, supporting Kelton's suggestion [6], we conclude that the large number of published surface free energies, based on

nucleation data, are of little use to predict macroscopic surface free energies.

The last chapter of this thesis (chapter 10) is devoted to a computational study of the effect of an *applied shear* on crystal nucleation in a lattice model: the two-dimensional Ising model. This type of non-equilibrium dynamics is rather artificial. It might be viewed as a rough description of the experimental situations of the droplet nucleation process in emulsions [223]. We find a dependence of the nucleation rate on the applied shear rate. On the one hand, at moderate shear rate, shearing a sub-critical cluster increase the number of kinks on its perimeter. The kinks are places where the growth of the cluster is favoured. We claim that this effect is essentially due to the discreteness of our system, and seem to be linear for small values of the shear rate. Moreover, we find similarities between our results and the same effect noticed in a model with an induced non-equilibrium microscopic disorder, along the line of Hurtado and coworkers [226, 227]. On the other hand, the higher shear rate increase the perimeter-to-area ratio of the critical clusters, leading to an effective decrease of the nucleation rate. To conclude, we also suggest that the clusters roughness (number of concave kinks in the growing clusters) might be a relevant order parameter, together with the biggest cluster size, to study the nucleation phenomenon.

Samenvatting[1]

Het onderzoek in dit proefschrift focusseert zich op de studie van nucleatie paden in verschillende systemen. Hiervoor gebruiken we bestaande en nieuwe simulatie methoden voor de studie van zeldzame gebeurtenissen, voornamelijk de Umbrella Sampling [12, 11] (US) en de Forward Flux Sampling (FFS) simulatie methode welke recentelijk ontwikkeld is door Allen et al. [13, 14, 15]. In tegenstelling tot andere path sampling technieken, kan FFS stationaire distributies bepalen voor zowel evenwicht en niet-evenwicht systemen. Om de nucleatie snelheid in verschillende systemen te berekenen passen we zowel US en FFS toe. Met behulp van FFS analyseren we paden die het systeem neemt bij de nucleatie van een nieuwe thermodynamisch stabiele fase vanuit een metastabiele fase. Met behulp van US berekenen we de vrije energie nucleatie barrières als functie van een voor de fase transitie relevante orde parameter. Bovendien berekenen we voor het eerst de vrije energie barrières met behulp van de FFS methode (hoofdstuk 3).

Met behulp van FFS bestuderen we kristal nucleatie van supergekoelde vloeistof in geladen systemen. Eerst onderzoeken we natrium chloride (NaCl). De berekening van de nucleatie snelheid met zowel US en FFS levert dezelfde resultaten op, waarmee we voor het eerst de FFS methode valideren voor kristal nucleatie. We zien ook dat de kritische cluster die gedurende het nucleatie proces gevormd wordt, de kristal structuur heeft van bulk NaCl. Het is interessant dat de kritische cluster duidelijke vlakken vertoont, resulterend in een kubusvorm (zie hoofdstuk 4). Vervolgens onderzoeken we een systeem van tegengesteld geladen colloïden, en stuiten op een vreemd gedrag (hoofdstuk 5). Geladen colloïden tonen een "dierentuin" van kristal fases, zoals zowel Smit, Frenkel en Vega en medewerkers [228, 229] hebben aangetoond in het geval van het Restricted Primitive model, en Hynninen et al. [17] in het geval van een Yukawa binary mixture. Door het laatste systeem bij constante temperatuur extreem samen te drukken, vinden we de groei van ongeordende fcc clusters met hogere vrije energie dan bij geordend CsCl, wat zowel de Stranski-Totomanow beraming [16], en het Classical Nucleation Theory (CNT) beeld [6] tegenspreekt. Binnen CNT, is de geprefereerde nucleatie van de kristal structuur met een hogere nucleatie barrière mogelijk wanneer een grote kinetische pre factor het effect van de hogere barrière compenseert. In CNT beschrijft de kinetische pre factor echter de snelheid met welke clusters groeien door binding en het loslaten van enkele deeltjes aan een vooraf bestaande crystallite, en de snelheid van toevoeging en verwijdering van deeltjes is nauwelijks anders voor fcc en CsCl clusters. Wij geloven daarentegen dat kleine clusters die in de metastabiele vloeistof groeien, een hogere waarschijnlijkheid hebben om een ongeordende fcc structuur te hebben.

[1] Translation by Daan Kiviet

Deze structuur kan echter niet dienst doen als template voor de daarop volgende CsCl groei, omdat een structurele fase transitie binnen de clusters kinetisch geïnhibeerd is.

Vervolgens bestuderen we hoe kristal nucleatie paden veranderen afhangen van thermodynamische condities in één en dezelfde metastabiele vloeistof: koolstof. Vloeibaar koolstof is een beetje vreemd, aangezien haar locale structuur dramatisch verandert afhankelijk van temperatuur en druk. Bij een temperatuur van 5000K en een druk van 80GPa, bevindt het zich vooral in een viervoudig gecoördineerde structuur, terwijl bij een temperatuur van 3800K en een druk van 30GPa het een drievoudig gecoördineerde structuur vertoont. Bij het bestuderen van nucleatie in deze twee vloeistoffen, zien we dat het minder aantrekkelijk is om een interface te creëren tussen een crystallite met een diamantachtige structuur en een grafietachtige vloeistof dan tussen hetzelfde crystallite een diamantachtige vloeistof. De ongebruikelijke oppervlakte structuur van de diamant cluster gaf aan dat er een slechte match is tussen een diamant rooster en een grafietachtige vloeistof. Wanneer we onze resultaten vervolgens extrapoleren naar koolstofrijke planeten en sterren, zien we dat een vrij hoge koolstof concentratie nodig is voor homogene diamant nucleatie: we kunnen concluderen dat het extreem onwaarschijnlijk is dat nucleatie van diamanten ooit plaatsvindt in de koolstofrijke middelste laag van planeten zoals Uranus en Neptunus, terwijl de benodigde thermodynamische condities voor diamant nucleatie wel aanwezig zijn in koolstofrijke witte dwerg sterren (zie hoofdstuk 6).

In hoofdstuk 7 herinterpreteren we een standaard thermodynamische op perturbatie gebaseerde theorie en passen het toe om zowel de vloeistof-damp en de vloeistof-vaste stof inter-facial vrije energie te berekenen in een systeem met verschillende afkappingen van de Lennard-Jones potentiaal. Hierbij maken we de simplificerende aanname (reeds gemaakt door Laplace) dat het scheidingsvlak tussen de twee fases oneindig scherp is, en vinden dan dat deze benadering aan de ene kant niet juist is wanneer vloeistof en damp tegelijkertijd bestaan, vanwege het feit dat hun scheidingsvlak dan vrij ruw is. Aan de andere kant, en tot onze verrassing, is de theorie goed bruikbaar om de vloeistof-vaste stof inter-facial vrije energie te bepalen van deze afgekapte model potentialen - deze toepassing is zover wij weten nieuw.

Gestimuleerd door werk van Shen en Debenedetti [155], bestuderen we ook de vloeistof naar vaste stof fase transitie, oftewel bubble nucleatie, van een Lennard-Jones vloeistof gebruikmakend van het FFS methode. Voor zover wij weten, is dit de eerste keer dat Forward Flux Sampling gebruikt wordt in combinatie met een Molecular Dynamics simulatie. Hierbij zien we dat nucleatie plaatsvindt via de vorming van compacte belletjes, in tegenstelling tot de web-like-system-spanning kritische clusters die door Shen zijn waargenomen. We redeneren dat het verschil tussen de onze resultaten en die van referentie [155] gedeeltelijk zijn toe te schrijven aan hun gebruik van globale order parameters, maar vooral aan het feit dat de simulaties van referentie [155] uitgevoerd zijn bij een state point dat vrij dicht bij de vloeistof-damp spinodal ligt van het bestudeerde model systeem. We vergelijken de berekende snelheid van bel nucleatie ook met de waarde zoals bepaald met de CNT methode. Hierbij valt het op dat om de simulatie en CNT voorspellingen te laten overeenkomen, het nodig is om een relatief lage waarde van de oppervlaktespanning (γ) van de Lennard-Jones vloeistof aan te nemen. Desondanks, is het voor een precieze vergelijking nodig om γ exact te berekenen (zie hoofdstuk 8).

In hoofdstuk 9 bestuderen we hoe de vloeistof-vaste stof inter-facial vrij energie in natrium chloride verschilt wanneer die berekend wordt met behulp van bulk eigenschappen of met de Klassieke Nucleatie Theorie. Zykova-Timan, Tosatti en medewerkers [191] hebben de vloeistof-vaste stof inter-facial vrije energie van de Tosi-Fumi NaCl model bij coexistence door gebruik te maken van de Young formule in een gesimuleerde vloeistof druppel, ingebed in zijn damp en gedeponeerd op een NaCl [100] kristal laag, en bepaalde een waarde welke ongeveer een derde van is van de waarde die wij met behulp van CNT vinden in hoofdstuk 4. Om de reden van deze mysterieuze discrepantie te vinden, analyseren we de vrij energie van NaCl clusters bij smelt condities waar vloeistof en vaste stof tegelijkertijd bestaan, en komen vervolgens tot de conclusie dat de oppervlakte vrije energie bloot staat aan vrij grote finite size correcties die binnen de thermodynamische theorie genegeerd worden. Derhalve concluderen we dat, Keltons suggestie bevestigend [6], de grote hoeveelheid vrije oppervlakte energieën die gepubliceerd zijn op basis van nucleatie gegevens, weinig nut hebben om macroscopische vrije oppervlakte energieën te voorspellen.

Het laatste hoofdstuk van dit proefschrift (hoofdstuk 10) is toegewijd aan de computationele studie van het effect van een toegepaste shear bij kristal nucleatie in een rooster model: het tweedimensionale Ising model. Dit soort niet-evenwicht dynamica is vrij artificieel. Het kan gezien worden als een ruwe beschrijving van de experimentele situatie van het druppel nucleatie proces in emulsies [223]. Wij vinden dat de nucleatie snelheid afhankelijk is van de toegepaste shear snelheid. Aan de ene kant vermeerdert bij een gematigde shear snelheid het shear-en van subkritische cluster het aantal breuken aan de rand. Deze breuken zijn plekken waar groei van het cluster gunstig is. Wij claimen dat dit effect in wezen veroorzaakt wordt door het discreet zijn van ons systeem, en lijkt het lineair te zijn voor kleine waardes van de shear snelheid. Bovendien vinden we overeenkomsten tussen onze resultaten en waarnemingen van hetzelfde effect door Hurtado en medewerkers [226, 227] in een model met geïnduceerde niet-evenwichtige microscopische wanorde. Aan de andere kant, verhoogt de hogere shear snelheid de omtrek-oppervlakte verhouding van de kritische clusters, wat leidt tot een effectieve vermindering van de nucleatie snelheid. Tot besluit, suggereren we dat de ruwheid van de clusters (gedefinieerd door het aantal concave breuken in de groeiende clusters) een relevante orde parameter kan zijn, samen met de grootste cluster grootte, om het nucleatie fenomeen te bestuderen.

La nucleazione

Cinque anni orsono decisi di partire alla volta dell'Olanda con l'intenzione di studiare un fenomeno fisico chiamato *nucleazione*. Anche se puo' suonare sconosciuto, cio' che viene indicato con il termine di nucleazione e' un fenomeno molto diffuso nella vita quotidiana di ognuno di noi.

Cominciamo pero' dall'inizio. Tutta la materia in Natura si puo' presentare in tre stati distinti: solido, liquido o gassoso. Prendiamo come esempio l'acqua: e' esperienza comune il fatto che a temperatura e pressione *ambiente* (riscontrabili nella cucina di casa) l'acqua esiste nello stato liquido, come quella che esce dal rubinetto del lavandino. Ora, noi italiani sappiamo bene che mettendo una pentola sul fuoco per preparare la pasta, dopo un po' di tempo l'acqua *bolle*: passa quindi dallo stato liquido a quello gassoso. Un altro esperimento casalingo consiste nel mettere una bottiglia di acqua "al fresco" nel congelatore. Sappiamo tutti che e' bene non dimenticarla per troppo tempo, visto che l'acqua solidifica diventando *ghiaccio*, e puo' anche rompere il vetro della bottiglia!

Appare chiaro da queste osservazioni come cambiando la temperatura a pressione costante, sia possibile portare un sistema fisico (l'acqua) da uno stato (liquido) a un altro (gassoso o solido). Ora voi vi chiederete: ma in tutto cio', la nucleazione che c'entra? La mia risposta e': "C'entra c'entra". Si chiama nucleazione proprio il *meccanismo* di trasformazione da uno stato della materia all'altro. In pratica, quello che succede *ad un certo punto* alla nostra bottiglia d'acqua nel congelatore e' la formazione *in un punto imprecisato* del liquido di un cristallo di ghiaccio piccolo piccolo, che poi cresce solidificando tutta l'acqua della bottiglia.

"Ma e' mai possibile che ancora oggi non si sappia esattamente come avviene la trasformazione dell'acqua in ghiaccio?". Vi stupiro' dicendovi che il fenomeno della nucleazione, pur essendo diffusissimo in Natura e antico quanto le stelle che sono in cielo, non e' ancora del tutto compreso. Questo costituisce una ragione in piu' per cui molti scienziati in tutto il mondo e da qualche secolo sono interessati a displicarne i misteri. Ma dietro a tutto questo studio, non c'e' solo puro diletto intellettuale: l'intenzione e' ben piu' ambiziosa. Capendo il meccanismo che governa questo fenomeno fisico, potremo imparare a controllarlo, limitandone i danni e beneficiandone dei vantaggi. E come se non bastasse, in futuro potremmo persino utilizzare la nucleazione a scopi tecnologici.

Iniziamo con il vedere la diffusione che la nucleazione ha in Natura. Senza andare troppo lontano, questo fenomeno puo' malauguratamente anche avvenire nel nostro organismo, causando disturbi piu' o meno gravi. L' anemia falciforme e' una malattia genetica debilitante, che colpisce centinaia di migliaia di bambini ogni anno in tutto il mondo. E' stato recentemente dimostrato che il suo primo evento patogeno e' la nucleazione di un mutante dell'emoglobina, la proteina del sangue responsabile del trasporto di ossigeno, con la

conseguente formazione di forme anomale. Esistono molte altre malattie dell'uomo come l'Alzheimer e la mucca pazza che iniziano con la nucleazione di alcune proteine. Persino, i meno gravi seppur dolorosi calcoli renali hanno origine da un fenomeno di nucleazione di un composto organico, l'ossalato di calcio.

Tuttavia, anche se dannosa per noi, la nucleazione puo' essere un processo molto importante per molti altri organismi viventi. Sempre di nucleazione si tratta se pensiamo al guscio delle chiocciole. Queste ultime sono animali invertebrati che formano il loro esoscheletro *nucleando* un composto inorganico, la calcite (carbonato di calcio). Lo stesso dicasi per il guscio di altri organismi marini tra cui le prelibate ostriche.

Sembra quindi evidente che la nucleazione della calcite avviene in condizioni ambiente, ossia a temperature e pressioni che si trovano sulla superficie della terra. Ma la nucleazione e' presente anche all'interno del nostro pianeta. Infatti nella crosta terrestre, dove temperature e pressioni sono molto elevate, ci sono le condizioni per cui il carbonio si trasforma nella gemma piu' preziosa e antica del mondo: il diamante. Ma attenzione: lo stesso carbonio a condizioni di pressione e temperatura diverse puo' formare, sempre per mezzo della nucleazione, un cristallo assai meno prezioso quanto utile: la grafite.

Un modo per capire cosa origini la formazione di fasi cosi' diverse sarebbe quello di fare esperimenti in laboratorio che riproducano la nucleazione di diamante e grafite a partire da un liquido costituito solo di carbonio puro. Tuttavia, le temperature e pressioni a cui questo fenomeno avviene sono proibitive in qualsiasi laboratorio moderno.

Una soluzione a questo problema e' l'uso di simulazioni al calcolatore. La simulazione al calcolatore e' nata piu' o meno dopo l'avvento dei primi calcolatori circa cinquanta anni fa, e puo' essere di supporto sia agli esperimenti, soprattutto quando non realizzabili (come nel caso delle formazione del diamante), sia che alle teorie, al fine di testarne la validita'.

Per mezzo delle simulazioni al calcolatore, e' quindi possibile studiare i meccanismi microscopici su cui si fonda la nucleazione. Torniamo al nostro esperimento della bottiglia di acqua nel congelatore; le simulazioni al calcolatore possono essere usate come una *lente di ingrandimento* che permette di sapere *quando* e *dove* si formeranno i piccoli cristalli di ghiaccio.

E proprio le simulazioni al calcolatore sono il mezzo da me utilizzato per investigare come si forma un cristallo di sale da cucina, provare che i diamanti non si possono trovare su pianeti gassosi come Urano e Nettuno, ma sono invece presenti nelle nane bianche, e approfondire come bolle un liquido (l'Argon). Quest'ultimo argomento ha delle immediate applicazioni tecnologiche, visto che l'ebollizione di un liquido se non controllata, puo' essere molto pericolosa, specialmente nel trasporto di gas naturali liquefatti o in reattori nucleari.

In futuro, la nostra speranza e' quella di arrivare ad una comprensione totale del processo di nucleazione, sia con l'intento di spiegare molti fenomeni naturali, ma anche con lo scopo di utilizzare la nucleazione in modo controllato a fini medici e tecnologici.

Acknowledgments-Ringraziamenti

Daan has been my PhD supervisor during the last five years. Working with Daan has been an amazing experience. His wide knowledge allowed me to learn interesting and different "hot topics" in the Physics of Matter. With Daan, I always had the impression to have the freedom to learn and explore several scientific issues. However, this exploration could not overcome a certain threshold, beyond which Daan would intervene to put me back on track. His enlightening "zipped" solutions to my scientific problems, have revealed to be as helpful as valuable (once unzipped). He was always patient during my learning, and gave me many possibilities to broaden my scientific knowledge, allowing me to visit labs in other countries, and attend to many physics schools and international conferences. Moreover, he transferred to me his enthusiasm, creating an enjoyable working atmosphere within the computational physics group at Amolf.

The same cooperative and friendly atmosphere could be found in the all bio-soft-matter simulation-theory-experiments Amolf's wing: the Overloop. I enjoyed and learnt a lot from scientific discussions with Pieter Rein and Bela, and from our "controversial" weekly group meetings. Also many post-docs actively and patiently contributed to the learning that finally led to my scientific work. Angelo who helped me to start. He had also been a really good friend, and initiated me to the fascinating world of the trumpet. Harald, who tough me with his kind attitude the way to be a good teacher, and gave me many valuable advices on writing down my work. The most supportive "woman-in-science" had been Rosalind. She explained me how to use the Forward Flux Sampling scheme, a technique I thoroughly adopted throughout all my work, and was an extremely valuable coworker. With Georgios I shared endless scientific conversations, whereas Peppino taught me the way to be relaxed still keeping the passion for science.

My PhD thesis could not have included all these chapters without the collaboration with many colleagues-now-friends: Eduardo (and our sodium chloride project, involving "la ballena piloto"), Luca Maria (and our endless conversations by phone), Zunjing ("Katanga, the whishing Chinese" full of energy), Tanya (and her lively temper) and Sorin (and his critic and analytic mind). I had enormously benefited from working with all of them, and last but not least, had a lot of fun!

My scientific adventure began in Rome, in the group of Francesco Sciortino, where I did my Master thesis guided also by Antonio, a funny "monarchist" post-doc from Napoli. Francesco gave me the possibility to approach the field of Physics of Matter studied by means of computer simulations... and I liked it a lot! Thus, in October 2002 I moved to Amsterdam, full of enthusiasm and curiosity. And my adventure in the *water-land* started...

Daan's group has always been multi-cultural and full of nice people. Just arrived, I received

a warm welcome by Tanya, Mark and Chinmay; a German, an English (Maltese) and an Indian post-doc willing to help me and involve me in their activities, ranging from a harmless singing chorus directed by Mark-the musician, to an exiting Judo lesson with the energetic-Tanya, and a funny trip to Germany, where Chinmay started learning Italian by reading my "really-really nice" Noam Chomsky's book.

At that time, a characteristic of Amolf was the relatively big size of the Italian community, mainly concentrated in the Overloop wing. A considerable issue in our "Little Italy", strangely enough, was the food. Important events were Angelo's cheese and Mirto from Sardegna, Marco J's "polenta" from Bergamo, my grandma's "fettine panate", and Ivan-Aifan Colvezza's notorious "magic" bags, filled with all the food cooked by his mum. There was also a lot of cooking activity: Fabiana experimented different kinds of "risotto", Angelo and Marco made an excellent "limoncello", and Fabrizio-babbo Capuani and his girlfriend Annamaria, delighted us with delicacies from "Napoli e dintorni". The crew was also made up of Marco-Costantino Lagomarziano with his positive way of life, and his friendly girlfriend Barbara, Bea-Donna Marino, "half woman-half elf" and her magic land, and Daniele (at the UvA) notorious for his amusing parties. However, with time the Italian community in Amolf suffered a shrinkage, the only new-comers being Paolo-Nederlandse spreker, Matteo-la coscienza del popolo italiano and his family, and Mimmo-il cuoco.

Time going by, the flow of people in our group never stopped, always bringing friendly people, fellows first, friends next: if-I-understand-correctly Georgios ("gboul"), Peppino-Peppino, Tati, with whom I swam in the dutch waters (swimming pool, not canals), Behnaz, with whom I shared the passion for "speekstein", and Rosalind, with whom I had a go to play music for a trumpet-saxophone duo. And also Koos and his availability, Axel and his penguin, Live and her babies, and Patrick and his improvised Italian-English translation.

Our group, the computational physics group, has been located for a long while in the "Overloop", continuation of the main Amolf building into a prefab one too hot in summer and too cold in winter. Even though properly thermalised by means of air-conditioners and heaters, seeking the "correct" temperature in our office has always been a delicate issue. On one side Marco J, such as "don Quijote" fighting against wind-mills, claimed his rights to keep the room temperature slightly lower than his body temperature (or "at least" at 25 degree Celsius), on the other side Dima (with his diplomacy), myself ("the chief penguin") and Rhoda (with her goodness) tried an exhausting and daily campaign to convince him that "cool is cool".

The Overloop also lodged "theorists", "experimentalists", and "bio-simulators", big words translated into friendly and cheerful people, such as Daan K, Frank, Julien, Simon, Kostya, Page, Aileen, Ruud, Rutger, Siebe, Liedewij, Laura, Gertjan and Nienke, only to mention "few" of them. They contributed to create an enjoyable working atmosphere, peaked at the funny and relaxing Friday evenings at the "East of Eden". In this enviable working environment, there were also "the visitors", young scientists from all over the world coming every year to Amolf, the "Mecca" for computer simulators. Thus, I could enjoy the presence of Nadia with her kindness (and her chocolate fondue), Yuri with his never-ending energy (and the yellow monster only he could tame), Bianca with her generosity (and her appelstrudel), and Eduardo. As all the other visitors, he was here to learn new simulation techniques. We then though it could be nice to work together at crystal nucleation from molten sodium chloride.

We spent a lot of time discussing together: I really appreciated his careful attitude towards science, his curiosity, his will and ability to learn always something new, and his sensible solutions to problems. But also enjoyed working with him, valuing his sense of humour, funny jokes and vitality. I am very happy to have had the luck to meet him, and willing to live with him many "scientific and non" adventures.

My non-scientific life was shared between "Little Italy" and the rest of the world, highly present here at Amolf, such as the french community with Nicolas "the climber", Boris "the runner", and Sebastian and Celine and their fantastic parties. Besides french parties, I discovered the importance of food and hospitality not only in the chinese culture, when having "luculliane" dinners first at Wenbing's later at Zunjing's home, but also in slovakian culture, as Jozef and Renata explained me while I was filling my mouth with cheese from Kosice, and of course in spanish culture, as I confirmed eating Andrea F's "patatas a la riojana". I also spent nice evenings chatting and cooking Italian-Greek-English food with Olgaki, an always-smiling greek. Her wedding in Corinthos with Panaio' was an unforgettable experience, visiting the ancient Greek ruins and dancing "sirtaki"with Georgiana and Thea.

The Italian "food-lovers" community extended its boundary also outside Amolf's gates. Andrea, Valentina and Lorenzino's house was always open for hungry (or lazy) brothers and sisters knocking at their door. Enrico's "crostata" was one of the best cake you could ever dream of (even better than my mum's one). Whereas at Marco and Pasquale's you could savour a tasty and "creative" regional cuisine from Calabria. The "stereotypical" Italian passion towards food and cooking, tantalised Salina's attention so much, to induce her to shoot a short movie titled "Cake" on it.

During these years, I discovered to appreciate dutch specialities such as Karnemelk, croquettes, and paling, traumatising "Little Italy", who threatened me to formally ask the Italian embassy for the withdrawal of my passport. However, my "dutch experience" went beyond the food: I had to see for myself the "housing" problem. Someone once told me: housing in Amsterdam is really difficult. Now I know he was right: in five years I moved seven times. However, looking back, this "inconvenience" allowed me to live in different and interesting neighbourhood in Amsterdam, from the Moroccan to the Jewish one, and most of all, to meet nice people. As soon as I arrived, I stayed at the guest house in Middenweg, a comfortable flat where I was lucky enough to share with a really nice couple: Tanya and Douggy, with which I experienced my first days in Amsterdam. After the guest house, I moved to Watergraafsmeer, a residential and quite neighbourhood for medium-class dutch-families very close to the lab, where I shared the apartment with the Ukrainian-Canadian Anna. After a "relaxation time" to adjust one another, I discovered her delicious Ukrainian borsch, and her patience when I started to learn the trumpet. We also shared a common interest in the "Alexander technique", taught us by Marja, a positive and calm dutch woman who also gave me few insights on the dutch culture and tips on good restaurants in Amsterdam. Next stop was a flat in the "Indische Buurt", a colourful neighbourhood mainly inhabited by Turkish and Moroccan Amsterdammers, where Laura and Peppino have been two discreet and very friendly flat-mates. The evenings spent with Peppino chatting in the kitchen, while drinking tea and always hearing someone calling upon "Tyson", built our endurable friendship. At last, I moved with Eduardo to the "Jewish quarter" of Amsterdam, in an old house with a nice garden. Thanks to the vicinity of the water, we could enjoy the Amsterdam experience

of “boat trips” along the canals with our friend and neighbour Christian.

Nothing that I have told you until now, would have been possible without the support of my family and friends in Rome (and the legendary yellow boxes labelled with the “Poste italiane” logo I have quite often received from my mum).

Questi anni hanno dato la conferma di quanto forte e profondo sia il mio legame con la citta' che mi ha dato i natali, *Roma*. Roma e' una citta' splendida, per la monumentalita' delle sue piazze, i colori dei suoi palazzi, la bellezza delle sue fontane. Ma ai miei occhi, quello che la rende ancora piu' “grande”, sono le persone che la abitano: la mia famiglia e i miei amici.

La mia “grande” famiglia mi ha sempre aiutato e mi e' stata vicina in tutti questi anni olandesi, imparando persino ad apprezzare “haring”, “Gouda kaas”, e “stroopwafel” da me inflitti come regalo a tutte le feste comandate. La lista e' lunga, ma non per questo difficile da ricordare: Mamma, Papa' e Maria, Valerio e Michela, nonna Elena, zio Alberto, zia Teresa, Caterina e il Principe e Giulio, Elisabetta e Rocco e Roberto, Giorgio, Luigi-cugino e Iacopo e Cristina, zio Francesco e zia Paola, Aurora e Andrea, Annalaura, zio Maurizio e zia Simona, Elena, Roberto. Mi piace pensare alla mia come a una famiglia estesa, dove i legami non sono solo quelli di sangue, ma anche quelli costruiti dalle vicissitudini e dal tempo passato insieme. Per questo, includo Francesca-Primo, l'amica con cui ho uno “storico” e profondo vissuto comune (e Sergio, Roberta e Francesco), e Duccio e Laura-Erla (ancge detta Obi-one), altro storico ramo della mia “grande” famiglia.

Anche i miei amici romani sono sempre stati presenti in questa mia avventura. Noncuranti della distanza, piu' di una volta hanno valicato le Alpi, calando fino nel freddo e umido Nord e rallegrandomi innumerevoli fine settimana. Protagonisti di questi viaggi sono stati Paolotto, Bob, Maria Vittoria Turini e Gianfranco, Francesco Paolo, Nicola, Felix, Giampaolo, Leonardo, Alessandro e Giuditta. Quest'ultima, insieme a Debora e Nadienji sono le amiche con cui ho piu' intensamente vissuto l'esperienza universitaria alla facolta' di Fisica di Roma, tra nottate sopra i libri, “presepi viventi”, feste a Capranica e gite a Saturnia insieme a Cristian Marco, Davide, Danielone, Marchija', Elena, Andrea Lunari e molti altri amici di cui sempre avro' un' indimenticabile ricordo.

The Roman Emperor Adriano built an imponent wall to prevent military raids by ancient Scottish tribes. By means of a big wall, he clearly indicated the boundary between the Roman Empire and the “Caledonian” region, nowadays better known as Scotland. However, differently from the Romans, I decided to dare more and, still full of enthusiasm and curiosity, go beyond "the wall" and reach the cold and hilly Edinburgh with Eduardo.